Design, Development and Testing of Solar Air Heater for Drying Applications

A thesis submitted in partial fulfilment of the requirements for the degree of

Doctor of Philosophy

by
G. Sureandhar
Roll No: **156151009**

Under the supervision of

Prof. P. Muthukumar
Prof. Senthilmurugan Subbiah

School of Energy Science and Engineering
Indian Institute of Technology, Guwahati
Guwahati – 781039, India
September, 2023

School of Energy Science and Engineering

Indian Institute of Technology, Guwahati

Guwahati – 781039, Assam, India

DECLARATION

I, hereby declare that the research findings in this thesis entitled **“*Design, Development, and Testing of Solar Air Heater for Drying Applications*”** are the results of original research work carried out by me under the supervision of Prof. P. Muthukumar, Department of Mechanical Engineering and Prof. Senthilmurugan Subbiah, Department of Chemical Engineering, Indian Institute of Technology Guwahati, for the award of the degree of Doctor of Philosophy. The results reported herein has not been submitted elsewhere for any degree or membership of any institute or university to the best of my knowledge and belief. Also, due acknowledgements have been made wherever the research findings of other researchers have been cited in this thesis.

Date:

Place:

G. Sureandhar

[Roll number: 156151009]

School of Energy Science and Engineering

Indian Institute of Technology, Guwahati

Guwahati – 781039, Assam, India

CERTIFICATE

This is to certify that the work contained in this thesis entitled **"*Design, Development, and Testing of Solar Air Heater for Drying Applications*"** by **G. Sureandhar (156151009),** a student of the School of Energy Science and Engineering, Indian Institute of Technology, Guwahati, for the award of the degree of Doctor of Philosophy has been carried out under my supervision and that this work has not been submitted elsewhere for any degree.

Date:
Place:

(Signature of Thesis Supervisor)
Prof. P. Muthukumar,
Professor, Department of Mechanical Engineering,
Indian Institute of Technology Guwahati,
Guwahati – 781039, Assam, India.

(Signature of Thesis Supervisor)
Prof. Senthilmurugan Subbiah
Professor, Department of Chemical Engineering,
Indian Institute of Technology Guwahati,
Guwahati – 781039, Assam, India.

Dedicated to

ALMIGHTY

ACKNOWLEDGMENTS

I would like to express my heartfelt gratitude to my supervisors, Prof. P. Muthukumar and Prof. Senthilmurugan Subbiah, for their unwavering scholastic guidance, invaluable advice, and constant motivation from the very start of my Ph.D. journey. Theirs's expertise in the subject was instrumental in shaping my research topic, and I will forever remain indebted to them for their generosity, selfless support, and continuous encouragement during the most challenging days of my academic life. Their unwavering dedication to research serves as a constant source of motivation for me.

I extend my sincere thanks to the members of my Doctoral Committee, Prof. Amaresh Dalal, Dr. Pankaj Kalita, and Dr. Ananda Lakshmi, for their valuable guidance, insightful comments, and keen interest throughout the research period. I am also grateful to NewGen IEDC and the School of Energy Science and Engineering, I.I.T Guwahati for providing financial assistance for setting up the necessary infrastructure and instrumentation.

I want to convey my appreciation to my project seniors, Dr. Srinivasan and Dr. Alok Kumar, for their invaluable assistance during my research work.

Furthermore, I would like to express my gratitude to my Doctoral Seniors, including Dr. Dev Kanta Rabha, Dr. Hakeem Niyas, Dr. Chilaka Ravichandra Rao, Dr. Bukke Kiran Naik, Dr. Jasinta Poonam Ekka, Dr. D. V. N. Lakshmi, Dr. Vishal Kumar Verma, Dr. Aanisha Akthar, Dr. Habtom Teklu, Dr. R. Nithin Narmada, Dr. K. Vigneshwaran, Dr. Lav Kumar Kaushik, Dr. S. Nivedhitha, Dr. Gurpreet Singh Sodhi, and Dr. Selva Senthil, for generously sharing their knowledge and experiences in the research field.

My sincere thanks also go to my lab-mates, including Dr. Mrinal Bhowmik, Dr. Viswanth Rambha, Dr. Muni Raja Tippa, Dr. Sunita Deb, Dr. J. Sunku Prasad, Dr. Pratibha Maurya, Ms. Neelam Dutta, Dr. M. Arun Kumar, Dr. Sayantan Jana, Mr. C. Aswin Karthik, Mr. Tat Suraj Arun, Mr. Shubham Parashar, Mrs. Juri Sonowal, Mr. Abhishek Parida, Ms. Nayanita Kalita, Dr. Sofia Rani Shaik, Ms. Akshini More, Mr. Puneet Kumar Nema, Dr. Anaya Bardhan, Mr. M. Balakumara Vignesh, Mr. Dinesh Kumar Gautam, Mr. Naveen Kumar, Dr. Priyamjeet Deka, Mr. V. Shanmugam, Mr. Jenga Venkatesh, Ms. Seema Bharati, Mr. Krishnendu Bala, Mr. Mukesh Gupta, and Ms. Pooja Koch.

Additionally, I extend my gratitude to Dr. Smruti Ranjan Dash, Dr. M. Rajendran, Dr. Rahul Narasimhan, Mr. M. Sathish Raj, Mr. S. R. Vigneshwaran, and Dr. C. Vignesh Kumar for their unwavering support at every stage of my research work.

I am also thankful to my friends, Mr. Prasath Balakrishnan, Mr. T. Ramakrishnan, Mr. C. Vijayan, Mr. Satheeswaran, Dr. Robin Marlar Rajendran, Dr. Pragadeesh, Dr. Vijay, Ms. Rashmi Selvam, and Ms. Padma Sheeba, for their unwavering support.

Last but not least, I would like to express my gratitude to the technicians, including Mr. Gokul Das, Mr. Pratap Das, Mr. Parvej Ahmed, Mr. Gobindo Boro, Mr. Bishnu Sarkar, Mr. Banajit Saloi, and Mr. Krishna Das, for their invaluable assistance during the fabrication of the experimental setup.

I would also like to acknowledge the institutions: Anna University-Chennai, PSG College of Technology-Coimbatore (D.T), Mailam Engineering College-Villupuram (D.T), Sri Mahabharathi Higher Secondary School-Namakkal (D.T), and Kalaimagal Matriculation School-Namakkal (D.T) for the quality education, unwavering support, and cherished memories that have enriched my life.

[G. Sureandhar]

ABSTRACT

This thesis work mainly focuses on the development of energy efficient solar air heater for drying of agricultural products, particularly for the climatic conditions of North Eastern region of India. A forced convective back pass type flat plate solar air heater has been developed and integrated with a mixed mode solar cabinet dryer in-order to reduce the drying time. North Eastern Regional Agricultural Marketing Corporation Limited (NERAMAC) played a vital role in getting Geographical Indication (GI) registry for Assam Karbi Anglong ginger, Assam Tezpur litchi, Meghalaya Khasi Mandarin, Sikkim large cardamom, Mizoram bird eye chilly, Tripura queen pineapple, Arunachal orange and Nagaland tree tomato. These products require huge amount of thermal and electrical power for preserving them. Apart from this, tea cultivation is one of the most prominent sectors, which plays a vital role in economic growth and employment of this region. Currently fossil fuels are used in a large extend for processing and storing the above mentioned products. Since, fossil fuel-based energy resources have negative impact on the environment and also due to the depletion of fossil fuel-based resources, researchers have focused the attention towards renewable energy-based resources such as biomass and solar energy for drying of the products. In 2016, Centre for Science and Environment (CSE) organised a conference with an objective of making the North Eastern states sustainable by 100% renewable energy. Among all types of renewable energy-based energy resources, solar energy has the unrealized potential of 62 GW only in North-Eastern part of India. From 1980s onwards, North Eastern Council (NEC) and Ministry of Non-Conventional Energy Sources (MNES) has implemented various solar energy-based products for different applications.

Solar energy can be converted into thermal energy with the help of solar thermal collectors. Solar thermal collectors can also be integrated with several processes for industrial applications depends upon the temperature requirements. Based on the temperature requirement and applications, the design and operation of solar thermal collector varies. For low temperature applications (<100°C), stationary collectors are most widely used. They are flat plate type or heat pipe based evacuated tube collectors. Most of the agricultural products drying requires hot air with low temperature (<70°C). Various configurations of solar thermal collectors for low temperature applications have been studied and found that flat plate collectors are most widely used for drying of the agricultural products. Due to the less thermal conductivity of air, the thermal conversion

efficiency and energy density of flat solar air heaters are normally less. In order to increase the thermal conversion efficiency, various performance improvement methods such as collector design modification, flow passage modification (absorber duct geometry, shape, turbulator, porous medium, baffles and number of passes) and techniques such as jet impinging, embedded heat storage, and nano coating implementations have been studied. Literatures suggested that incorporating roughness geometry over the absorber plate surface is an effective method for improving the heat transfer coefficient, thereby the thermal performance of the SAH also enhanced.

Incorporating various design of roughness element or ribs needs careful consideration in physical parameters such as angle of attack, height, pitch etc., for achieving better thermo-hydraulic performance. Even though various researchers performed investigations on different geometries of roughness element to improve thermo-hydraulic performance, the issues associated with the decreasing in heat transfer rate along the length of the absorber plate are not addressed. Further, very few studies were focused on minimizing the top loss occurs in the SAH

In order to achieve the objective of developing an energy efficient SAH model, at first, it is necessary to select the SAH with better Thermo-hydraulic performance parameter (THPP). The literature study reveals that arc rib embedded SAH performs better in THPP. Hence, arc rib embedded SAH configuration is selected for further improvement in overall performance. The arc rib embedded SAH has been tested analytically and experimentally in the Reynolds number (Re) of up to 40,000 by varying the relative roughness height ratio (0.0213 to 0.0422), relative angle of attack (0.3333 to 0.6666) and relative roughness pitch ratio (10) under the input condition with solar insolation (500 to 1,000 W/m^2). An analytical investigation was performed for the normal smooth duct and arc rib embedded SAH by solving mathematical model in MATLAB. Then, the results of the analytically arc rib embedded SAH were validated with the reference literature. From the analytical results, it was found that, the heat transfer rate and thermal conversion efficiency reduces along the length of the air flow inside the SAH duct.

In order to improve the thermal conversion efficiency, a new configuration of SAH., embedding the arc rib over the absorber plate was developed. Instead of using uniform roughness height embedment along the length of the absorber plate, embedding arc rib with varied roughness height over the absorber surface has been used. In order to extract the maximum energy available in the absorber plate, it was embedded with copper arc rib with a relative roughness height ratio of 0.0422 up to 1/4th of its length and remaining 3/4th of the absorber plate was embedded with copper arc rib having relative roughness height ratio of 0.0541. The performances of the varied arc ribs embedded SAH were analytically compared with smooth duct and fixed arc rib embedded SAH for 1m and 2m lengths.

Six different configurations of SAH were tested analytically and compared their thermal performance. Smooth duct {S(1m) and S(2m)}, fixed arc rib {FAR(1m) and FAR(2m)}, and varied arc ribs {VAR(1m) and VAR(2m)} are the SAH configurations with 1m and 2m length investigated analytically by solving mathematical models in MATLAB. Various thermodynamic and heat transfer parameters were compared for the mass flow rate ranges from 0.02 to 0.06 kg/s with an input solar insolation range of 100 to 1000 W/m^2. The analytical investigation showed that THPP of VAR (1.44 to 2.54) performed better than fixed arc rib (1.38 to 2.41). These models were compared for various important parameters such as hot air outlet temperature, thermal efficiency, exergy efficiency and irreversibility generated. It was found that varied arc ribs embedded SAH able to generate hot air outlet temperature of 318 K (45°C) with maximum thermal efficiency of 79% which was higher than the smooth duct and fixed arc rib embedded SAH configurations. For the same conditions, the thermal efficiency and hot air outlet temperature of fixed arc rib embedded SAH was 77.7% and 316.8 K (43.8°C). Similarly, for smooth duct SAH, it was 69.2% and 314.7 K (41.7°C) respectively.

Further, the THPP of the varied arc ribs embedded SAH were compared with the different rib configurations for the Reynolds number ranges from 6604 to 19952 and the comparison proves that the THPP of varied arc ribs (1.44 to 2.54) embedded SAH performs better than inclined and transverse rib (0.67 to 1.15), metal grit rib (0.88 to 1.56), wedge shaped rib (1.08 to 1.67), inclined continuous rib (1.08 to 1.46), V rib (1.56 to 1.48), chamfered rib (1.44 to 1.61), rib groove (1.49 to 1.71), wire mesh (1.5 to 1.7), chamfered rib groove (1.57 to 1.72), conic curve profile rib (1.44 to 1.50), inclined baffles (0.99 to 1.1), jet with arc shaped rib (0.69 to 0.85), metal waste (0.95 to 1.1), protruded ribs in arc shapes (1.11 to 1.92), twisted rib (1.38 to 2.08), V down rib (1.61 to 1.74), V down perforated baffles (0.69 to 0.74) and V ribbed triangular duct (1.56 to 1.72). Also, it was observed that maximum hot air outlet temperature achieved in VAR(2m). Hence, the SAH with varied arc ribs

embedment having 2m length was fabricated for testing inside Indian Institute of Technology, Guwahati, Assam.

The experimental tests on varied arc ribs embedded SAH configurations were carried out between 09:00 hrs and 15:00 hrs for two different mass flow rates, 0.0098 kg/s and 0.0175 kg/s. The performance of the fabricated varied arc ribs embedded SAH was calculated from the recorded readings of temperature, solar intensity and mass flow rate etc., The experiments were performed continuously for four days from 12th November, 2020 to 15th November, 2020. For 12th and 13th November, 2020 (day 1 and 2), the system was operated with the mass flow rate of 0.0175 kg/s and for 14th and 15th November, 2020 (day 3 and 4), it was operated with the mass flow rate of 0.0098 kg/s respectively. The maximum solar radiation intensity of 697 W/m^2 was recorded at 11:00 hrs and atmospheric temperature of 305.11 K (32.11°C) was recorded at 09:00 hrs on day 1 (12th Nov, 2020) respectively. The maximum hot air outlet temperature of 341.5 K (68.5°C) recorded during 11:00 hrs on day 4. The maximum thermal efficiency of 57% was achieved at 15:00 hrs on day 2. Hence, the concept of incorporating the varied arc ribs embedment over the absorber plate surface of the SAH tested and found suitable for integrating with indirect type or mixed mode solar dryer used for the agricultural product drying as a low temperature application.

NOMENCLATURE

T_{Pm}	Mean absorber plate temperature (K)
T_i	Air inlet temperature into the SAH (K)
T_O	Hot air outlet temperature from the SAH (K)
T_a	Ambient air temperature (K)
T_{Sun}	Sun temperature (K)
I	Solar insolation or solar heat flux input (W/m^2)
$\Delta T_f, T_f$	Mean fluid temperature (K)
Q_u, Q_{u1}, Q_{u2}	Heat gained by the hot air from SAH (W)
A_P	Mean aperture area of the absorber plate or absorber plate surface area (m^2)
F_P	Collector efficiency factor
F_R	Collector heat removal factor
Nu_s	Nusselt number of smooth ducts SAH
f_s	Frictional factor of smooth duct SAH
Nu_r	Nusselt number of roughened ducts SAH
f_r	Frictional factor of roughened duct SAH
h	Convective heat transfer coefficient (W/m^2 K)
$D_e\, or, D_h$	Equivalent or hydraulic diameter of the SAH (m)
U_L	Overall heat loss coefficient (W/m^2 K)
m	Mass flow rate of air flowing inside the duct (kg/s)
$C_P, \text{or}\, C_{pa}$	Specific heat capacity of the air (J/kg K)
$P_m\, or, W_p$	Blower power or pumping power (W)
C	Conversion efficiency (from mechanical power to blower power)

E_n	Net exergy gain (W)
$E_S, or\ EX_S,$ $or\ EX_{Input}$	Exergy supplied to the system or Exergy input to the system (W)
IR	Irreversibility of the SAH system (W)
EX_i	Exergy available at the inlet section of the SAH (W)
EX_o	Exergy available at the outlet section of the SAH (W)
EX_w	Exergy of blower power (W)
EX_{up}	Exergy utilised potential (W)
EX_{LO}	Optical exergy losses (W)
EX_{LI}	Exergy loss due to absorption of solar radiation by the absorber plate (W)
EX_{ENV}	Exergy losses due to convection and radiation heat transfer from the absorber plate to the environment (W)
EX_{HTWF}	Exergy losses due to heat transfer from the absorber plate to the working fluid (air) flow (W)
EX_{LP}	Exergy loss due to friction generated during fluid (air) flow (W)
$S_{gen,\Delta p}$	Entropy generated due to pressure drop (W/K)
$S_{gen,\Delta T}$	Entropy generated due to heat transfer (W/K)
$S_{gen,total}$	Total entropy generated due to both heat transfer and pressure drop (W/K)
$N_{s,gen}$	Entropy generation number
B_e	Bejan number
ψ	Irreversibility distribution ratio
h_w	Convective heat transfer coefficient due to wind (W/m^{2}K)
h_{rgs}	Radiative heat transfer coefficient between glazing and sky (W/m^{2}K)
h_{rpg}	Radiative heat transfer between absorber plate and glazing (W/m^{2}K)
h_{cpg}	Convective heat transfer coefficient between absorber plate and glazing (W/m^{2}K)

h_{cbf}	Convective heat transfer coefficient between bottom plate and fluid (hot air) (W/m^{2}K)
h_{cpf}	Convective heat transfer coefficient between absorber plate and fluid (hot air) (W/m^{2}K)
h_{rbp}	Radiative heat transfer coefficient between bottom plate and absorber plate (W/m^{2}K)
U_b	Bottom loss coefficient (W/m^{2}K)
Greek symbols	
τ	Transmitivity of the glazing material
α	Absorptivity of the absorber plate
$(\tau\alpha)_e$	Equivalent transmittance-absorptance
ρ_a	Density of air
α_a	Attack angle of the arc rib
η_{Th}	Thermal efficiency of the SAH
η_{eff}	Effective efficiency of the SAH
η_{Ex}	Exergy efficiency of the SAH
η_F	Efficiency of fan
η_m	Efficiency of electrical motor
η_{Tr}	Efficiency of electrical transmission
η_{TPP}	Efficiency of thermal power plant
η_{pump}	Pumping efficiency of SAH blower
Abbreviations used	
THPP	Thermo-hydraulic performance parameter
SAH	Solar air heater
S(1m)	Smooth duct solar air heater of 1m length
FAR(1m)	Fixed arc rib duct solar air heater of 1m length
VAR(1m)	Varied arc ribs duct solar air heater of 1m length
S(2m)	Smooth duct solar air heater of 2m length

FAR(2m)	Fixed arc rib duct solar air heater of 2m length
VAR(2m)	Varied arc ribs duct solar air heater of 2m length
FPC	Flat plate collector
ETC	Evacuated tube collector
CPC	Compound parabolic collector
LFR	Linear Fresnel collector
PTC	Parabolic trough collector
CTC	Cylindrical trough collector
PDR	Parabolic dish reflector
HFC	Heliostat field collector
VARSAH	Varied arc ribs embedded solar air heater
DNI	Direct normal radiation
GOI	Government of India
SV	Salvage value
GRF	Global recovery factor or capital recovery factor or money recovery factor
FYC	First yearly cost
SFF	Sinking fund factor
YSF	Yearly salvage value
YMC	Yearly maintenance cost
YC	Yearly cost
YUEG	Yearly useful energy gain
SI	Sustainability index
WER	Waste exergy ratio
EIF	Environmental impact factor
EPBT	Energy payback time
PBP	Payback period
FCS	Fuel consumption savings
P	Principal or initial investment

TABLE OF CONTENTS

LIST OF FIGURES

LIST OF TABLES

Chapter 1 Introduction

1.1 Preface

The increasing demand for sustainable and renewable energy sources has ignited a global shift towards exploring innovative technologies. One of the prominent clean energy solutions is solar thermal energy, which offers an efficient means to harness the sun's energy for many applications. Among the various solar technologies, solar air heaters have garnered significant attention due to their diverse applications in industries and households, such as space heating, crop drying, and food processing. This thesis presents the design, development, and testing of a solar air heater specifically tailored for drying applications, aimed at improving its performance and enhancing its contribution to the sustainable energy landscape.

Drying is a crucial process in various industries, including agriculture, food processing, textiles, and pharmaceuticals. Conventional drying methods, such as fossil fuel-fired furnaces and electric heaters, contribute significantly to greenhouse gas emissions and are subject to rising energy costs. Consequently, there is an urgent need for more sustainable, cost-effective, and environmentally friendly drying technologies. Solar air heaters, with their ability to convert solar radiation directly into thermal energy, have emerged as a promising solution to address these challenges.

1.2 Solar Air heating system for drying application

The solar air heater (SAH) system consists of several components that work together to generate hot air using solar radiation. The main components of an SAH system and its integration is shown in *Fig. 1.1*. The solar collector is the most critical component of an SAH system. It is responsible for capturing and absorbing solar radiation and converting it into heat. The collector is usually made up of a flat plate or an array of tubes with a selective coating that absorbs the maximum amount of solar radiation. The air ducts are responsible for transporting the heated air from the solar collector to the drying chamber. The ducts can be made of metal, plastic, or fiberglass, and they are insulated to prevent heat loss. The blower is responsible for circulating the heated air through the drying chamber. It can be powered by electricity or by a solar-powered motor. The drying chamber is the area where the drying process takes place. It can be a simple enclosure made of wood or metal, or it can be a more sophisticated system with multiple chambers and a conveyor belt. The control system is responsible for regulating the airflow and temperature to maintain optimal drying conditions. It can include sensors, thermostats, and switches that control the fan speed and airflow direction. In some cases, a backup heating system may be required to supplement the solar energy input. This can be a gas, electric, or biomass heater that can provide heat when the solar radiation is insufficient.

An energy storage system can be used to store excess solar energy during the day and release it during periods of low solar radiation. This can improve the efficiency and flexibility of the SAH system and ensure a constant supply of hot air. The components of an SAH system can vary depending on the design and application. However, the basic principle remains the same to capture and convert solar energy into heat and use it for drying applications.

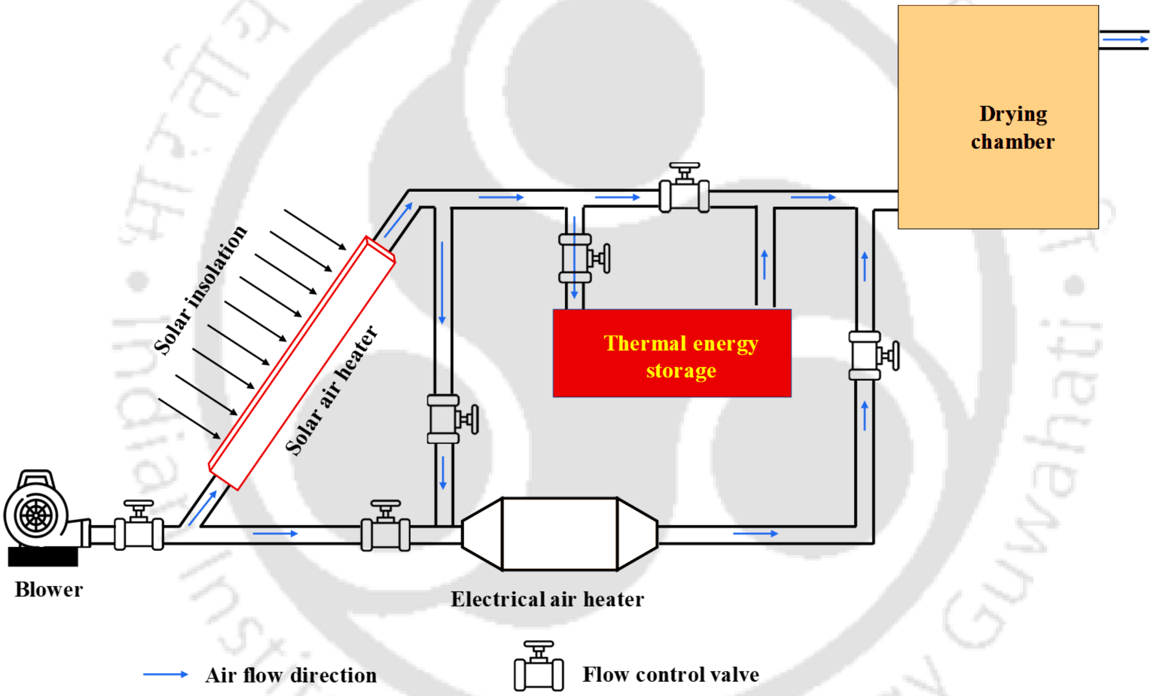

Fig. 1.1 Components of solar air heater and its integration

1.2.1 Solar thermal collectors for SAH

The main difference between a solar air heater (SAH) and a solar thermal collector is that a SAH heats air as the working fluid, while a solar thermal collector heats water or another liquid as the working fluid. A SAH is a type of solar thermal collector, but not all solar thermal collectors are SAHs.

There are several types of solar collector designs for solar air heaters (SAHs), each with its own advantages and disadvantages. The best solar collector design for an SAH depends on various factors, including the climate, application, available space, and budget. In general, the collector should have a high solar absorption efficiency, low heat losses, and be durable and easy to maintain. Some of the common solar collector designs for SAHs are:

Flat Plate Collector: Flat plate collectors are the most common and widely used solar collector design for SAHs. They consist of a flat plate that is coated with a selective material to absorb solar radiation. The absorbed heat is transferred to the air passing through the collector. Flat plate collectors are simple, durable, and cost-effective. However, they have a lower efficiency than other designs and may not perform well in cold climates.

Evacuated Tube Collector: Evacuated tube collectors are more efficient than flat plate collectors and are suitable for cold climates. They consist of multiple glass tubes that are evacuated to reduce heat losses. The tubes are coated with a selective material that absorbs solar radiation and transfers the heat to a metal absorber. Evacuated tube collectors are more expensive than flat plate collectors but have a higher efficiency and can provide higher temperature output.

Transpired Collector: Transpired collectors are a newer type of collector design that uses a perforated absorber panel to absorb solar radiation. The panel is mounted on the south-facing wall of a building and allows air to pass through the holes, where it is heated by the absorbed solar radiation. Transpired collectors are low-cost and can provide high-temperature output. However, they may not be suitable for all applications and require a south-facing wall.

Unglazed Collector: Unglazed collectors are the simplest type of collector design and consist of a black metal plate that is exposed to the sun. The plate absorbs solar radiation and transfers the heat to the air passing through the collector. Unglazed collectors are suitable for low-temperature applications, such as pool heating and ventilation. However, they have a lower efficiency than other designs and are not suitable for cold climates.

Concentrating Collector: Concentrating collectors use mirrors or lenses to focus solar radiation onto a small area, which increases the temperature of the air passing through the collector. Concentrating collectors are suitable for high-temperature applications, such as industrial drying and space heating. However, they are more expensive and complex than other designs and require regular maintenance.

The following are some of the factors that should be considered when selecting the best solar collector design for an SAH:

Efficiency: The efficiency of a solar collector refers to the amount of solar energy that is converted into heat. The higher the efficiency, the more heat can be generated, and the better the performance of the SAH system. Flat plate collectors are the most common design and have a typical efficiency of 60-80%. Evacuated tube collectors are more efficient and can achieve efficiencies of up to 90%. Concentrating collectors can achieve even higher efficiencies of up to 50-60%.

Cost: The cost of the solar collector is a critical factor that can significantly affect the overall cost of the SAH system. Flat plate collectors are the most cost-effective design and are widely used due to their simplicity and affordability. Evacuated tube collectors are more expensive than flat plate collectors but have a higher efficiency. Concentrating collectors are the most expensive and complex design and are usually used for high-temperature applications.

Climate: The climate in the installation area can affect the performance and efficiency of the solar collector. In colder climates, where there is less solar radiation, collectors with higher efficiency, such as evacuated tube collectors, may be more suitable. In hotter climates, where there is more solar radiation, flat plate collectors may be more suitable.

Similarly, with respect to drying temperature requirements following general guidelines can be given based on the literature:

For low-temperature applications (below 50°C), such as space heating or crop drying, unglazed collectors are more suitable than glazed collectors, because they have lower heat losses and lower costs. Unglazed collectors can be either flat-plate or transpired. Flat-plate collectors consist of a dark-coloured absorber plate with air ducts behind it. Transpired collectors consist of a perforated metal sheet that allows air to pass through it. Transpired collectors have higher heat transfer coefficients and lower pressure drops than flat-plate collectors, and they can also prevent backflow of air at night.

For medium-temperature applications (between 50°C and 100°C), such as water heating or desiccant regeneration, glazed collectors are more suitable than unglazed collectors, because they have higher thermal efficiencies and higher outlet temperatures. Glazed collectors can be either flat-plate or evacuated-tube. Flat-plate collectors consist of an enclosure containing a dark-coloured absorber plate with fluid circulation passageways and a transparent cover. Evacuated-tube collectors consist of a series of parallel glass tubes that contain an absorber plate and a heat pipe filled with a working fluid. The tubes are evacuated to reduce heat loss by convection and radiation. Evacuated-tube collectors have higher thermal efficiencies and higher outlet temperatures than flat-plate collectors, but they also have higher costs and lower durability.

For high-temperature applications (above 100°C), such as power generation or cooling with an absorption chiller, concentrating collectors are more suitable than non-concentrating collectors, because they have higher thermal efficiencies and higher outlet temperatures. Concentrating collectors can be either parabolic troughs or dishes. Parabolic troughs consist of long curved mirrors that focus the solar radiation on a linear receiver tube that contains a working fluid. Parabolic dishes consist of circular mirrors that focus the solar radiation on a point receiver that contains a working fluid or a Stirling engine. Concentrating collectors have higher thermal efficiencies and higher outlet temperatures than non-concentrating collectors, but they also have higher costs and require tracking systems to follow the sun's movement.

In conclusion, selecting the best solar collector design for an SAH requires considering several factors, such as efficiency, cost, climate, and application. Flat plate collectors are the most common and cost-effective design, while evacuated tube collectors are more efficient and suitable for colder climates. Other designs, such as transpired collectors, unglazed collectors, and concentrating collectors, have specific advantages and disadvantages and should be evaluated based on the specific application requirements.

1.2.2 Solar Air Heater

The schematic of a typical solar air heater is shown in *Fig. 1.2*. It mainly consists of absorber, air flow passage, glazing, bottom plate (backing material), and insulation.

- Absorber: The absorber is the main component of a solar air heater. The absorber plate is typically made of metal or plastic and is painted black to maximize solar absorption.
- Airflow passages: Airflow passages are channels within the collector that allow air to flow through. They can be designed in a variety of ways, such as serpentine or straight through.

- Glazing: The glazing is the transparent cover that allows solar radiation to enter the collector while minimizing heat loss. It can be made of various materials, such as glass, plastic, or polycarbonate.
- Bottom plate (Backing material): The backing material is a layer behind the absorber plate that helps to reflect and trap heat within the collector.
- Insulation: Insulation is used to minimize heat loss from the collector to the surrounding environment. It is usually placed on the sides and bottom of the collector.
- Blower: A blower can be added to the solar air heater to increase the flow rate of air through the collector and improve the efficiency of the system.
- Control system: A control system can be used to regulate the temperature of the air leaving the collector. This can be done through the use of a thermostat or other temperature sensing device connected with DAQ (Data Acquisition System).

Overall, solar air heaters are simple yet effective devices that can help to reduce energy costs and greenhouse gas emissions by utilizing the abundant energy of the sun.

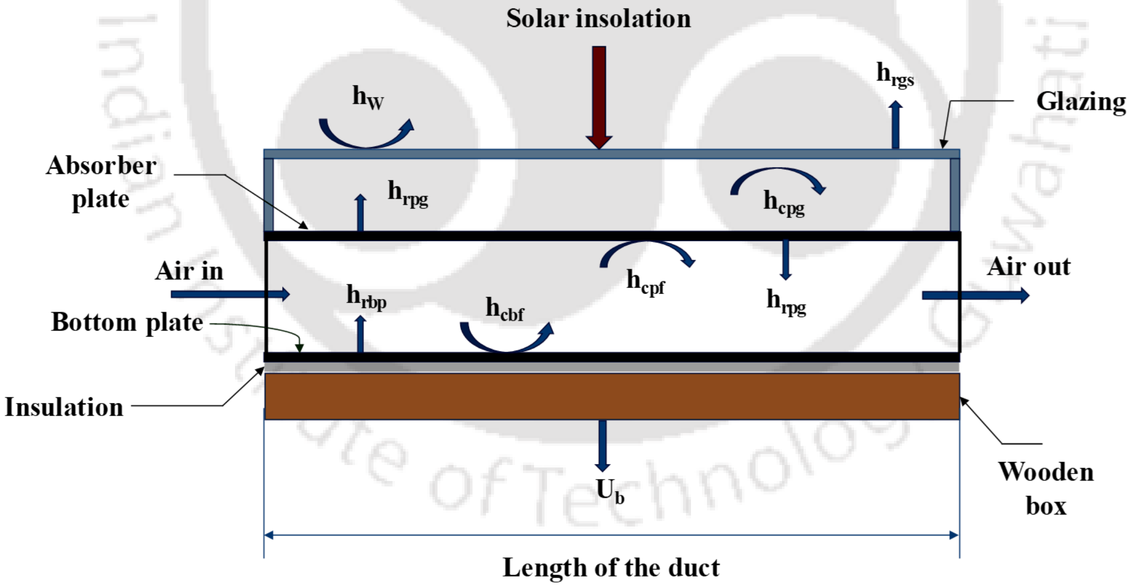

Fig. 1.2 Energy interactions in SAH

The energy interactions between the sub-system in the SAH system given by,

At glazing:

$$\alpha_g I + h_{rpg}\left(T_{Pm} - T_g\right) + h_{cpg}\left(T_{Pm} - T_g\right) = \left(h_w + h_{rgs}\right)\left(T_g - T_a\right) \text{..............................} 1.1$$

At absorber plate:

$$\alpha_P\left(\tau_g I\right)=h_{cpf}\left(T_{Pm}-T_f\right)+h_{cpg}\left(T_{Pm}-T_g\right)+h_{rpb}\left(T_{Pm}-T_b\right)+h_{rpg}\left(T_{Pm}-T_g\right) \text{…………....1.2}$$

At fluid (air) flow region:

$$h_{cpf}\left(T_{Pm}-T_f\right)=h_{cbf}\left(T_f-T_b\right)+\left[\left(\frac{mC_{pf}}{W}\right)\left(\frac{dT_f}{dx}\right)\right] \text{……………………………………1.3}$$

At bottom plate region:

$$h_{cbf}\left(T_f-T_b\right)+h_{rpb}\left(T_{Pm}-T_b\right)=U_b\left(T_b-T_a\right) \text{………………………………………...1.4}$$

1.2.3 Classification of solar air heaters

The solar air heater used for drying and space heating applications usually produces an output temperature of up to 80°C. For operating at this temperature, flat plate-type collectors are used. This flat plate collector is a non-concentrating / non-imaging type that is cheap and simple in construction. The Sun’s radiation transmits into the glazing surface, heating up the absorber plate. The air (medium) that gains the thermal energy from the absorber plate and that is connected in series with the dryer is used for drying various agricultural products. The various types of SAH classification is given in Fig. 1.3.

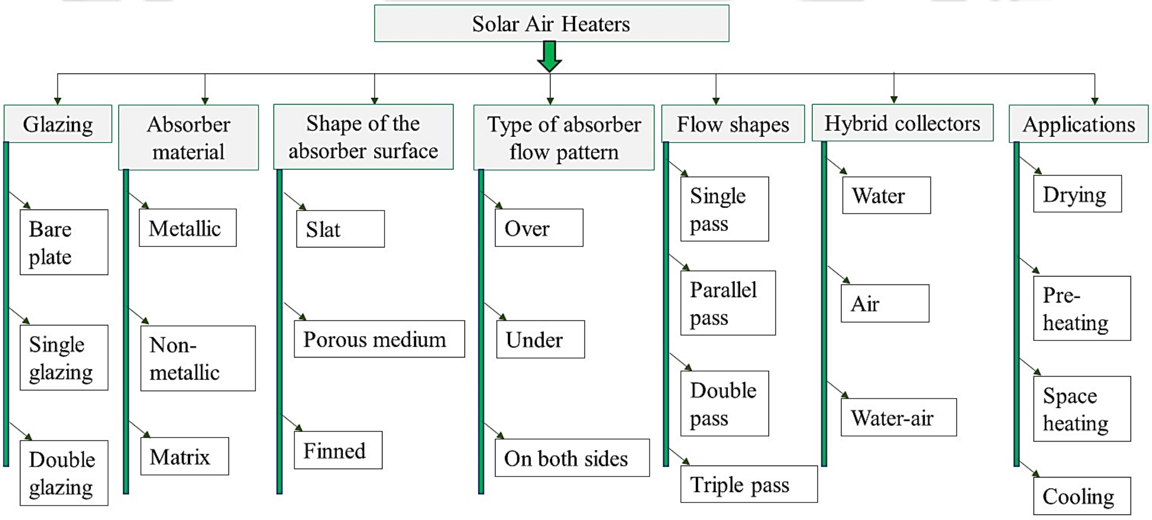

Fig. 1.3 Classification of SAH

The flat plate type solar air heaters are classified based on the following basis:

Based on the number of glazing - Initially, the SAH ducts are designed with a bare plate to absorb the solar radiation. Later it was found that the conversion efficiency of the bare plate SAH is very less due to the heat loss from the top surface, In-order to reduce the loss happens due to the interactions of absorber plate with environment through natural convection, a transparent glass cover was fitted over the absorber plate that transmits solar radiation. Based on the concentration ratio, absorber surface temperature either single or double or multiple glazing installed to minimize the top loss.

Based on the absorber material type - Some metallic surfaces are prone to corrosion for some specific heat transfer fluids. For some special case of heat transfer, non-metallic surfaces are also used as an absorber material. Air is the most common heat transfer fluid used for various applications. Due to its poor thermal conductivity, the heat transfer area required to be optimised. For compact design with higher energy density, matrix type absorber materials are used instead of plain metallic surface.

Based on the shape of the absorbing surface - Depending upon the heat transfer fluid property and mode of the heat transfer, slat type, porous medium, and fin or baffle embedded SAH are used for different types of applications. Slat type SAHs are good in transferring the heat, but cannot store thermal energy. But, porous medium based absorbing surfaces are more compact and has higher contact surface that enhances the heat transfer rate. Also, sometimes fins are embedded over the absorber surface area in-order to increase the heat transfer coefficient. Baffles are used to provide structural support and directs the fluid flow inside the duct or passage. Baffles are embedded either over the absorber plate or the duct passage.

Based on the type of flow pattern - In flat plate type SAH, in-order to gain the energy available in the absorber plate, the process fluid can be blown in three different forms. The collector, in which the air blown over the absorber plate is called as front pass type SAH, the collector in which the air blown under side of the absorber plate is called as bottom pass SAH. There is a special type of collector, here the air absorbs the thermal energy from both sides of the absorber plate is called as parallel pass SAH.

From the study conducted by several researchers, it was found that the SAH's thermal performance depends on various parameters such as solar radiation intensity, channel flow passage depth, and convective heat transfer between the absorber surface area and air (medium). The above classification is mentioned based on the method of extracting solar energy.

1.2.4 Merits and demerits of solar air heaters

The various advantages of using a solar air heater compared with other solar collectors are given below,

- No other fluid is used as an operating medium, only air is the direct fluid medium used for the application. Hence the system is less complicated and it is more compact.
- There is no problem with corrosion because air is the only medium used. There won't be any vibrations during operation. The system is always stationary.
- Cheap cost of initial investment and no operation cost. Hence maintenance is also very easy.
- No problem with freezing during operation. There is no phase change, also air is available in an atmosphere that does not cost, and no need for process fluid treatment.
- The working pressure is also limited to operate in an ambient condition, hence the system is safer during operation. There are no safety issues in the operation.
- There is no noise and vibration during operation.

Although solar air heater has more advantages over other collectors, these solar air heaters also have some disadvantages, which are listed below:

- Air is the only fluid used as a medium of heat transfer in the SAH, the thermo-physical properties of the air are poor to help in the heat transfer operation. Also, the energy density capacity of the air is less due to low thermal conductivity and less specific heat capacity.
- Due to the less density of the air, it is a must to handle a large volume of air for the application.
- In order to store the energy obtained from the SAH, air cannot be used as a storage medium, due to its low thermal capacity. Hence some other materials are required to store the fluid.

1.3 Applications of Solar air heater

Solar air heaters are devices that use solar energy to heat air for space heating, drying, and other industrial applications. Here are some common applications of solar air heaters:

- Space heating: Solar air heaters can be used to heat the air in a building or a room, thereby reducing the amount of energy required for heating. They can be particularly useful in colder climates where heating is required for a significant part of the year.

- Drying: Solar air heaters can be used to dry agricultural products, food, wood, and other materials. This can be particularly useful in areas where there is a lot of sunshine and drying is required for preservation or other purposes.
- Industrial processes: Solar air heaters can be used to heat air for industrial processes such as drying, curing, and baking. They can also be used to heat air for ventilation and air conditioning systems.
- Water heating: Solar air heaters can be used in conjunction with a water heating system to preheat the water before it enters the water heater. This can reduce the amount of energy required to heat the water and can be particularly useful in areas where there is a lot of sunshine.
- Agricultural applications: Solar air heaters can be used to create a warm microclimate for plants, thereby extending the growing season and increasing crop yields.

Overall, solar air heaters are a versatile and environmentally-friendly technology that can be used in a wide range of applications.

1.4 Solar air heaters in the Global and Indian market

The global market for solar air heaters has experienced significant growth in recent years, primarily driven by the increasing demand for sustainable, cost-effective, and environmentally friendly heating and drying solutions. Governments, industries, and households around the world are increasingly recognizing the potential of solar air heaters as an effective means of reducing energy consumption, minimizing greenhouse gas emissions, and lowering energy costs. This section provides an overview of the global and Indian markets for solar air heaters, highlighting key trends, challenges, and opportunities.

1.4.1 Global Market for Solar Air Heaters

The global solar air heater market has witnessed steady growth, with various regions around the world embracing solar technologies as a viable alternative to conventional energy sources. Some of the key factors fuelling this growth includes:

- Increasing energy demand: The rising global energy demand has led to a surge in the exploration and adoption of renewable energy sources, including solar energy.

- Government initiatives and incentives: Governments worldwide have been implementing policies and incentives to promote the development and utilization of renewable energy technologies, such as tax credits, feed-in tariffs, and subsidies.
- Growing awareness and concern for the environment: As awareness regarding the environmental impact of conventional energy sources grows, there is a greater push towards the adoption of clean, renewable energy solutions like solar air heaters.
- Technological advancements: The continuous advancements in solar air heater designs, materials, and efficiency have made these systems more attractive and accessible to a broader range of customers.

1.4.2 Indian Market for Solar Air Heaters

India, with its abundant sunshine and escalating energy demand, offers immense potential for the growth and adoption of solar air heaters. Some of the key factors driving the Indian solar air heater market includes:

- Favorable geographic location: India's geographic location near the equator ensures that it receives ample solar radiation throughout the year, making solar air heaters an effective solution for meeting heating and drying needs.
- Government support: The Indian government has actively promoted solar energy adoption through various initiatives, such as the National Solar Mission and the Solar Energy Corporation of India (SECI), which have set ambitious targets for solar energy generation and offer incentives for solar energy utilization.
- Increasing energy demand: India's rapidly growing population and economic development have led to a surge in energy demand, necessitating the exploration of alternative, sustainable energy sources like solar air heaters.
- Application in diverse sectors: Solar air heaters find applications across various sectors in India, such as agriculture, textiles, food processing, and pharmaceuticals, which are integral to the country's economy.
- Rural electrification and off-grid applications: Solar air heaters can play a crucial role in rural electrification and off-grid applications, where conventional energy sources are often unreliable or unavailable.

1.5 Challenges in the development of SAH and adaption in the Indian market

Several challenges exist in developing and adapting solar air heaters in the Indian market. Some of these challenges include:

- High capital costs: Solar air heaters can have high initial costs compared to traditional heating systems, which can be a barrier for adoption in India, where cost is a significant consideration for consumers.
- Lack of awareness: Many consumers in India are unaware of the benefits of solar air heaters, making it difficult for companies to market and sell these products.
- Lack of suitable infrastructure: The installation of solar air heaters requires appropriate infrastructure, such as adequate space and proper orientation of the solar collectors. This can be a challenge in urban areas where space is limited.
- Variations in climate: India has diverse climatic conditions, which can make it challenging to design solar air heaters that are suitable for all regions of the country.
- Lack of standardization: There is currently no standardization of solar air heaters in India, which can lead to inconsistencies in quality and performance.

To overcome these challenges, companies developing solar air heaters in India need to focus on educating consumers about the benefits of these products and work on reducing the cost of production. They also need to design solar air heaters suitable for India's diverse climatic conditions and work with the government to create standardization and policies that support adopting these technologies.

Furthermore, the Indian government can provide incentives and subsidies to encourage the adoption of solar air heaters and can also support the development of suitable infrastructure for installation and maintenance of these systems. By addressing these challenges, solar air heaters can significantly meet India's energy needs while reducing the country's dependence on fossil fuels and mitigating climate change.

1.6 Motivation of the thesis work

The agricultural products and cash crops such as tea leaf, ginger, turmeric, jackfruit, different varieties of chilies including ghost chili, and spice varieties such as cardamom, bay leaf, and black pepper are cultivated. These products are dried and exported to different parts of the globe. The products that are dried in the open atmosphere reduce the quality of the product, and drying using an electrical drier causes greenhouse gas emission. In order to implement sustainability in the agricultural sector, solar energy that is available free of cost and eco-friendly nature can be used to generate hot air for drying applications. The commercially available electrical heater and steam heating cause emissions, and the system is more complex with high operating costs. To overcome the above-mentioned challenges, the solar air heater is one of the most promising solutions for sustainability in agriculture.

1.7 Organisation of the thesis

The thesis work is organized into the following chapters.

Chapter 1. Introduces the background of this research, global energy consumption, various kinds of fuels used for generating power, Indian energy scenario. Various solar thermal collectors, operating temperature range, and applications are also discussed. The various designs of a solar air heater (flat plate type configuration) are also discussed.

Chapter 2. Detailed literature review on solar flat plate type collector for drying applications, Various heat transfer enhancement techniques, and methodology to predict the performance of the SAH are also discussed. The experimental procedures and various measuring equipment are also discussed.

Chapter 3. This chapter describes the back-pass type SAH design, and various mathematical equations used for heat transfer and thermodynamic analysis are discussed. The analytical method of predicting the performance of the SAH is also discussed. The performance of the three geometries of SAH configurations, such as smooth duct SAH, fixed arc rib embedded SAH, and varied arc ribs embedded SAH for 1m and 2m lengths, are compared analytically.

Chapter 4. This chapter discusses the experimental studies on varied arc ribs-embedded SAH under two different mass flow rate conditions. The experimental studies are performed to study the thermal conversion efficiency, various exergy loss components, and the magnitude and entropy generated during the operation of the SAH.

Chapter 5. Details regarding the enviro-economic benefits of the SAH are presented in this chapter. The economic analysis was performed based on the geographical location, initial investment, thermal conversion efficiency of the equipment, and operation and maintenance cost. Further, the environmental analysis that includes embodied energy, annual fuel energy savings, amount of CO_2 reduced, and carbon credits earned are also presented in this chapter.

Chapter 6. This chapter summarizes the conclusions of significant outcomes from the analytical and experimental investigations conducted. The future scope for the research and recommendations for improving the performance of the SAH is also presented.

1.8 Summary

This chapter briefly introduces about solar thermal collectors, classification of solar thermal collectors, applications, advantages and disadvantages. Later the motivation of the thesis work and the structure of the thesis are explained sequentially.

Chapter 2 State-of-the-art

2.1 Preface

Generation of electricity or thermal energy from solar radiation is one of the most promising methods to decarbonize the energy sector. Humans have used direct solar energy conversion technologies for over 2,500 years (since Archimedes' time). However, massive research into developing the technology to convert solar energy into various other required forms of energy such as heat, electricity, and sound has begun after industrialization, to reduce the impact of Green House Gas (GHG) emissions caused by fossil fuel combustion. As a result, researchers focused on developing innovative solar collectors to maximize the utilization of solar energy based on the needs such as power generation (solar PV-based electricity and thermal-based electricity generation) and process heat generation (hot air, hot water, and steam). Therefore, researchers have been focused on developing solar thermal energy conversion devices for process heating applications. Solar air heating is a promising technology that enables the widespread utilization of solar energy for process heating applications up to 100°C. However, there is always a need for improvements in the thermal performance of the existing solar air heating devices. Hence, developing a versatile analytical model to analyse the design features is critical. Before combining solar air heater (SAH) models with real-world applications, they need to be experimentally validated. Therefore, the state-of-the-art on various designs of SAHs, enhancement techniques to improve thermo-hydraulic performance, analytical and experimental methods to study SAH performance, and computational methodologies to visualize and study fluid flow behaviour inside the SAH duct are discussed in this chapter.

2.2 Design of solar air heater

In this section, state of the art on various aspects of designing the SAH has been discussed. The various concepts in design such as the application of use and required range of temperatures, selection of absorber plate type, tracking system requirement, mode of energy collection / transfer, mode of operation (natural or forced) and flow configuration inside the flow channel are presented. Also, the thermodynamic view of designing and optimizing the various heat transfer parameters for energy efficient design and economic operation of the SAH are also discussed as follows.

2.2.1 Concepts in design of SAH

The procedure to design any solar thermal collector with minimum entropy generation was performed and the concept of maximum utilization of energy for minimum entropy generation adopted were discussed by Torres-Reyes et al., (2001). Various available designs of solar thermal collectors and its range of applications are reviewed by Sansaniwal et al., (2018). The review stated that solar collectors were classified as stationary, single-axis, and two-axis tracking systems. The study recommended stationary collectors with a concentration ratio of 1 to 5 for the temperature range of 30 to 240°C. At the same time, the collectors with single and two-axis tracking systems were used for the temperature range of 60 to 300°C and 100 to 2000°C, with a concentration ratio of 10 to 50 and 100 to 1500, respectively. But for the low temperature applications such as agricultural products drying, Saxena et al., (2015) reviewed various SAH designs. From his review, it was found that the absorber plate was classified as non-porous and porous. The porous type absorber plate helps in reducing the convective energy losses involved in the non-porous type absorber plate and maximizes the utilization of input solar energy. However, the pumping power increases in the porous type absorber plate. Further, the SAH is classified as single, double, and two-pass SAH based on the flow passage configuration. The heat transfer correlations and the various flow passage configuration in SAH proposed by various researchers are given in *Table 2.1 (* Tchinda, 2009).

Based on the mode of flow operation (with or without blower), Benhamza et al., (2021) conducted an experimental investigation on SAH with fins, operated under natural convection heat transfer mode. Investigations were performed by varying length to width ratio from 1 to 5, the height of the air duct from 0.02 to 0.2, number of fins from 0 to 60 to generate hot air for drying application in the range of 40 to 70°C. From analysis, it was found that the optimal hot air temperature for drying was 52°C, for the length to width ratio of 1.28, duct height of 0.067 m, embedded with 49 fins attained the thermal efficiency of 51.78 % respectively. Later, Mugi and Chandramohan, (2021) performed an experimental investigation in SAH under natural and forced convection mode of operation for okra drying. The experimental investigation was performed between 08:00 to 17:00 hrs. The experimental results showed that the maximum energy and exergy efficiencies obtained for natural convection were 61.49 % and 2.44 %, while for forced convection were 74.98 % and 2.03 % respectively.

2.2.2 Selection of SAH for drying applications

Stationary collectors are well suitable for drying applications. A comparative analysis on the performance of the flat plate collector and tubular collector was performed by Abo-Elfadl et al., (2021b) by operating the SAH under single and double pass flow configurations. The mass flow rate of air was varied from 0.025 to 0.075 kg/s during the experiments. The results showed that the tubular type SAH with double pass flow configuration performed better than the flat plate type SAH. The thermal efficiency of the tubular type SAH and flat plate type SAH with double pass flow configuration at 0.075 kg/s were found to be 86 % and 71 %, respectively. But previously in 2014, Sokhansefat et al., (2014) compared the performance of FPC and ETC for both hot and cold climatic condition. Although the thermal performance of ETC slightly higher than the FPC, for the similar aperture area of 2.04 m^2, the investment required for FPC was 1000 $ lesser than ETC and the payback time obtained was 7.8 years for FPC whereas for ETC, it took 9.7 years. Also, ETCs are most widely used for the temperature requirement of above 80°C and up to 130°C. Hence, based on our requirement of agricultural product drying (around 45 to 65°C), most of the reported literatures were on FPC type.

2.2.3 Various design configurations in flat plate absorber plate

Experimental investigation on SAH with five different absorber plates: corrugated, trapeze, reverse corrugated, reverse trapeze, and smooth duct were performed by Benli, (2013) and experiments were performed by varying the mass flow rate from 0.02 to 0.05 kg/s having absorber plate with aperture surface area 1.7 × 0.7. The results found that the corrugated type absorber plate achieved higher thermal efficiency of 39 % at 0.036 kg/s. Whereas smooth flat plate SAH showed a lower efficiency of 13 % for the same mass flow rate. Later, Fudholi and Sopian, (2018) reviewed SAH to study its thermal performance. Different SAH systems were studied, such as single pass, double pass, corrugated, porous media absorber, grooved, and internal and external recycle models. The review found that the thermal conversion efficiency of the SAH ranges between 30% to 79%. Investigation of thermal performance of triple-pass and quadruple-pass SAH performed experimentally by Khanlari et al., (2020b) for municipal sewage sludge drying. The study was performed on a V-groove type absorber plate for the mass flow rates of 0.009 kg/s and 0.012 kg/s. The study concluded that quadruple pass SAH with a V-groove type absorber plate achieved a maximum thermal conversion efficiency of 81.7 % at 0.012 kg/s than triple-pass SAH.

In general, Double pass SAH are used to minimize the top loss incurred during the operation. Hence, Guler et al., (2020) performed an experimental investigation in double pass (DP-SAH). The effect of the mean absorber on thermal performance was studied experimentally. The experimental investigations were carried out in the geometrical location of latitude (37.69 °N) and longitude (30.34 °E) for a fixed mass flow rate of 0.011 kg/s, operated from 09:00 to 15:00 hrs. The experimental results showed that the average thermal conversion efficiency of DP-SAH with mesh absorber achieved was 79.22 % higher than DP-SAH having thermal efficiency of 71.37 % respectively.

Also, collector shapes such as flat plate and tubular type were modelled based on the temperature requirement. Mostly tubular design collectors were used for the high temperature range of application. Hence, Abo-Elfadl et al., (2021b) compared the performance of tubular and flat plate SAH. Experimental investigation performed for both single and double pass operation by varying mass flow rates 0.075, 0.05, 0.025 kg/s, operated during 08:00 to 16:00 hrs. Experimental results showed that the tubular double pass SAH attained the maximum thermal efficiency of 86 % at 0.075 kg/s with the corresponding exergy efficiency of 1.75 %.

2.2.4 Design optimization

Some of the researchers focused on optimizing the design of the SAH. Expressions for mass flow number, entropy generation number, and Sol-Air temperature (stagnation layer temperature) based non-dimensional parameters were developed to optimize the performance [Torres-Reyes et al., (2001) and Torres-Reyes et al., (2004)]. The results showed that the minimum entropy generation number of 0.91 was obtained for the optimum collector area of 32.8 m^2 operating at the mass flow rate of 0.47 kg/s under an input heat flux of 900 W/m^2.

Optimization of multi-pass type SAH with flat plate absorber was performed by Luan and Phu, (2021) using the preference selection index method. The analysis was performed by varying mass flow rate from 0.01 to 0.02 kg/s, channel depth from 15 to 30 mm, and collector length from 1.5 to 2.5 m, respectively. The effective energy efficiency of 52.1 % and exergy efficiency of 4.7 % were achieved under the optimal operating conditions (mass flow rate: 0.01 kg/s; collector length: 2.5 m, and channel depth: 0.02 m). Benhamza et al., (2021) performed multi-objective optimization on flat plate collector type SAH under natural convection for drying food products. The study was carried out by varying length to width ratio from 1 to 5, air flow duct height from 0.02 to 0.2 m, with fin number from 0 to 60. The optimal conditions of length to width ratio, air flow duct height, and the number of fins are 1.28, 0.067 m, and 49, respectively. Thermal efficiency of 51.78 % and hot air outlet temperature of 52°C were obtained under these optimal operating conditions.

2.2.5 Effect of corrugation and perforations in absorber plate

Various designs of the absorber plate shape of the SAH were analysed by various authors and the observations are discussed briefly in this section. Experimental investigations on SAH with corrugated absorber plate was performed by Reddy et al., (2021). The authors were studied two configurations of corrugated sheets, i.e., one with reverse trapezoidal and the other with cross corrugated trapezoidal type. During the experiments, the air mass flow rate was varied from 0.0039 to 0.0156 kg/s for three different tilt angles, namely 15°, 30°, and 45°. The experimental results showed that cross-corrugated trapezoidal absorber plate type SAH has a maximum energy efficiency of 39.4 % at 0.0156 kg/s for the tilt angle of 45°. Hassan et al., (2021) performed experimental investigations on a flat plate, V-corrugated, and perforation in the V-corrugated type absorber plate SAH. The experimental studies were carried out under single and double pass operations. In single-pass operation, all the air was passed under the absorber plate. Whereas in the case of double pass operation, the air enters the collector system in three different configurations, namely, air enters only over the absorber plate, 1/3rd of the air enters over the absorber plate, and 2/3rd mixed under the absorber plate, and 2/3rd of the air enters over the absorber plate and 1/3rd mixed under the absorber plate. The experimental results showed that the perforated V-corrugated sheet under double pass operation with 2/3rd of the air entering over the absorber plate and 1/3rd mixed under the absorber plate achieved a maximum thermal efficiency of 71.85 % among all mentioned flow configurations.

2.2.6 Novel impinging jet flow configuration – Thermal, economic and environmental concept of design

Impinging jet type flow configuration in the SAH was a novel method of circulating air inside the flow channel duct. Very few researchers have focused on this impinging jet type SAH and some of them analysed the economic and environment aspects. Goel and Singh, (2021) evaluated the performance of flat plate absorber with continuous longitudinal fins. The developed SAH used impinging jet-type flow configuration. The experimental investigation was focused on studying the effect of mass flow rate (0.056 kg/s to 0.112

kg/s), fin spacing ratio (0.23 to 0.46), jet diameter ratio (0.046 to 0.076) and stream wise pitch ratio (0.23 to 0.46) on thermal efficiency. The experimental results showed that the highest thermal efficiency of 74% was obtained for stream wise pitch ratio of 0.46, jet diameter ratio of 0.076, and fin spacing ratio of 0.23. Farahani and Shadi, (2021) compared the energy, environment, and economic aspects of SAH with and without the impinging jets. The study was conducted on four different absorber plate configurations: multi V rib embedded flat plate, U-shaped turbulator, winglet with wavy groove, and discrete V down rib flat plate. The analysis was performed by varying the Reynolds number from 2,000 to 25,000, angle of tilt from 20 ^{o} to 70 ^{o}, for heat flux input of 300 W/m^2 to 1000 W/m^2. The results showed that the discrete V down rib flat plate collector with impinging jet achieved maximum thermal efficiency of 59.43 % for tilt angle and Reynolds number of 60.3^{o} and 4081, respectively. Also, the corresponding collector cost is 30 $ and reduced the emission of CO_2, SO_2, and NO by 984 kg, 8.98 kg, and 2.33 kg, respectively.

This section discusses the state-of-art on various designs of SAHs based on flow configuration and temperature range. It was observed that stationary collectors are well suited for drying agricultural products (Srivastava and Rai, 2017). Further, the literature suggested that the entropy generation minimization technique should be considered for designing an efficient SAH alongside the energy analysis (Dincer and Cengel, 2001; Prasad and Sahu, 2017; Sciacovelli et al., 2015). Economic and environmental aspects of the SAHs should also be considered while developing the SAH.

Table 2.1 Heat transfer coefficient correlations used in different configuration of flow passage channel in SAH

Flow passage configuration type	**Heat transfer coefficients**	**References**
A bare plate solar air heater	$h_f = Nu\left[1+\frac{MD}{L}\right]\left[\frac{k}{D}\right]$; where, $Nu = 0.0182(\text{Re})^{0.8}(\text{Pr})^{0.4}$ $M = 14.3\log_{10}(N) - 7.9$; $N = \frac{L}{D}$; if $0 < \frac{L}{D} \le 60$ and $N = 60$ if $\frac{L}{D} > 60$	Tan and Charters, (1969)
Single pass one cover solar air heater and single pass two cover solar air heater	$Nu = 5.4 + \frac{(0.00190)\left[\frac{(\text{Re})(\text{Pr})(D_e)}{L}\right]^{1.71}}{1+(0.00563)\left[\frac{(\text{Re})(\text{Pr})(D_e)}{L}\right]^{1.71}}$, for $[\text{Re} < 2300]$ $Nu = 0.116\left[(\text{Re})^{2/3} - 125\right](\text{Pr})^{1/3}\left[1+\left(\frac{D_e}{L}\right)^{2/3}\right]\left(\frac{\mu}{\mu_w}\right)^{0.14}$, for $(2300 < \text{Re} < 6000)$ $Nu = 0.018(\text{Re})^{0.08}(\text{Pr})^{0.4}$, for $(\text{Re} > 6000)$ Also, it can be computed by using $Nu = \frac{hD_e}{k} = 0.333(\text{Re})^{0.8}(\text{Pr})^{1.3}$	Heaton et al., (1964) Tan and Charters, (1970)
Back pass solar air heater	$Nu = 5.385 + \beta\left(\frac{b}{L}\right)$, for $(\text{Re} < 2550)$ $\beta = (0.0148)(\text{Re})$, for $(2550 < \text{Re} < 10^4)$ $\beta = 9.37(\text{Re})^{0.471}$, for $(10^4 < \text{Re} < 10^5)$	Garg et al., (1984)
Parallel pass solar air heater: Type 1	$Nu = (0.027)(\text{Re})^{0.8}(\text{Pr})^{1/3}\left(\frac{\mu}{\mu_w}\right)^{0.14}$	Forson et al., (2003)

Flow passage configuration type	**Heat transfer coefficients**	**References**
Parallel pass solar air heater: Type 2	For laminar flow, $Nu = 4.4 + \dfrac{(0.00398)\left[\dfrac{\left[(0.7)(\mathrm{Re})(\mathrm{Pr})(D_e)\right]}{L}\right]^{1.66}}{1+(0.0114)\left[\dfrac{(\mathrm{Re})(\mathrm{Pr})(D_e)}{L}\right]^{1.12}}$ For turbulent flow, $Nu = (0.018)(\mathrm{Re})^{0.08}\left[1+\left(\dfrac{D_e}{L}\right)^{0.7}\right]$	Forson et al., (2003)
Solar air heater with slats	For natural convection heat transfer, $Nu = 1+1.44\left[1-\dfrac{(1708)(\sin(1.8\phi))^{1.6}}{(Ra)(\cos(\phi))}\right]\left[1-\dfrac{1708}{(Ra)(\cos(\phi))}\right]+\left[\dfrac{(Ra)(\cos(\phi))}{5830}-1\right]$, if $0 \le \phi \le 60$ and $0 \le Ra \le 10^5$. For fully developed laminar flow inside tube or duct, $Nu = 4.36$ For fully develop turbulent flow inside tube or ducts, $Nu = \dfrac{\left(\dfrac{f}{8}\right)(\mathrm{Re})(\mathrm{Pr})}{1.07+12.7\sqrt{\left(\dfrac{f}{8}\right)}\left[(\mathrm{Pr})^{\frac{2}{3}}-1\right]}\left[\dfrac{\mu}{\mu_w}\right]^{0.11}$	Ammari, (2003) Matrawy, (1998)
Two pass solar air heaters	$Nu = \left(\dfrac{n}{8}\right)\dfrac{(\mathrm{Re}-1000)(\mathrm{Pr})}{1+(12.7)\left(\dfrac{n}{8}\right)^{0.5}\left(\mathrm{Pr}^{0.67}-1\right)}$, where $n = \sqrt{(0.79)\left[\ln(\mathrm{Re})\right]-1.64}$	Verma et al., (1992) Wijeysundera et al., (1982)

Flow passage configuration type	**Heat transfer coefficients**	**References**
Double pass flat plate solar air heater with recycle	$Nu=(0.0158)(\mathrm{Re}^{0.8})\left[1+\left(\frac{D_e}{L}\right)^{0.7}\right]$	Ho et al., (2005)
Double pass flat plate solar air heater with longitudinal fins	For laminar flow in a f[illegible]onvection heat transfer (for constant heat flux), $Nu=5.4+\frac{(0.0019)\left[(\mathrm{Re})(\mathrm{Pr})\left(\frac{D_e}{L}\right)\right]^{1.71}}{1+(0.00563)\left[(\mathrm{Re})(\mathrm{Pr})\left(\frac{D_e}{L}\right)\right]^{1.17}}$ for $(\mathrm{Re}\leq 2300)$ For transition flow, $Nu=(0.116)\left[(\mathrm{Re})^{\frac{2}{3}}-125\right]\left[(\mathrm{Pr})^{\frac{1}{3}}\right]\left[1+\left(\frac{D_e}{L}\right)^{\frac{2}{3}}\right]\left[\frac{\mu}{\mu_w}\right]^{0.14}$ $(2300<\mathrm{Re}<6000)$ For turbulent flow (for constant heat flux and one side insulated), $Nu=0.018(\mathrm{Re})^{0.8}(\mathrm{Pr})^{0.4}$	Naphon, (2005)
Triple pass solar air heaters	$Nu=(0.036)(\mathrm{Re})^{0.8}(\mathrm{Pr})^{0.8}$	Chandra et al., (1990)
Multi pass flat plate solar air heater with external recycle	For laminar flow, $Nu=4.4+\frac{(0.00398)\left[\frac{[(0.7)(\mathrm{Re})(D_e)]}{L}\right]^{1.66}}{1+(0.0114)\left[\frac{(0.7)(\mathrm{Re})(D_e)}{L}\right]^{1.12}}$	Ho et al., (2005)

Flow passage configuration type	Heat transfer coefficients	References
	For turbulent flow, $Nu=(0.0158)(\mathrm{Re})^{0.8}\left[1+\left(\frac{D_e}{L}\right)^{0.7}\right]$ For flow through flat plates and collector storage walls, $Nu=(0.0158)(\mathrm{Re})^{0.8}$	
Solar air heater with a compound parabolic concentrator	For laminar flow, $Nu=4.9+\dfrac{(0.0606)\left[\frac{(\mathrm{Re})(\mathrm{Pr})(D_e)}{L}\right]^{1.2}}{1+(0.0909)\left[\frac{(\mathrm{Re})(\mathrm{Pr})(D_e)}{L}\right]^{0.7}[\mathrm{Pr}]^{0.17}}$, for ($\mathrm{Re}<2100$) For turbulent flow, $Nu=(0.0158)(\mathrm{Re})^{0.8}$	Tchinda, (2008)
V- groove solar air collector	$Nu=Nu_o+(\beta)\left(\frac{b}{L}\right)$, where $Nu_o=2.821$, $\beta=0.126$,for (Re < 2800) $Nu_o=\left(\frac{(1.9)}{10^6}\right)(\mathrm{Re})^{1.79}$, where $\beta=225$ $Nu_o=(0.0302)(10^{-6})(\mathrm{Re})^{0.74}$, where $\beta=(0.242)(\mathrm{Re})^{0.74}$	Karim and Hawlader, (2006)
Single pass solar air heater with packed bed:	$Nu=\left(\frac{0.255}{\in}\right)\left[(\mathrm{Re})^{\frac{2}{3}}\right]\left[(\mathrm{Pr})^{\frac{1}{3}}\right]$	Choudhury and Garg, (1993)

Flow passage configuration type	**Heat transfer coefficients**	**References**
Double pass solar air heater with packed bed	$f=150\left[\frac{(1-\in)}{\mathrm{Re}}+1.75\right]$, where, $\in$ is void fraction or porosity	Ramadan et al., (2007)

2.3 Heat transfer enhancement techniques adopted in the solar air heater

Maximum utilization of the incoming solar energy can be accomplished by adopting passive heat transfer augmentation methods in the airflow passage. Mounting a vortex generator over the surface of the absorber plate is one such technique to boost the thermal efficiency of solar thermal devices. These ribs induce turbulence in the flow which assists in breaking the laminar sublayer thereby increasing the thermo-hydraulic efficiency of the SAH. In this section, various heat transfer enhancement techniques adopted by researchers are discussed in detail.

2.3.1 Various enhancement techniques

The latest review reported by Arunkumar et al., (2020) reported the usage of various flow turbulence enhancers adopted in SAH, and the influence of their geometrical attributes (shape, size), and orientation, on the thermal performance. It was emphasized in their study that fin-shaped turbulators like tubes and helix can be used to extract heat from the absorber plate surface to greater depth. The various methods of enhancing the thermal performance of SAH was reviewed by Arunkumar et al., (2020) is given in *Fig. 2.1*. The literature related to adding ribs (roughness geometry / turbulators) for heat transfer enhancement is added below.

2.3.2 Enhancement using ribs

The experimental investigations on SAH with 90° broken transverse ribs on the absorber plate was performed by Sahu and Bhagoria, (2005). The experiments were performed by varying Re (3000-12000), roughness pitch (10-30), and solar insolation (750-880 W/m^2) for the fixed channel aspect ratio (8), test section length (1.5 m), relative roughness height (0.0338) and hydraulic diameter (0.044 m). The results showed that the maximum thermal efficiency of 83.5 % was obtained at Re =12000, for a pitch of 20 mm. Like ribs, grooves are also the helpful in generating the turbulence in the fluid flow that enhances the heat transfer. Hence, an experimental investigation conducted by Jaurker et al., (2006) to investigate the performance of rib grooved SAH also examined. The experimental investigation focused on empirical formulations of heat transfer correlations by varying Re (3000-21000), relative roughness height (0.0181-0.0363), relative roughness pitch (4.5-10), and grove position to pitch ratio (0.3-0.7). Test results showed that Nusselt number, frictional factor, and THPP were enhanced by 2.7 times, 3.6 times, and 1.76 times, respectively than smooth duct SAH. From the above review it was found that different shapes of ribs over the absorber surface has significant effect in performance.

Hence, a review on study of different shapes and various other physical parameters such as pitch, gaps size, and roughness height of the rib used to improve the thermal performance of SAH are reported. Tanda, (2011) performed a comparative analysis on SAH with different rib arrangements such as angled continuous ribs, transverse continuous ribs, transverse broken ribs, and discrete V-shaped ribs. To study the thermal performance, experimental investigations were carried out by varying Reynolds numbers from 5,000 to 35,000 for constant heat flux values of 500 and 1000 W/m^2. The experimental results reported that among the studied rib configuration, maximum enhancement was attained by the transverse broken ribs which returned 2.05 times improvement in Nusselt number in comparison with smooth duct SAH under the same operating conditions.

Kumar et al., (2012) performed experimental investigations on multiple V-shaped ribs with a gap arrangement over the absorber plate surface in a SAH. Investigations were performed by varying the relative gap distance from 0.24 to 0.8 and relative gap width from 0.5 to 1.5 in the Reynolds numbers ranging from 2,000 to 20,000. Test results showed that the maximum THPP value of 3.6 was attained for a relative gap distance of 0.69 and width of 1, for a Reynolds number of 20,000. Thermal performance of the transverse wire ribs was analysed by Prasad, (2013). The experimental investigations were performed by varying the relative roughness height ratio (0.01126 to 0.0279) and pitch ratio (10 to 40) for the mass flux (0.0262 kg/sm^2 to 0.0881 kg/sm^2). The experimental results showed that the maximum values of the collector heat removal factor, collector efficiency factor, and thermal efficiency were found to be 1.786, 1.806, and 1.842 times over smooth duct SAH. Later, Behura et al., (2016) conducted experimental studies in SAH roughened with artificial elements on three sides. The experiments were performed by varying pitch ratio (10-20), relative roughness height ratio (0.0135-0.0247), and mass flow rate (0.011-0.025 kg/s). It was observed that the thermal efficiency was improved by 48% over a single-sided roughened duct for the temperature rise parameter of 0.016 m^{2}K/W.

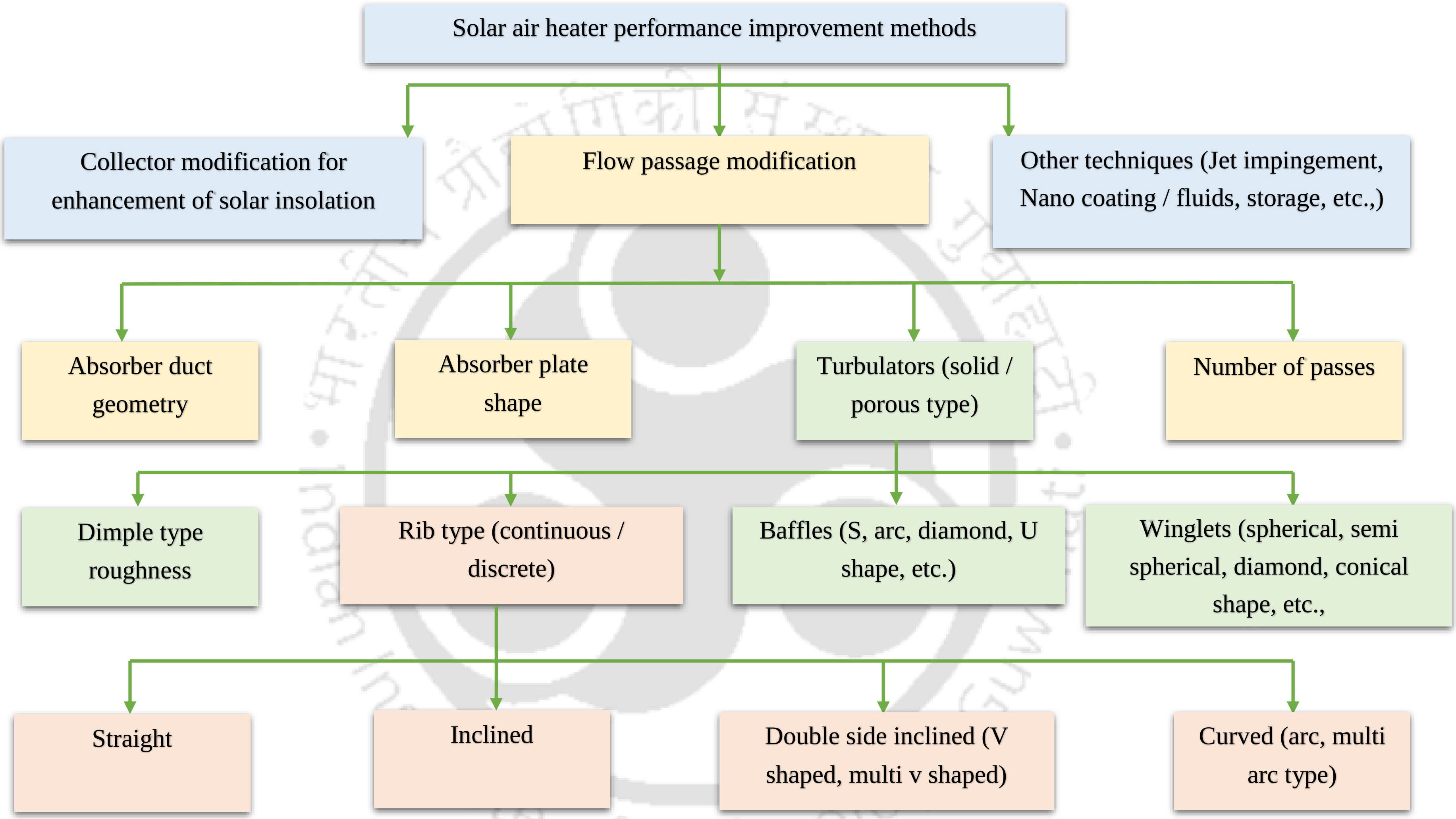

Fig. 2.1 Solar air heater thermal enhancement techniques

Then, heat transfer analysis of SAH using twisted rib as a roughened element was performed by Kumar and Layek, (2019) experimentally. Heat transfer correlations were formulated by varying the relative roughness pitch from 6 to 10, rib inclination angle from 30° to 90°, and twist ratio from 3 to 7 for the Reynolds number ranges from 3500 to 21000. The investigation reported that the maximum enhancement in Nusselt number was 2.46 over smooth duct SAH for the rib inclination angle, pitch ratio, and the twist ratio of 60°, 8, and 3 respectively. In order to enhance the turbulence in the flow and to break the laminar sub layer formation neat the wall surface, three-sided roughness elements were also used and tested by some researchers.

Qasem et al., (2020) evaluated the THPP of 220 different types of ribs used in the SAH. The different types of ribs such as rectangular/square, arc/wavy, V-shaped, wedge-shaped, protrusion, and metal mesh were reviewed for the Reynolds number ranging from 2500 to 20000. The optimal performance was evaluated based on minimum entropy generation and maximum thermal efficiency. The results suggested that the multi-V-shaped rib with a gap was found to have optimal performance, for the Reynolds number less than 11000, whereas the S-shaped rib for the Reynolds number ranges from 11000 to 16000, and protrusion roughness geometry for the Reynolds number of operation higher than 16000 showed the optimal performance. Afshari et al., (2020) experimentally tested the effect of rectangular-shaped turbulators in the SAH. The thermal performance of SAH was tested by varying the flow rate from 0.009 to 0.015 kg/s. From experimental results, it was reported that 72.4 % was the highest thermal efficiency obtained by operating the SAH with the flow rate of 0.015 kg/s at 13:00 hrs.

Jain et al., (2021) reviewed the performance of the SAH having roughness elements as turbulators. The effect of physical parameters of the different types of roughness elements on the thermal efficiency and THPP were reviewed for the Reynolds number ranging from 4000 to 14000. The review suggested that the combination of discrete multi-V-shaped and staggered ribs obtained a better thermal efficiency of 75 % for the Reynolds number of 14000. Nidhul et al., (2021) reviewed the performance of SAH with different shapes of ribs and evaluated the thermal performance of SAH with V-shaped ribs. The exergetic efficiency of the different ribs in the SAH was reviewed to analyse the variation of exergy efficiency. It was identified that the SAH with multi-V-rib with a gap obtained the maximum enhancement in exergy efficiency of 31.6 % and 91.9 % over normal V-rib and smooth duct SAH. From the above study, it was inferred that the proper physical parameters play a major role in enhancing the performance of the SAH.

2.3.3 Criteria for rib selection

By varying the shape and other physical dimensions of the ribs over the absorber plate, the performance of the various different geometries was reviewed and compared. The main purpose of embedding ribs over the absorber plate is to improve the heat transfer coefficient, thereby the heat transfer rate will be improved.

The optimum value of physical parameters including relative roughness pitch, relative roughness height ratio and relative attack angle for maximum energy utilization are listed in *Table. (2.2-2.4)* respectively. The comparative review by different researchers were briefed as follows.

Table 2.2 Values of relative roughness pitch at which maximum value of heat transfer rate for different artificial roughness geometries used in solar air heater duct

S. No	Rib geometry	Value of relative roughness pitch (p/e)
1	Transverse continuous rib	10
2	Transverse broken ribs	13.33
3	Inclined rib with a gap	10
4	Combination of inclined and transverse rib	8
5	V shaped rib	10
6	Discrete v rib	8
7	Wedge shaped rib	7.57
8	Rib groove	6
9	Chamfered rib	7.09
10	Dimple shaped rib	10
11	Metal grit rib	17.5
12	W shaped rib	10
13	Discrete W-shaped rib	10
14	U shaped rib	10
15	Multi-v-shaped rib	8

Table 2.3 Values of relative roughness height at which maximum value of heat transfer rate for different artificial roughness geometries used in solar air heater duct

S. No	Rib geometry	Value of relative roughness height
1	Transverse continuous ribs	0.033
2	Transverse broken ribs	0.033
3	Inclined continuous rib	0.023
4	Inclined rib with a gap	0.037

S. No	Rib geometry	Value of relative roughness height
5	Combination of inclined and transverse ribs	0.030
6	V shaped rib	0.034
7	Discrete v rib	0.043
8	Wedge shaped rib	0.033
9	Rib groove	0.036
10	Chamfered rib	0.032
11	Expanded metal mesh	0.039
12	Dimple shaped rib	0.037
13	Arc shaped rib	0.042
14	Metal grit rib	0.044
15	W shaped rib	0.033
16	Discrete W-shaped rib	0.033
17	U shaped rib	0.039
18	Multi-V-shaped rib	0.043

Table 2.4 Values of the angle of attack at which maximum value of heat transfer rate for different artificial roughness geometries used in solar air heater duct

S. No	Rib geometry	Value of angle of attack $(^0)$
1	Transverse broken rib	90
2	Inclined continuous rib	60
3	Inclined rib with a gap	60
4	V shaped rib	60
5	Discrete v rib	60
6	Expanded metal mesh	61.9
7	Arc shaped rib	60
8	W shaped rib	60
9	Discrete w shaped rib	60
10	Multi-v-shaped rib	60

Lanjewar et al.,(2015) reviewed the various artificial roughness elements used in SAH. The review mainly focused on heat transfer correlations developed for different shapes of artificial roughness elements used in the SAH. The review suggested that the single arc rib roughness element performs better than double arc rib roughened SAH. Later, Yadav and Thapak, (2016) reviewed the thermo-hydraulic performance of the SAH embedded with an artificial roughness element. A comprehensive review of 21 different types of roughness geometries embedded over the absorber surface area of the SAH compared for thermo-hydraulic performance. The comparative investigation test showed that the arc rib embedded absorber plate attained the maximum THPP value of 2.54 for the Reynolds number of 15,000, having attack angle, aspect ratio, and relative roughness height, relative pitch distance of 60^0, 15, 0.02, and 10 respectively.

Similarly, Singh Bisht et al., (2018) reviewed the effect of various roughness geometry on the thermohydraulic performance of the SAH. The study was carried out to review the variation of Nusselt number, frictional factor, and thermohydraulic performance of the SAH for the Reynolds number ranging from 4000 to 18000 respectively. From the review, it was identified that the value of Nusselt number and frictional factor varies in the range of 20 to 320 and 0.006 to 0.047 respectively. The Maximum value of THPP value was 4.3, attained by SAH with circular protrusion arranged in angular arc position by operating the SAH in the Reynolds number of 18000. From the above discussion, it was inferred that Thermo-hydraulic performance parameter (THPP) was the major parameter deciding the selection of ribs. Also, it was found that in protrusion type of enhancing, circular protrusion attained maximum enhancement and arc rib obtained maximum THPP. Apart from ribs, there were some other methods used by researchers to improve the thermal performance of SAH as discussed below.

2.3.4 Enhancement using winglets

Along with the ribs, embedding the winglets (vortex generators) over the absorber surface area promotes the breaking of the laminar sub-layer formation and creates turbulence in the air flow. The effect of combined ribs and winglets were studied by Promvonge et al., (2011b), the author performed an experimental investigations to study the performance of the SAH air flow channel fitted with combined ribs and delta winglet. Experiments were performed for the delta winglet placed in two different arrangements, pointing downstream (PD) and pointing upwards (PU) by varying Reynolds number from 5000 to 22000 and attack angle from 30° to 60°. The results showed that the SAH configuration with PD winglet could deliver a maximum THPP of 1.39 at an attack angle of 30° and a Reynolds number of 5,000. We have found that combination of ribs and winglets enhances the performance of the SAH. Similarly, various other combinations such as combinations of ribs and baffles could channelize the air flow and helpful in even heat transfer along the cross section. Hence, a literature review on usage of various other combinations of thermal enhancement techniques are discussed briefly as follows.

Chamoli et al., (2012) reviewed the turbulent promoters used to improve the thermal performance of the solar thermal systems. The investigations reported that ribs and baffles could create turbulence in the flow, thereby the thermo-hydraulic performance could be improved. The effective technique of improving the thermal performance can be done by altering the physical parameters of different turbulators.

The detailed study on the performance optimization of the arcuate shaped turbulator was explained briefly by Gholami et al., (2019). They also performed a thermo-economic optimization on the arcuate-shaped curve form of the obstacles in a SAH. The optimization of the SAH operation was performed by varying the air flow rate from 0.001 to 0.5 kg/s, air inlet temperature from 273 to 300 K, absorber surface area from 1 to 5 m^2, for the input fixed heat flux of 800 W/m^2, and hot air outlet temperature up to 410 K. The optimized results showed that the best performance achieved by the SAH operated with the airflow rate of 0.017 kg/s, for the absorber surface area of 2.6 m^2, achieved the outlet temperature of hot air as 78°C.

2.3.5 Enhancement using baffles

Baffles in the SAH flow channel passage were used to hold the structure, channelize the flow of air and generates turbulence thereby increases its heat transfer coefficient. Hence, investigations in SAH performance using different shapes of baffles discussed. The effect its physical parameters over the performance were also discussed as follows.

Akpinar et al., (2010) performed an experimental investigation in baffled SAH with different types of obstacles on the absorber plate. Experiments were performed for two different mass flow rates of operation (0.0074 kg/s and 0.0052 kg/s) mounted by fixing triangular type, leaf type, and rectangular type obstacles. Results showed that the baffled SAH with leaf-type obstacles achieved maximum thermal efficiency of 82 % at 0.0074 kg/s with corresponding exergy efficiency of 44 %. Sometimes instead of solid baffles, porous material was also used. Porous media has the higher thermal heat transfer coefficient due to its surface area. Hence, Bayrak et al., (2013) performed an experimental investigation in SAH with staggered and non-staggered porous baffle configurations. The experiments were performed by varying the baffle thickness from 6 mm and 10 mm, for the air mass flow rates ranging from 0.016 to 0.025 kg/s. The experimental results showed that the SAH with staggered porous baffle of thickness (6 mm) arrangement configuration yielded the maximum thermal efficiency of 77.57 % at 0.025 kg/s.

Khanlari et al., (2020) examined the effect of the single baffle and double baffles incorporated in the SAH operated with parallel pass conditions used for drying applications.

The experimental investigations were performed for the air mass flow rates of 0.009 kg/s and 0.011 kg/s. The comparative test results showed that the double baffled SAH operated in parallel pass obtained a higher thermal efficiency of 75.1 % over a single baffled SAH at 0.011 kg/s. Baissi et al., (2020) developed heat transfer correlations for SAH with perforated and non-perforated delta baffled vortex generators. Experiments were performed by varying relative longitudinal length of obstacle (3 to 5), relative transverse length of obstacle (0.6 to 1), and Reynolds number (2500 to 12000) for the fixed relative roughness height of 0.8 and attack angle of 45^o. Experimental results showed that the perforated baffles achieved a maximum THPP of 2.26 operated with a Reynolds number of 11382, for relative longitudinal obstacle length and relative transverse obstacle length of 0.3 and 0.6 respectively.

Thanh Luan and Minh Phu, (2021) analysed the performance of the inclined baffle mountings in SAH numerically. Analysis was performed by varying baffle angle from 0 to $60^o$and clearance ratio from 0.6 to 1.4, for the Reynolds number ranging from 1,000 to 20,000. The results showed that the minimum entropy generation number of 3.683 occurs for the operating condition of Reynolds number, clearance ratio, and baffle angle of 14,500, 0.6, and 59^orespectively with a corresponding THPP of 0.7374. In order to study the effect of baffle configuration on the performance of SAH, Eddine, (2021) performed a numerical investigation on SAH with baffles (50 % up, 50 % down, 50 % middle, and 100 % baffled). CFD analysis was carried out by varying the Reynolds number from 2354 to 8340 for the five classical turbulence models (standard k-ε, realizable k-ε, Renormalization group RNG k-ε, standard k-ω, and shear stress transport SST k-ω). Sharma et al., (2021) numerically investigated the thermal performance of six different baffled SAH (transverse, inclined transverse, dimple, inclined dimple, arc, and sine wave baffle configurations). Analysis was performed by varying the Reynolds number from 3000 to 18000, for a fixed relative roughness pitch ratio of 10, and a fixed relative roughness height ratio of 0.271. The results showed that the sine wave baffled SAH attained the maximum THPP value of 2.05 with the Reynolds number of air was 15000. Pandey and Kumar, (2021) studied the effect of V-baffle blocks with staggered race track perforation embedded in SAH over thermo-hydraulic performance. The indoor environment-based thermo-hydraulic investigation was performed by varying relative roughness height from 0.4 to 0.7, relative pitch from 2 to 10, and Reynolds number ranging from 5,000 to 15,000 for the fixed attack angle of 45°. The maximum THPP of 1.435 was achieved for a relative roughness height of 0.5, and a relative pitch of 4 at operated with a Reynolds number of 13021. From analysis, it was found that 0.75 was the maximum value of THPP obtained by 50 % down baffled SAH model. From the above literature it was found that, incorporation of baffles could also be able to improve the thermal performance.

2.3.6 Enhancement using metal waste

Apart from the above mentioned methods, few research works have been carried out by embedding the metallic waste over the absorber surface area for improving the thermal performance. Phu et al., (2019) investigated the thermo-hydraulic performance of SAH embedded with helically coiled metal shavings as a roughness element. Heat transfer correlations were developed by varying Reynolds numbers from 5000 to 20000, relative roughness pitch ratio from 4.7 to 9.4, and relative roughness height ratio from 0.26 to 0.43. The Maximum THPP value of 1.5 was achieved for the corresponding relative roughness height ratio and relative roughness pitch ratio of 0.35 and 4.7 with the Reynolds number of 19000. Phu et al., (2020) investigated the performance of the SAH roughened with helically coiled metal waste as a roughened element. The analytical investigation was performed to examine the thermal performance of the SAH by varying the relative roughness pitch, relative roughness height, and absorber surface area for the Reynolds number ranging from 1200 to 20000 operated with a constant input heat flux of 1000 W/m^2. From analysis, it was predicted that the optimum absorber surface area of 3.5 m^2 has maximum exergetic efficiency of 2.71 % for relative roughness ratio of 0.6, and relative roughness pitch ratio of 4. Phu et al., (2020) performed an analytical investigation on SAH embedded with metallic waste as a roughness element. Analysis was performed by varying Reynolds numbers ranging from 1200 to 20000, for the fixed input solar insolation of 1000 W/m^2. From simulations, air flow penetration through roughness elements, dead zone, recirculation, reattachment point, and laminar sub-layer formation was visualized. The results showed that the maximum exergy loss happened due to the absorption of radiation by the absorber plate from input heat flux, which constitutes around 70 % of the losses.

Hence, from the above discussion, one can infer that metal waste can be used as a turbulent promoter. Also, these metal waste in different shapes improve the thermo-hydraulic performance of the SAH, thereby the thermal conversion efficiency also improves.

In this section, a detailed state-of-the-art on various heat transfer enhancement technique is presented. Mounting baffles along the flow passage and embedding various roughness elements over the surface area of the absorber plate generate turbulence by disturbing laminar sub-layer formation. These roughness elements also generate secondary flow in the SAH responsible for improving the thermo-hydraulic performance of the SAH. The turbulence created due to the vortex generator also increases the thermal conversion efficiency of the SAH. Hence, a clear description of selecting heat transfer augmentation techniques for designing a SAH and operational parameters is presented. The heat transfer correlations for different roughness geometries is presented in *Table 2.5* Singh et al., (2018).

Table 2.5 Heat transfer correlations of various ribs (turbulators) used in SAH models

Roughness geometry used	Range of parameters	Heat transfer correlation equations	References
Transverse wire rib	$e/D_e = 0.018$ to 0.052 $Re = 3000$ to 18000	$Nu = 0.000824\left(\frac{e}{D_e}\right)^{-0.178}\left(\frac{W}{H}\right)^{0.284}(\mathrm{Re})^{1.062}$, for $(e \leq 35)$ $Nu = 0.0037\left(\frac{e}{D_e}\right)^{-0.469}\left(\frac{W}{H}\right)^{0.245}(\mathrm{Re})^{0.812}$, for $(e \geq 35)$ $f = 0.06412\left(\frac{e}{D_e}\right)^{0.019}\left(\frac{W}{H}\right)^{0.0237}(\mathrm{Re})^{-0.185}$	Gupta et al., (1993)
V – shaped continuous wire ribs	$e/D_e = 0.01$ to 0.03 $p/e = 10$ to 40 $\alpha = 30^{o}$ to 90^{o}	$Nu = 0.067(\mathrm{Re})^{0.888}\left(\frac{e}{D_e}\right)^{0.424}\left(\frac{\alpha}{60}\right)^{-0.077}\exp\left[(-0.782)\left(\ln\left(\frac{\alpha}{60}\right)\right)^2\right]$ $f = 6.266(\mathrm{Re})^{-0.425}\left(\frac{e}{D_e}\right)^{0.565}\left(\frac{\alpha}{60}\right)^{-0.093}\exp\left[(-0.719)\left(\ln\left(\frac{\alpha}{60}\right)\right)^2\right]$	Momin et al., (2002)
W shaped ribs	$e/D_e = 0.018$ to 0.03375 $p/e = 10$ $\alpha = 30^{o}$ to 75^{o}	$Nu = 0.0613(\mathrm{Re})^{0.9079}\left(\frac{e}{D_e}\right)^{0.4487}\left(\frac{\alpha}{60}\right)^{-0.1331}\exp\left[(-0.5307)\left(\ln\frac{\alpha}{60}\right)^2\right]$ $f = 0.6182(\mathrm{Re})^{-0.2254}\left(\frac{e}{D_e}\right)^{0.4622}\left(\frac{\alpha}{60}\right)^{0.52}\exp\left[(-0.28)\left(\ln\frac{\alpha}{60}\right)^2\right]$	Lanjewar et al., (2011a)

Roughness geometry used	**Range of parameters**	**Heat transfer correlation equations**	**References**
	Re = 2000 to 20000		
Rib groove combination	e/D$_e$ = 0.0181 to 0.0363 p/e = 4.5 to 10 g/p = 0.3 to 0.7 Re = 3000 to 21000	$Nu=0.002062\left(\frac{e}{D_e}\right)^{0.349}\left(\frac{p}{e}\right)^{3.318}(\mathrm{Re})^{0.936}\exp\left[(-0.868)\left(\ln\left(\frac{p}{e}\right)\right)^{2}\right]\left(\frac{g}{e}\right)^{1.108}$ $\exp\left[2.486\left(\ln\frac{g}{p}\right)^{2}+1.406\left(\ln\frac{g}{p}\right)^{3}\right]$ $f=0.001227\left(\frac{e}{D_e}\right)^{0.585}\left(\frac{p}{e}\right)^{7.19}(\mathrm{Re})^{-0.199}\exp\left[(-1.854)\left(\ln\frac{p}{e}\right)^{2}\right]\left(\frac{g}{p}\right)^{0.645}$ $\exp\left[\left(1.513\left(\ln\frac{g}{p}\right)^{2}\right)+\left(0.8662\left(\ln\frac{g}{p}\right)^{3}\right)\right]$	Jaurker et al., (2006a)
Grit shaped wire ribs	e/D$_e$ = 0.035 to 0.044 p/e = 12.5 to 36 l/s = 1.72 to 1	$Nu=0.0024\left(\frac{e}{D_e}\right)^{0.42}\left(\frac{l}{s}\right)^{-0.146}\left(\frac{p}{e}\right)^{-0.27}(\mathrm{Re})^{1.3}$ $f=15.55\left(\frac{e}{D_e}\right)^{0.91}\left(\frac{l}{s}\right)^{-0.27}\left(\frac{p}{e}\right)^{-0.51}(\mathrm{Re})^{-0.263}$	Karmare and Tikekar, (2007)

Roughness geometry used	Range of parameters	Heat transfer correlation equations	References
	Re = 4000 to 17000		
Arc shaped wire ribs	e/D_e = 0.0213 to 0.0422 p/e = 10 W/H = 12 α/90 = 0.333 to 0.666 Re = 3000 to 21000	$Nu = 0.001047\left(\frac{e}{D_e}\right)^{0.3772}\left(\frac{\alpha}{90}\right)^{-0.1198}(\mathrm{Re})^{1.3186}$ $f = 0.14408\left(\frac{e}{D_e}\right)^{0.1765}\left(\frac{\alpha}{90}\right)^{0.1185}(\mathrm{Re})^{-0.17103}$	Saini and Saini, (2008)
Discrete w shaped ribs	e/D_e = 0.0168 to 0.0338 p/e = 10 α = 30° to 75° Re = 3000 to 15000	$Nu = 0.105(\mathrm{Re})^{0.873}\left(\frac{e}{D_e}\right)^{0.453}\left(\frac{\alpha}{60}\right)^{-0.081}\exp\left[(-0.59)\left(\ln\frac{\alpha}{90}\right)^{2}\right]$ $f = 5.68(\mathrm{Re})^{-0.40}\left(\frac{e}{D_e}\right)^{0..59}\left(\frac{p}{e}\right)^{8.9}\left(\frac{\alpha}{90}\right)^{-0.081}\exp\left[(-0.579)\left(\ln\frac{\alpha}{60}\right)^{2}\right]\left(\frac{\alpha}{90}\right)^{-0.49}$	Kumar et al., (2008)
Multi V rib	e/D_e = 0.019 to 0.043	$Nu = 0.0000335(\mathrm{Re})^{0.92}\left(\frac{e}{D_e}\right)^{0.77}\left(\frac{W}{w}\right)^{0.43}\exp\left[(-0.61)\left(\ln\frac{\alpha}{90}\right)^{2}\right]\left(\frac{\alpha}{90}\right)^{-0.49}$	Hans et al., (2010)

Roughness geometry used	**Range of parameters**	**Heat transfer correlation equations**	**References**
	p/e = 3 to 8 α = 30º to 75º W/w = 1 to 10 Re = 2000 to 20000	$\exp\left[(-0.1177)\left(\ln\frac{W}{w}\right)^2\right]\left(\frac{p}{e}\right)^{8.54}\exp\left[(-2.0407)\left(\ln\frac{p}{e}\right)^2\right]$ $f=0.000447(\mathrm{Re})^{-0.3188}\left(\frac{e}{D_e}\right)^{0.73}\left(\frac{W}{w}\right)^{0.22}\exp\left[(-0.52)\left(\ln\frac{\alpha}{90}\right)^2\right]$ $\left(\frac{\alpha}{90}\right)^{-0.39}\left(\frac{p}{e}\right)^{8.9}\exp\left[(-2.133)\left(\ln\frac{p}{e}\right)^2\right]$	
W shaped rib	e/D$_e$ = 0.018 to 0.03375 p/e = 10 α = 30º to 75º Re = 2000 to 20000	$Nu=0.0613(\mathrm{Re})^{0.9079}\left(\frac{e}{D_e}\right)^{0.4487}\left(\frac{\alpha}{60}\right)^{-0.1331}\exp\left[(-0.5307)\left(\ln\frac{\alpha}{60}\right)^2\right]$ $f=0.6182(\mathrm{Re})^{-0.2254}\left(\frac{e}{D_e}\right)^{0.4622}\left(\frac{\alpha}{60}\right)^{0.0817}\exp\left[(-0.28)\left(\ln\frac{\alpha}{60}\right)^2\right]$	Lanjewar et al., (2011a)
Discrete V down rib	e/D$_e$ = 0.015 to 0.043 p/e = 4 to 12 d/W = 0.2 to 0.8	$Nu=0.00236(\mathrm{Re})^{0.90}\left(\frac{p}{e}\right)^{3.50}\left(\frac{\alpha}{60}\right)^{-0.023}\left(\frac{d}{w}\right)^{-0.043}\left(\frac{g}{e}\right)^{-0.014}\left(\frac{e}{D_e}\right)^{0.47}$ $\exp\left[(-0.84)\left(\ln\frac{p}{e}\right)^2\right]\exp\left[(-0.72)\left(\ln\frac{\alpha}{60}\right)^2\right]$	Singh et al., (2011a)

Roughness geometry used	**Range of parameters**	**Heat transfer correlation equations**	**References**
	$\alpha = 30^{o}$ to 75^{o} g/e = 0.5 to 2 Re = 3000 to 15000	$\exp\left[(-0.05)\left(\ln\frac{d}{w}\right)^{2}\right]\exp\left[(-0.15)\left(\ln\frac{g}{e}\right)^{2}\right]$ $f = 0.00413(\mathrm{Re})^{-0.126}\left(\frac{p}{e}\right)^{2.74}\left(\frac{\alpha}{60}\right)^{-0.0034}\left(\frac{d}{w}\right)^{-0.058}\left(\frac{g}{e}\right)^{0.031}\left(\frac{e}{D_e}\right)^{0.70}$ $\exp\left[(-0.685)\left(\ln\frac{p}{e}\right)^{2}\right]\exp\left[(-0.93)\left(\ln\frac{\alpha}{60}\right)^{2}\right]$ $\exp\left[(-0.058)\left(\frac{d}{w}\right)^{2}\right]\exp\left[(-0.21)\left(\ln\frac{g}{e}\right)^{2}\right]$	
Dimple shaped roughness	$e/D_e = 0.021$ to 0.036 p/e = 10 to 20 W/H = 11 $\alpha = 45^{o}$ to 75^{o}	$Nu = 0.0071(\mathrm{Re})^{1.1386}\left(\frac{e}{D_e}\right)^{0.3629}\left(\frac{p}{e}\right)^{-0.047}\left(\frac{\alpha}{60}\right)^{-0.0048}\exp\left[(-0.7792)\left(\ln\frac{\alpha}{60}\right)^{2}\right]$ $f = 0.004869(\mathrm{Re})^{0.223}\left(\frac{e}{D_e}\right)^{0.2663}\left(\frac{p}{e}\right)^{-0.059}\left(\frac{\alpha}{60}\right)^{0.0042}$ $\exp\left[(-0.4801)\left(\ln\frac{\alpha}{60}\right)^{2}\right]$	Sethi et al., (2012)

Roughness geometry used	Range of parameters	Heat transfer correlation equations	References
Circular protrusion arranged in circular arc	e/D_e = 0.015 to 0.03 p/e = 12 to 24 α = 45º to 75º Re = 3600 to 18100	$Nu=0.154(\mathrm{Re})^{1.017}\left(\frac{p}{e}\right)^{-0.38}\left(\frac{e}{D_e}\right)^{0.521}\left(\frac{\alpha}{60}\right)^{-0.213}\exp\left[(-2.023)\left(\ln\frac{\alpha}{60}\right)^{2}\right]$ $f=7.207(\mathrm{Re})^{-0.56}\left(\frac{p}{e}\right)^{-0.18}\left(\frac{e}{D_e}\right)^{0.176}\left(\frac{\alpha}{60}\right)^{0.38}\exp\left[(-1.412)\left(\ln\frac{\alpha}{60}\right)^{2}\right]$	Yadav et al.,(2013)
Reverse L shaped rib	e/D_e = 0.042 p/e = 7.14 to 17.86 Re = 3800 to 18000	$Nu=0.032(\mathrm{Re})^{0.8332}\left(\frac{p}{e}\right)^{0.3479}\exp\left[\left(-0.1004\left(\ln\left(\frac{p}{e}\right)^{2}\right)\right)\right]$ $f=0.2805(\mathrm{Re})^{-0.2617}\left(\frac{p}{e}\right)^{0.0815}\exp\left[(-0.0319)\left(\ln\left(\frac{p}{e}\right)^{2}\right)\right]$	Gawande et al., (2016b)
Multi- gap V- Down Ribs Combined with Staggered Ribs	e/D_e = 0.026 to 0.057 p/e = 4 to 14 α = 40º to 80º Re = 4000 to 12000	$Nu=0.0225(\mathrm{Re})^{0.98}\left(\frac{p}{e}\right)^{-0.06}\left(\frac{e}{D_e}\right)^{0.18}\left(\frac{\alpha}{60}\right)^{0.04}$ $f=0.3715(\mathrm{Re})^{-0.15}\left(\frac{p}{e}\right)^{0.21}\left(\frac{e}{D_e}\right)^{0.65}\left(\frac{\alpha}{60}\right)^{0.57}$	Deo et al., (2016)

2.4 Review of solar air heater based on different rib geometries

Due to the lower thermal conductivity of the air, the convective heat transfer coefficient inside the SAH is very less, this leads to low thermal conversion efficiency. As discussed earlier, mounting various artificial roughness element over the absorber surface breaks the laminar sublayer near the wall and improves the wall heat transfer coefficient, which leads to higher thermal efficiency. In this section, the effect of different rib elements that promotes the turbulence are presented. The schematics of various roughness geometries are shown in *Fig. 2.2***.** Thermal and thermo-hydraulic analysis variation with respect to physical parameter of the rib element are presented in the following sections.

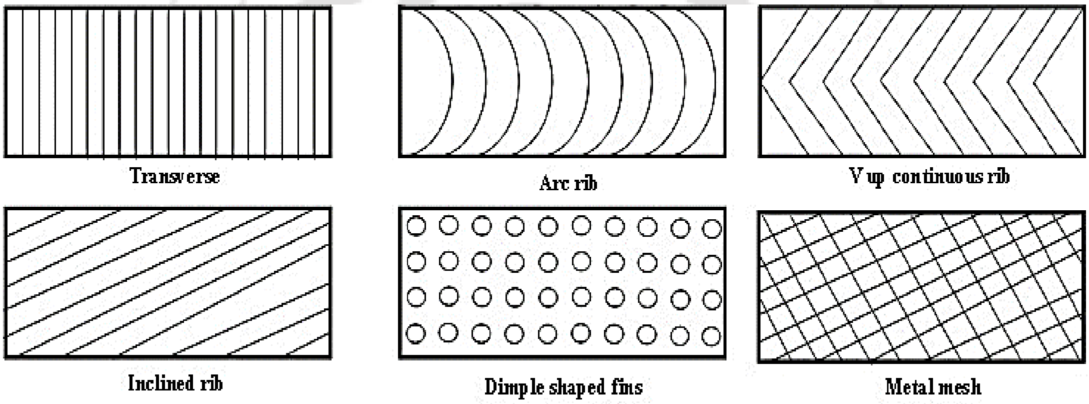

Fig. 2.2 Schematic layout of some of roughness geometries used in SAH

2.4.1 Arc wire rib configuration

Based on the flow passage channel modification, embedding turbulators over the absorber surface area considered as the cheapest method for improving the thermo-hydraulic performance of the SAH. The effect of various shapes of arc rib and its effect on the thermal performance are discussed in the following sections.

Saini and Saini, (2008) performed an experimental study in a SAH duct embedded with the arc rib fin arrangement. The influence of geometrical parameters in arc rib on the overall performance of SAH was studied by varying relative roughness height from 0.0213 to 0.0422, relative attack angle of 0.333 to 0.666, with a Reynolds number ranging from 2000 to 17000, for the fixed duct aspect ratio of 12 and relative pitch of 10. The results showed that heat transfer rate enhanced by 3.80 times more than a smooth duct. Later, Kumar and Saini, (2009) performed numerical analysis on arc-shaped ribs on the inner side of the absorber plate in SAH. Numerical analysis was carried out by varying relative roughness ratio (0.0299 and 0.0426), wire arc angle (30º and 60°), and relative arc angle (0.333 and 0.666) for Re (6000 to 18000), fixed heat flux input (1000 W/m^2), duct aspect ratio (12) and relative roughness pitch of 10. The maximum enhancement of THPP was 1.7, achieved for relative arc angle (0.333), and relative roughness height (0.0426) at Re (6000).

Exergy analysis on SAH having an arc-shaped rib arrangement as a roughness element was performed by Sahu and Prasad, (2016). Analysis performed by varying relative roughness height ratio from 0.0213 to 0.0422, relative attack angle ratio from 0.333 to 0.666, solar insolation from 500 to 1000 W/m^{2,} for the Reynolds number ranging from 4000 to 40000, having fixed relative roughness pitch ratio of 10. The results showed that the maximum exergy efficiency of 3.6% was achieved at a Reynolds number of 15,000 with an optimum relative angle of attack, relative roughness height ratio, and fixed pitch ratio of 0.3333, 0.0422, and 10 respectively. After this detailed exergy analysis, Thermo-hydraulic performance of SAH having same arc-shaped wire rib element as a roughness element was investigated by Sahu and Prasad, (2017). Analysis was carried out for the Reynolds number ranging from 2000 to 35000, roughness ratio from 0.0213 to 0.0422, and flow attack angle ratio from 0.333 to 0.666 for a fixed pitch ratio of 10. It was observed that the maximum thermal efficiency of 79.8 % was achieved at an attack angle ratio of 0.3333, and a relative roughness height ratio of 0.0422 for the Reynolds number value of 35,000.

Based on the above study, further the study on the thermo-hydraulic performance, energy and exergy efficiency were studied by various researchers. Sahu and Prasad, (2016) analytically investigated the performance of an arc wire ribbed SAH and smooth duct SAH. Analysis was performed by varying the relative roughness height ratio from 0.0213 to 0.0422, relative attack angle ratio from 0.3333 to 0.6666, for the solar insolation ranging from 500 to 1000 W/m^2, with a fixed pitch ratio of 10. The maximum enhancement in exergy efficiency of 56 % was achieved for the relative roughness height ratio of 0.0422 over a smooth duct. Prasad and Sahu, (2017) analytically investigated the thermal performance of arc ribbed roughness in SAH. The analytical investigation was carried out by varying the Reynolds number from 1650 to 21,500, solar radiation from 600 to 1000 W/m^2, relative roughness height from 0.0256 – 0.0422, and relative attack angle ratio of 0.33 to 0.66 for the fixed relative roughness pitch of 10. The highest exergy efficiency of 2.51 % was achieved for the respective input heat flux solar radiation and Reynolds number of 850 W/m^2 and 6460. Sahu and Prasad, (2019) performed thermodynamic analysis on an arc rib wire roughened SAH analytically. Analysis conducted by varying rib ratio from 0.021 to 0.042, attack angle ratio from 0.33 to 0.66, for the Reynolds number ranges from 450 to 21500, solar radiation from 800 to 1000 W/m^2, operated with the mass flow rate per unit area ranges from 10 to 550 kg/m^{2}hr, with fixed pitch ratio of 10. The maximum exergy efficiency of 3.17 % was achieved at a Reynolds number, rib ratio, and an attack angle ratio of 3624, 0.042, and 0.33 respectively.

Gill et al., (2017) conducted a numerical investigation on SAH embedded with broken arc ribs. Analysis was performed by varying relative gap positions (0.2 to 0.8) and Reynolds number (2000 to 16000) for fixed relative roughness height ratio (0.043), pitch ratio (8), and angle of attack (30 ^{o}). The maximum enhancement of THPP (1.94) was achieved for the relative gap position ratio (0.65) at Re (12000). Further, Gill et al., (2017) performed a numerical investigation on the staggered piece in a broken arc rib SAH. Numerical analysis was carried out by varying relative staggered rib size (1 to 6) and Reynolds number (2000 to 16000), for the fixed relative staggered rib position ratio (0.4), relative roughness pitch ratio (10), relative arc angle (30 ^{o}), relative gap position ratio (0.65), relative gap width ratio (1.0) and relative roughness height ratio (0.043). The numerical results showed that the maximum THPP (2.27) was achieved for relative staggered rib size (4) at Re (12000).

Furthermore, research works on the investigation of the performance of SAH were conducted by different combinations in arc rib. Gill et al., (2021) performed investigations on broken arc ribs combined with a staggered piece in SAH. The experimental and numerical investigation was performed by varying non-dimensional staggered rib position (0.2 to 0.8), roughness pitch ratio (4 to 12), gap width ratio (0.5 to 2.5), gap position ratio (0.2 to 0.8), roughness height ratio (0.022 to 0.043), arc angle (15 to 75^o), and staggered rib piece size (1 to 6) for the Reynolds number ranging from 2,000 to 16,000. The maximum THPP of 2.33 was achieved for arc angle and roughness height ratio of 30 ^{o} and 0.043 operated with the Reynolds number value of 12,000. A numerical analysis on arc and fan-shaped rib roughness elements embedded in SAH were performed by Singh et al., (2021). CFD analysis was performed by the varying angle of shape (115 ^{o}, 120 ^{o}, 125 ^{o}) and Reynolds number (3000 to 21000) for fixed arc shape radius (14 mm) and fan radius (8.5 mm). The highest THPP (2.87) was achieved for the shape angle (120 ^{o}) at Re (21000).

In-order to enhance the heat transfer coefficient, various modifications and combinations of shapes in arc ribs were designed and analysed. Sahu et al., (2021) conducted an experimental investigation on SAH embedded with arc-shaped ribs in upstream and downstream forms. Experiments were performed by varying relative roughness pitch from 8 to 15, for the air mass flow rates (0.01 to 0.0471 kg/s), and attack angle (45^{o} to 75^{o}), for the relative roughens height ratio of 0.0454. The maximum thermal efficiency of 71.6 % was achieved for the upstream arc rib model with an attack angle of 60 ^{o} and a relative roughness pitch of 8 operated at 0.0471 kg/s. Recently, Ghritlahre, (2021) performed an experimental investigation in a smooth duct SAH and SAH having arc-shaped ribs. Experiments were carried out for arc rib fin facing both upstream and downstream directions for the airflow rate of operation varying from 0.007 to 0.022 kg/s, with a fixed relative roughness height ratio of 0.0395, rib size (2.5 mm), relative roughness pitch (10), arc angle (60 ^{o}) and duct width of 330 mm. The results showed that the apex upstream arc rib SAH obtained a higher thermal efficiency of 73.2 %, with corresponding exergy efficiency of 2.64 % operated at 0.022 kg/s. Singh and Singh, (2018a) reviewed the effects of various rib geometries of SAH on the thermo-hydraulic performance. Also, from thermo-hydraulic consideration, the study showed that due to the curved secondary flow, the arc rib created a lesser pressure drop than V-rib.

2.4.2 V rib configuration

Embedding V-ribs over the absorber surface area was one of the methods of enhancing the thermal performance of SAH. The various research works based on V-rib embedding and the study on the energy and exergy efficiencies are discussed in the upcoming sections. Singh et al., (2011) studied the influence of geometrical properties of a V down rib fin SAH on effective efficiency. Experimental investigations were carried out by varying relative roughness pitch (4 to 12), relative gap position (0.20 to 0.80), angle of attack (30 ^{o} to 75 ^{o}), relative gap width (0.5 to 2.0), relative roughness height (0.015 to 0.043) and heat flux input (500 to 1000 W/m^2) for the temperature rise parameter (0.003 to 0.027 Km^2/W). The experimental study revealed that the maximum enhancement in effective efficiency of 1.9 times achieved for relative roughness pitch (8), relative gap position (0.65), angle of attack (60 ^{o}) for the relative gap width (1.0), relative roughness height (0.043) and heat input (1000 W/m^2) respectively over the smooth duct.

Later, the effect of various geometries of turbulators on the heat and fluid flow characteristics of the SAH reviewed by Alam et al.,(2014). The review was performed for the Reynolds number range of 2000 to 20000 for different ribs in SAH. The review results showed that the multi V-rib SAH attained the maximum THPP value of 3.3 for the Reynolds number of 16000. The optimum rib geometry for the maximum thermo-hydraulic performance are presented in the *Tables 2.3, 2.4* and *2.5*. Based on the above study, further Nidhul et al., (2021) reviewed the effect of various rib roughness elements of SAH thermodynamically and performed exergy analysis on SAH with V-rib configurations. From the review, it was found that the major exergy losses were due to absorption of solar radiation which constituted around 65 to 75 %, next through optics constitutes around 20 %, and exergy losses due to heat transfer to air, environment, and pumping are nearly 1 to 6 % respectively. Also, among V-rib configurations, it was found that multi V-rib configuration enhanced its exergetic efficiency by about 31 % over normal V-rib configuration. Abo-Elfadl et al., (2021a) performed experimental investigations on SAH with a V-shaped transverse rib finned absorber. The experimental investigations were performed for both single and double pass conditions, by varying the air mass flow rates (0.025, 0.05, 0.075 kg/s). The results showed that the maximum thermal efficiency of 88.5 % was achieved by double pass V-shaped transverse finned SAH operated at 0.075 kg/s air flow rate.

2.4.3 Grooves, protrusion and conic profiles

Grooves are the deep line cut formed over the surface of the absorber plate to enhance the thermal performance. Ribs are additional element embedded over the absorber surface but in the case of grooves, the layer of material removed from the plate. Protrusions are formed by punching the metal layer. Different shapes of the protrusions can also be made as per the requirement. The various literatures published based on grooves, protrusions and conics were discussed in this section.

2.4.3.1 Heat transfer enhancement using grooves

Layek et al., (2007) investigated the performance of SAH with chamfered rib groove roughness element. Analysis was performed by varying relative roughness pitch (4.5 to 10), relative roughness height (0.022 to 0.04), relative groove position (0.3 to 0.6), and chamfer angle (5^o to 30^o). The results of the investigation showed that the minimum entropy generation was achieved for relative roughness pitch, relative groove position, and chamfer angle of 6, 0.4, and 18°. Abuşka and Şevik, (2017) conducted experimental investigations in smooth duct single-front pass flat plate and V-groove single pass SAH duct. Experiments were performed using aluminium and copper as absorber materials by varying the mass flow rate from 0.04 to 0.1 kg/s. Results showed that copper V-groove SAH performed better than smooth duct, attained thermal efficiency of 60 %, and exergy efficiency of 12 %. Tuncer et al., (2020) performed an experimental investigation to study the thermal performance of a V groove-shaped roughness element embedded in a triple pass SAH. The performance-groove-shaped triple pass SAH compared to parallel and double pass SAH. An experimental investigation was performed by varying the air flow rate from 0.011 to 0.015 kg/s. The V grooved triple pass SAH performed better than double and parallel pass SAH with a maximum exergy efficiency range of 14.6 -18.9 %, instantaneous thermal efficiency of 90.6 %, and annual average annual thermal efficiency in the range of 70.9 - 78.1 %. Tuncer et al., (2020) compared the thermal performance of parallel pass flat plate, double pass the flat plate, and triple pass V- groove type SAH. Experiments were performed by varying the mass flow rate from 0.011 to 0.015 kg/s. The test results showed that the V-groove type triple pass solar air heater performed higher thermal efficiency of 78.18 % and exergy efficiency of 18.95 %. Dong et al., (2021) performed a numerical investigation on SAH with inclined groove ripple surfaces. Analysis was carried out by varying groove depth (1, 1.5, 2 mm), groove arrays (2 to 8), and attack angle (45 ° to 90 °). From analysis, it was found that the highest THPP of 1.94 was achieved for the parameter groove depth, groove arrays, and attack angle of 2 mm, 8, and 45°, for the Reynolds number of 12,000.

2.4.3.2 Heat transfer enhancement using protrusions

Apart from ribs, grooves, very few research works on improving the SAH using protrusions were reported by some authors. Yadav et al., (2014) performed an analytical investigation on the performance of an arc shape-oriented protrusion roughness element in SAH. The performance was carried out by varying relative roughness height ratio from 0.015 to 0.03, pitch ratio from 12 to 24, Reynolds number from 1000 to 40000, and arc angle from 45 to 75 °, for the heat flux input from 500 to 1000 W/m^2. From analysis, it was reported that the maximum exergy efficiency of 2.2 % was achieved at a relative roughness pitch ratio, relative roughness height ratio, and an arc angle of 12, 0.03, and 60° respectively. Later, Kumar and Verma, (2022) performed a 3D numerical simulation on SAH with (SPR) sinusoidal protrusion rib model. Analysis was carried out by varying the Reynolds number from 4000 to 15000, transverse pitch from 10 to 18 mm, and longitudinal pitch from 10 to 18 mm for the constant heat flux of 1000 W/m^2, with a fixed aspect ratio of 5. From analysis, it was found that maximum enhancement in THPP value was 2.02, obtained for the roughness pitch of 10 mm operated with the airflow Reynolds number value of 4000.

2.4.3.3 Heat transfer enhancement using conic profiled turbulators

Conics are different mathematical profiles that are also used for promoting the turbulence along the length of the flow. Phu and Hap, (2020) investigated the effect of conical curve rib embedded on the performance of SAH through numerical simulation. The simulation was performed by varying the Reynolds number from 1200 to 28,000 and conic constants from -4 to 0. Simulated results showed that the maximum effective efficiency value of 67.2 % obtained for the conic constant of -4 (hyperbola) operated with the Reynolds number of 2786 with corresponding exergy efficiency of 1.527 %. Ngo and Phu, (2020) performed a numerical investigation on SAH with multiple conic curve profile rib on the THPP. A 2D simulation analysis was carried out by varying conic constant from 0 to -4, for the Reynolds number ranging from 4,000 to 15,000 to study the turbulent kinetic energy, velocity streamlines behaviour, and location of poor heat transfer. From the simulation, it was found that the hyperbolic curve (conic constant of -4) achieved the maximum THPP value of 1.56, for the Reynolds number of 8000.

2.4.4 Uniform cross sectioned transverse ribs

Apart from arc rib wire and V-rib configurations, various alphabetical shapes were also used as a roughness element to enhance the heat transfer properties of the SAH.

2.4.4.1 Heat transfer enhancement using L-shaped ribs

Gawande et al., (2016b) investigated the thermal performance of reverse L-shaped rib configuration in SAH. The numerical analysis was performed by varying the relative roughness pitch from 7.14 to 17.86, and the Reynolds number ranging from 3800 to 18000, for the constant heat flux and relative roughness height ratio of 1000 W/m^2 and 0.042 respectively. From the analysis, it was found that the THPP value of 1.9 was the maximum enhancement obtained over a smooth duct for the relative roughness pitch of 7.14, and 15,000 was the corresponding Reynolds number of the flow. Later, Pashchenko, (2018) performed a numerical simulation to investigate the influence of L-shaped rib embedded in

SAH on the thermo-aerodynamic characteristics. The simulation was performed by varying Reynolds number from 4000 to 20000, and fin pitch distance from 30 to 60 mm. The report showed that the maximum value of thermo-aerodynamic characteristics value was 1.91 attained for fin pitch distance of 30 mm with a corresponding Reynolds number of 15000.

2.4.4.2 Heat transfer enhancement using S, T, Y shaped ribs

Experimental investigations on SAH embedded with an S-shaped ribs performed by Wang et al., (2020). Experiments were performed by varying Reynolds number from 2000 to 20000, relative roughness pitch from 20 to 30, relative roughness width from 3 to 5, relative roughness height from 0.023 to 0.036, and relative gap width from 1 to 2, for the input solar radiation intensity of 450 to 650 W/m^2. Results showed that the Nusselt number was enhanced by 5.42 times more than smooth duct SAH for relative rib width (4), relative rib spacing (20), and relative gap spacing (1.5) operated with the Reynolds number of 19258.

Transverse ribs are different shapes of continuous turbulators situated across the width of the SAH. Naphon, (2005) conducted a numerical investigation to study entropy generation in double pass SAH with longitudinal fins. A study was performed for the fixed input heat flux of 600 W/m^2, by varying fin numbers into 45, 50, and 55, also for the fin height of 5 and 8 cm, operated with the air mass flow rate ranging from 0.02 to 0.1 kg/s. From the investigation, it was observed that the minimum entropy generation number of 0.933 was achieved at 0.02 kg/s with 55 fins, fa in height of 8 cm.

2.4.4.3 Heat transfer enhancement using Circular, triangular, square, rectangular and tapered cross sectioned ribs

Various uniform cross sectioned transverse ribs such as circular, equilateral triangular, square, rectangular shaped ribs are embedded on the surface on SAH. Yadav and Bhagoria, (2013) performed the thermo-hydraulic performance on circular transverse rib embedded SAH. Numerical simulation performed by varying Reynolds number (3800 to 18000), relative roughness pitch ratio (7.14 to 35.71), and relative roughness height ratio (0.021 to 0.042) for constant heat flux and duct aspect ratio of 1000 W/m^2 and 5. From analysis, it was observed that the maximum THPP (1.65) was achieved for the relative roughness pitch ratio (10.71), and relative roughness height ratio (0.042) for Re (15000). Singh et al., (2022c) performed numerical analysis on circular and semi-circular ribs in SAH. Analysis was carried out by varying Reynolds numbers from 3800 to 18000 and relative roughness ratio ranging from 0.03 to 0.06, for a fixed pitch distance of 10 mm. The predicted results showed that semi-circular rib roughened SAH was achieved the maximum THPP value of 1.76 operated with the Reynolds number value of 15000. Mahanand and Senapati, (2021) performed numerical analysis on quarter circular rib roughened SAH. The simulation was performed by varying relative roughness pitch ratio (7.14 to 17.86) and Re (3800 to 18000) for constant heat flux (1000 W/m^2) and relative roughness height ratio (0.042). The maximum THPP (1.88) was achieved for relative roughness height (0.042) and relative roughness pitch (7.14) at Re (15000).

Yadav and Bhagoria, (2014a) performed a 2D CFD analysis on SAH embedded with an equilateral triangular sectioned rib on an absorber plate. Numerical simulation was performed by varying Reynolds number from 3800 to 18000, relative roughness pitch ratio from 7.14 to 35.71, relative roughness height ratio from 0.021 to 0.042, for the fixed heat flux input of 1000 W/m^{2,} and duct aspect ratio of 5. The investigated results showed that the maximum value of THPP was 2.11, achieved for a relative roughness height ratio of 0.042 and relative roughness pitch ratio of 7.14 operated with the Reynolds number value of 15000. Kumar et al., (2019) numerically performed the heat transfer analysis on equilateral triangular cross-sectioned SAH embedded with square ribs. Numerical simulations were performed by varying relative roughness height ratio (0.013 to 0.05), relative roughness pitch ratio (5 to 13), and Reynolds number (3900 to 17900). The maximum THPP (1.97) was achieved for relative roughness height ratio (0.05), and relative roughness pitch ratio (10) at Re (17900).

Yadav and Bhagoria, (2014b) performed CFD analysis on square sectioned transverse rib in SAH. Numerical analysis was performed by varying Reynolds number (3800 to 18000), relative roughness pitch ratio (7.14 to 35.71), and relative roughness height ratio (0.021 to 0.042) for fixed heat flux of 1000 W/m^2. The analysed results showed that the maximum THPP (1.881) was achieved for relative roughness height ratio (0.042), and pitch ratio (7.14) at Re (12000). Singh et al., (2022b) numerically investigated the performance of SAH with square ribs. Heat transfer correlations were formulated by varying pitch (10 – 25 mm), Reynolds number (4000 to 18000), for the constant heat flux of 1000 W/m^2, and relative roughness height ratio of 0.06. The maximum enhancement in Nusselt number value was 147.7 for the pitch of 10 mm at Reynolds of operation 18000. Gupta and

Varshney, (2017) predicted the thermal performance of rectangular sectioned tapered rib roughened SAH numerically. Simulations were performed varying Reynolds number from 3800 to 18000, relative roughness pitch ratio (3.6 to 17.9), relative roughness height ratio (0.042 to 0.084), and tapered angle (1.6 ^{o} to 3.2 ^{o}) for fixed aspect ratio of 5. The maximum THPP value of 1.91 was achieved for relative roughness pitch (10.7) and tapered angle (1.6 ^{o}) at Re (12000).

After reviewing the performance of the circular and square cross sectioned ribs, a comparative study was performed by Sunil Kumar et al., (2021) numerically. The author studied the exergetic performance of semi-circular and square ribs in SAH ducts having triangular cross-sections. The simulation was performed by varying the heat flux ranging from 600 to 1000 W/m^2, relative roughness pitch ratio (5 to 20), and relative roughness ratio (0.01 to 0.04). The semi-circular rib SAH obtained an exergetic efficiency, which was 26 % higher than square rib SAH.

2.4.5 Non-uniform cross sectioned ribs

Various researchers proposed different shapes of non-uniform cross sectioned ribs to enhance the thermo-hydraulic performance of the SAH. The detailed study on shape effect of wavy fins, twisted ribs, discrete wavy profiled ribs were studied as given below.

2.4.5.1 Enhancement using wavy profiled ribs

Priyam and Chand, (2016 and 2018) performed an analytical investigation on SAH having wavy fins. Investigations were carried out by varying fin spacing from 1 to 5 cm, wavelength from 3 to 20 cm, amplitude from 0.5 to 2.5 cm, for air mass flow rate ranging from 0.0138 to 0.0834 kg/s. From the analysis, it was observed that the maximum thermal efficiency value of 78.8 % was reported for the airflow rate of 0.0138 kg/s having a wavelength of 3 cm, fin spacing of 1 cm, and amplitude of 2.5 cm. Singh and Singh, (2018a) performed a 3D numerical study on a non-uniform cross-sectioned SAH duct having square wave profiled transverse ribs as roughness elements. Analysis was carried out by varying the relative roughness pitch (4 to 30) and fixed relative roughness height ratio (0.043) for Reynolds numbers ranging from 3000 to 15000. The maximum enhancement of the THPP value of 1.43 was achieved for a relative roughness pitch of 10 and the Reynolds number of air flow inside the duct was 12000. Sharma et al., (2022) studied the performance of the discrete triangular wave SAH configuration numerically. Analysis was carried out by varying Reynolds numbers ranging from 6000 to 24000, with non-dimensional amplitude (0.025 to 1), and non-dimensional wavelength (0.113 to 0.453). The maximum THPP value of 1.612, achieved for non-dimensional amplitude and non-dimensional wavelength of 0.1, and 0.453 operated with the Reynolds number of air-flow inside duct was 6000.

2.4.5.2 Enhancement using twisted ribs

Anup Kumar and Apurba Layek, (2019) analytically investigated the performance of the SAH having a twisted rib as a roughness element. Investigations were performed by varying relative roughness pitch from 6 to 10, rib orientation angle from 30 to 90 ^{o}, and twist ratio from 3 to 5, for the heat flux input ranging from 600 to 1000 W/m^2. From the analysis, it was found that the maximum enhancement of 1.81 times in both energy and exergy efficiencies was achieved for the rib orientation angle, heat flux input, relative roughness pitch and twist ratio of 60^{o}, 800 W/m^2, 8, and 3 respectively.

2.4.5.3 Enhancement using inclined and broken transverse ribs

The broken ribs always have a higher number of corners and edges that is responsible for the cause of swirl action thereby breaks the laminar sub-layer formation. The turbulence in the flow improves the thermal efficiency of the SAH. Rahmani and Nikbakht, (2017) performed an experimental investigation on an inclined broken rib roughened geometry in a SAH. The thermo-hydraulic performance analysis of SAH was performed by varying the Reynolds number from 3000 to 6500, heat flux input from 800 to 1000 W/m^2, for the fixed angle of attack of 60 ^{o}, relative roughness pitch of 10, relative roughness height of 0.0377, relative gap position of 0.25 and relative gap width of 1. The results showed that the maximum enhancement in THPP value of 1.23 was achieved for the Reynolds number of 5151 with a heat flux input of 1000 W/m^2. In order to visualize the effect of the turbulence caused by the multiple broken transverse ribs, Singh et al., (2019) performed a numerical study on SAH. The investigation was performed by varying Reynolds numbers from 3000 to 18000, relative roughness pitch ratio of 10, relative roughness height ratio of 0.043, and relative roughness width ratio of 7, for a fixed aspect ratio of 12.1 and constant heat flux input of 1000 W/m^2. From analysis, it was found that the highest THPP value of 2.1 was achieved for the Reynolds number of 15000. Pashchenko, (2019) investigated the effect of angle of inclination for transverse rib embedded SAH numerically. The simulation was carried out by varying the angle of inclination from 0 ^{o} to 90 ^{o} and operated with the air inlet velocity ranging from 0.5 to 2 m/s. From analysis, it was observed that a maximum hot air outlet temperature of 50°C was obtained for the angle of inclination of 60 ^{o} from 13:00 to 14:00 hrs.

2.4.6 Review of SAH on different configuration of vortex generators

Vortex generators are aerodynamic geometry that helps in transferring the energy from the absorber plate to the fluid. This separates the fluid in the flow region, the disturbances in the fluid region enhances the energy transfer. Several researchers used different shapes of the vortex generators, which are briefly explained in this section. Xiao et al., (2020) performed numerical analysis on SAH with inclined trapezoidal vortex generators of various configurations such as upwind aligned, mixed staggered, upwind staggered, and downwind aligned. The analysis was performed by varying Reynolds numbers from 6,000 to 18,000, for the width ratios of 0.267 and 0.333, height ratio values of 0.12, 0.24, 0.36, and longitudinal pitch ratios of 1,2,3. From analyses, it was found that upwind aligned SAH achieved a maximum THPP of 1.88, with corresponding energy and exergy efficiencies of 63.5 %, and 8.8 %. A 2D CFD analysis to investigate the effect of circular vortex generators embedded in the inlet section of SAH was performed by Gawande et al., (2014). The investigations were performed by varying Reynolds number from 3800 to 18000, and relative roughness pitch ratio from 10 to 25, for a fixed relative roughness height of 0.03. The results showed that the maximum THPP of 1.5 was achieved for a relative roughness pitch of 25 with a Reynolds number of operations of 18000. Later, Kumar and Layek, (2021) conducted an experimental investigation in SAH having smooth duct SAH and embedded with winglet type vortex generator. The investigations were performed by varying relative roughness pitch from 5 to 12, relative roughness width from 3 to 7, with an attack angle of 30 to 75 ^{o}, operated with the input solar intensity of the radiation ranging from 600 to 1,000 W/m^2 and air flow rate ranging from 1.12 to 5.23 kg/s. The maximum enhancement in the thermal, effective, and exergy efficiencies were 2.12, 1.99, and 2.03 times over the smooth duct, respectively. The performance of SAH having a combined baffle and delta winglet vortex generator was analysed by Sari et al., (2021). The analysis was performed by varying Re (1000 to 10000), the number of baffles, and pairs of delta winglet vortex generators. The results show that the maximum thermo-hydraulic performance (2.55) was achieved for six baffled-three pairs of delta winglet vortex generators with corresponding thermal efficiency (14.7 %) and exergy efficiency (28.23

%) at Re (10000). An experimental investigation on perforated delta-shaped winglet SAH was performed by Raj Kumar et al., (2022). Experimental investigations were carried out by varying Reynolds numbers from 2,000 to 12,000 with a spacer length up to 300 mm, for the fixed relative roughness height ratio of 0.8, the relative longitudinal length of 2, and relative transversal length of 0.66, for the fixed angle of incidence of 90°. The experimental results showed that the maximum thermo-hydraulic efficiency value of 3.14 was achieved for the Reynolds number 12,000.

2.4.7 Dimples

Dimples were considered as an effective way to enhance the heat transfer with lesser pressure drop. Generally, dimples were created by punching over the absorber plate surface, so there was no external surface embedding. Saini and Verma, (2008) performed heat transfer analysis to investigate the behaviour of dimple-shaped roughness elements in the SAH. The experimental investigation was carried out by varying Re from 2000 to 12000, relative roughness height ratio from 0.018 to 0.,037, and relative pitch ratio from 8 to 12. The experimental results showed that the dimple-shaped roughness SAH enhances heat transfer by 3.5 times more than smooth duct SAH, a relative roughness height ratio of 0.0379, and a relative pitch ratio of 10 at a Reynolds number of 12,000.

Arranging dimple shapes in an arc form also tried by some of the researchers to enhance the thermal performance. Sethi et al., (2012) studied the thermo-hydraulic performance of dimple shape roughened geometry in SAH. The experimental investigation was performed by varying Reynolds number from 3600 to 18000, relative roughness pitch from 10 to 20, relative roughness height from 0.021 to 0.036, and arc angle from 45 ⁰ to 75 ⁰ for a fixed duct aspect ratio of 11. The result showed that the heat transfers enhanced triples times more than smooth duct SAH for a relative roughness height of 0.036 and arc angle of 60 ⁰. From the above study, it was identified that dimples enhanced the thermal performance due to its easy manufacturing process.

2.4.8 Corrugated, perforated and finned configurations

There were some of the heat transfer sheets that aren't plane surface, instead corrugated sheets, perforated during manufacturing (moulding). Various modified sheets such as Notched flat profile, corrugated sheets and perforated plates were widely used by recuperative and regenerative heat exchangers. Similarly, for low temperature application based SAH also tested using this non-flat surface. To study the effect of the corrugated absorber and corrugated-perforated finned absorber on thermal performance, Hassan et al., (2021) conducted an experimental investigation in SAH. The experiments were performed by varying the mass flow rates from 0.025 to 0.075 kg/s operated both in single back pass (SPSAH) and double pass (DPSAH) for three different configurations (1/3 DP, 2/3 DP, DP). The experimental results showed that 2/3 DP corrugated-perforated DPSAH attained the maximum thermal efficiency of 71.85 % with corresponding exergy efficiency of 0.975 %. Using flat, reverse trapeze, reverse corrugated, trapeze, and corrugated configurations Benli, (2013) performed a thermal analysis in SAH experimentally. Experiments were performed by varying mass flow rates from 0.02 to 0.05 kg/s, operated from 09:00 to 17:00. Results showed that the maximum thermal efficiency of 55 % was achieved by corrugated type SAH with minimum dimensionless exergy loss at 0.036 kg/s.

2.5 Literature closure

From the literature survey, the following conclusions are made,

- Several researchers developed various designs of SAH models with different configurations to extract the energy available in an absorber plate of the SAH. The design of SAH is classified based on flow passage, the mode of heat transfer, and operation. Several researchers developed mathematical models based on the energy interactions within the subsystem. The heat transfer correlation for each parameter of the SAH based on source, system, and surroundings developed are studied.
- Several researchers focused on flow passage construction to minimize the top loss generated during absorption of solar radiation and to maximize the utilization of energy, thereby thermal conversion efficiency improved.
- Few studies focused on stabilizing the energy output of the SAH. To achieve a steady output, various researchers focused on designing SAH with inbuilt and external thermal energy storage devices.
- Depending upon the need of the application, many researchers conducted performed experimental investigations on SAH operation under natural convection and forced convection modes of operation.
- Many researchers focused on predicting the performance of the SAH analytically, using mathematical equations. The main focus of the analytical investigation of SAH

is to determine the thermo-hydraulic performance and thermodynamic analysis for various operational design parameters and input conditions.

- Most of the researchers focused on improving the convective heat transfer rate between the absorber plate and the adjacent fluid layer. To improve the convective heat transfer coefficient, various roughness elements are embedded over the surface of the absorber plate to promote turbulence in the flow. Also, various researchers studied the effect of different shapes of baffles to direct the fluid flow.
- To study the fluid behavior inside the air heater duct channel, many researchers performed fluid flow simulation using ANSYS Fluent, to visualize the turbulence generated by the roughness element and its effect on thermo-hydraulic performance. Turbulent kinetic energy and turbulent dissipation rate near the absorber wall surface due to the embedding of vortex generators, path lines of velocity magnitude, flow separation, reattachment point, and recirculation area were also visualized using simulation.
- Most of the researchers performed an experimental investigation on SAH to study the heat transfer and thermodynamic behavior that includes thermal conversion efficiency, exergy efficiency, entropy analysis, environmental impact assessment, and economic analysis. Also, various researchers formulated heat transfer correlations to study the performance by varying its physical parameters.
- The major energy loss happens in the SAH system mainly due to top loss and exergy loss happens mainly due to absorption of solar radiation, exergy loss due to glazing, and exergy losses due to convection and radiation heat transfer from the absorber plate to the environment. No literature is exactly available focusing on the reduction of the above losses. Hence, it is most important to focus on improving the heat transfer rate from the absorber plate to air in order to the irreversibility and inefficiency of the SAH system.
- Although various researchers have been involved in improving the performance of the SAH, there is no literature available on improving the heat transfer rate along the length of the airflow. In general, the heat transfer rate, and thermal efficiency along the length reduce due to the reduction of the temperature difference between the absorber plate and air along the length of the fluid flow.

2.6 Objectives of the thesis

Based on the closure of the literature review, the objectives are considered for the present thesis work:

- To study the thermodynamic and heat transfer behaviour of the existing SAH system using a mathematical model.
- To design an energy-efficient solar air heater with a capacity (100 W to 500 W) and hot air outlet temperature (45°C to 65°C) for drying of seasonal agricultural products and cash crops.
- To compare the thermo-hydraulic performance of the developed SAH system with the existing SAH systems and smooth duct SAH system analytically.
- To study the energy, exergy, and entropy of the developed SAH system analytically for determining the irreversibility generated in the system.
- To fabricate and test the performances of an energy-efficient SAH system under a forced convective heat transfer mode of operation for two different mass flow rate conditions.
- To analyse the heat transfer performance of fabricated varied arc ribs embedded SAH system experimentally and compare the thermal performance with existing different SAH system.

Chapter 3 Design, development, and performance prediction of varied arc ribs embedded in SAH

3.1 Preface

It has been observed from the literature that the arc rib fin arrangement embedded in solar air heater performs better than the various other fin arrangements such as metal mesh rib, wire rib, transverse rib, inclined rib, dimple shaped, V-shaped, U shaped, W shaped, and arc rib. Hence, in the present work, the performance of the arc rib fin with fixed and variable arc rib fin arrangement on the absorber plate is studied. The arrangement of fin in the present study is unique and so far not have been reported in the literature. In the present chapter, the thermodynamic behaviour and heat transfer analysis of a SAH having varied arc ribs fin arrangement in the absorber plate using a theoretical model is reported. Further, the influence of absorber plate length (1 and 2 m) and different arc rib fin configurations at various mass flow rates of air (0.02 kg/s to 0.06 kg/s) are also studied. The reported absorber plate has a variable and fixed arc rib fin arrangement and its heat transfer characteristic and thermal performance are compared with a smooth plate. The performance of the various arc rib fin arrangements in the SAH are determined by predicting the mean absorber plate temperature and outlet air temperature. The heat and thermal characteristics (Nusselt number, THPP, and friction factor), efficiencies (thermal, effective, and exergy), collector efficiency factor, collector heat removal factor and exergy loss are presented.

3.2 Design of solar air heater system

The schematic of the SAH with variable arc rib fin arrangement in the absorber plate is shown in *Fig. 3.1*. The SAH consists of an absorber plate with a variable arc rib fin arrangement, a glazing, bottom plate, and an insulated wooden box at the bottom of the air heater. The solar radiation is incident on the absorber plate through the glazing, and the heat energy gained from the absorber plate is dissipated through the fin arrangement. The heat exchanging fluid is passed between the absorber plate and the bottom plate.

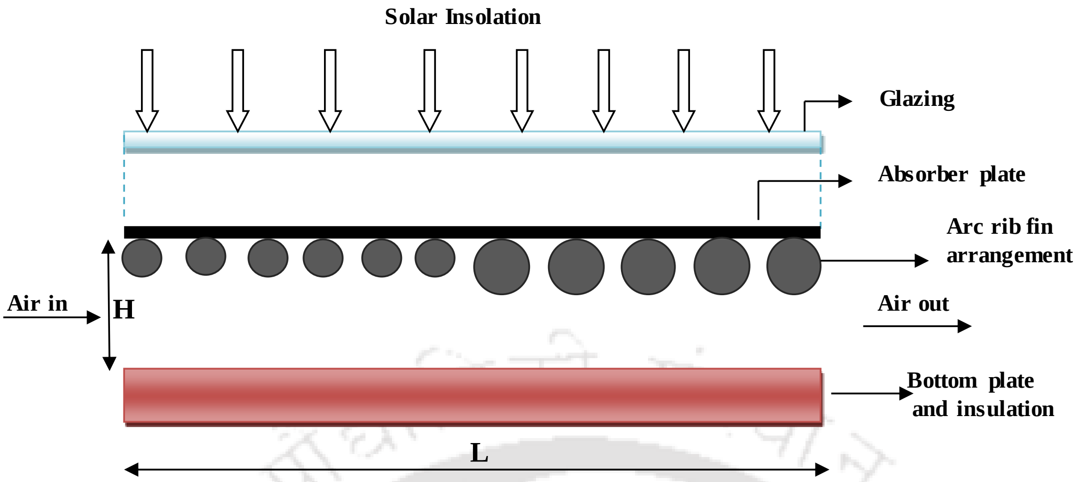

Fig. 3.1 Schematic layout of variable arc rib fin arrangement in a SAH

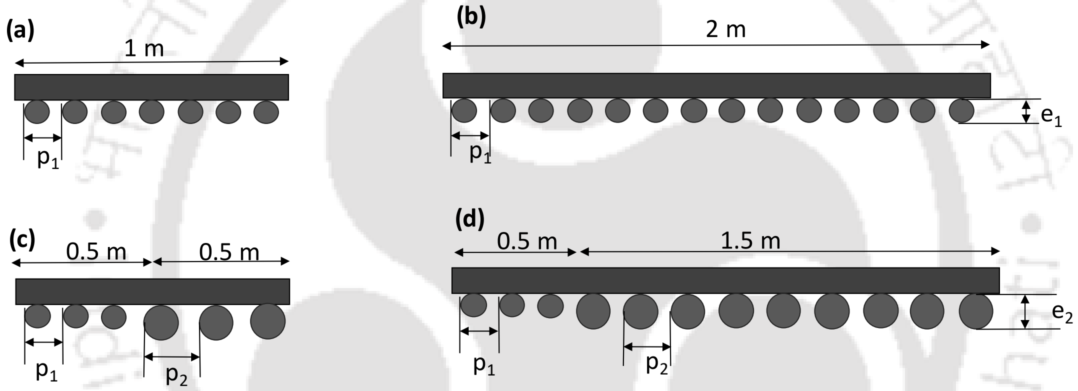

Fig. 3.2 Arc rib fin configurations; (a) and (b) fixed arc rib fin arrangement with e/D_e of 0.0422; (c) and (d) variable arc rib fin arrangement with e/D_e of 0.0422 and 0.0541

The fixed and the variable type of arc rib fin arrangements of lengths 1 m and 2 m are shown in *Fig. 3.2*. The relative roughness height of the fin in fixed arc rib fin arrangement is 0.0422, and in the case of variable arc rib fin, the relative roughness heights are fixed as 0.0422 and 0.05417. The fin pitch p_1 and p_2 are maintained at 20 mm and 25 mm, respectively.

The diameter of the fin is chosen as (e_1) 2 mm and (e_2) 2.5 mm, as shown in Fig. 3.2 (c) and (d). The length, width, and height of the SAH are 1000 mm, 300 mm, and 25 mm, respectively. The geometrical parameters of the SAH (width and height) and its material properties are selected from Saini and Saini, (2008). The geometrical and material properties of the SAH are presented in *Table 3.1*.

Table 3.1 The geometrical and material parameters of the SAH with arc rib fin arrangement

Parameters [Saini and Saini, (2008)]	**Value**
Width of the air flow duct (m)	0.3
Depth of the air flow duct (m)	0.025
Thermal conductivity of insulation and glass (W/mK)	0.037 and 0.75
Thickness of insulation x_{ins} (m)	0.05
Product of effective transmittance and absorptance $(\tau\alpha)_e$	0.85
Absorber plate and glass cover emissivity (ε_p and ε_g)	0.9 and 0.88
Glass cover - thickness (m)	0.004
Ambient temperature T_a (K)	300
Wind velocity V (m/s)	1
Solar radiation I (W/m^2)	1000
Relative roughness pitch ratio p/e	10
Relative angle of attack α/90	0.3333
Relative roughness height ratio e/D_e (Fixed arc rib)	0.0422
Modifications in physical parameters for the present study:	
Relative roughness height ratio e/D_e (Varied arc ribs) – Present work	0.0422 and 0.0541

3.3 Mathematical modelling of SAH system

A theoretical model is developed to study the performance of the SAH with arc rib fin configurations at various flow rate. The procedure followed for predicting the overall performance of the SAH is shown in the flowchart (*Fig. 3.3*). The geometrical and material parameters of the SAH reported in the present work are selected from the experimental investigation reported by Saini and Saini, (2008). Further, the initial values of temperature, required for iterative calculations are assumed based on the study conducted by Sahu and Prasad, (2016).

The analytical equations are solved using a computer program in MATLAB to study the solar air heater's performance with various arc rib fin arrangements. The climatic (solar radiation intensity, ambient temperature and wind speed), geometrical (width, depth and length of the duct, relative roughness height and pitch, attack angle) and operational values (mass flow rate) are the input parameters to the program.

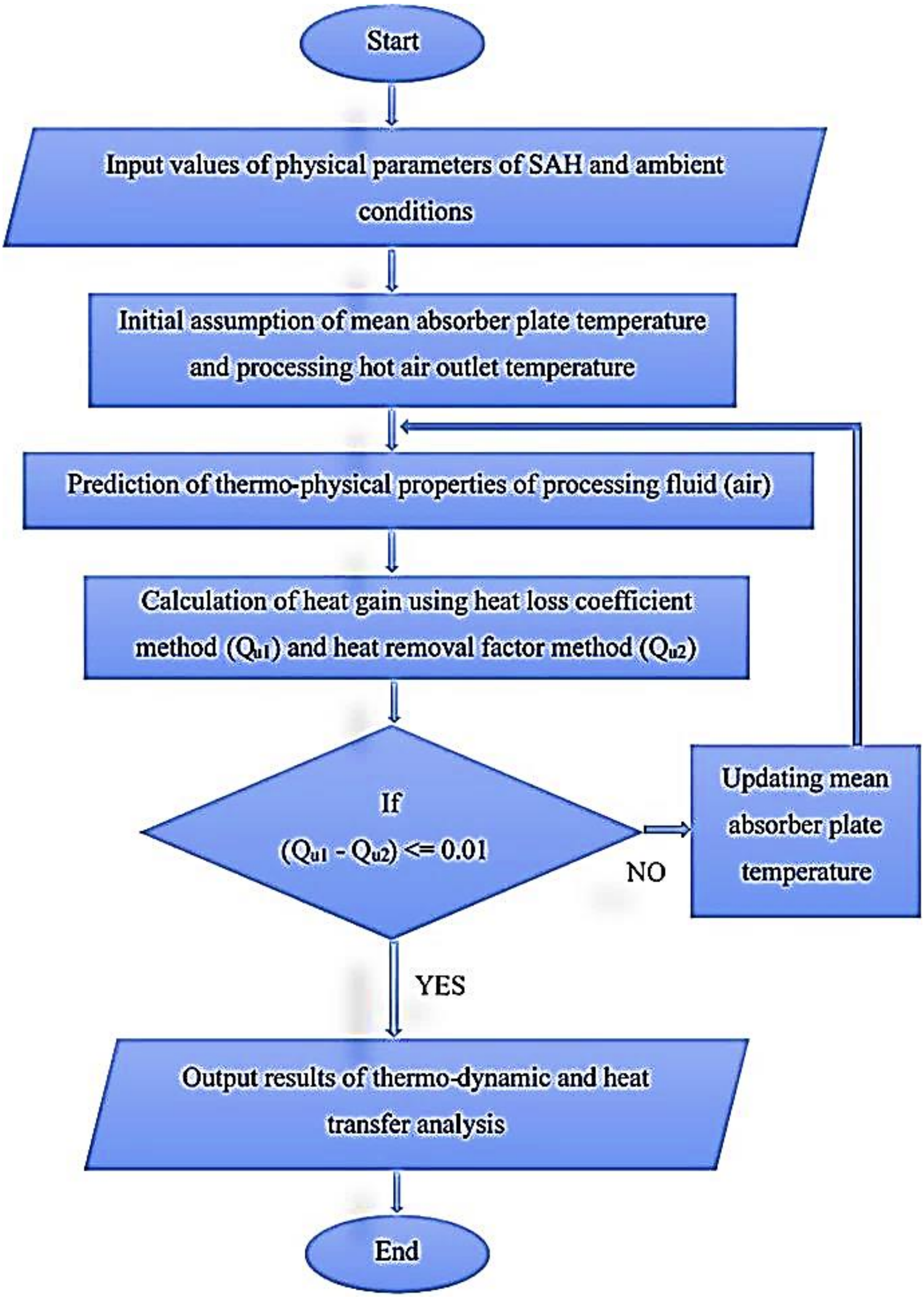

Fig. 3.3 Flow chart for analytical modelling to determine the performance of SAH

The input parameters employed for numerical calculations are taken from the experimental investigation reported by Saini and Saini, (2008), as shown in *Table 3.1*. The numerical procedure is initiated by assuming that the inlet and ambient temperature are equal. The outlet temperature is assumed to be 20°C less than the mean plate temperature and further, the mean plate temperature is calculated by taking the average of inlet and outlet temperature of the SAH similar to the study conducted by Sahu and Prasad, (2016). After this, useful heat gained by heat loss coefficient method (Q_{u1}) and heat removal factor method (Q_{u2}) determined by using their formulas. If $\left[(Q_{u1} - Q_{u2}) \geq 0.01\right]$, the procedure is repeated until the solution converges by updating the value of mean absorber plate temperature (T_{Pm}). Using the updated values, the iterations are repeated until obtaining the termination criteria $\left[(Q_{u1} - Q_{u2}) \leq 0.01\right]$. Using the above procedure and assumptions, heat and thermal characteristics (Nusselt number, THPP, and friction factor), efficiencies (thermal, effective, and exergy), collector efficiency, and collector heat removal factor are determined. The procedure for predicting the overall performance of the SAH is shown in the flowchart *Fig. 3.3* and the corresponding stepwise procedure is described below.

Step 1. *Material selection*

The geometrical parameters of the SAH and its material properties are selected from Saini and Saini, (2008). The ambient conditions are given as input for estimating the performance as given in the *Table 3.1*.

Step 2. *Initial assumption of mean absorber plate temperature and process air temperature at outlet.*

The initial assumption of temperature value of the absorber plate (T_{Pm}) and outlet air temperature (T_O) for iterative calculations, estimated based on the procedure followed by Sahu and Prasad, (2016) are given in Eqs. 3.1 and 3.2.

$$T_{Pm} = \frac{T_O + T_i}{2} + 10\,^{\circ}C \tag{3.1}$$

$$T_O = T_{Pm} - 20\,^{\circ}C \tag{3.2}$$

The air outlet temperature from the SAH is determined using Eqs. 3.3 and 3.4 [Sahu and Prasad, (2016)] as given below,

$$T_O = T_i + \Delta T_f \tag{3.3}$$

$$\Delta T_f = \left(\frac{\Delta T_f}{I}\right)(I) \tag{3.4}$$

***Step 3.** Calculation of heat gain*

After initial assumptions, useful heat gained by heat loss coefficient method (Q_{u1}) and heat removal factor method (Q_{u2}) is determined by using Eqs 3.5 to 3.7. The iterations are repeated until obtaining the termination criteria $\left[(Q_{u1} - Q_{u2}) \leq 0.01\right]$.

Heat gained by the air (heat loss coefficient method - Q_{u1}, Sahu and Prasad, 2016)

$$Q_{u1} = \left[I(\tau\alpha)_e - U_L(T_{Pm} - T_a)\right] A_P \tag{3.5}$$

Heat gained by the air (heat removal factor method - Q_{u2}, Sahu and Prasad, 2016)

$$Q_{u2} = F_R \left[I(\tau\alpha)_e - U_L\left(\frac{T_o - T_i}{2}\right)\right] A_P \tag{3.6}$$

$$T_{Pm} = T_a + \left(\frac{I(\tau\alpha)_e - \left(\frac{Q_{u2}}{A_P}\right)}{U_L}\right) \tag{3.7}$$

Based on the above procedure, the iteration stops after reaching the convergence criteria. This is followed by the thermodynamic analysis and heat transfer analysis of the SAH using the following mathematical equations.

***Step 4.** Determination of Nusselt number, friction factor and THPP*

The Nusselt number is determined using the Dittus-Boelter equation, and the frictional factor is predicted using the Blasius equation for the smooth duct as given by Eqs. 3.8 and 3.9.

$$Nu_s = 0.024(\mathrm{Re})^{0.8}(\mathrm{Pr})^{0.4} \tag{3.8}$$

$$f_s = 0.085\left(\mathrm{Re}^{-0.25}\right) \tag{3.9}$$

In case of arc rib configuration, the correlations developed by Saini and Saini, (2008) for arc rib fin arrangement are used as given below in Eqs. 3.10 to 3.12.

$$Nu_r = 0.001047\left(\mathrm{Re}^{1.386}\right)\left(\left(\frac{e}{D_e}\right)^{0.3772}\right)\left(\left(\frac{\alpha_a}{90}\right)^{-0.1198}\right) \tag{3.10}$$

$$f_r = 0.14408\left((\mathrm{Re})^{-0.17103}\right)\left(\left(\frac{e}{D_e}\right)^{0.1765}\right)\left(\left(\frac{\alpha_a}{90}\right)^{0.1185}\right) \tag{3.11}$$

$$h = \frac{k\,Nu}{D_e} \tag{3.12}$$

The THPP of the SAH is evaluated using Eq. 3.13.

$$THPP = \frac{\dfrac{Nu_r}{Nu_s}}{\left(\dfrac{f_r}{f_s}\right)^{1/3}} \tag{3.13}$$

***Step 5.** Determination of collector factors*

The collector efficiency factor is the ratio of actual useful energy gained by the SAH to the useful energy gain if the entire absorber plate is maintained at the fluid inlet temperature. The collector efficiency factor and collector heat removal factor are predicted using Eqs. 3.14 and 3.15 [Sahu and Prasad, 2016].

$$F_P = \frac{h}{h + U_L} \tag{3.14}$$

$$F_R = \left(\frac{mC_P}{U_L A_P}\right)\left[\exp\left(\frac{U_L A_P F_P}{mC_P}\right) - 1\right] \tag{3.15}$$

***Step 6.** Determination of thermal and effective efficiency*

The efficiencies of the SAH is determined by predicting the thermal and effective efficiencies using Eqs. 3.16 and 3.17 [Sahu and Prasad, 2016].

$$\eta_{Th} = \frac{Q_u}{IA_p(\tau\alpha)_e} \tag{3.16}$$

$$\eta_{eff} = \frac{Q_u - \left(\dfrac{P_m}{C}\right)}{IA_P\left(\tau\alpha\right)_e} \tag{3.17}$$

Step 7. *Exergy analysis of the SAH system*

Exergy analysis performed to investigate the merit of using the SAH system. SAHs are used to replace the electric heaters for generating the hot air. For forced convection operation, SAHs are operated using blower to circulate the air inside the duct. Also, the magnitude of exergy dissipation and parameter causing the maximum dissipation are also calculated by using the exergy analysis approach.

The magnitude of various exergy losses and irreversibility can be calculated using the procedure given by Sahu and Prasad, (2019). This helps us in determining the various parameters involved in exergy and entropy are given in Eqs. 3.18 to 3.27.

$$\eta_{Ex} = \frac{EX_n}{EX_S} = \frac{EX_{up}}{EX_{Input}} \tag{3.18}$$

Where $EX_S = (A_P)(I)\left\{1 - \left(\frac{T_a}{T_{sun}}\right)\right\}$ (3.19)

Irreversibility of the system is given as,

$$\sum EX_{in} - \sum EX_{out} = IR \tag{3.20}$$

Exergy balance in the SAH,

$$EX_i + EX_s + EX_w - EX_o = IR \tag{3.21}$$

$$IR = EX_s - [EX_o - EX_i - EX_w] \tag{3.22}$$

$$IR = EX_s - [EX_{up}] \tag{3.23}$$

Exergy utilised potential *(EX_{up} or E_n)* is the useful exergy or utilised exergy or net exergy while converting solar energy into thermal energy,

$$EX_{up} = EX_o - EX_i - EX_w \tag{3.24}$$

Exergy available at the outlet section of the SAH (EX_o),

$$EX_o = mC_{pa}(T_o - T_i) \tag{3.25}$$

Exergy available in the inlet section of the SAH (EX_i),

$$EX_i = (mC_{pa}T_a)\left\{\ln\left(\frac{T_o}{T_i}\right)\right\} \tag{3.26}$$

Exergy due to blower work (EX_w)

$$EX_w = \left(\frac{T_o}{T_i}\right)\left(W_p\right) = \left(\frac{T_o}{T_i}\right)\left(P_m\right) \tag{3.27}$$

Based on the system’s interactions, exergy can also be calculated based on an indirect method described by Phu et al., (2020). The various components of exergy losses are given in Eqs. 3.28 to 3.32.

a) Optical exergy losses:

$$EX_{LO} = \left(IA_P\right)\left(1-\left(\tau\alpha\right)_e\right)\left\{1-\left[\left(\frac{4}{3}\right)\left(\frac{T_a}{T_{sun}}\right)\right]+\left[\left(\frac{1}{3}\right)\left(\frac{T_a}{T_{sun}}\right)^4\right]\right\} \tag{3.28}$$

b) Exergy losses due to absorption of solar radiation by the absorber plate

$$EX_{LI} = \left\{\left(IA_P\right)\left(\tau\alpha\right)_e\right\}\left\{1-\left[\left(\frac{4}{3}\right)\left(\frac{T_a}{T_{sun}}\right)\right]+\left[\left(\frac{1}{3}\right)\left(\frac{T_a}{T_{sun}}\right)^4\right]-\left[1-\left(\frac{T_a}{T_{Pm}}\right)\right]\right\} \tag{3.29}$$

c) Exergy losses due to convection and radiation heat transfer from the absorber plate to the environment

$$EX_{ENV} = \left[\left(U_L\right)\left(A_P\right)\right]\left(T_{Pm}-T_a\right)\left[1-\left(\frac{T_a}{T_{Pm}}\right)\right] \tag{3.30}$$

d) Exergy losses due to heat transfer from absorber plate to the working fluid (air) flow

$$EX_{HTWF} = \left[\left(IA_P\right)\left(T_a\right)\left(\eta_{Th}\right)\right]\left[\left(\frac{1}{T_f}\right)-\left(\frac{1}{T_{Pm}}\right)\right] \tag{3.31}$$

e) Exergy loss due to friction created during fluid (air) flow

$$EX_{LP} = \frac{m\left(\Delta p\right)\left(T_a\right)}{\rho T_f} \tag{3.32}$$

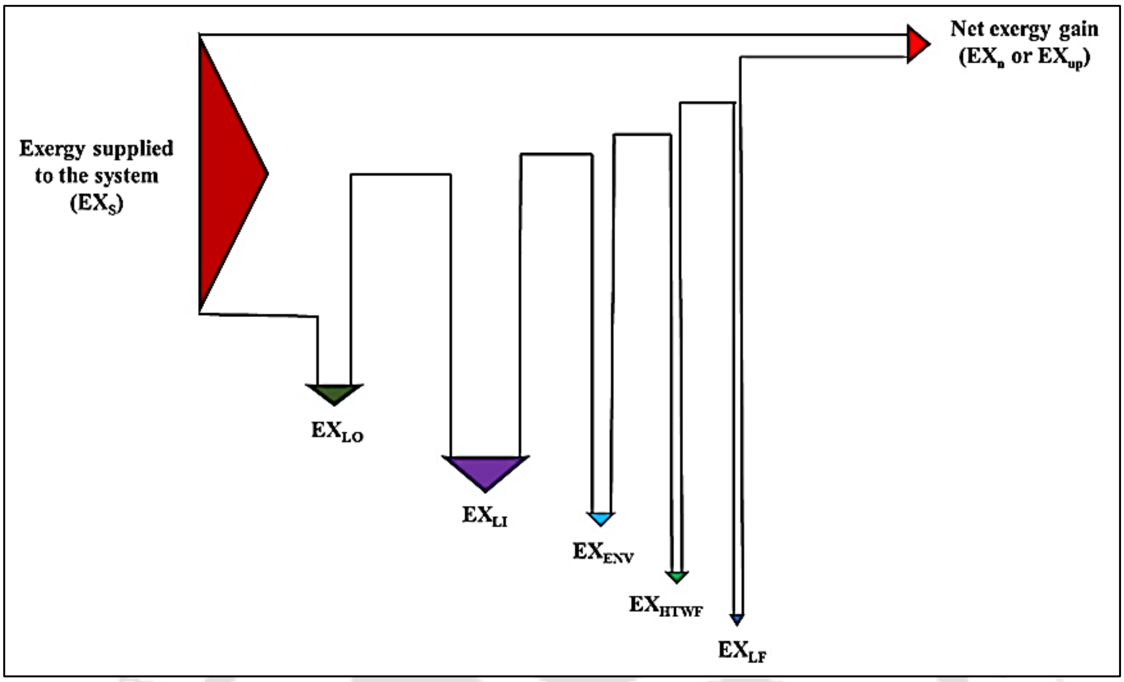

Fig. 3.4. Various components of exergy losses

The total exergy losses are determined by summing the above-mentioned exergy loss components as given in Eq. 3.33,

$$\sum EX_{Loss} = EX_{LO} + EX_{LI} + EX_{ENV} + EX_{HTWF} + EX_{LP} \tag{3.33}$$

The exergy supplied to the system or the exergy input to the system is given by Eq. 3.34,

$$EX_{Input} = (IA_P)\left\{1 - \left[\left(\frac{4}{3}\right)\left(\frac{T_a}{T_{sun}}\right)\right] + \left[\left(\frac{1}{3}\right)\left(\frac{T_a}{T_{sun}}\right)^4\right]\right\} \tag{3.34}$$

The functioning of SAH based on forced convection, the entropy associated with external energy supplied by the blower ($S_{gen,\Delta p}$) generates entropy due to mass transfer (entropy generated due to pressure drop) (Eq. 3.35),

$$S_{gen,\Delta p} = \frac{W_p}{T_i} \tag{3.35}$$

The blower power (W_P) consumption during the forced convection process, (Eq. 3.36)

$$W_p = P_m = \frac{m(\Delta p)}{(\eta_{pump})(\rho_a)} \tag{3.36}$$

The entropy generated ($S_{gen,\Delta T}$) due to heat transfer process (Eq. 3.37),

$$S_{gen,\Delta T} = mC_{pa}\left\{(\ln)\frac{T_o}{T_i}\right\} \tag{3.37}$$

Entropy generation is given by (Eq. 3.38),

$$S_{gen} = S_{gen,\Delta p} + S_{gen,\Delta T} \tag{3.38}$$

In this SAH system, the entropy is generated due to both heat and mass transfer operations, therefore the total entropy generation is gives as (Eq. 3.39),

$$S_{gen,total} = T_a\left\{\left(S_{gen,\Delta p}\right) + \left(S_{gen,\Delta T}\right)\right\} = T_a\left(S_{gen}\right) \tag{3.39}$$

Entropy generation number is defined as the magnitude of total entropy generated for the given solar energy input to the system (Eq. 3.40) [Prasad and Sahu, 2017],

$$N_{s,gen} = \frac{S_{gen,total}}{IA_p\left(\tau\alpha\right)_e} \tag{3.40}$$

Bejan number is defined as the ratio of entropy generated due to thermal difference to the total entropy generated (entropy generated due to both thermal and pressure difference) which is given by Kumar and Verma, (2021) and Sciacovelli et al., (2015) as shown below in Eq. 3.41,

$$B_e = \frac{S_{gen,\Delta T}}{S_{gen,\Delta T} + S_{gen,\Delta p}} \tag{3.41}$$

Irreversibility distribution ratio is defined as the ratio of entropy generated due to pressure drop to the temperature gain (heat transfer) given by Kumar et al., (2010) and Layek et al., (2007) as shown in Eq. 3.42.

$$\Psi = \left(\frac{S_{gen,\Delta p}}{S_{gen,\Delta T}}\right) = \frac{\text{entropy generated due to pressure drop}}{\text{entropy generated due to heat transfer}} \tag{3.42}$$

3.4 Results and Discussion - Analytical model

The influence of absorber plate length and various arc rib fin arrangements on the performance of SAH are analysed. A comparison among the different configurations of arc rib fin arrangement (fixed and variable) is studied and compared with a smooth duct at different mass flow rate of air. The variations in the mean absorber plate temperature, air outlet temperature, Nusselt number, friction factor, THPP, thermal analyses (energy, exergy, and entropy), collector efficiency factor, and collector heat removal factor are discussed in the following subsections.

3.4.1 Model validation

The developed theoretical model is validated with the experimental work of Saini and Saini, (2008). They studied the heat transfer and thermal characteristics of an arc rib fin arrangement embedded in a SAH. The geometrical and operating parameters of the fin and SAH reported in the experimental work by Saini and Saini, (2008) are adopted in the present theoretical model. The average deviation of the theoretical Nusselt number obtained from the model matches within ± 3.9 % of experimental Nusselt number values reported in Saini and Saini, (2008). As illustrated in *Fig. 3.5,* the theoretical values predicted from the present model are in good agreement with the experimental values of the Nusselt number reported by Saini and Saini, (2008).

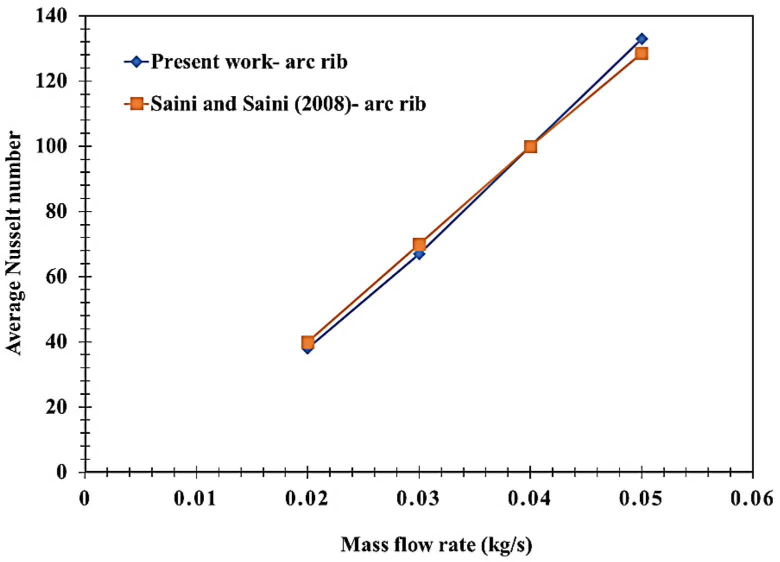

Fig. 3.5 Validation of analytical model with experimental values for average Nusselt number at various mass flow rates of air

3.4.2 Influence of absorber plate length and arc rib fin arrangement on temperature variations

3.4.2.1 Hot air outlet temperature variation

The effect of absorber plate length on the outlet air temperature of the SAH with various arc rib fin arrangements are discussed in *Fig. 3.6*.

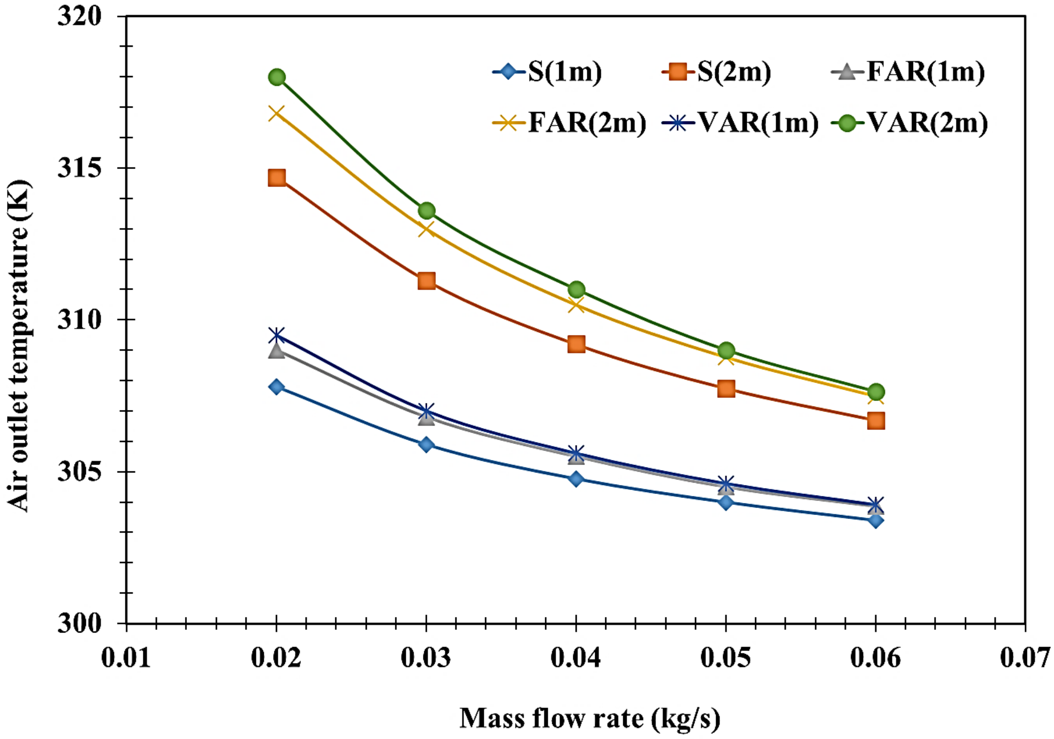

Fig. 3.6 Variations in air outlet temperature at various mass flow rates of air

It is observed from Fig.3.6 that the maximum air outlet temperature of SAH is achieved at a lower mass flow rate of air. The length of the absorber plate influences the outlet air temperature from the SAH. The maximum temperature of 318 K is observed in variable arc rib fin arrangement, followed by fixed arc rib fin arrangement (316.8 K) and smooth duct (314.7 K) of 2 m length at an air flow rate of 0.02 kg/s. In the case of a 1 m length absorber plate, maximum temperature is observed in variable arc rib fin arrangement (309.5 K), followed by fixed arc rib fin arrangement (309 K) and smooth duct (307.8 K) at 0.02 kg/s. The absorber plate length of 2 m reported higher outlet air temperature when compared with a 1 m length in fixed and variable arc rib fin arrangements. A temperature difference of 8.5 K is achieved by varying the length of the absorber plate from 1 m to 2 m in the case of the variable arc rib fin arrangement at 0.02 kg/s. The maximum air outlet temperature is reported at a lower flow rate, and increasing the length of the absorber plate assists the fluid in gaining maximum temperature and results in proper utilization of the heat energy received by the absorber plate.

3.4.2.2 Mean absorber plate temperature variation

The effects of absorber plate length and arc rib fin arrangements on the mean absorber plate temperature are shown in *Fig. 3.7*.

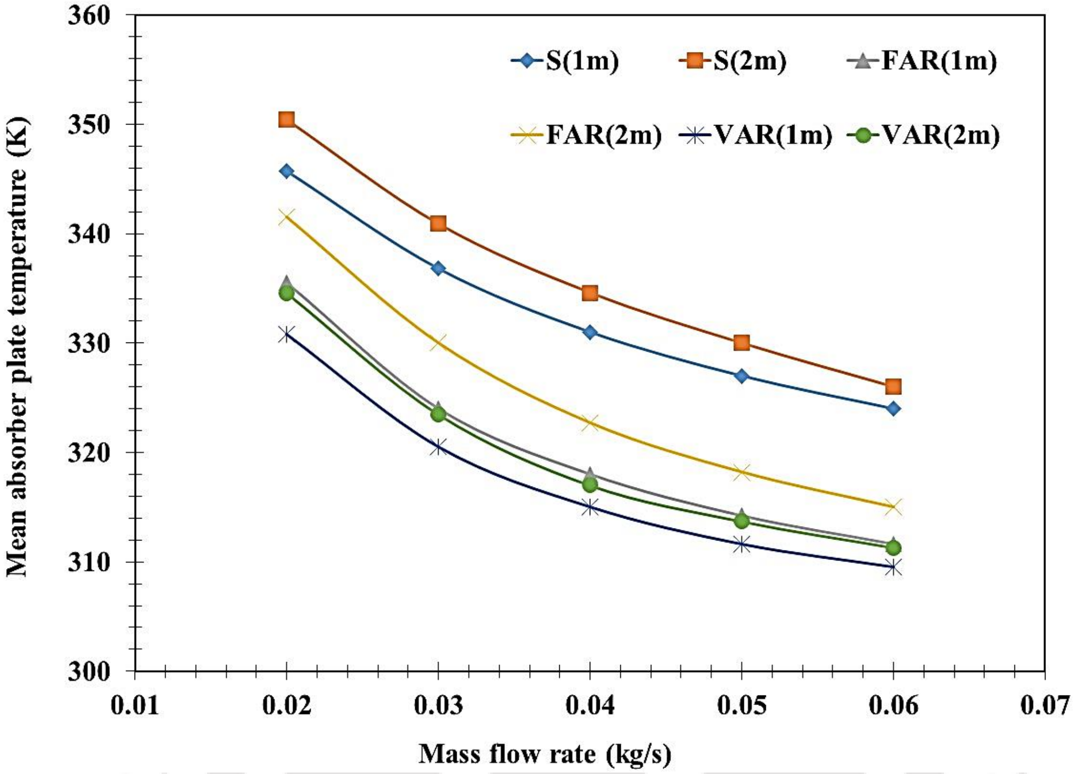

Fig. 3.7 Variations in mean absorber plate temperature at various mass flow rates of air

It is observed that, the mean absorber plate temperature of SAH decreases as the air flow rate increases. It is seen that the smooth ducts of 2 m and 1 m, reported higher mean absorber plate temperature of 350.4 K and 345.7 K, respectively, for flow rate of 0.02 kg/s. The maximum mean absorber plate temperature is reported in the smooth duct due to the absence of fin arrangement in the absorber plate. Thus, it is inferred that the effective utilization of heat energy from the absorber plate to heat exchanging fluid is low in case of smooth duct. The fixed arc rib fin arrangement is reported to have a mean absorber plate temperature of 335.5 K and 341.5 K for 1 and 2 m length, respectively, for 0.02 kg/s. In the case of variable fin arrangement, the mean absorber plate temperature is observed to be 330.8 K (1 m) and 334.6 K (2 m), respectively, for 0.02 kg/s. The variable arc rib fin arrangement reported the lowest mean absorber plate temperature both in 1 and 2 m length.

The variable arc rib arrangement assists in higher dissipation of heat energy from the absorber plate to heat exchanging fluid resulting in lower mean absorber plate temperature.

3.4.3 Collectors factor predictions

3.4.3.1 Determination of collector efficiency factor

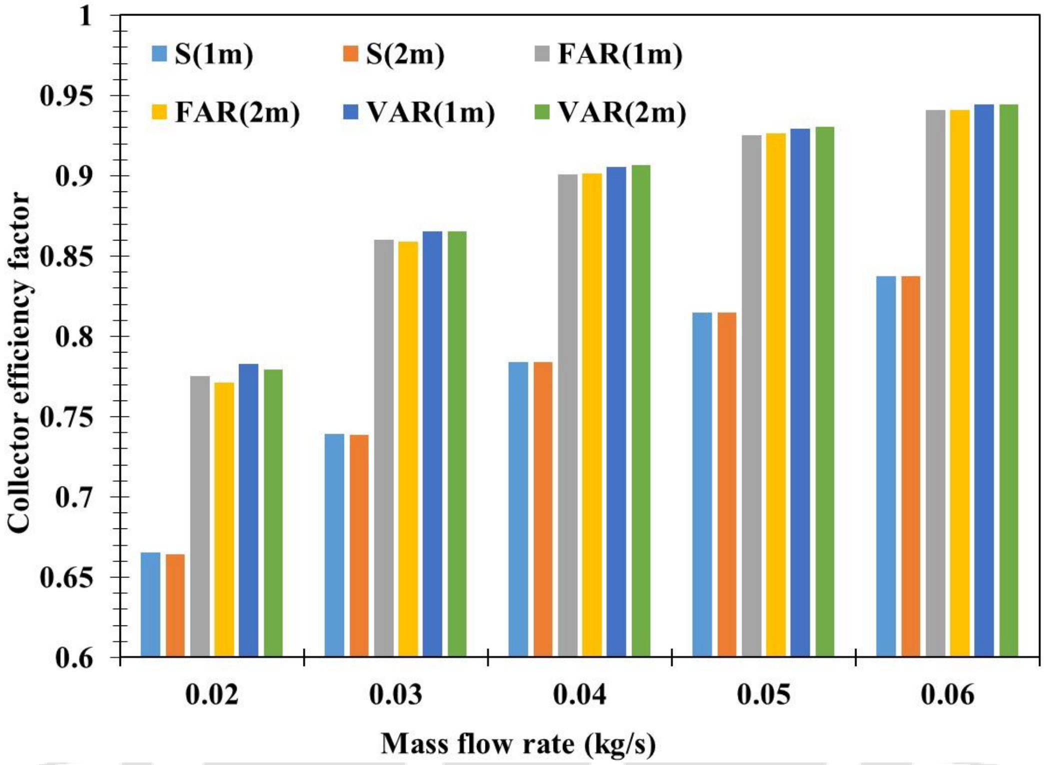

Fig. 3.8 Variations in collector efficiency factor at various mass flow rates of air

Fig. 3.8 shows the effects of various arc rib fin arrangements and length of the absorber plate on the collector efficiency factor. The collector efficiency factor increases as the air flow rate increases. The maximum collector efficiency factor is reported in 2 m length variable arc rib fin arrangement (0.9446) followed by fixed arc rib fin (0.9409) and smooth duct (0.8375) at a flow rate of 0.06 kg/s. As the flow rate increases from 0.02 kg/s to 0.06 kg/s, an increment of 17.4% in collector efficiency factor is observed in the case of 2 m variable arc rib fin arrangement. Since the heat transfer coefficient of the collector depends on the surface roughness (rib geometry) of the heat transfer surface and thermo-physical properties of heat transfer fluid. Due to the higher heat transfer rate because of the higher heat transfer coefficient in the ribbed geometry makes the VAR embedded SAH to produce higher collector efficiency factor than the FAR and smooth duct SAH.

3.4.3.2 Determination of collector heat removal factor

According to *Fig. 3.9*, the collector heat removal factor increases as the air flow rate increases. The maximum heat removal factor is reported in variable arc rib fin arrangement (0.93) followed by fixed arc rib fin (0.92) and smooth duct (0.82) at a flow rate of 0.06 kg/s for 1 m length. As the flow rate increases from 0.02 kg/s to 0.06 kg/s, an increment of 19.4% in heat removal factor is observed for 1 m variable arc rib fin arrangement. It is observed that the thermal efficiency of the variable arc rib fin arrangement is high as compared to other geometries, as shown in *Fig. 3.14*. It leads to a higher heat transfer rate from absorber plate to heat exchanging fluid, and this increase in thermal efficiency is attributed to the higher collector heat removal factor in variable arc rib fin arrangement.

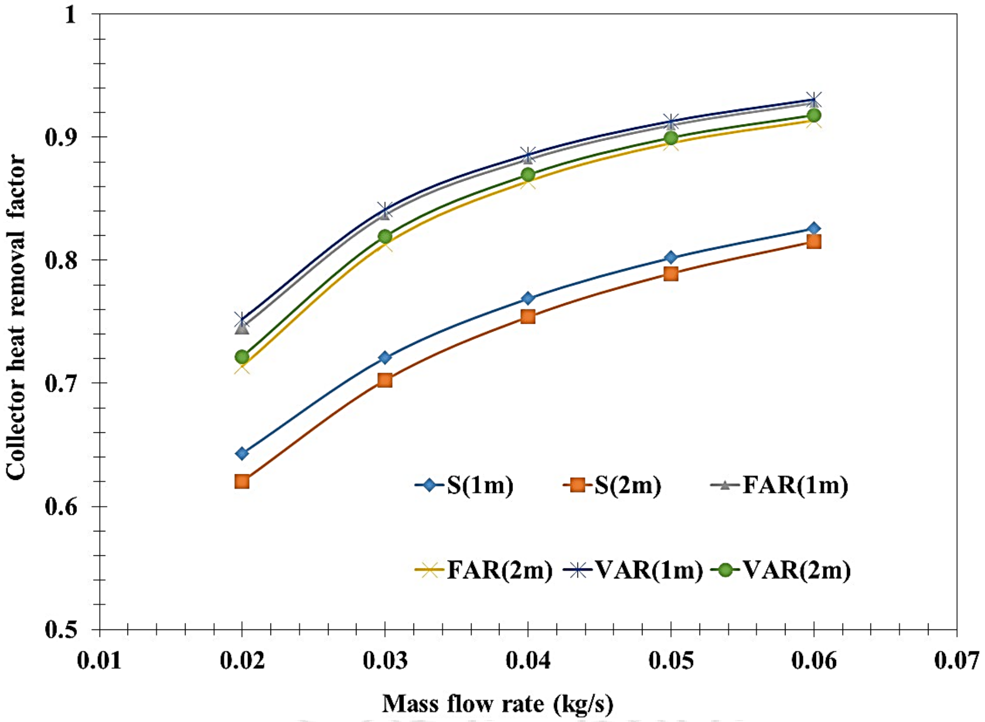

Fig. 3.9 Variations in collector heat removal factor at various mass flow rates of air

3.4.4 Thermo-hydraulic characteristics evaluation

3.4.4.1 Nusselt number analysis

The effects of various arc rib fin arrangements and length of absorber plate on Nusselt number at various flow rates are predicted and presented in *Fig. 3.10*. The Nusselt number increases as the flow rate of air increases from 0.02 kg/s to 0.06 kg/s. The highest Nusselt value is reported in the variable arc rib fin arrangement of 178 (1 m) and 173 (2 m), respectively, for 0.06 kg/s. The increase in Nusselt number is attributed to the significant disturbance created in the viscous sublayer by the fin arrangement, which in turn reduces the boundary layer formation and the resistance offered to heat transfer. This phenomenon is reported to be higher in the case of the variable arc rib fin arrangement, results in achieving significant heat transfer enhancement. The fixed arc rib arrangement resulted in a Nusselt value of 167 for 2 m and 168 for 1 m at 0.06 kg/s. The smooth ducts reported a value of 56.5 (1 m) and 56.4 (2 m) at 0.06 kg /s. The enhancement of Nusselt number is higher by a factor of 3 in variable arc rib fin arrangement of 2 m when compared with a smooth duct of 2 m length.

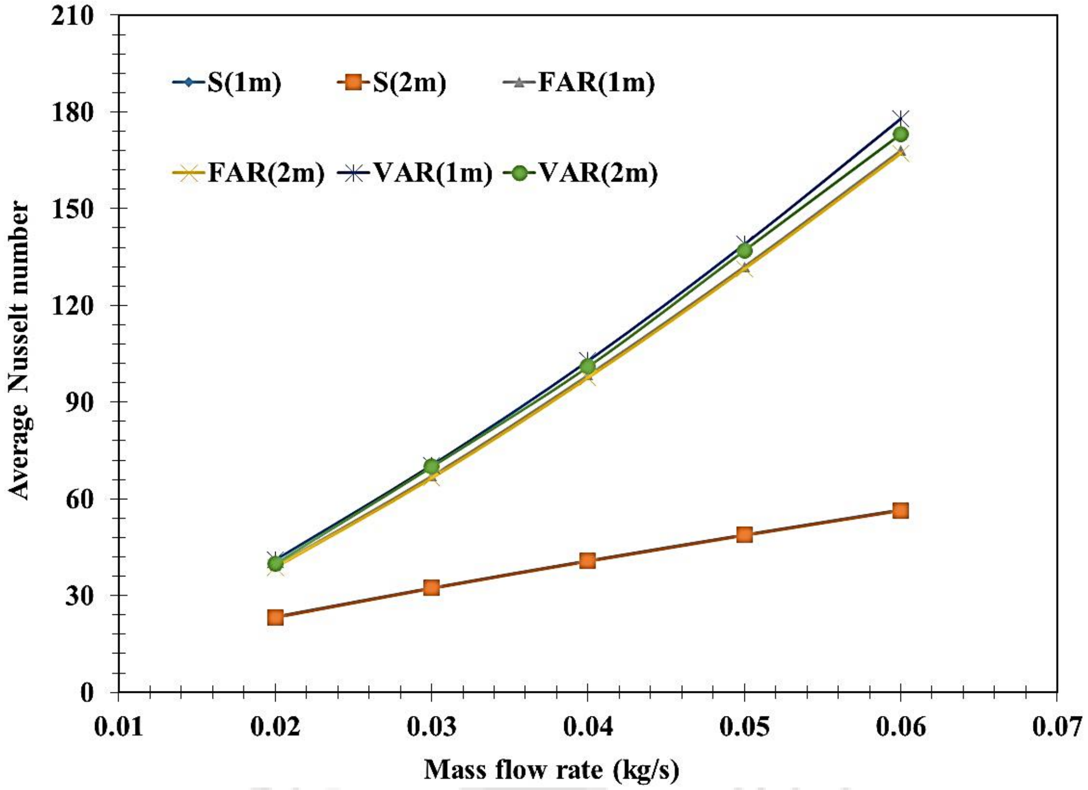

Fig. 3.10 Variations in average Nusselt number at various mass flow rates of air

3.4.4.2 Frictional factor and pressure drop analysis

The effects of various arc rib fin arrangements and length of absorber plate on friction factor at various air flow rates are shown in *Fig. 3.11*. It is observed that as the flow rate of air increases from 0.02 kg/s to 0.06 kg/s, the frictional factor reduces by 23 %, 17.4 % and 17.1%, respectively in smooth, fixed and variable fin arrangements. The frictional factor is observed to be maximum in variable arc rib fin arrangement followed by fixed arc rib fin and the smooth duct at an air flow rate of 0.02 kg/s. The formation and shedding of the vortexes due to variable and fixed arc rib fin arrangement results in higher frictional factors in the SAH. It is observed that the frictional factor in variable arc rib fin at 2 m (0.0167) is marginally higher than the fixed arc rib fin at 2 m (0.0161) at a flow rate of 0.02 kg/s. The smooth ducts of 1 m and 2 m length reported the lowest frictional factor value of 0.0094, at a flow rate of 0.02 kg/s, which is attributed to the absence of fin arrangement in the absorber plate.

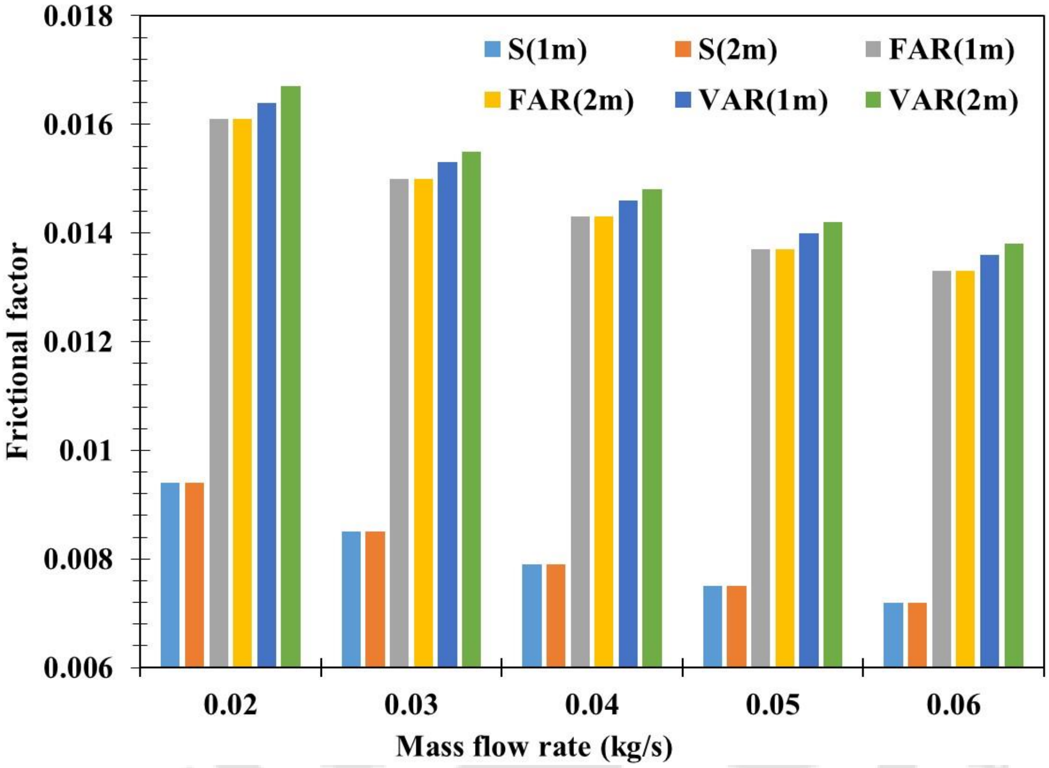

Fig. 3.11 Variations in frictional factor at various mass flow rates of air

By increasing the mass flow rate and length of the solar air heater, it is observed from *Fig. 3.12***,** that pressure drop also increases. Pressure drop of 2m length heater is more than 1m length heater. At 1 m and 2 m length VAR configuration has maximum value of pressure drop respectively. By increasing the mass flow rate from 0.02 kg/s to 0.06 kg/s, the pressure drop increases by 27.9 Pa and 56.7 Pa for VAR (1 m) and VAR (2 m). At 0.02 kg/s and 0.06 kg/s, pressure drop of VAR (2 m) increases by 0.33 Pa and 2.15 Pa than S (2 m), 3.94 Pa, 31.7 Pa than FAR (2 m) respectively.

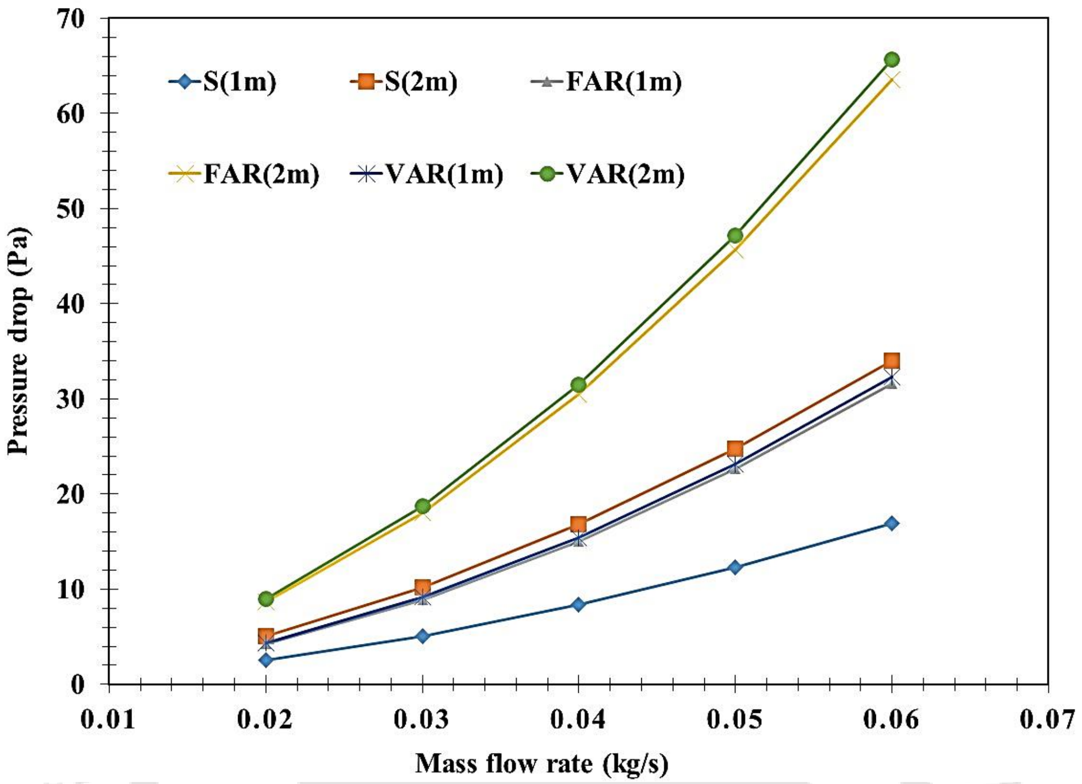

Fig. 3.12 Variations in pressure drop at various mass flow rates of air

3.4.4.3 Thermo-hydraulic performance parameter (THPP) evaluation

The effects of various arc rib fin arrangements and length of the absorber plate on the THPP of SAH at different flow rates are discussed in *Fig. 3.13*. The performance of a SAH is related to the THPP value, and it must be higher than 1. It is reported that the THPP value increases as the air flow rate is increased. The THPP value of variable arc rib fin arrangement for 1 m (2.54) is slightly higher than the variable arc rib fin arrangement of 2 m (2.46) at a flow rate of 0.06 kg/s. Similarly, in the case of fixed arc rib fin arrangement, the THPP value is reported to be 2.41 and 2.42 for 2 m and 1 m length of absorber plate, respectively, for a flow rate of 0.06 kg/s. As the flow rate is increased from 0.02 kg/s to 0.06 kg/s, the THPP value increases by 42 % (1.45 to 2.54) for the variable arc rib fin arrangement of 2 m length. THPP of the SAH is carried out to determine the significance of heat gain due to embedment of rib over the frictional loss. Although rib embedded SAH incurs higher frictional loss, it very minor loss. Hence, due to which the rib embedded SAH has higher THPP than the smooth duct SAH. Therefore, the embedment of varied arc ribs enhances the thermo-hydraulic performance of the SAH.

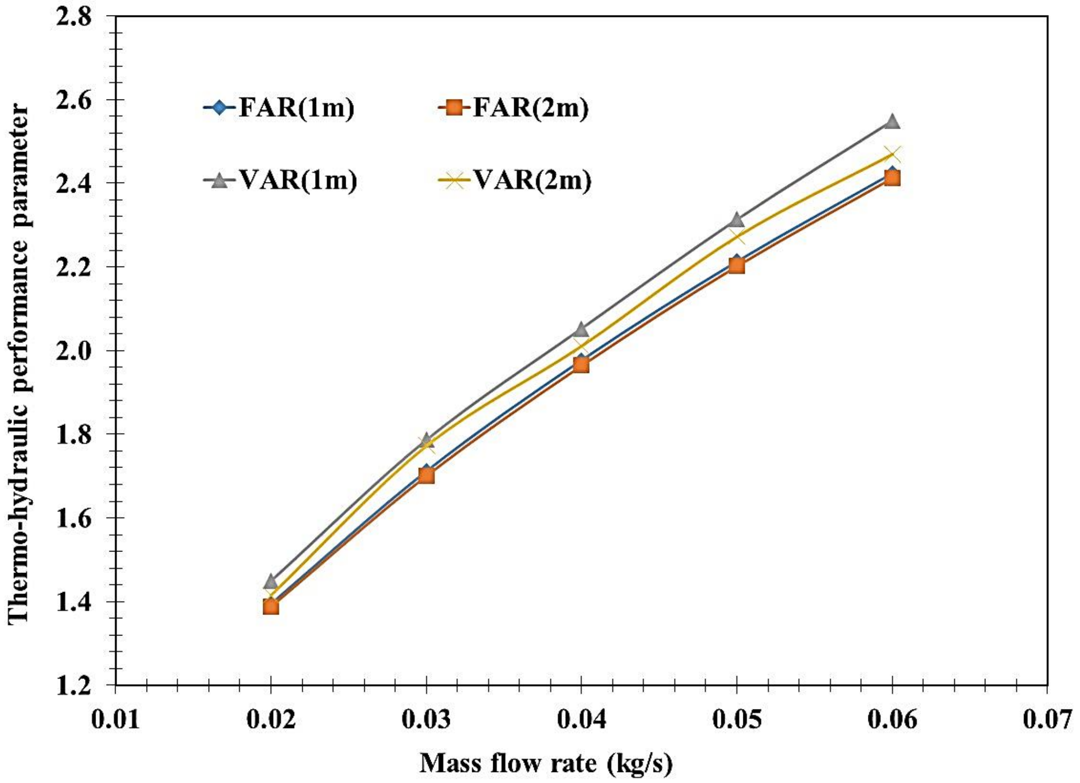

Fig. 3.13 Variations in thermo-hydraulic performance parameter at various mass flow rates of air

3.4.4.4 THPP comparison: Varied arc ribs configuration with different other rib configurations

The THPP values of various models of rib fins (roughness element) has been compared with varied arc ribs model. The varied rib model is compared with arc rib model developed by Saini and Saini, (2008), inclined and transverse roughened rib model developed by Varun et al., (2008), metal grit fin attached SAH model developed by Karmare and Tikekar, (2007), wedge shaped rib roughened configuration developed by Bhagoria et al., (2002), Inclined continuous rib model developed by Aharwal et al., (2008), heat transfer analysis performed in V shaped rib roughened absorber model experiment conducted by Momin et al., (2002), second law analysis performed by Layek et al., (2007) in chamfered rib roughened absorber model, heat transfer analysis made by Jaurker et al., (2006) in rib grooved roughened model and thermal analysis made by Saini and Saini, (1997) in metal mesh as roughness element. These comparisons show that, by increasing the mass flow rate, the performance of novel varied arc ribs model performs better than other models as shown in *Fig. 3.14* and *Table 3.2.*

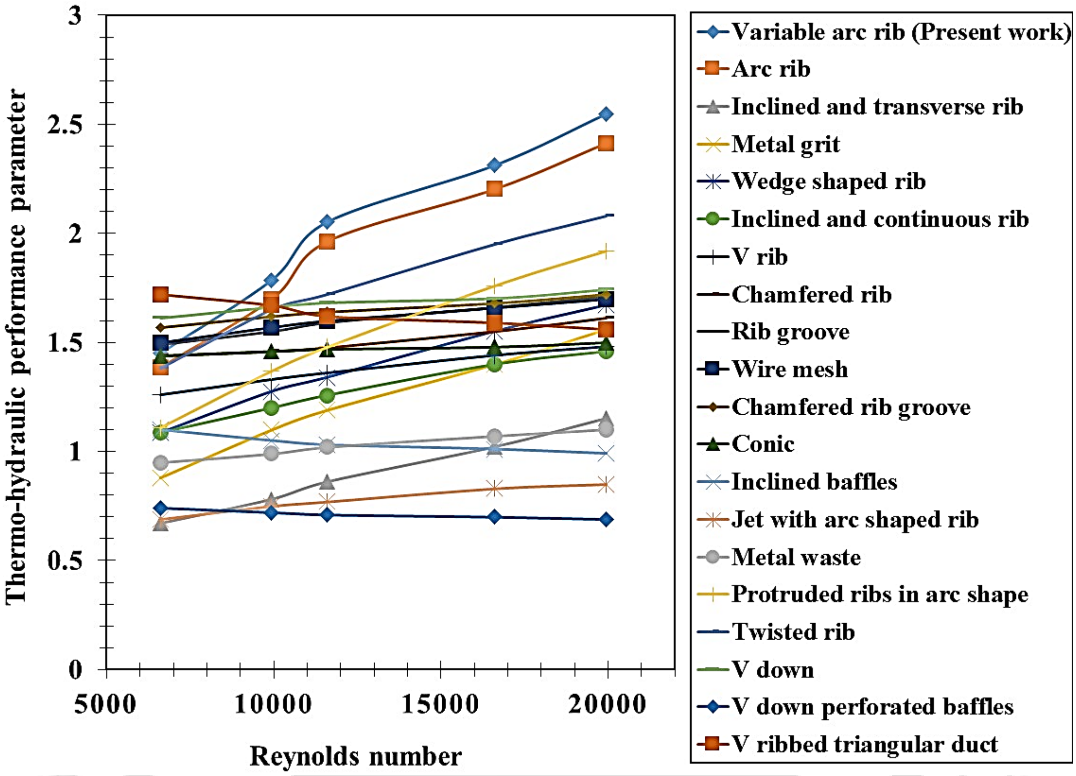

Fig. 3.14 Comparisons of thermo-hydraulic performance parameter of varied arc ribs with different other rib configurations at different Reynolds number range

Table 3.2 Comparison of THPP of different rib geometries for the Reynolds number ranges from 6604 to 19952

S. No	Rib geometry	Author (s)	THPP range
1	Varied arc ribs – present work	Sureandhar et al., (2021a)	1.44 to 2.54
2	Arc rib	Saini and Saini, (2008)	1.38 to 2.41
3	Inclined and transverse rib	Varun et al., (2008)	0.67 to 1.15
4	Metal grit rib	Karmare and Tikekar, (2007)	0.88 to 1.56
5	Wedge shaped rib	Bhagoria et al., (2002)	1.08 to 1.67
6	Inclined continuous rib	Aharwal et al., (2008a)	1.08 to 1.46
7	V rib	Momin et al., (2002)	1.26 to 1.48
8	Chamfered rib	Layek et al., (2007)	1.44 to 1.61
9	Rib groove	Saini and Saini, (1997)	1.49 to 1.71
10	Wire mesh	Gupta and Kaushik, (2009a)	1.5 to 1.7

S. No	Rib geometry	Author (s)	THPP range
11	Chamfered rib groove	Karwa et al., (1999)	1.57 to 1.72
12	Conic curve profile rib	Ngo and Phu, (2020)	1.44 to 1.50
13	Inclined baffles	Phila et al., (2020), Luan and Phu, 2020)	0.99 to 1.1
14	Jet with arc shaped rib	Nadda et al., (2017)	0.69 to 0.85
15	Metal waste	Phu et al., (2019)	0.95 to 1.1
16	Protruded ribs in arc shapes	Yadav et al., (2013)	1.11 to 1.92
17	Twisted rib	Kumar and Layek, (2019b)	1.38 to 2.08
18	V down rib	Singh et al., (2011a)	1.61 to 1.74
19	V down perforated baffles	Chamoli and Thakur, (2013), Chamoli and Thakur, (2016)	0.69 to 0.74
20	V ribbed triangular duct	Nidhul et al., (2020)	1.56 to 1.72

3.4.5 Energy analysis

3.4.5.1 Thermal efficiency evaluation

From *Fig. 3.15,* it is observed that as the flow rate increases, the thermal efficiency is also found to increase. The thermal efficiency of a 1 m length absorber plate is always higher than 2 m length. Thermal efficiency is the ratio of energy utilized to the product of solar radiation and surface area of the absorber plate. Therefore, an increase in the surface area of the absorber plate reduces the thermal efficiency of the SAH. The absorber plate surface area of 2 m length solar air heater is larger than 1m. The variable arc rib fin arrangement reported the maximum thermal efficiency of 79.0 % for 1 m and 77.4 % for 2m at a flow rate of 0.06 kg/s. The fixed arc rib fin arrangement reported a thermal efficiency if 77.7 % and 75.5 % for 1 m and 2 m length of the absorber plate, respectively, for 0.06 kg/s. Similarly, the smooth ducts reported an efficiency of 69.2 % and 67.5 % for 1m and 2m length of the absorber plate, respectively, for 0.06 kg/s. The higher thermal efficiency in

VAR SAH signifies that, embedment of varied arc ribs enhances the heat gain from the absorber plate to air. Due to the turbulence generated near the wall surface improved the thermo-hydraulic performance results in higher thermal conversion efficiency in VAR SAH.

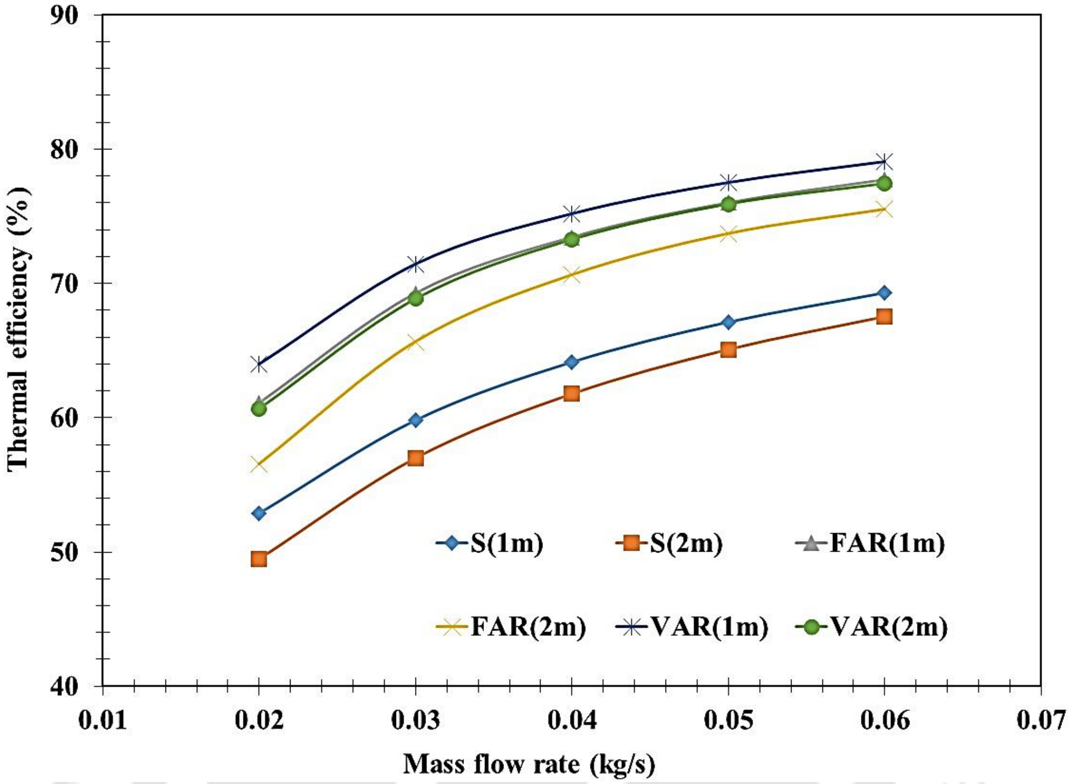

Fig. 3.15 Variations in thermal efficiency at various mass flow rates of air

3.4.5.2 Effective efficiency evaluation

The effects of various arc rib fin arrangements and length of the absorber plate on the effective efficiency of the SAH are shown in *Fig. 3.16*. It is observed that the effective efficiency increases as the air flow rate increases. It is a function of thermal efficiency and blower power. The effective efficiency is reported to be higher in variable arc rib fin arrangement with 76.0 % and 74.2 % at a flow rate of 0.06 kg/s, respectively for 1 m and 2 m length of absorber plate. Similarly, the fixed arc rib fin arrangement reported efficiency of 74.7 % and 72.4 %, and in the case of smooth duct, 67.6 % and 65.8 % efficiency are reported at 1 m and 2m length of absorber plate at 0.06 kg/s, respectively. Also, the effective efficiency signifies the effect of heat gain over the mass flow rate and pressure drop. During turbulent flow, the turbulent pressure drops is the function of square of the velocity that makes the higher blower power consumption at higher mass flow rate. Hence due to which by increasing the mass flow rate after some point the effective efficiency doesn’t increase.

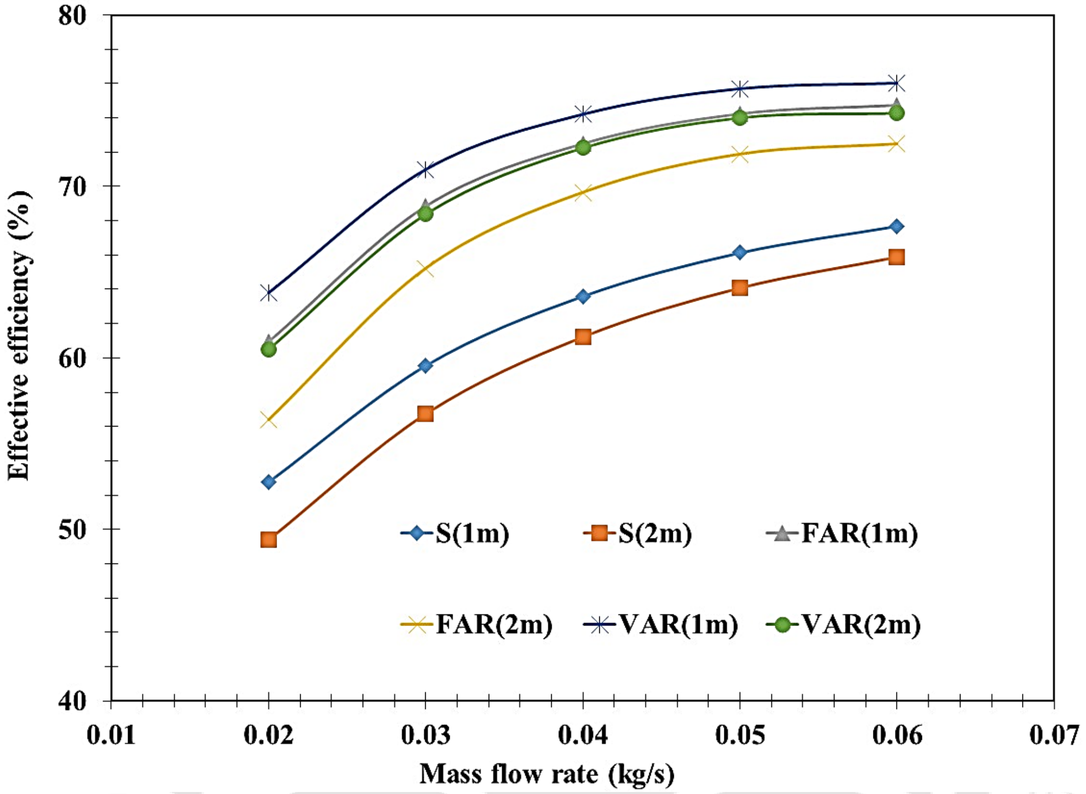

Fig. 3.16 Variations in effective efficiency at various mass flow rates of air

3.4.6 Exergy analysis

3.4.6.1 Exergy efficiency evaluation

The effects of various arc rib fin arrangements and length of absorber plate on the exergy efficiency of the SAH are shown in *Fig. 3.17*. The exergy efficiency reduces as the air flow rate increases. The exergy efficiency of the variable arc rib fin arrangement is reported to be maximum (2.5 %), followed by fixed arc rib fin arrangement (1.5 %) and smooth duct (1.2 %) at a flow rate of 0.02 kg/s for 2 m length absorber plate. A similar trend is observed in 1 m length of absorber plate with variable arc rib fin arrangement having maximum exergy efficiency of 2.3 % followed by fixed arc rib of 0.9 % and smooth duct of 0.7 % at a flow rate of 0.02 kg/s. It is observed that the exergy efficiency for 1 m variable and fixed arc rib arrangement is negative at a flow rate of 0.06 kg/s. This is attributed due to the increased pumping power requirement at a higher flow rate (0.06 kg/s), and subsequently, the thermal energy collected is lower than the pumping power required at the flow rate of

0.06 kg/s. At higher mass flow rate, the pressure drop varies power of square, that will eventually increase the blower power consumption. Simultaneously, amount of exergy gain reduces which leads to negative exergy efficiency. Hence, exergy efficiency signifies effect of mass flow rate over blower power consumption and thermal gain.

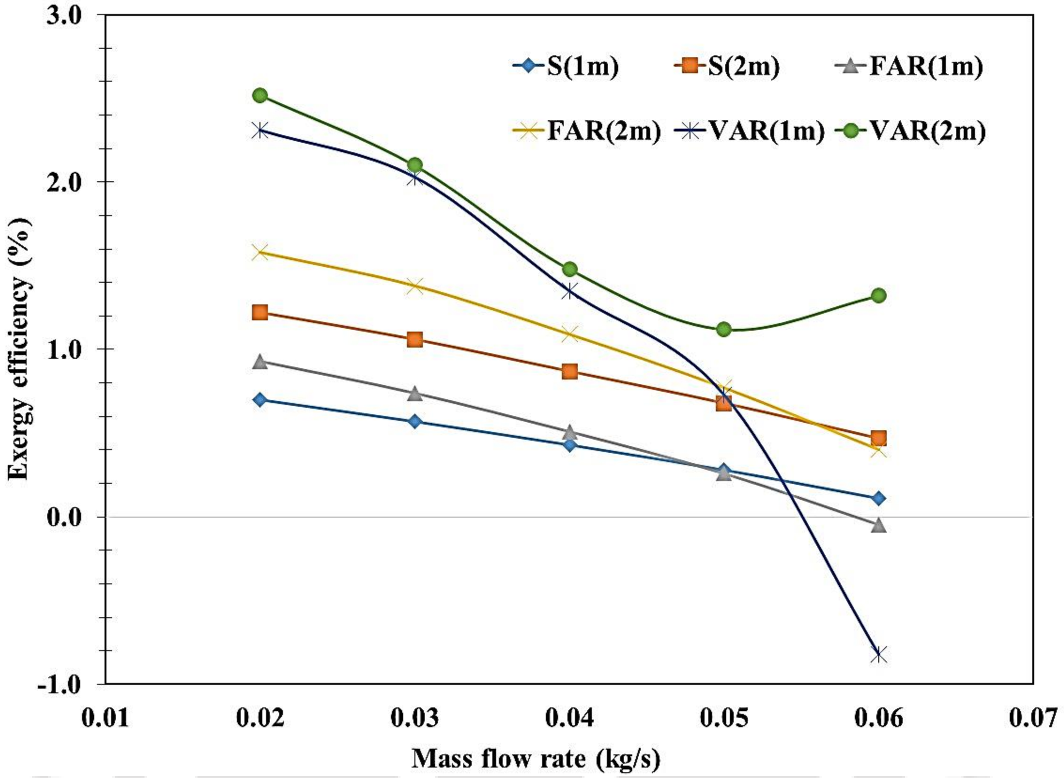

Fig. 3.17 Variations in exergy efficiency at various mass flow rates of air

3.4.6.2 Components of exergy losses

The detailed exergy losses in the six different configurations of SAH system for the mass flow rates ranging from 0.02 kg/s to 0.06 kg/s are calculated based on the formula given by Phu et al., (2020). *Fig. 3.18*, represents the different types of exergy loss components associated with the SAH operating under forced convection. The variation of each exergy loss component for the mass flow rates ranging from 0.02 kg/s to 0.06 kg/s are explained as follows.

The various exergy losses occurring during the SAH system’s interaction with source (Sun) and surroundings (environment) are due to: (a) glazing (optical losses), (b) absorption phenomena (absorption of solar radiation by the absorber plate), (c) convective and radiation phenomena (convective and radiative heat transfer from absorber plate to environment), (d) heat transfer from absorber plate to working fluid, and (e) friction loss.

Among these losses, for all kinds of configurations [Smooth duct, FAR, VAR], the maximum exergy loss occurs due to absorption phenomena (absorption of solar radiation by absorber plate) and glazing (optical exergy loss). Also, the exergy loss in 2 m length SAH is always higher than the 1 m duct length SAH, due to the increase in surface area.

Due to the presence of the varied arc ribs the heat transfer rate from the absorber plate to air (heat transfer fluid) is higher, hence the absorber solar radiation by the plate is continuously transferred to ribs. This makes the VAR SAH to generates higher exergy loss due to absorption of solar radiation than smooth duct and FAR SAH. While increasing the mass flow rate from 0.02 kg/s to 0.06 kg/s, the exergy loss due to absorption of solar radiation varies from 450 W to 473 W for the given exergy input of 570 W in VAR (2 m). Similarly, for VAR (1 m) for the given exergy input of 285 W, the value varies from 227 W to 238 W respectively. The exergy loss due to glazing is independent of operating parameters, it depends only on design parameter (surface area of absorber plate). Hence, the exergy loss due to glazing doesn’t varies due to change in mass flow rate of operation. The numerical investigation shows that 45 W and 90 W is the exergy loss happened due to glazing in 1 m and 2 m SAH respectively. Around 95% – 98% of the exergy loss occurs mainly due to glazing and absorption of solar radiation.

The consumption of blower power is very less in comparison with heat gain, also the system operating temperature is less than 100°C (373 K). Hence, remaining losses (convective and radiative heat transfer from absorber plate to environment, heat transfer from absorber plate to air and frictional loss) comprises 2% - 5%, has less significant effect over exergy performance of the SAH.

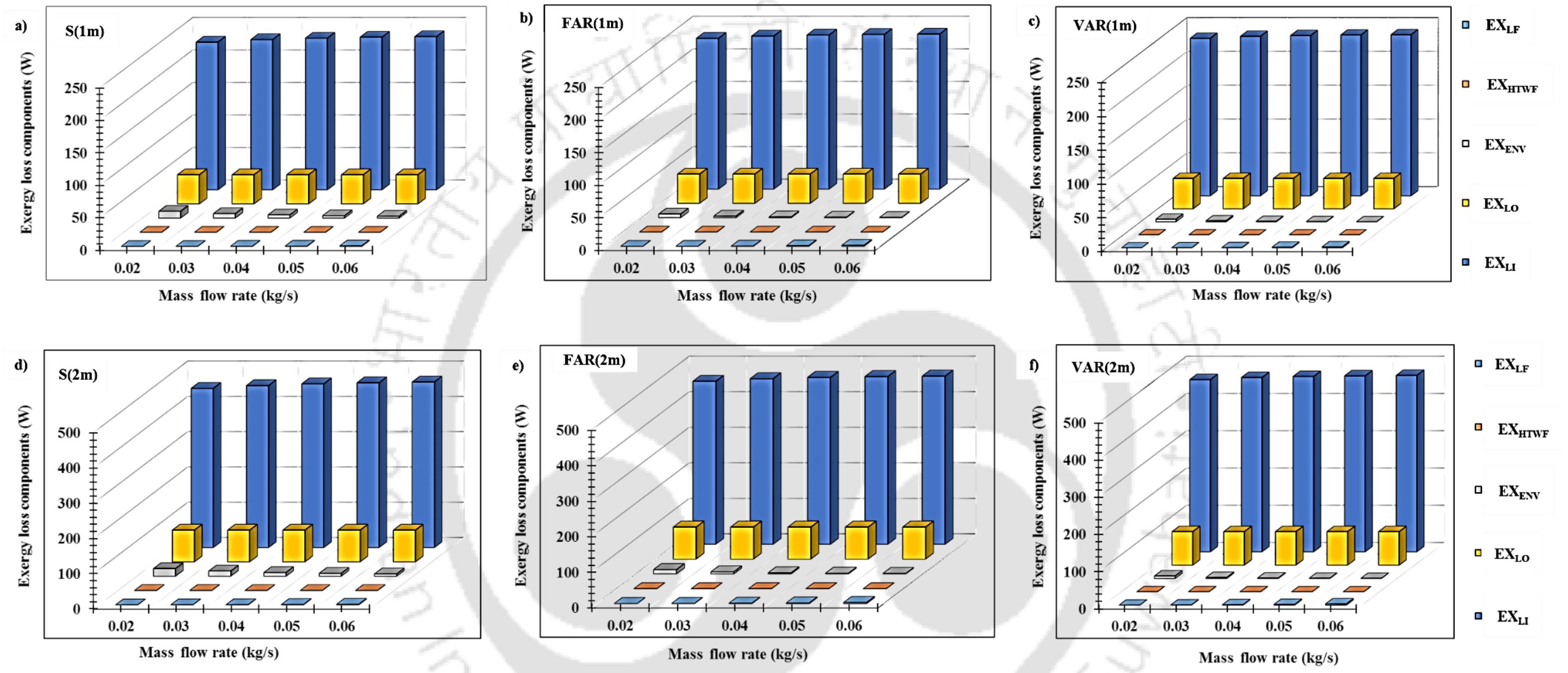

Fig. 3.18. Variations in different exergy loss components at various mass flow rates of air for (a) S (1 m), (b) FAR (1 m), (c) VAR (1 m), (d) S (2 m), (e) FAR (2 m), (f) VAR (2 m)

3.4.7 Entropy analysis

3.4.7.1 Entropy generation due to heat transfer

From *Fig. 3.19*, it is observed that, entropy generated due to heat transfer, increases as the mass flow rate increases. The value is higher for 2 m SAH than 1 m SAH. Among, 1 m and 2 m length of the SAH, VAR (1 m) and VAR (2 m) SAH generated higher entropy generation due to heat transfer than smooth duct and FAR SAH. Since entropy generation due to heat transfer is a function of direct proportionate to outlet temperature and mass flow rate of hot air from the SAH, VAR (2 m) generates higher hot air outlet temperature in the range of 307.6 K at 0.02 kg/s to 318 K at 0.06 kg/s. By increasing the mass flow rate from 0.02 kg/s to 0.06 kg/s, entropy generation due to heat transfer increases by 0.3423 W/K for VAR (2 m). While operating the VAR (2 m) SAH at 0.02 kg/s, due to heat transfer, it generates the entropy value higher than S (2 m) by 0.2107 W/K and FAR (2m) by 0.0787 W/K. Similarly, during 0.06 kg/s flow rate condition, VAR (2m) generates 0.186 W/K higher than S (2 m) and 0.02 W/K higher than FAR (2 m) respectively.

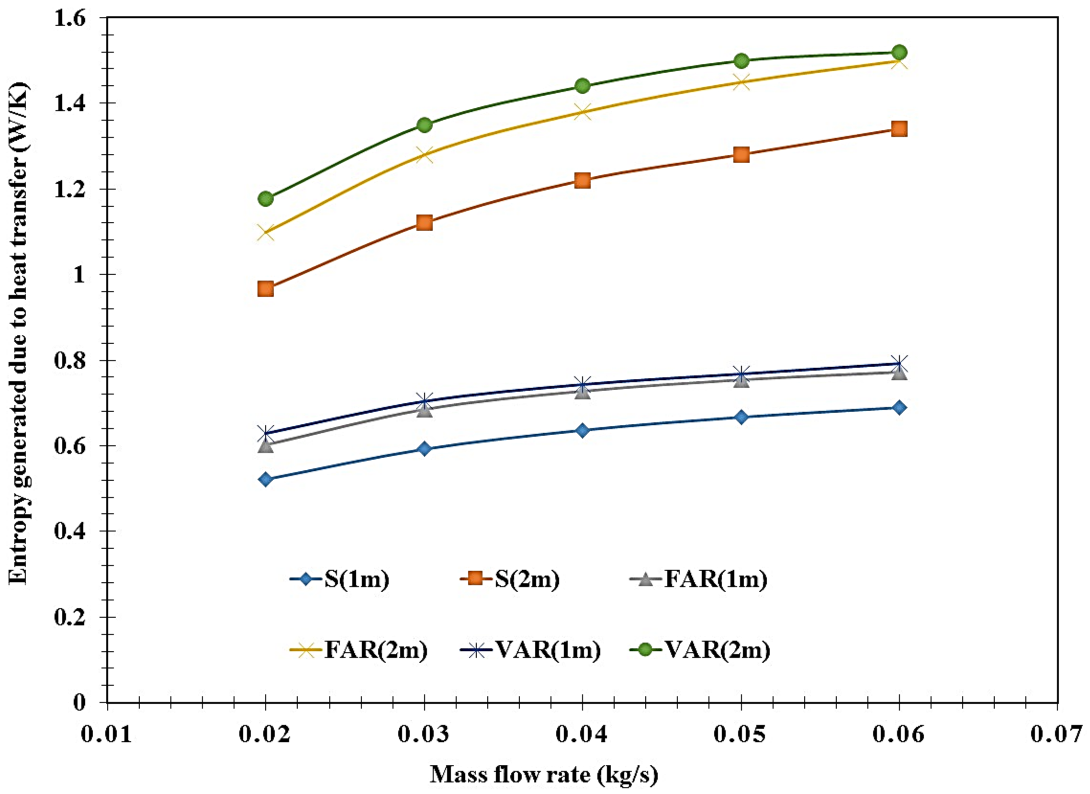

Fig. 3.19 Variations in entropy generation due to heat transfer at various mass flow rates of air

3.4.7.2 Entropy generation due to pressure drop

Fig. 3.20 shows that entropy generated due to pressure drop increases in polynomial variation, with respect to increase in mass flow rate. The value is higher for 2 m length SAH than 1 m due to higher blower power consumption. Comparison result shows that, among 1 m length and 2 m length of SAH, VAR (1 m) and VAR (2 m) SAH has higher value than smooth duct and FAR SAH configurations. By increasing the mass flow rate from 0.02 kg/s to 0.06 kg/s, the $(\Delta s)_{gen,\,\Delta P}$ increases by 0.01278 W/K. At 0.02 kg/s and 0.06 kg/s, the value of $(\Delta s)_{gen,\,\Delta P}$ for VAR (2 m) increases by 0.000226 W/K and 0.0054 W/K than S (2 m), increases by 0.000015 W/K and 0.004 W/K than FAR (2 m) respectively.

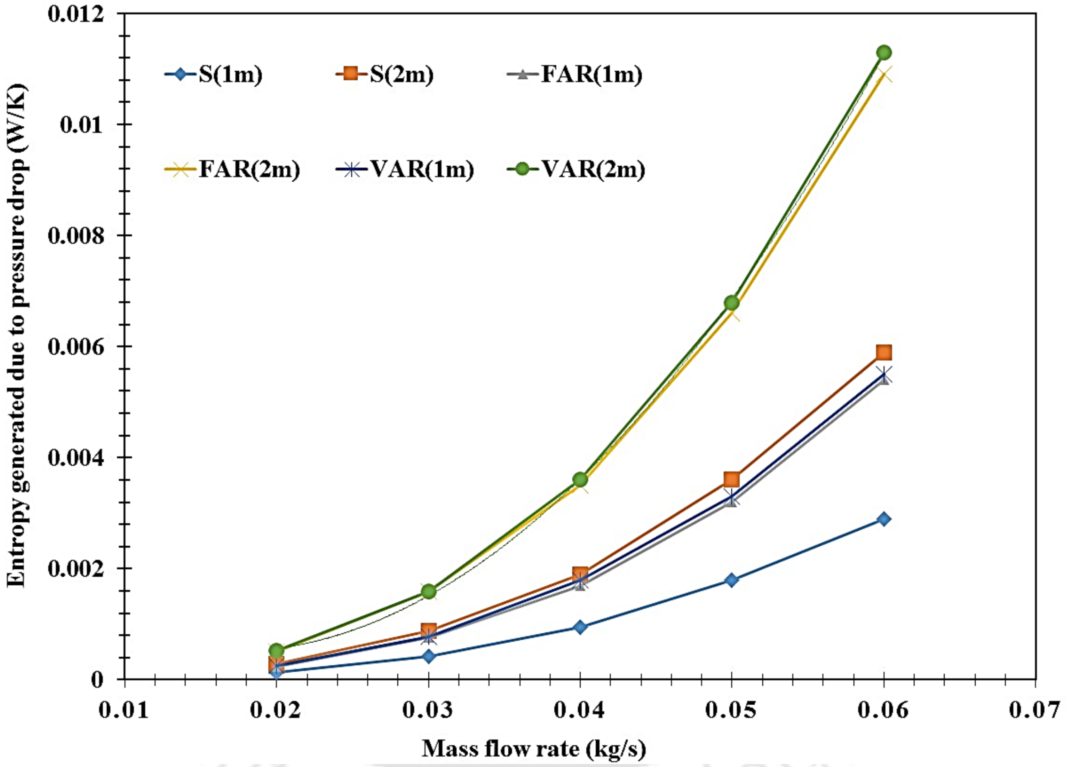

Fig. 3.20 Variations in entropy generation due to pressure drop at various mass flow rates of air

3.4.7.3 Total entropy generated

Fig. 3.21, shows the variation of total entropy generated due to heat transfer and pressure drop. It was observed that the total entropy generated for 2 m SAH is higher than 1m SAH. The value of total entropy generated increases with increase in mass flow rate for both 1 m and 2 m length SAH. VAR (1 m) and VAR (2 m) model has higher total entropy generation than smooth duct and fixed arc rib SAH of both 1 m and 2 m. By increasing the air flow rate from 0.02 kg/s to 0.06 kg/s the total entropy generated increases by 105.8 W.

Consequently, for both 0.02 kg/s and 0.06 kg/s, VAR (2 m) SAH increase by 64 W and 56 W than S (2 m) SAH, also it increases by 23W and 8W than FAR (2 m) respectively.

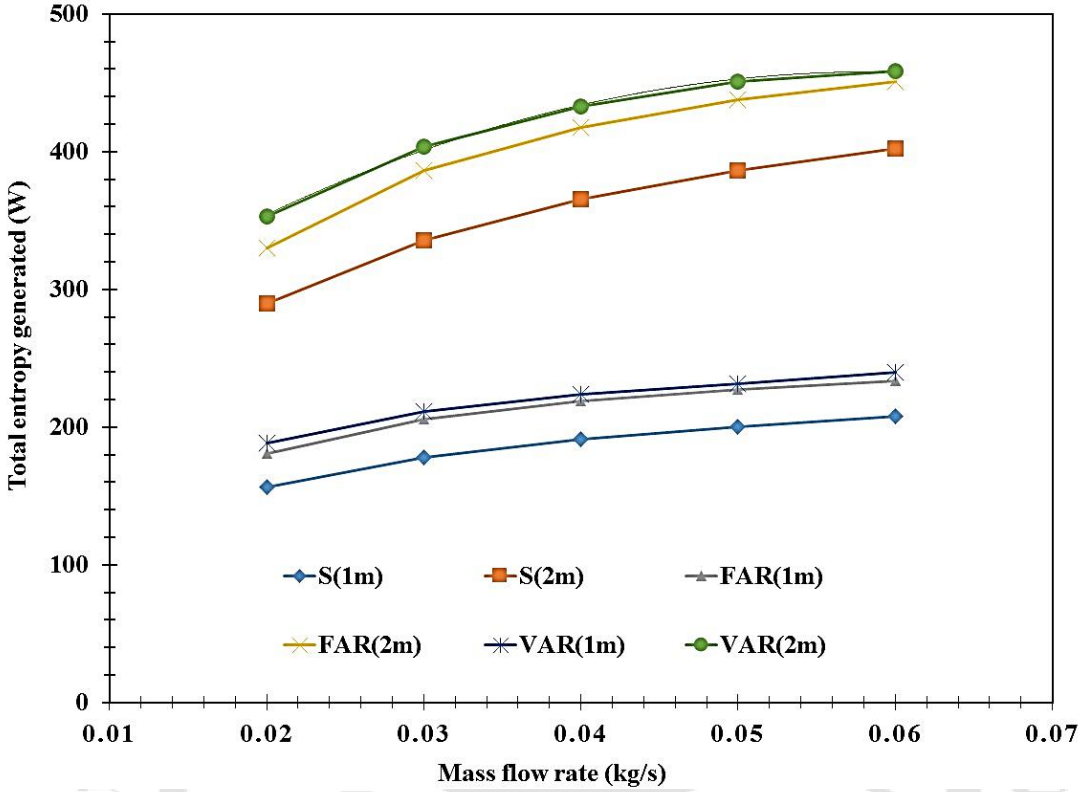

Fig. 3.21 Variations in total entropy generation at various mass flow rates of air

3.4.7.4 Bejan number

Bejan number is the ratio of entropy generated due to heat transfer and total energy generated due to pressure drop and heat transfer. It is seen from *Figs. 3.20* and *3.19*, that entropy generation for heat transfer is comparatively higher than entropy due to pressure drop in air. Hence, lower value of Bejan number signifies higher pressure drop. The value close to 1 represents a solar heater that operates with lesser friction (low pressure drops). It can be observed from the *Fig. 3.22*, that the variation of Bejan number with respect to mass flow rate and length does not have significant effect. In an overall, the value of Bejan number varies from 0.9997 to 0.9926. Also, the value of Bejan number reduces with respect to increase in mass flow rate.

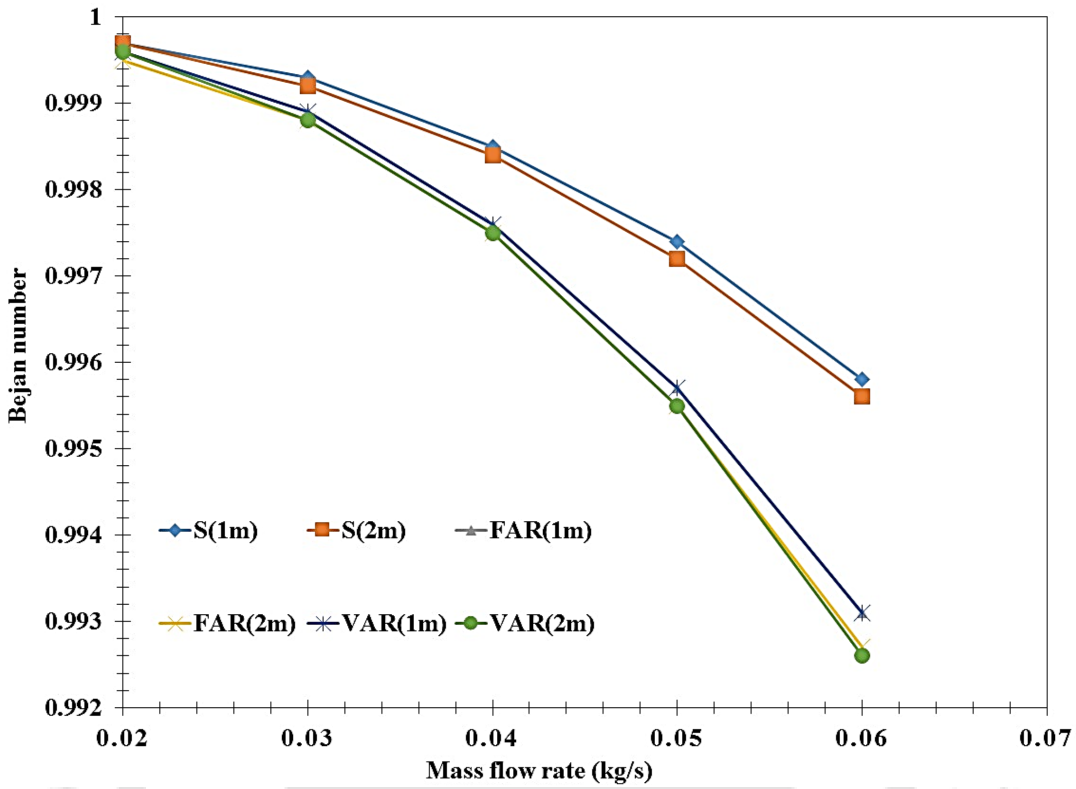

Fig. 3.22 Variations in Bejan number at various mass flow rates of air

3.4.7.5 Entropy generation number

Entropy generation number is the ratio of total entropy generated due to pressure drop and heat transfer to the amount of energy input to the system. Entropy generation number is a dimensionless number that signifies entropy generates with respect to input. From *Fig. 3.23*, it is observed that, entropy generation number increases with increase in mass flow rate. Also, from Fig.3.23, it is observed that the entropy generation number is higher for 1 m length of SAH than 2 m length of SAH. Among all six different SAH’s, VAR (1 m) SAH has highest entropy generation number. By increasing the mass flow rate from 0.02 kg/s and 0.06 kg/s, the entropy generation number added by 0.1066 units and 0.1068 units than S (1 m) SAH, also it rises by 0.0267 units and 0.021 units than FAR(1m) SAH respectively. Increase in entropy generation number represents the system has higher irreversibility rate for the given energy input.

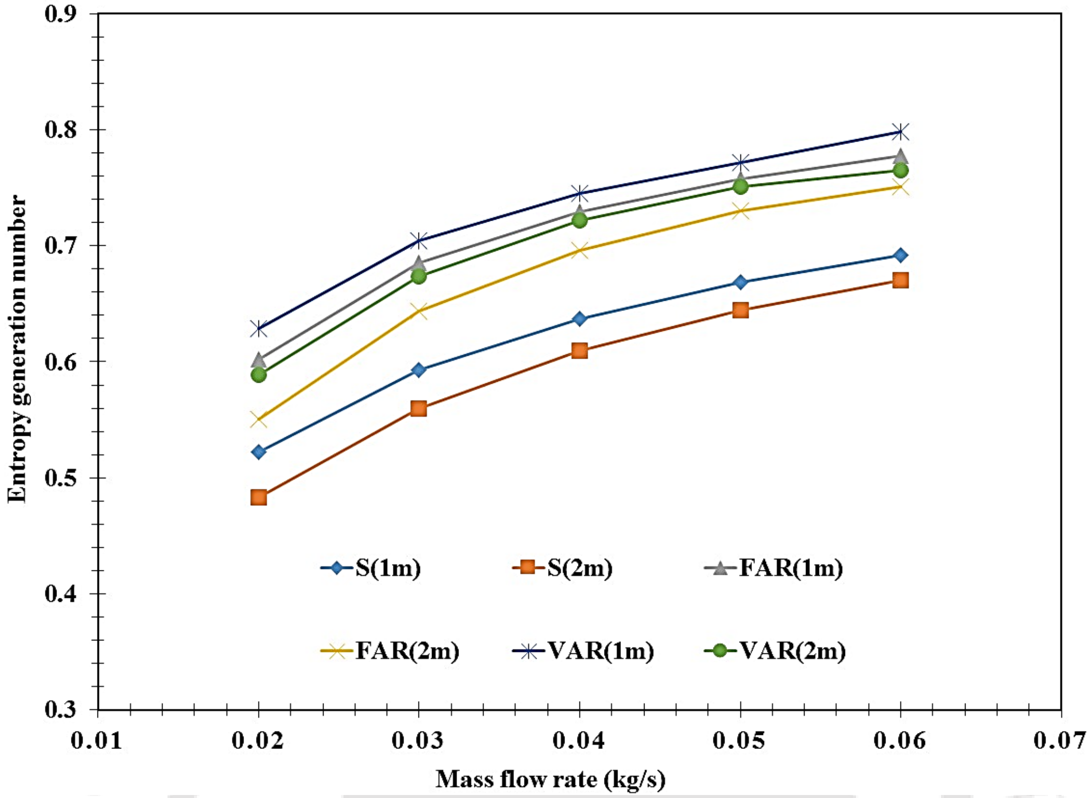

Fig. 3.23 Variations in entropy generation number at various mass flow rates of air

3.4.7.6 Irreversibility distribution ratio

Irreversibility distribution ratio is defined as ratio of entropy generated due to pressure drop and heat transfer. From *Fig. 3.24*, it was observed that, irreversibility distribution ratio increases with increase in mass flow rate logarithmically. S (1 m) and S (2 m) have a lesser irreversibility distribution ratio than fixed and varied arc ribs SAHs. Also, it is noticed that VAR (1 m) and VAR (2 m) have similar irreversibility distribution ratio values as that of FAR (1 m) and FAR (2 m). Hence increase in pressure drop does not have a significant effect on the performance of SAH, but system inclined towards more irreversibility.

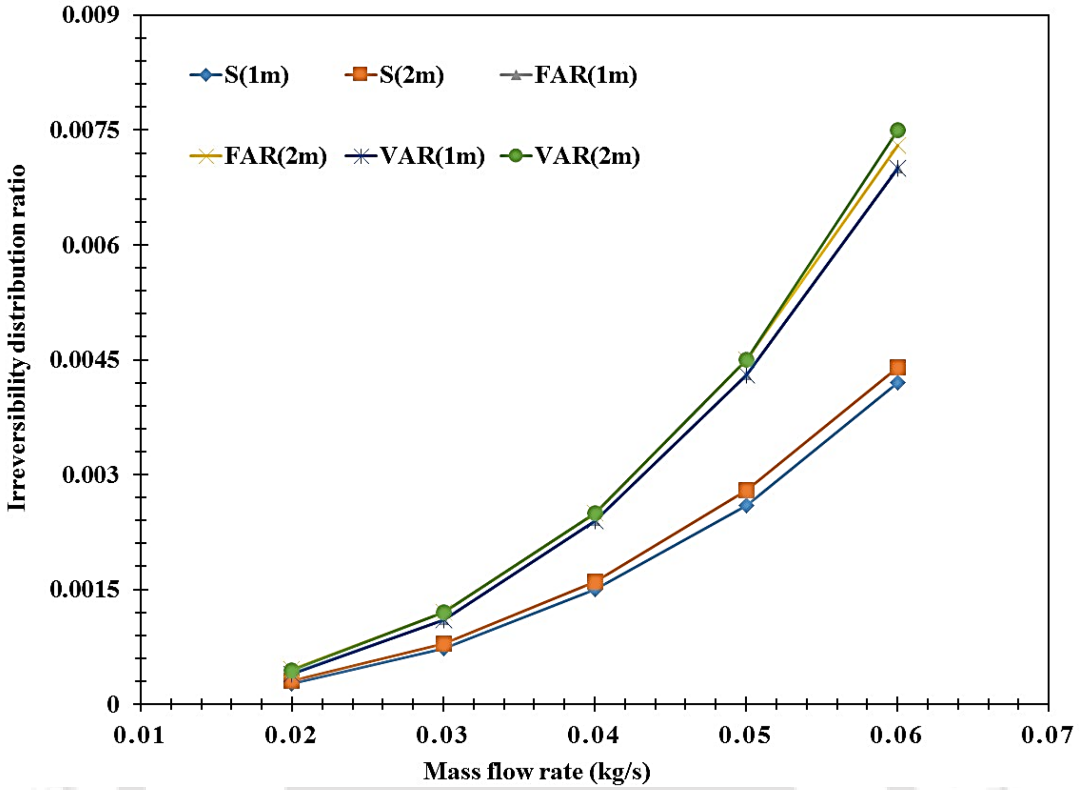

Fig. 3.24 Variations in irreversibility distribution ratio at various mass flow rates of air

3.5 Summary

A thermal model is developed for analysing the influences of arc rib fin arrangement and length of absorber plate on the heat transfer characteristics of a SAH. The arc rib fin arrangement is designed by varying the fin relative roughness height ratio (e/De) in the absorber plate. Solar air heater with fixed arc rib fin configuration with e/De (0.0422) and variable arc rib fin configuration with two different relative roughness height ratios of e/De (0.0422 and 0.0541) are modelled. The influence of absorber plate length (1 and 2 m) on the solar air heater performance is compared with the configurations mentioned above at various mass flow rates of air (0.02 kg/s to 0.06 kg/s). The outlet air temperature of solar air heater, mean absorber plate temperature, heat transfer characteristics (Nusselt number and frictional factor), thermo-hydraulic performance parameter, efficiencies (thermal, effective, and exergy), collector efficiency factor, and collector heat removal factor are predicted at different air flow rates. The variable arc rib fin arrangement in the solar air heater leads to maximum utilization of available solar energy from the absorber plate and reported maximum outlet air temperature and lower mean absorber plate temperature when compared to fixed arc rib fin arrangement and smooth duct SAH. Further, the variable arc rib fin arrangement has better heat transfer and thermo-hydraulic characteristics than the fixed arc rib fin arrangement and smooth duct. Thus, it was observed that embedding varied arc ribs over the absorber plate surface has remarkable effect in the thermo-hydraulic performance of the SAH.

Chapter 4 Experimental investigations of varied arc ribs embedded in SAH

4.1 Preface

From the literature (Aharwal et al., 2008b; Alam et al., 2014b; Bharadwaj et al., 2013; Bhushan and Singh, 2011; Jaurker et al., 2006b; A. Lanjewar et al., 2011; A. P. Singh et al., 2014; A. S. Yadav and Bhagoria, 2013a), it is evident that performance of SAH depends on the fin geometries (shape, attack angle, relative roughness, height, pitch, and width). Yadav and Thapak (A. S. Yadav and Thapak, 2016b) compared the THPP values of different roughness elements and reported that arc rib performed better than other elements. Singh and Singh (2018) observed that arc ribbed wire element has lower pressure drop and higher THPP when compared to V rib elements due to curved secondary flow. The present work compares the overall performance of fixed and variable arc ribbed wire in a SAH analytically. It is observed that the variable arc rib had higher outlet air temperature, Nusselt number, THPP, efficiencies (η_{th}, η_{eff} and η_{ex}) than fixed arc rib.

The arc ribbed wire configuration is selected for its better THPP in the present study from the literature review. There is no profound literature on the experimental investigation of variable arc ribbed wire configuration. Thus, a variable arc ribbed wire configuration embedded on the absorber plate is designed and tested. The inlet and outlet temperature of the SAH, absorber plate, air inside the duct, stagnation, glazing, and bottom plate temperatures are measured. Further, the overall performance of the SAH is determined from the Nusselt number, useful heat gain, collector factors, total loss coefficient and efficiencies (η_{th}, η_{eff} and η_{ex}).

4.2 Experimental setup

A back pass SAH with variable arc ribbed wire configuration in the absorber plate operated in forced convection mode was designed and tested in the climatic conditions of North Guwahati, Assam, India. A schematic layout of the SAH is shown in *Fig. 4.1*. The experiments were conducted at Indian Institute of Technology Guwahati, located at a latitude of 26°110' N and a longitude of 91°440' E. The SAH was made of a wooden structure consisting of a glazing glass, an absorber plate, variable arc ribbed wire, polyurethane insulation, bottom plate, blower, flow control valve, inlet and outlet section.

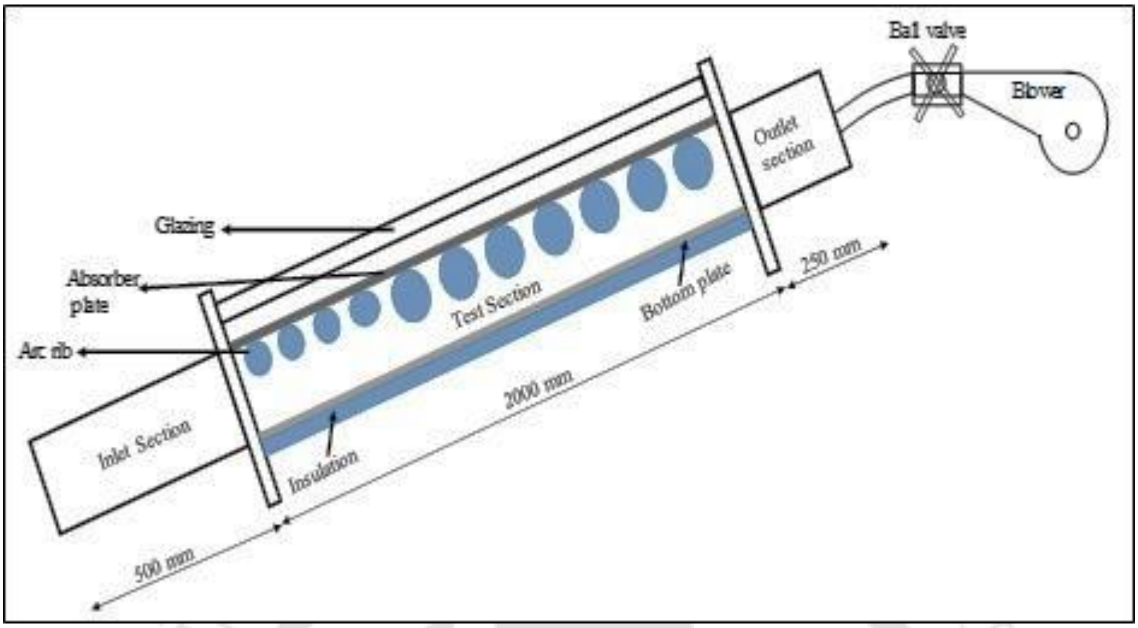

Fig. 4.1 Schematic layout of the varied arc ribs embedded SAH setup

The solar air heater components used in the experimental setup are presented in *Fig. 4.2.* The size of glazing glass, absorber plate, bottom plate and SAH duct is 2 m × 1 m. The absorber plate of 2 mm thickness is coated with black paint. The variable arc ribbed wire made of copper is welded at the bottom side of absorber plate. The variable arc ribbed wire configuration is shown in *Fig. 4.3*. The initial 0.5 m length of the absorber plate has an arc ribbed wire of 2 mm diameter with a pitch of 20 mm between each rib, and from 0.5 m to 1.5 m length, arc ribbed wire of 2.5 mm diameter with a pitch of 25 mm is attached. The bottom plate is made of mild steel of 2 mm thickness and is placed above the polyurethane insulation. The setup is elevated at an angle of 26.18° facing towards the south. The distance between the glazing and absorber plate is 50 mm. The distance between the absorber plate and bottom plate is 25 mm. The length of inlet, test and outlet sections are 500 mm, 2000 mm, and 250 mm respectively. The blower unit is attached to the outlet section of the SAH. A ball valve is placed between the blower and SAH to control the flow. The geometrical parameters of arc ribbed wire and SAH are listed in *Table 4.1***.**

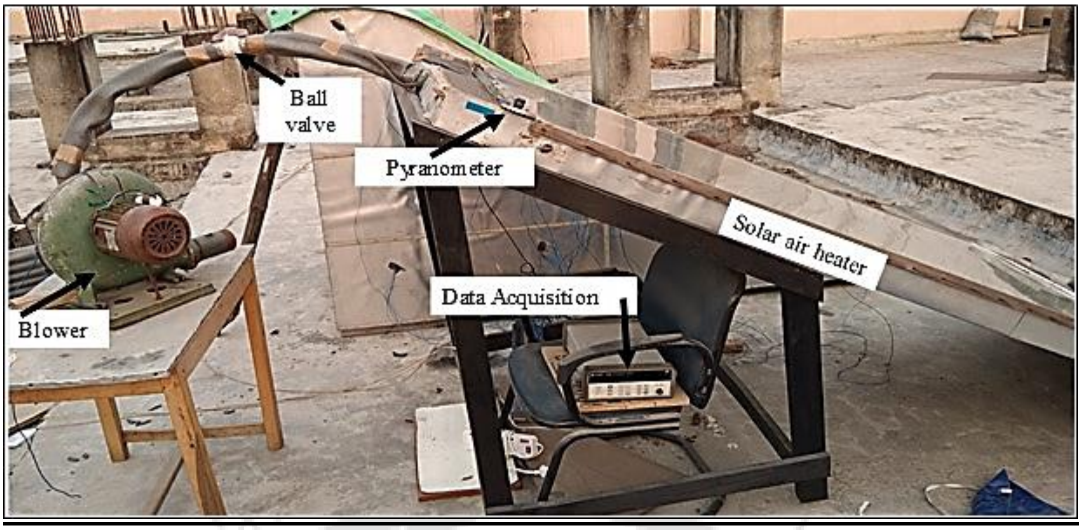

Fig. 4.2 Experimental layout of the solar air heater

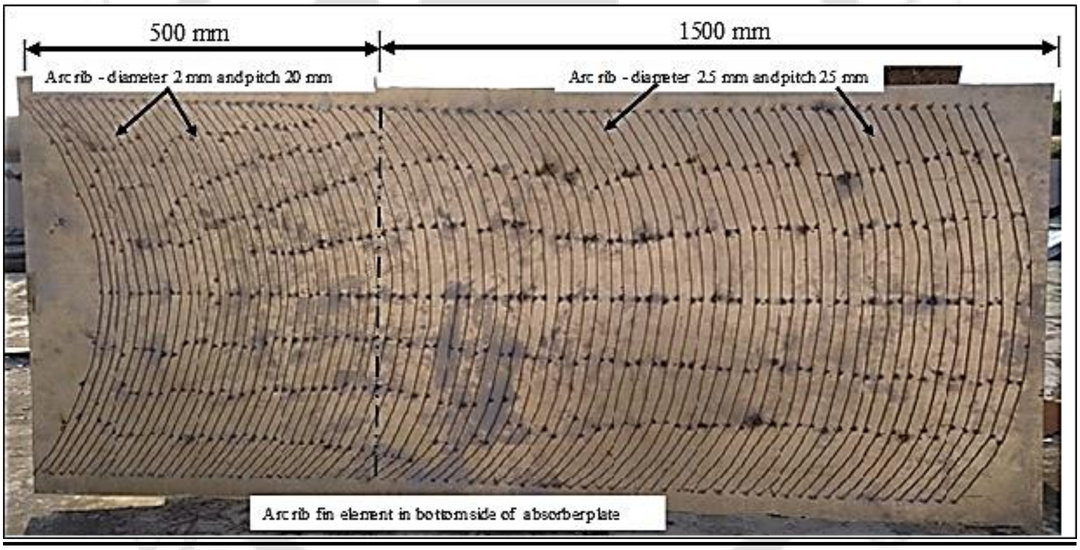

Fig. 4.3 Variable arc rib fin arrangement in the absorber plate

Table 4.1 Geometrical parameters of arc ribbed wire and SAH

S. No	Parameters	Value
1	SAH test section length	2 m
2	Width of the airflow duct	1 m
3	Depth of the airflow duct	0.025 m
4	Absorber plate thickness – (galvanized iron)	2 mm
5	Arc rib fin diameter – (copper)	2 mm and 2.5mm
6	Variable arc wire rib height ratio e/D_e (up to 0.5 m of the absorber plate)	0.0408
7	Variable arc wire rib height ratio e/D_e (from 0.5 m to 2 m of the absorber plate)	0.0510
8	Variable arc wire rib pitch ratio (p/e)	10

S. No	Parameters	Value
9	Mass flow rate – m_1	0.0175 kg/s
10	Mass flow rate – m_2	0.0098 kg/s
11	Flow attack angle ratio ($\alpha/90$)	0.3333
12	Tilt angle	26.18°

4.3 Experimental procedure

The SAH surface was cleaned, and the dust and dirt in the glazing surface were removed periodically. The experiments were started at 9:00 hr and ended at 15:00 hr. The flow rate was controlled using ball valve. At fully open conditions, the flow rate was 0.0175 kg/s, and at partially open conditions, a flow rate of 0.0098 kg/s was measured. The SAH was operated at 0.0175 kg/s for two consecutive days (Day 1 and Day 2) at fully open conditions and at 0.0098 kg/s for the next two days (Day 3 and Day 4) at partially open conditions. Pre-calibrated T type thermocouples were evenly placed at 500 mm gap along the SAH to measure the absorber plate and airflow temperature in the duct. At each set of experiments, inlet and outlet temperature of SAH, glazing, stagnation and bottom plate temperature were recorded. The solar insolation was measured using a pyranometer, and the velocity at the SAH outlet was determined using an anemometer. The temperature and voltage values were recorded at 60 s intervals using thermocouple and pyranometer, respectively, and were logged to a data acquisition system. The instruments used for measuring temperature, velocity, pressure, and solar isolation are listed in *Table 4.2* with their accuracy range.

Table 4.2 Measured parameters and its accuracy

S.No	Parameter	Instruments	Accuracy
1	Temperature	T type - Thermocouple	± 0.2°C
2	Velocity	Testo 405i - anemometer	± 0.1 m/s
3	Solar Insolation	Apogee; Model: SP-110; Pyranometer	± 5 %
4	Pressure	Testo 512 – Digital pressure meter	± 0.5 %

The selection of physical parameters for the fixed arc rib (FAR) solar air heater was based on an experimental investigation conducted by Saini and Saini (2008). After validating the FAR SAH model, the various modes of energy and exergy losses in the FAR SAH were studied. The analytical study revealed that in order to improve the thermal conversion efficiency and exergy efficiency, it was necessary to enhance the heat transfer rate along the length of the air flow path and minimize top loss. This led to the investigation of a newly developed varied solar air heater (VAR) model, which involved increasing the surface area of the arc rib with a proliferated diameter. By comparing the analytical performance of the FAR and VAR SAH, it was determined that the newly developed model's THPP, energy, and exergy efficiency outperformed the existing FAR SAH. The physical parameters for the VAR SAH were determined after reviewing relevant literature and conducting an analytical comparison. Subsequently, an experimental setup was fabricated and tested for the varied arc rib-embedded SAH.

4.4 Results and Discussion: Experimental investigation

India spans approximately 30° of longitude, stretching from 97°25'E in Arunachal to 68°7'E in Gujarat. The country operates on a single time zone, known as Indian Standard Time (IST), which is centred in Mirzapur (82°33'E) near Allahabad, Uttar Pradesh. However, for the purpose of this thesis, the fundamental parameter readings of the source, system, and surroundings were recorded based on the local geographical conditions of Guwahati, Assam (91°440'E), which is one hour ahead of IST. It is important to note that throughout the thesis, we have consistently followed the official IST time zone. In all graphs, the values plotted represent averages of one-hour recorded data, within the time intervals of 09:00 hr to 15:00 hr. Specifically, the values recorded between 09:00 to 09:59 hr, 10:00 to 10:59 hr, 11:00 to 11:59 hr, 12:00 to 12:59 hr, 13:00 to 13:59 hr, 14:00 to 14:59 hr, and 15:00 to 15:59 hr were designated as 9, 10, 11, 12, 13, 14, and 15 hr, respectively, for clarity and consistency.

4.4.1 Solar radiation intensity and ambient air temperature

The variations in solar intensity and ambient temperature were measured from 12th November 2020 to 15th November 2020 from 9:00 hr to 15:00 hr for 6 hr each day. The average solar intensity and ambient temperature in each day is 556 W/m^2 and 303.7 K (day 1), 537 W/m^2 and 301.6 K (day 2), 525 W/m^2 and 301.3 K (day 3), and 555 W/m^2 and 301.9 K (day 4) as shown in *Fig. 4.4*. The maximum solar radiation was observed between 10:00 hr and 12:00 hr, and varied from 679 W/m^2 to 654 W/m^2 during day 1 to day 4.

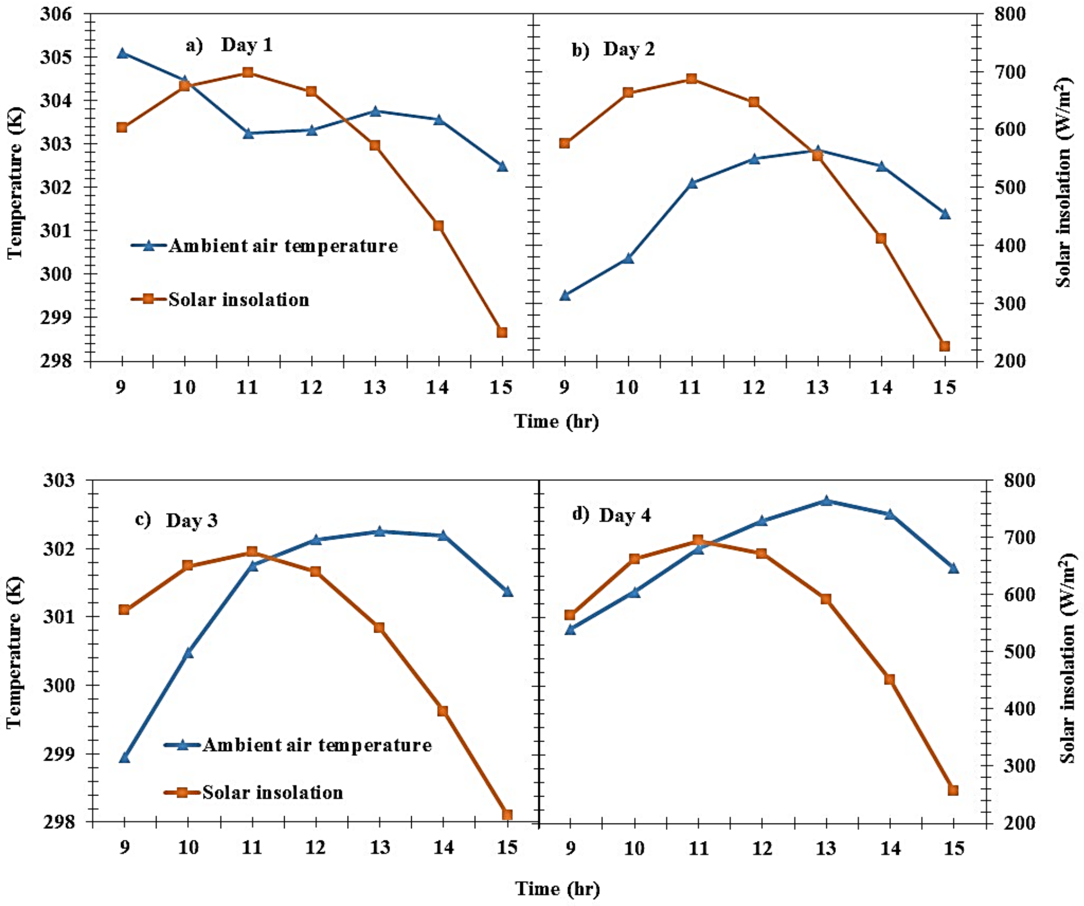

Fig. 4.4. Variations in solar radiation intensity (insolation) and ambient air temperature with time

4.4.2 Effect of varied arc ribs arrangement on heat transfer characteristics performance

4.4.2.1 Nusselt number and heat transfer coefficient variations

Fig. 4.5 shows the variation in Nusselt number in the SAH against time at various flow rates. The Nusselt number was varied between 13.4 and 18.0 at a flow rate of 0.0175 kg/s. At a flow rate of 0.0098 kg/s, the Nusselt number was varied from 10.6 to 12.5. The average Nusselt number in the SAH on each day was observed to be 16.6 (day 1), 17.5 (day 2), 11.7 (day 3), 11.9 (day 4). The maximum Nusselt number of 18 was obtained at a higher flow rate (0.0175 kg/s) during peak sunshine hour (12:00 hr). As the flow rate was increased from 0.0098 kg/s to 0.0175 kg/s, the average Nusselt number was also found to increase by 44.9 % (11.8 - 0.0098 kg/s; and 17.1 - 0.0175 kg/s).

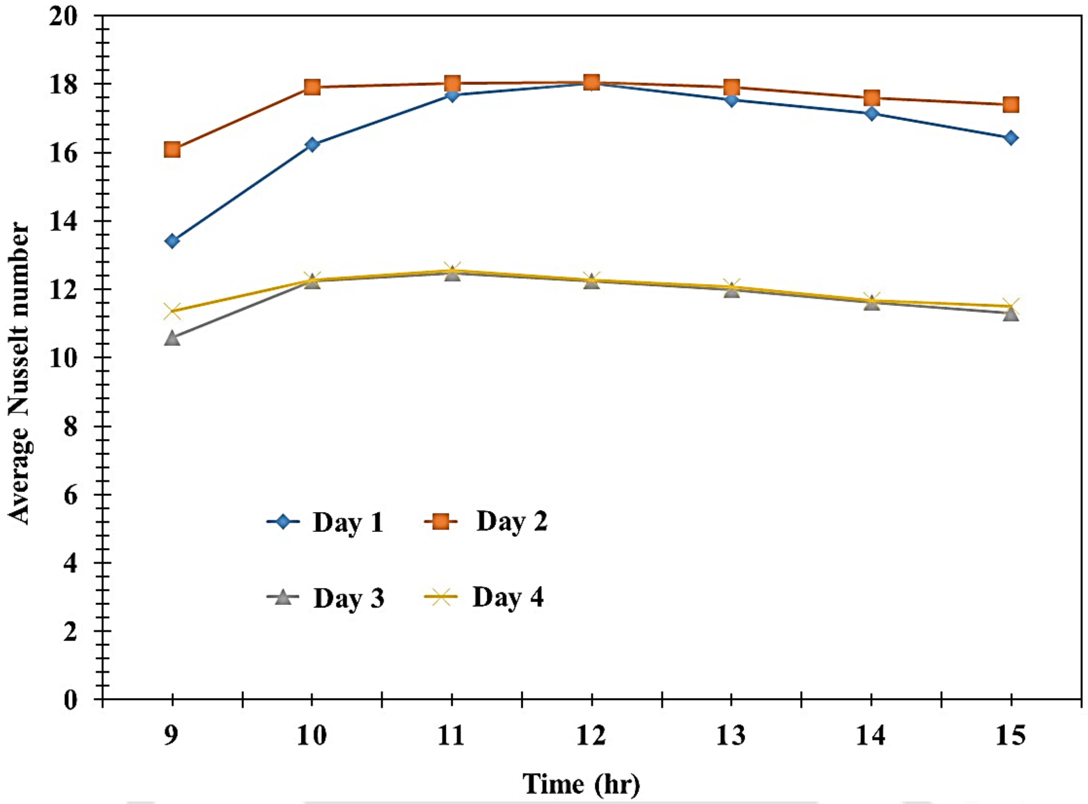

Fig. 4.5 Variations in average Nusselt number with time

Fig. 4.6 represents the variation of average heat transfer coefficient between absorber plate and fluid (air) in SAH with respect to time for 0.0175 kg/s and 0.0098 kg/s respectively. The average heat transfer coefficient was varied between 6.57 and 8.84 for 0.0175 kg/s. For 0.0098 kg/s flow rate, the value of average heat transfer coefficient was varied between 5.19 and 6.15 respectively. The average heat transfer coefficient values on each day was found as 8.15 (day 1), 8.60 (day 2), 5.77 (day 3) and 5.86 (day 4) respectively. As the flow rate was increased from 0.0098 kg/s to 0.0175 kg/s the average heat transfer coefficient was also found to increases from 5.81 - 0.0098 kg/s; and 8.38 - 0.0175 kg/s).

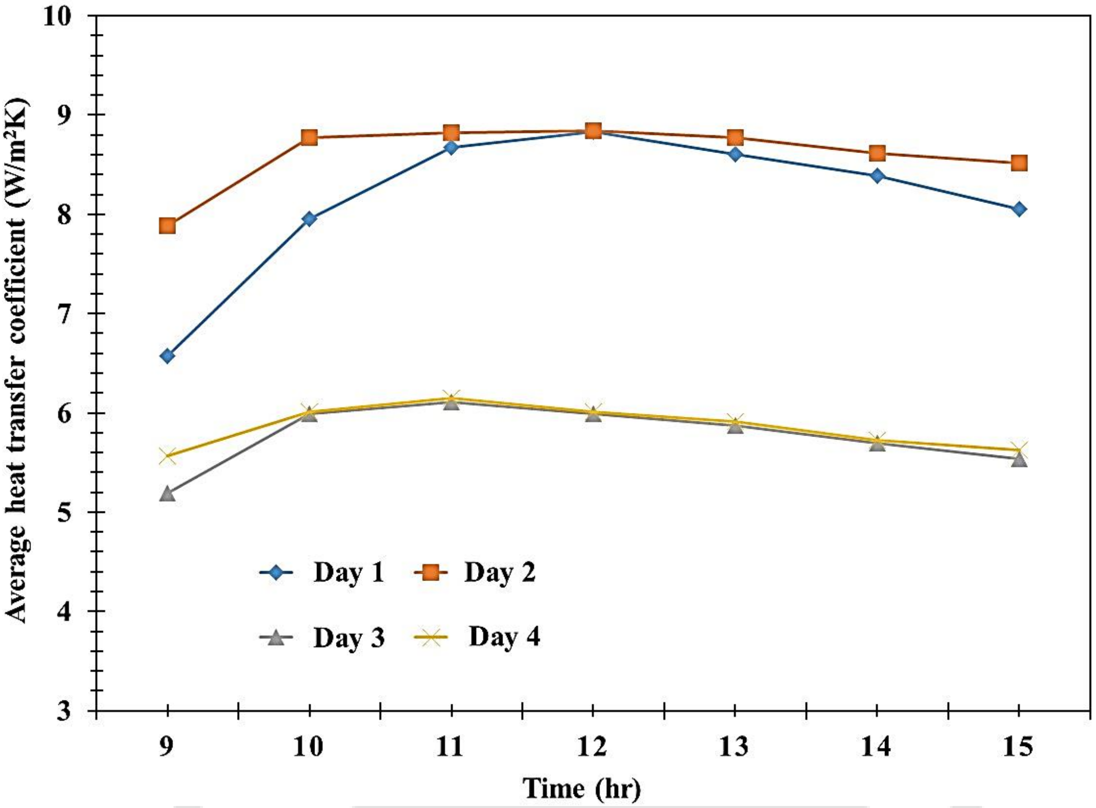

Fig. 4.6 Variations in average heat transfer coefficient with time

4.4.2.2 Frictional factor and pressure drop evaluation

The frictional factor depends on the mass flow rate and surface geometry of the system. Because of different rib configuration, there was a flow blockage, that significantly affects the pressure drop, which finally affects the frictions factor value. The maximum frictional factor (0.0144) attained for the minimum mass flow rate (0.0098 kg/s). The maximum pressure drops (0.4750 Pa) attained for maximum mass flow rate conditions (0.0175 kg/s) was 2.88 times higher than operating in 0.0098 kg/s. Also, operating the SAH at maximum flow rate improved the heat transfer coefficient. By increasing the mass flow rate from 0.0098 to 0.0175 kg/s, the heat transfer coefficient was improved from 61 to 130 W/m^{2}K, which is 2.13 times increment in heat transfer. Change in mass flow rate of operation does not have greater effect in frictional factor, but has found better effect in heat transfer improvement as shown in *Table 4.3.*

Table 4.3 Values of frictional factor and pressure drop

Parameter	**Day1**	**Day2**	**Day3**	**Day4**
Mass flow rate (kg/s)	0.0175	0.0175	0.0098	0.0098
Frictional factor (dimensionless)	0.0131	0.0131	0.0144	0.0144
Pressure drop (Pa)	0.4750	0.4750	0.1645	0.1645

4.4.2.3 Collector factors and overall heat loss coefficients

The variation of collector factors (FP and FR) and total loss coefficient are shown in *Fig. 4.7***.** The average collector efficiency factor (FP) on each day was varied from 0.90 to 0.96 between day 1 and day 4. The average collector heat removal factor (FR) on each day was varied from 0.53 to 0.75 between day 1 and day 4. The average total loss coefficient on each day was varied from 4.8 W/m^{2}K to 6.3 W/m^{2}K between day 1 and day 4. It is observed that as the flow rate increases, the collector factors (FP and FR) are also found to increase. The total loss coefficient is inversely proportional to the collector factors (FP and FR). Thus, as the flow rate increases the total loss coefficient decreases. Priyam and Chand, (2016) reported a similar behaviour in a SAH, having wavy finned artificial roughness element.

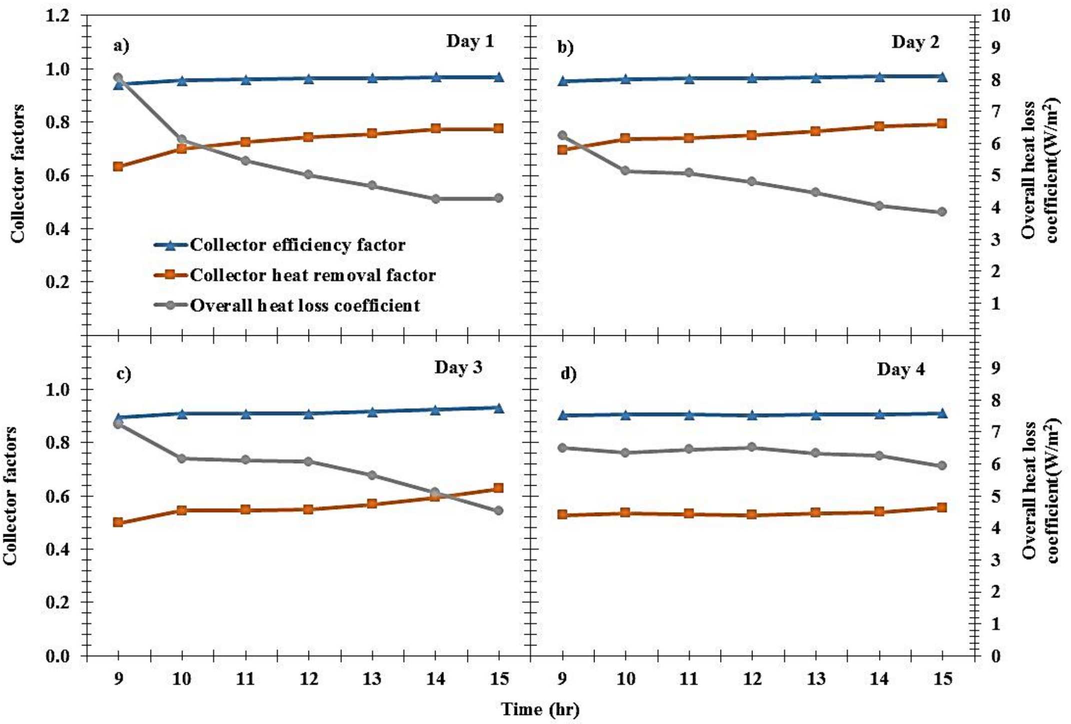

Fig. 4.7 Variations in collector factors and overall heat loss coefficient with time

4.4.3 Effect of varied arc ribs arrangement on energy conversion performance

4.4.3.1 Mean absorber plate temperature and fluid (air) temperature: Variations along the length of the SAH duct

Figs. 4.8 and *4.9,* represent the average temperature variation of air inside the duct and absorber plate measured between x= 0.01 m and x= 2 m along the length of the SAH at different flow rates (Day 1 and 2 - 0.0175 kg/s; Day 3 and 4 - 0.0098 kg/s). The maximum average absorber plate temperature of 356.3 K and air temperature of 336.7 K were achieved at 2 m length (0.0098 kg/s) of the SAH on day 4. The temperature drop between the absorber plate and air reduces along the length of the plate. It is observed that the temperature difference between the absorber plate and the air is higher at the inlet section between x= 0.01 m to 0.5 m of SAH having a fixed arc rib. The temperature difference reduces significantly between x = 0.5 m and 2 m of the SAH having variable arc rib arrangement. It is observed that at a flow rate of 0.0098 kg/s on day 4 at the inlet (x=0.01 m), the temperature drop between plate and air was 42.1°C and reduced to 19.6°C at the outlet (x=2 m) due to variable arc ribbed wire configuration.

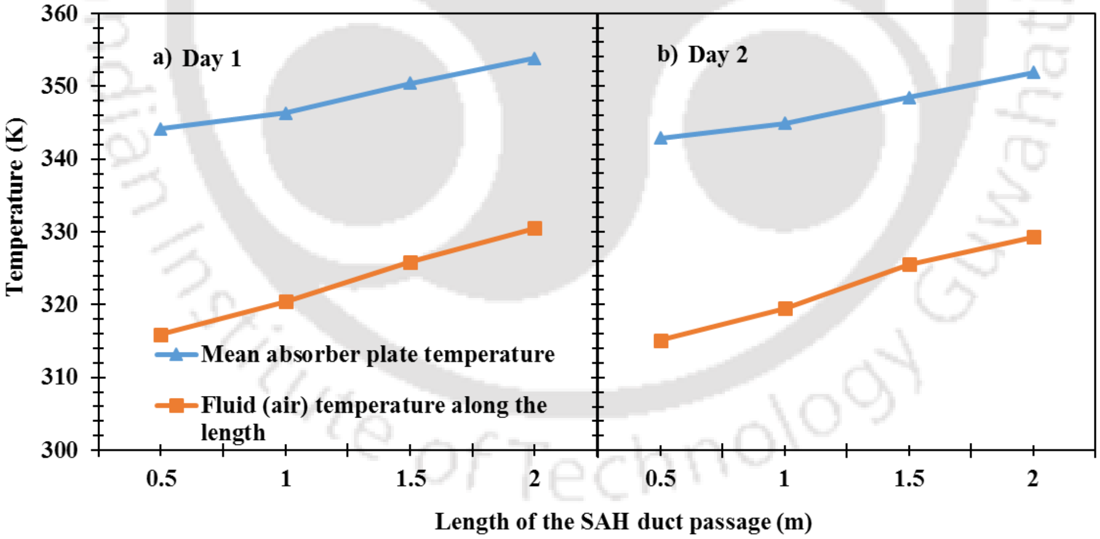

Fig. 4.8 Variations in mean absorber plate temperature and fluid (air) temperature along the length for 0.0175 kg/s air flow rate

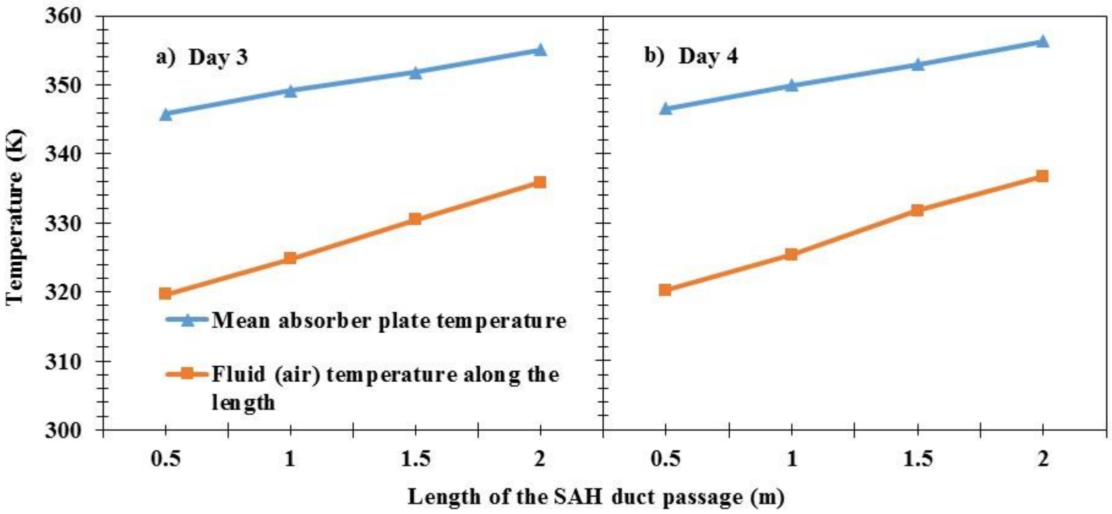

Fig. 4.9 Variations in mean absorber plate temperature and fluid (air) temperature along the length for 0.0098 kg/s air flow rate

4.4.3.2 Mean absorber plate temperature and hot air temperature at SAH outlet: Hourly variations

Figs. 4.10 and *4.11* show the variations in average absorber plate and outlet air temperature of the SAH at various flow rates. The average outlet temperature was in the range of 313.6 K to 335.9 K at a flow rate of 0.0175 kg/s. At a flow rate of 0.0098 kg/s' the air temperature was varied between 316.1 K and 341.5 K. The maximum average absorber plate temperature (363.3 K) was achieved at a flow rate of 0.0098 kg/s on day 3 at 11:00 hr and the corresponding outlet air temperature was 341.3 K. The average outlet air temperature on each day was observed as 329.4 K (day 1), 328.1 K (day 2), 332.3 K (day 3) and 333.5 K (day 4). At low flow rates (0.0098 kg/s - day 3 and day 4), the heat transfer from the absorber plate to air is high. Thus, the average outlet air temperature was higher at low flow rate (day 3 and 4).

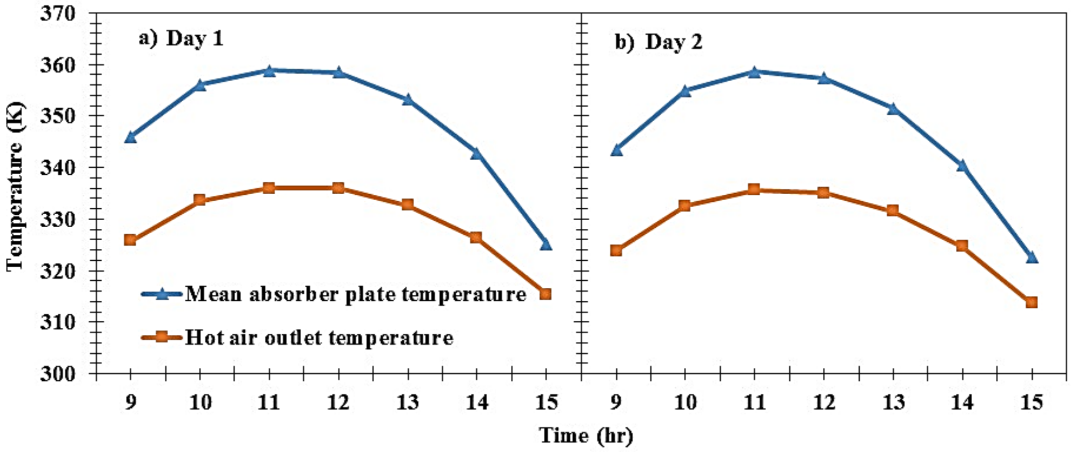

Fig. 4.10 Variations in mean absorber plate temperature and hot air outlet temperature for 0.0175 kg/s air flow rate with time

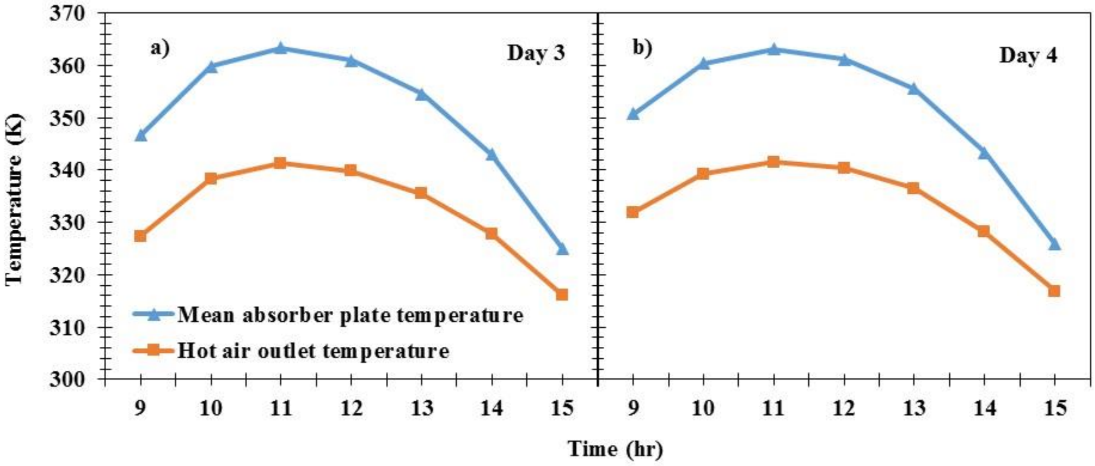

Fig. 4.11 Variations in mean absorber plate temperature and hot air outlet temperature for 0.0098 kg/s air flow rate with time

4.4.3.3 Hourly variations in inlet and outlet temperature of the air

Figs. 4.12 and *4.13*, show the variations in inlet and outlet temperatures of the SAH at various flow rates. It is observed that the average temperature drop between the inlet and outlet on each day was 298.6 K (day 1), 299.5 K (day 2), 304 K (day 3), and 304.6 K (day 4). During peak sunshine hours between 10:00 hr and 12:00 hr, the average outlet temperature from the SAH was in the range of 334.4 K and 340.3 K between day 1 and day 4. Kant et al., (2016) mentioned that the allowable temperature for drying of various agricultural products lies between 313 K and 343 K. The proposed SAH's outlet temperature provides a favourable temperature to dry the various agricultural and food products and hence can be integrated with various types of solar dryers.

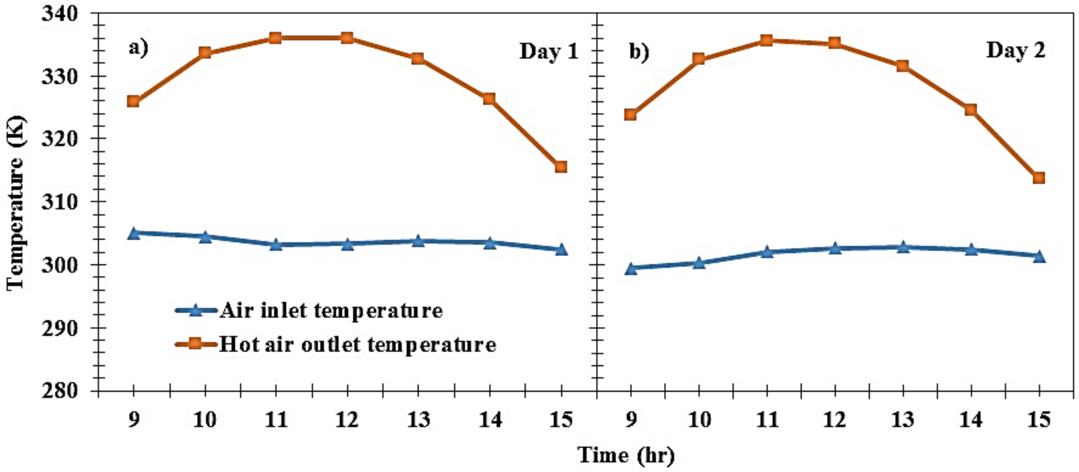

Fig. 4.12 Variations in air inlet and hot air outlet temperature for 0.0175 kg/s air flow rate with time

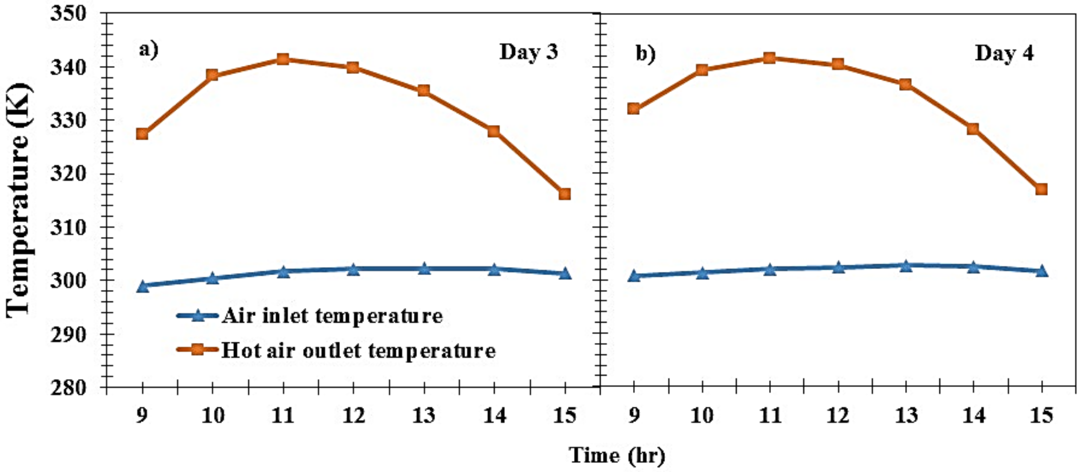

Fig. 4.13 Variations in air inlet and hot air outlet temperature for 0.0098 kg/s air flow rate with time

4.4.3.4 Hourly variation in stagnation layer, glazing, and bottom plate temperature

Figs. 4.14 and *4.15***,** show the variations in average stagnation, glazing, and the SAH's bottom plate temperatures at various flow rates. The average stagnation temperature in each day was varied from 338.9 K to 342.9 K between day 1 and day 4. The average bottom temperature in each day was in the range of 326.7 K to 334.8 K between day 1 and day 4. The average glazing temperature in each day was in the range of 320.5 K to 321.7 K between day 1 and day 4. It is observed that the average stagnation temperature is higher than the bottom plate temperature, followed by glazing temperature. In the case of stagnation temperature, the air present in between the glazing and absorber plate is stagnant and it absorbed solar intensity continuously through the glazing and reported maximum temperature value. The air flowing inside the duct absorbed heat energy from the absorber and bottom plate and hence the bottom plate temperature is lower than stagnation temperature. The heat loss occurring from the glazing to the ambient is higher and hence glazing temperature is lower than bottom and stagnation temperature.

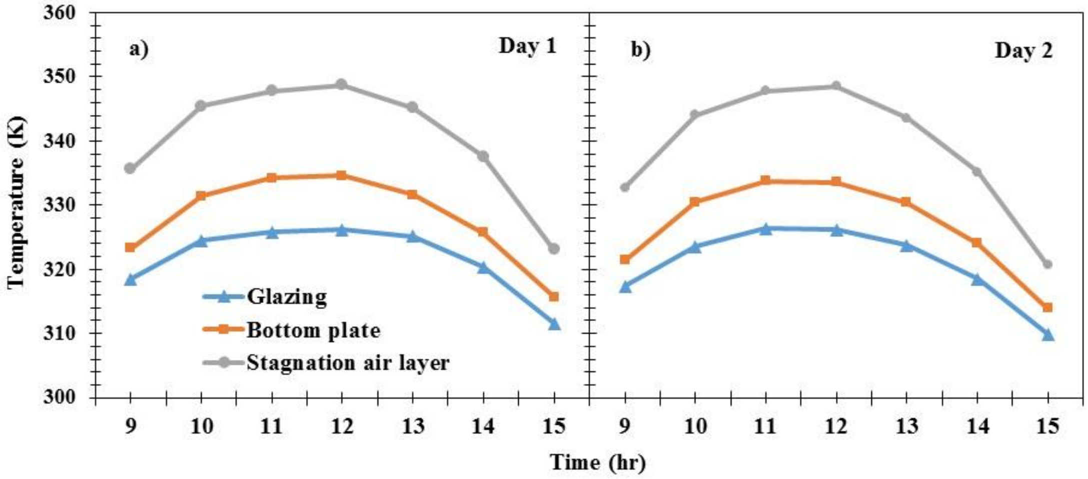

Fig. 4.14 Hourly variations in glazing, bottom plate and stagnation air layer temperature for 0.0175 kg/s air flow rate with time

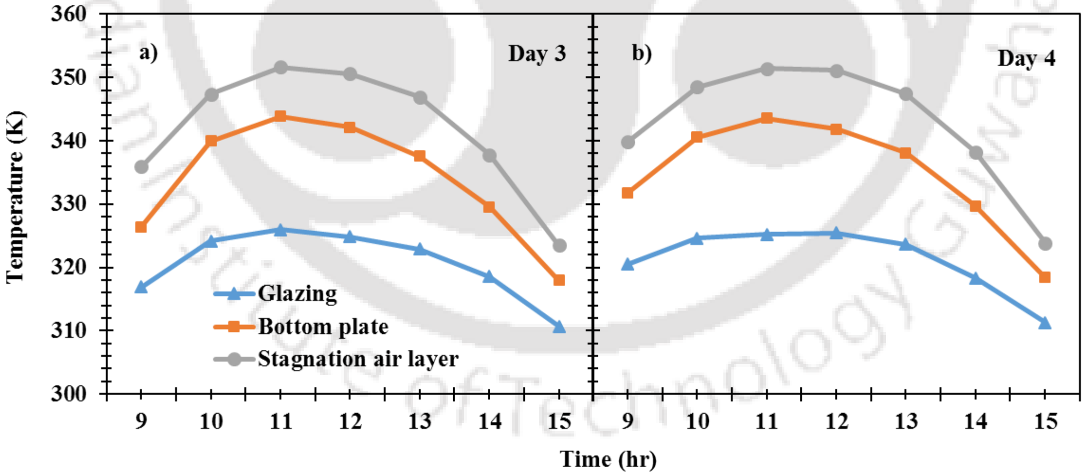

Fig. 4.15 Hourly variations in glazing, bottom plate and stagnation air layer temperature for 0.098 kg/s air flow rate with time

4.4.3.5 Thermal efficiency: Hourly variations

Fig. 4.16 shows the variation in SAH's thermal efficiency against time at various flow rates. The average efficiency (η_{th}) on each day was observed to be 48.8 % (day 1), 52.0 % (day 2), 35.0 % (day 3), 33.2 % (day 4). The thermal efficiency was observed to be maximum at a high mass flow rate. As the flow rate was increased from 0.0098 kg/s to 0.0175 kg/s, the average thermal efficiency increased by 47.8 % (34.1 % - 0.0098 kg/s and 50.4 % - 0.0175 kg/s). The solar radiation and thermal efficiency are inversely proportional, and at high flow rates, the heat transfer rate is higher and results in increasing the system's efficiency Heydari and Mesgarpour, (2018). It is observed that the thermal efficiency was high during the low solar radiation period, and a similar phenomenon is reported by Rabha et al., (2017) and Fudholi et al., (2015).

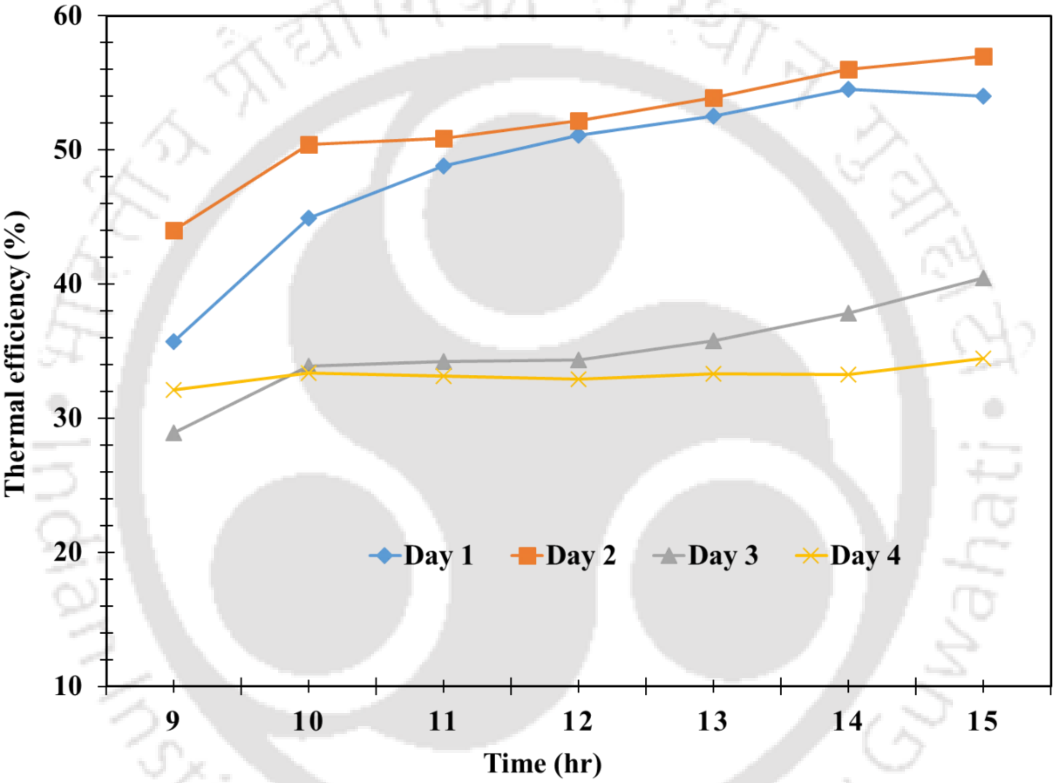

Fig. 4.16 Variations in thermal efficiency with time

4.4.3.6 Comparison of thermal efficiency: Varied arc ribs configurations with different other rib configurations

Significance of Varied Arc Ribs: Fig.4.17 shows the superior thermal efficiency of the Variable Arc Ribbed model, which achieves an efficiency of 50.4% at a notably low mass flow rate of 0.0175 kg/s. This is particularly significant when compared to other rib configurations that fail to reach similar efficiencies even at higher flow rates. The copper wire in the varied arc ribs serves as a thermal conductor and induces turbulence, thereby contributing to this elevated efficiency.

Convective Heat Transfer: One of the key insights from Fig. 4.17 is the role of turbulent flow in enhancing the convective heat transfer coefficient. This is a pivotal factor for efficient heat exchange and is less prominent in traditional models like Longitudinal Fins, which are more conducive to laminar flow.

Thermal Resistance and Fluid Dynamics: Fig. 4.17 also highlights the minimized thermal resistance in the Variable Arc Ribbed model, which facilitates efficient heat transfer. This is in stark contrast to models like V Corrugated Fins, where the intricate geometry complicates fluid dynamics and increases thermal resistance.

Material Selection and Heat Conservation: The choice of copper wire in the Variable Arc Ribbed model likely contributes to its superior thermal conductivity, thereby enhancing heat transfer rates. This is unlike PCM Models where latent heat storage is suboptimally utilized.

Optimized Geometry: The Variable Arc Ribbed model is designed to have an ideal surface area-to-volume ratio, which is crucial for maximizing heat transfer while being cost-effective in terms of material usage.

Implications for Future Research: The findings from Fig. 4.17 is not only set a new standard in thermal efficiency but also provide a compelling direction for future research. The performance of the Variable Arc Ribbed model highlights the limitations of existing models and suggests that an optimal balance of design complexity and thermal performance is achievable.

In summary, Figure 4.17 serves as a pivotal point of discussion in the thesis, offering a nuanced understanding of the factors contributing to the superior thermal efficiency of the Variable Arc Ribbed model.

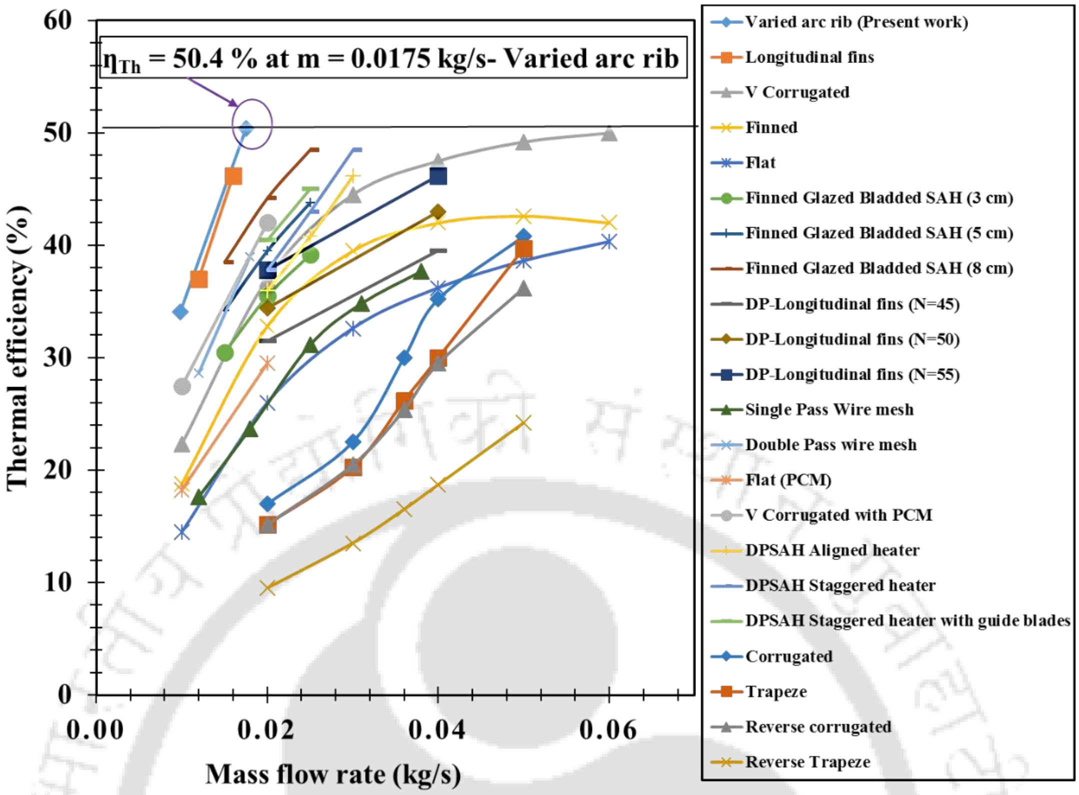

Fig. 4.17 Comparison of thermal efficiency for varied arc ribs with different other rib configurations at different mass flow rate of air

Table 4.4 Comparison of thermal efficiency of present model with various fin design

Reference	Fin model	Mass flow rate (kg/s)	Average Thermal efficiency (%)
(Present work) Sureandhar et al., (2022)	Variable arc ribbed	0.0098	34.1
		0.0175	50.4
Chabane et al., (2014)	Longitudinal fins	0.012	37.0
		0.016	46.2
Kabeel et al., (2016a)	V corrugated	0.01	22.3
		0.02	37
		0.03	44.5
		0.04	47.5
		0.05	49.2
		0.06	50
	Finned plate	0.01	18.8
		0.02	32.8
		0.03	39.5
		0.04	42
		0.05	42.6
		0.06	42

	Flat plate	0.01	14.5
		0.02	26
		0.03	32.6
		0.04	36.2
		0.05	38.6
		0.06	40.3
Kabeel et al., (2018)	Finned glazed bladed (FGBSAH 3cm)	0.015	30.5
		0.02	35.5
		0.025	39.2
	Finned glazed bladed (FGBSAH 5cm)	0.015	34.2
		0.02	39.5
		0.025	43.8
	Finned glazed bladed (FGBSAH 8cm)	0.015	38.5
		0.02	44.2
		0.025	48.5
Naphon, (2005)	Double pass SAH longitudinal fins (N45)	0.02	31.5
		0.04	39.5
	Double pass SAH longitudinal fins (N50)	0.02	34.4
		0.04	43
	Double pass SAH longitudinal fins (N55)	0.02	37.8
		0.04	46.2
Aldabbagh et al., (2010)	Single pass wire mesh	0.012	17.6
		0.018	23.7
		0.025	31.1
		0.031	34.8
		0.038	37.7
	Double pass wire mesh	0.012	28.7
		0.018	38.9
Kabeel et al., (2016b)	Flat PCM	0.01	18.2
		0.02	29.5
	V corrugated with PCM	0.01	27.2
		0.02	42
Abdullah et al., (2018)	DPSAH Aligned heater	0.02	36.0
		0.025	40.8
		0.03	46.2
	DPSAH Staggered heater	0.02	37.8
		0.025	43
		0.03	48.5
	DPSAH Staggered heater with guide blades	0.02	40.5
		0.025	45
Benli, (2013**)**	Corrugated	0.02	17
		0.03	22.5
		0.036	30
		0.04	35.2
		0.05	40.8
	Trapeze	0.02	15.2

		0.03	20.3
		0.036	26.2
		0.04	30
		0.05	39.7
	Reverse corrugated	0.02	15.2
		0.03	20.5
		0.036	25.4
		0.04	29.5
		0.05	36.2
	Reverse trapeze	0.02	9.5
		0.03	13.5
		0.036	16.5
		0.04	18.7
		0.05	24.2

4.4.3.7 Effect of varied e/D_e ratio on thermal efficiency: Variations along the length of the SAH duct

The variation in thermal efficiency for different e/D_e ratio along the length of the varied arc ribs SAH is shown in *Fig. 4.18.* From the literature, it is observed that the thermal efficiency reduces along the length of SAH [Choudhury et al., (1995); Ong, (1995); Saini and Saini, (1997); Youcef-Ali and Desmons, (2006); Zhu et al., (2019)]. In the proposed SAH, the thermal efficiency was found to reduce significantly along the length from x= 0 to x= 1 m and then increases after x = 1 to 1.5m and then reduces between x = 1.5 m to 2m. The SAH has an e/D_{e1} of 0.0408 till x= 0.5 m and an e/D_{e2} of 0.0510 from x =0.5 to 2 m. The variable arc rib fin arrangement assists in reducing the temperature drop between air and absorber plate significantly and further the thermal efficiency is observed to increase in the section between x = 1 to x = 2m having higher e/D_{e2} value.

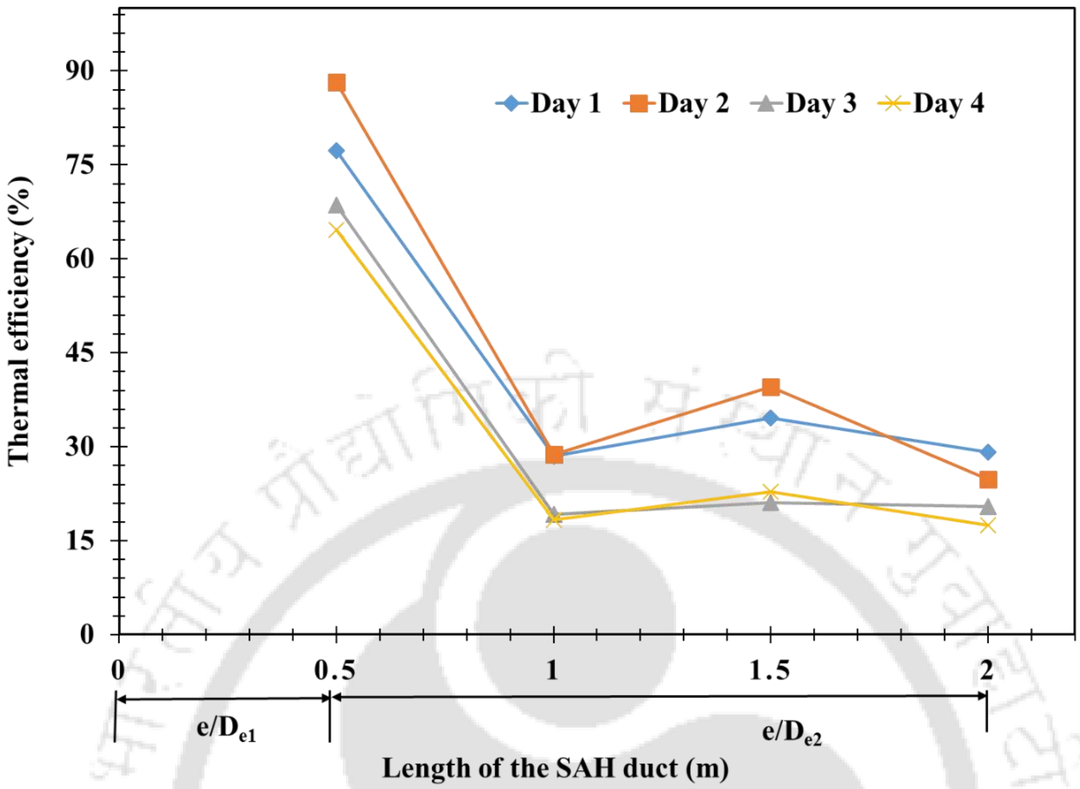

Fig. 4.18 Variations in thermal efficiency along the length of the SAH duct air flow passage

4.4.3.8 Effective efficiency: Hourly variations

Fig. 4.19 shows the variation in the SAH's effective efficiency against time at various flow rates. The average efficiency (η_{eff}) on each day was observed to be 48.2 % (day 1), 51.4 % (day 2), 34.6 % (day 3), 32.8 % (day 4). The efficiency (η_{eff}) was observed to be maximum at a high mass flow rate. As the flow rate was increased from 0.0098 kg/s to 0.0175 kg/s the average efficiency (η_{eff}) was increased by 47.7 % (33.7 % - 0.0098 kg/s; and 49.8 % - 0.0175 kg/s). It is observed that the reported effective and thermal efficiency are similar because the proposed variable arc rib SAH is operated in a lower flow rate. From the literature, it is observed that at low flow rate, the difference between thermal and effective efficiency is minimal [Bhushan and Singh, (2012); Chand and Chand, (2018); Gupta and Kaushik, (2009); Kumar et al., (2015); Mittal et al., (2007); Singh et al., (2011)].

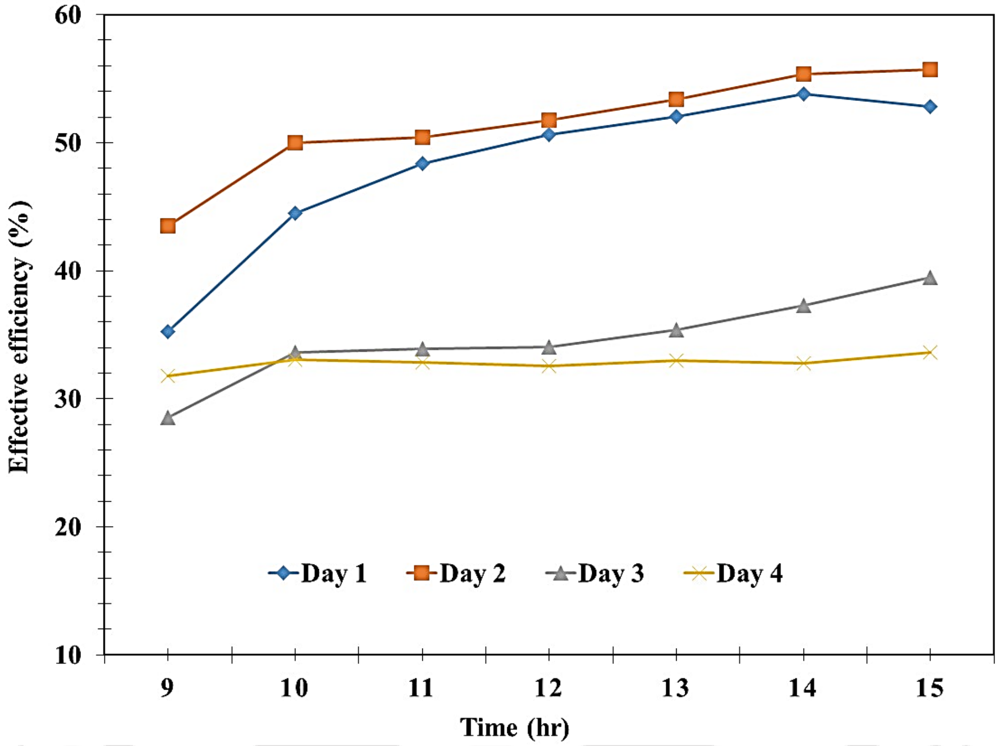

Fig. 4.19 Variations in effective efficiency with time

4.4.4 Exergy analysis of varied arc ribs embedment in SAH

4.4.4.1 Exergy efficiency: Hourly variations

Fig. 4.20 shows the variation of the SAH's exergy efficiency against time at various flow rates. The efficiency (η_{ex}) was varied between 1.1 % and 2.8 % at a flow rate of 0.0175 kg/s. At a flow rate of 0.0098 kg/s, the efficiency (η_{ex}) was varied from 0.8 % to 2.2 %. The average efficiency (η_{ex}) on each day was observed to be 2.0 % (day 1), 2.2 % (day 2), 1.7 % (day 3), 1.7 % (day 4). The efficiency (η_{ex}) was observed to be maximum at a high mass flow rate. As the flow rate was increased from 0.0098 kg/s to 0.0175 kg/s, the average efficiency (η_{ex}) was increased by 23.8 % (1.7 % - 0.0098 kg/s; and 2.1 % - 0.0175 kg/s). During the peak sunshine period (11:00 hr), the SAH reported maximum exergy efficiency of 2.82 %.

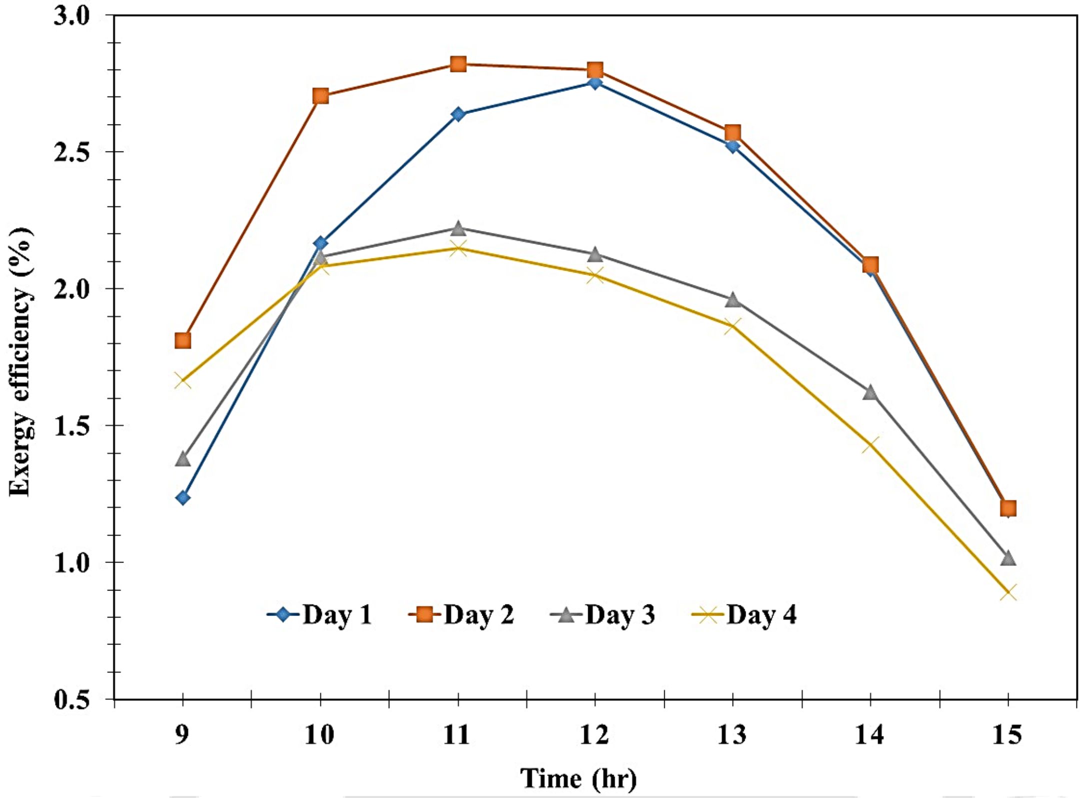

Fig. 4.20 Variations in exergy efficiency with time

4.4.4.2 Study on various components of exergy losses

The detailed study on exergy losses in the system for consecutive four days were conducted (Phu et al., 2020). The various exergy losses occurring during the SAH system's interaction with source (Sun) and surroundings (environment) are due to: (a) glazing (optical losses), (b) absorption phenomena (absorption of solar radiation by the absorber plate), (c) convective and radiation phenomena (convective and radiative heat transfer from absorber plate to environment), (d) heat transfer from absorber plate to working fluid, and (e) friction loss.

4.4.4.2.1 Exergy loss components: Daily average variations

Fig. 4.21, represents daily average variation of exergy loss components for all four days with two different mass flow rates (Day 1 and 2 - 0.0175 kg/s; Day 3 and 4 - 0.0098 kg/s). The variation of five different ways in which exergy loss incurs are average variations during 09:00 hrs to 15:00 hrs of operation. Since exergy is associated with SAH system, Source (Sun) and Surroundings (environment), the mass flow rate of air doesn't have any significant effect. The effect of exergetic performance of FAR SAH was already performed by Sahu and Prasad,(2016) for the Reynolds number range (4,000-36,000) and found that, mass flow rate doesn't have any significant effect. Surface area of the collector (absorber) plays a vital role in determining the exergetic performance of the SAH.

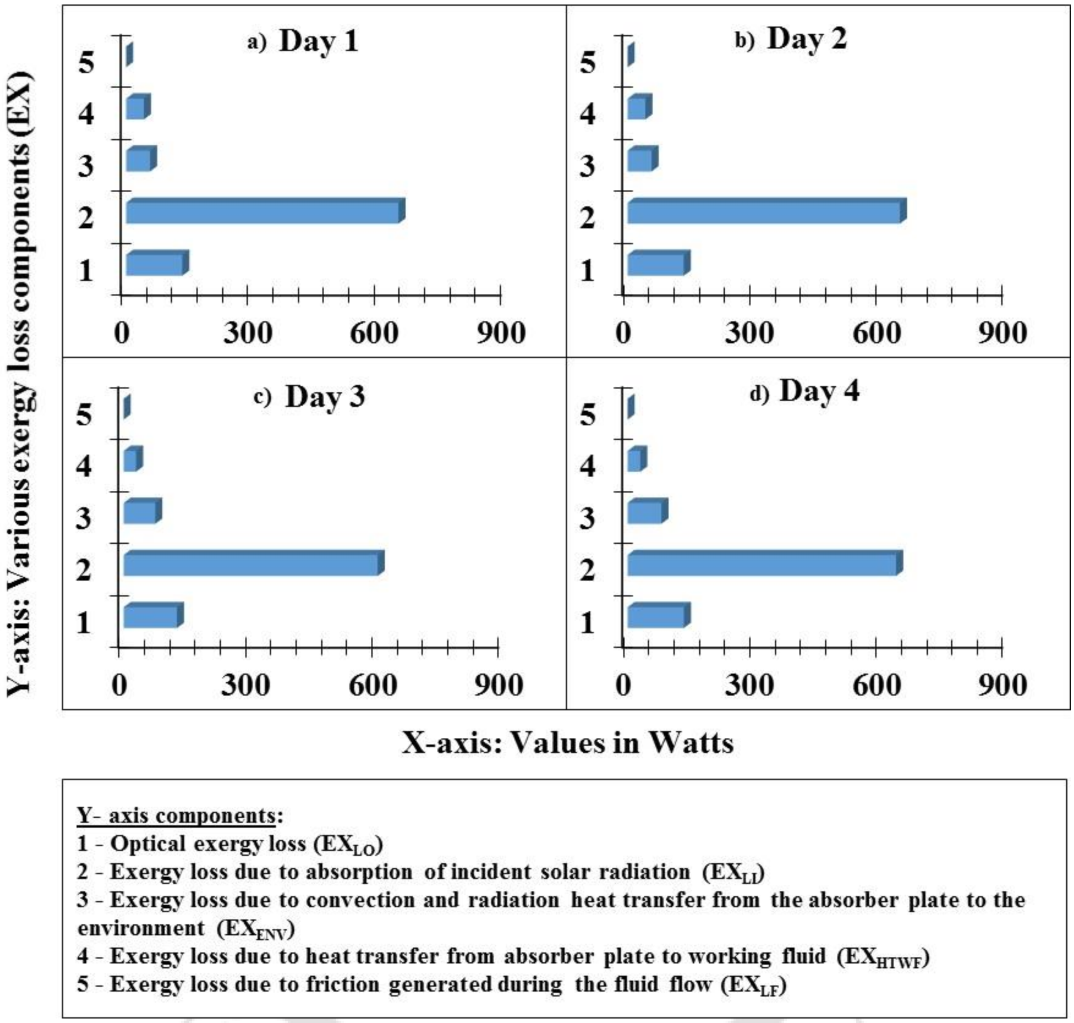

Fig. 4.21 Daily average variations in exergy loss components of VARSAH

For all consecutive four days, the major exergy loss incurs mainly due to absorption of solar radiation by the absorber plate and optical glazing which comprises of around 89% of the total exergy loss. The daily average exergy loss due to absorption of solar radiation for the consecutive four days were 644 W (day 1), 620 W (day 2), 601 W (day 3) and 635 W (day 4) respectively. The daily average exergy loss due to optical glazing (E_{LO}) in SAH system was observed as 133 W (day 1), 128 W (day 2), 126 W (day 3) and 133 W for (day 4) respectively, which was the second maximum exergy loss in the system.

The exergy loss due to convection and radiation heat transfer from the absorber plate to environment and loss due to heat transfer from the absorber plate to heat transfer fluid (air) comprises around 10% of the total exergy losses. The variation of exergy loss due to convective and radiative heat transfer from absorber plate to environment for the consecutive four days were 57 W (day 1), 53 W (day 2), 75 W (day 3), 80 W (day 4) respectively. The exergy loss due to heat transfer from absorber plate to the working fluid (air) flow was observed as 42 W (day 1), 44 W (day 2), 30 W (day 3) and 30 W (day 4) respectively for the consecutive four days. The exergy loss due to friction generated (blower power) was very less, and negligible.

4.4.4.2.2 Exergy loss components: Hourly variations

Fig. 4.22, represents the hourly variation of different exergy loss components in SAH system for all four consecutive days with two different mass flow rates (Day 1 and 2 - 0.0175 kg/s; Day 3 and 4 - 0.0098 kg/s) of operation. From the results, it is observed that the losses are higher during peak sunshine hours of the operation. Hence solar insolation and absorber surface area are the two main factors determines the exergetic performance of the SAH than mass flow rate of operation.

The maximum exergy loss incurred due to absorption of solar radiation by the absorber plate which was contributed around 73% - 75% of total exergy loss. It varied from 313.61 W to786.71 W for day 1, 771 W to 283.5 W for day 2, 748.55 W to 266.95 W for day 3 and 773 W to 322 W for day 4 respectively. Next optical exergy loss which contributed around 15%. This was varied from 166.5 W to 59.8 W for day 1, 163.7 W to 53.8 W for day 2, 161.4 W to 51.1 W for day 3 and 166.4 W to 61.7 W for day 4 respectively.

Nearly 11% of exergy loss incurred due to convective and radiative heat transfer from absorber plate to environment and heat transfer from absorber plate to working fluid. The exergy losses due to convection and radiation heat transfer from the absorber plate to the environment in the SAH system was varied from 80.3 W to 11.7 W for day 1, 77.1 W to 9.27 W for day 2, 109.2 W to 13.5 W for day 3, 113.7 W to 18.2 W for day 4 respectively. The exergy loss due to heat transfer from absorber plate to the working fluid (air) flow in the SAH system varied as 60.3 W to 11.3 W for day 1, 62.5 W to 10.1 W for day 2, 42.5 W to 7.2 W for day 3, 42.1 W to 7.5 W for day 4 respectively. The exergy loss due to friction was very less and negligible.

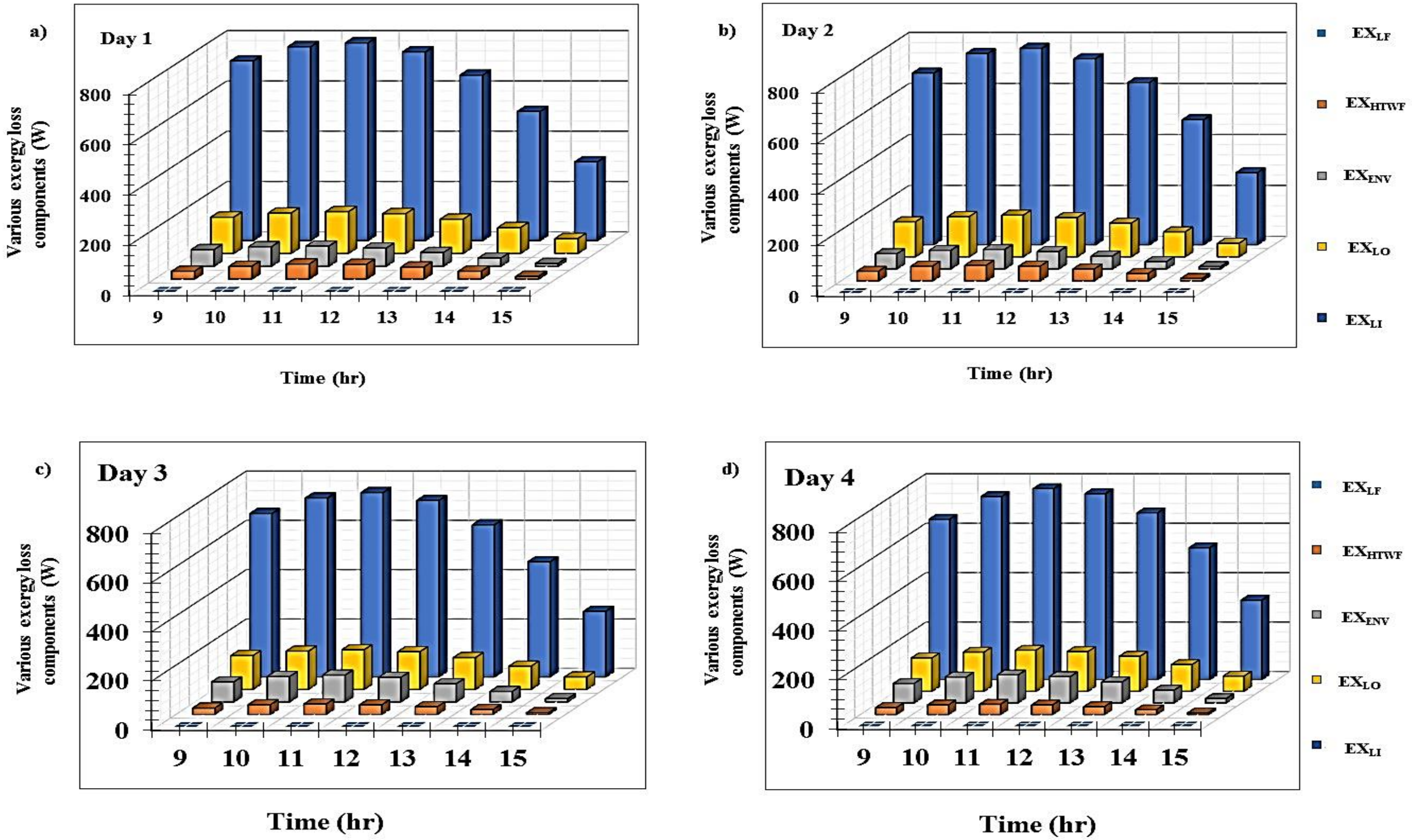

Fig. 4.22 Hourly variations in exergy loss components for VARSAH

4.4.5 Entropy analysis of varied arc ribs embedded SAH

4.4.5.1 Entropy generation due to heat transfer

In *Fig. 4.23***,** with respect to time, a comparison of entropy generation due to heat transfer for two different mass flow rates (day 1 and 2) with 0.01758 kg/s and (day 3 and 4) with 0.00985 kg/s was performed experimentally. It is observed that by increasing the mass flow rate from 0.00985 kg/s to 0.01758 kg/s, the entropy generation due to heat transfer was found to increase. The variation based on time, for day 1 operation (0.740 W/K to 1.812 W/K), for day 2 operation (0.706 W/K to 1.861 W/K) operating with 0.01758 kg/s. Similarly, for day 3 (0.473 W/K to 1.22 W/K) and for day 4 (0.485 W/K to 1.218 W/K) operating mass flow rate of 0.00985 kg/s respectively. The maximum $(\Delta S)_{HT}$ of 1.861 W/K achieved for 0.01758 kg/s during day2 at 11 AM. The average value of $(\Delta S)_{HT}$ for consecutive four days were 1.431 W/K, 1.485 W/K, 0.966 W/K and 0.982 W/K respectively. From experiments, it was observed that, the entropy generation due to heat transfer increases with increase in heat source energy flux input to the system and mass flow rate.

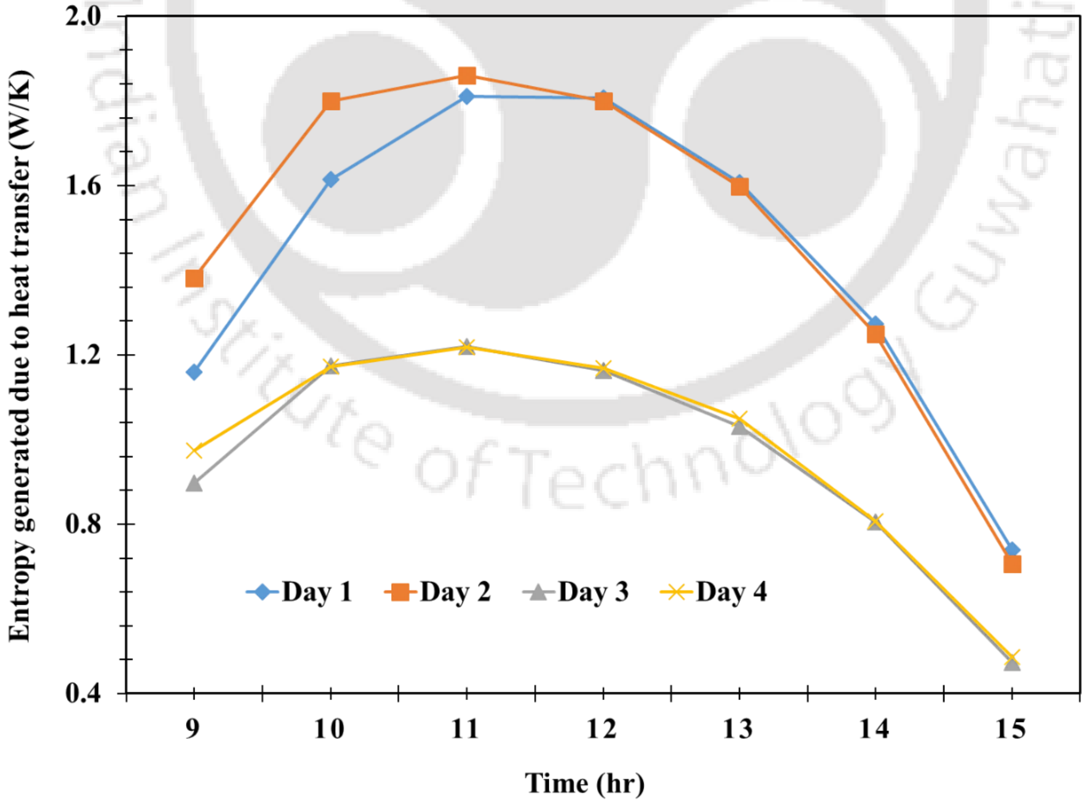

Fig. 4.23 Variations in entropy generation due to heat transfer with time

4.4.5.2 Entropy generation due to pressure drop

In *Fig. 4.24*, for the consecutive four days, with respect to time from 09:00 hrs to 15:00 hrs, the variation of entropy generated due to pressure drop inside the SAH duct studied experimentally. It is observed that, entropy generated due to pressure drop varies directly proportional to mass flow rate, because the increase in mass flow rate from 0.00985 kg/s to 0.01758 kg/s leads to increase the value of entropy generation by pressure drop. The variation based on the time, for day 1 (2.44 e^{-5} W/K to 2.46 e^{-5} W/K), for day 2 (2.46 e^{-5} W/K to 2.48 e^{-5} W/K) operating with 0.01758 kg/s. Similarly, for day 3 (4.78 e^{-6} W/K to 4.83 e^{-6} W/K) and for day 4 (4.77 e^{-6} W/K to 4.79 e^{-6} W/K) operated with 0.00985 kg/s respectively. The average value of entropy generation due to pressure drop for the consecutive days are 2.45 e^{-5} W/K, 2.47 e^{-5} W/K, 4.80 e^{-6} W/K and 4.78 e^{-6} W/K respectively. The maximum $(\Delta S)_{\Delta P}$ of 2.489 e^{-5} W/K achieved for air flow rate of 0.01758 kg/s operation. It is seen that, the entropy generation due to pressure drop depends only on mass flow rate, independent of the heat flux of the source $(\Delta S)_{\Delta P}$.

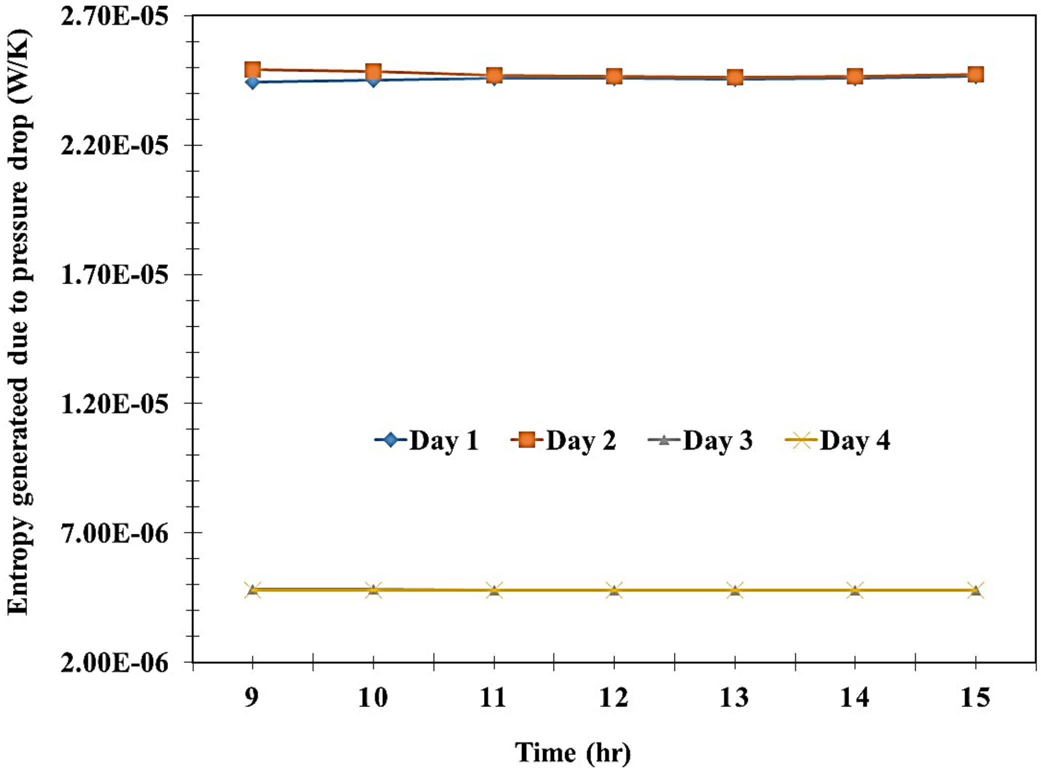

Fig. 4.24 Variations in entropy generation due to pressure drop with time

4.4.5.3 Total entropy generation

In *Fig. 4.25***,** the experimental results for the variation of total entropy generated during daily operation of SAH from 09:00 hrs to 15:00 hrs are and compared for all consecutive four days of operation. In this present experiment, in-equilibrium of the system occurs due to thermal and pressure difference, that drives the system to gain thermal energy. The total entropy of the system therefore comprises of entropy generation due to thermal and pressure differences with respect to surrounding condition. The total entropy content value was varied with respect to time, for day 1 (224 W to 549 W), for day 2 (213 W to 562 W) operating with 0.01758 kg/s. Similarly, for day 3 (143 W to 368 W) and for day 4 (146 W to 368 W) with flow rate of 0.00985 kg/s respectively. The average value of total entropy created were 435 W, 448 W, 291 W and 297 W respectively for consecutive four days. The maximum value of total entropy generation of 549 W generated at 11:00 hrs of 0.01758 kg/s on day 1. From, the experimental results, it was found that, both the mass flow rate and solar heat flux input to the system has greater effect on the total entropy generation. By comparing *Figs. 4.23* and *4.24*, irrespective of time and mass flow rate, always it was found that, $(\Delta S)_{HT} >> (\Delta S)_{\Delta P}$. Hence, the predominant factor affecting total entropy created was mainly due to entropy of heat transfer $\{(\Delta S)_{HT}\}$.

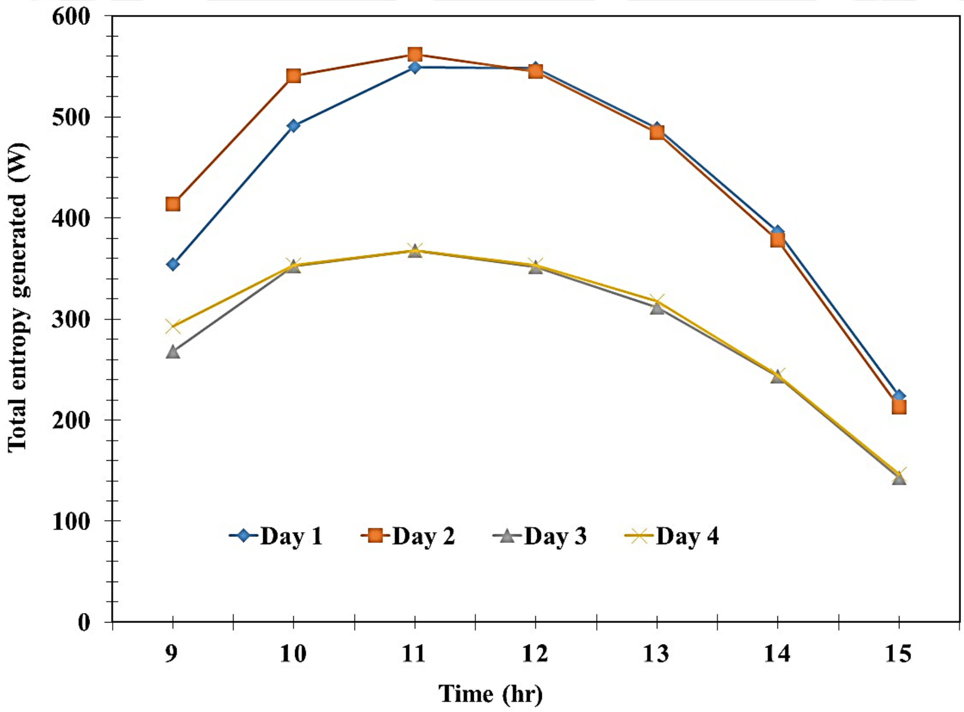

Fig. 4.25 Variations in total entropy generation with time

4.4.5.4 Bejan number

Fig. 4.26 represents the variation of Bejan number with respect to time for all four days. It was understood that Bejan number is much more sensitive to both mass flow rate and solar radiation intensity. With the increase in the mass flow rate to the system, the value of (Be) reduces. Day 1 and 2 operated with the maximum mass flow rate (0.01758 kg/s) has lesser value of (Be) which represents that with increase in mass flow rate the entropy generation due to pressure drop increases. Although, at higher mass flow rate (0.01758 kg/s), the system achieves maximum exergy efficiency, at the same time the total entropy generation was also higher, which leads to the reduction of (Be). Rise in entropy generation due to thermal difference and pressure drop are the major reason for reduction in (Be) at higher mass flow rate (0.01758 kg/s).

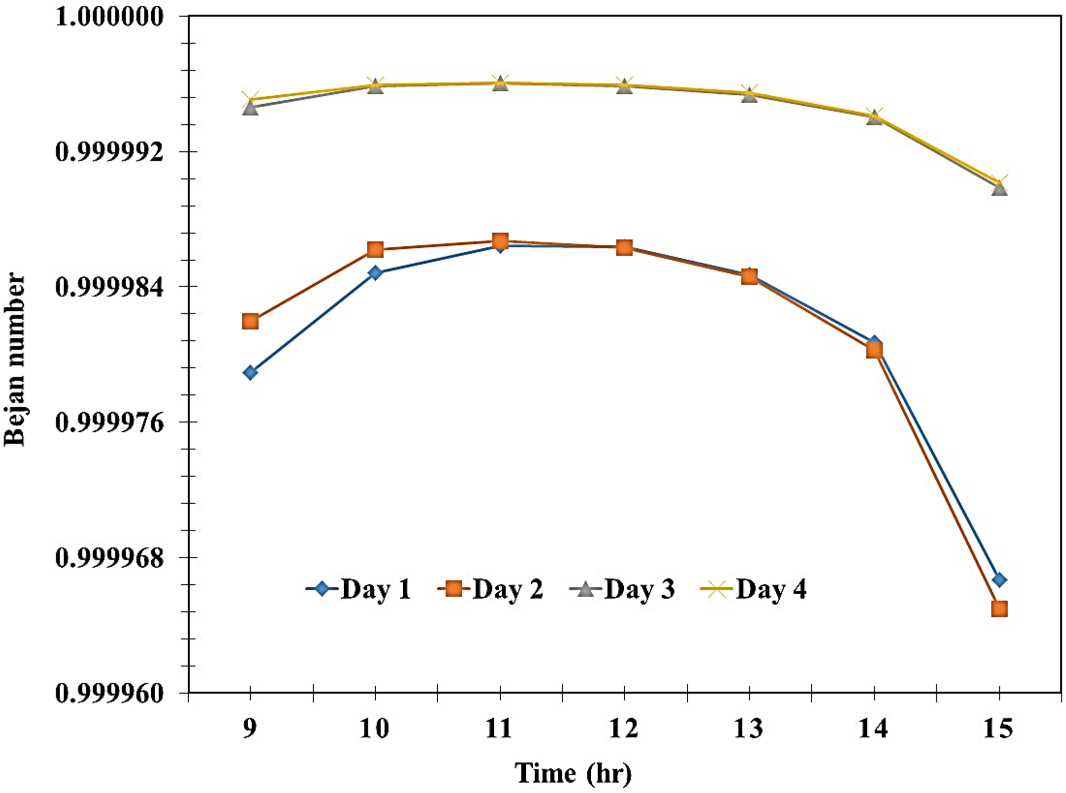

Fig. 4.26 Variations in Bejan number with time

4.4.5.5 Entropy generation number

Fig. 4.27 represents the variation of entropy generation number with respect to time for the consecutive four days of operation from 09:00 hrs to 15:00 hrs. The entropy generation number was varied for day 1 (0.346 to 0.529), day2 (0.423 to 0.559) with the flow rate of

0.01758 kg/s, also similarly for day 3 (0.276 to 0.395) and day 4 (0.306 to 0.336) of 0.0098 kg/s respectively.

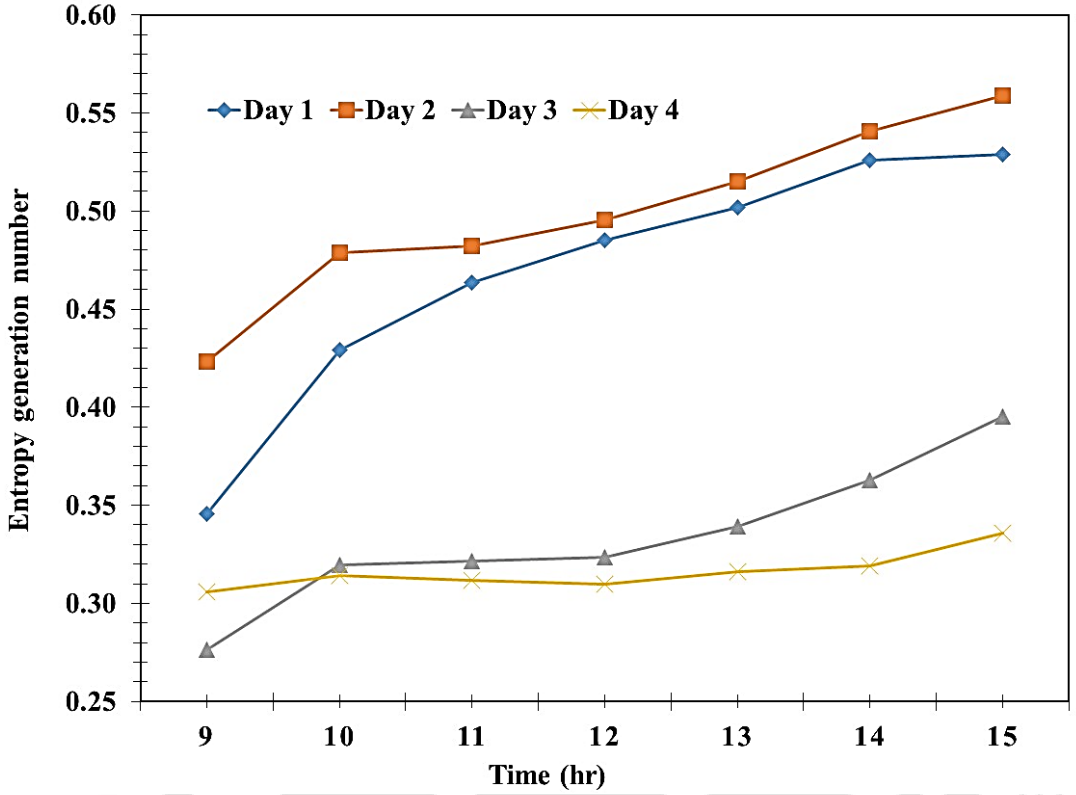

Fig. 4.27 Variations in entropy generation number with time

The maximum value of entropy generation number (0.559) was achieved during 15:00 hrs on day 2 at 0.01758 kg/s. The daily average value was varied as 0.469, 0.499, 0.334 and 0.316 for consecutive 4 days of experiment. The maximum value of entropy generation number (0.599) was achieved for 0.01758 kg/s at 15:00 hrs on day 2. From the above results, it is seen that the maximum value of the entropy generation number reached for the maximum mass flow rate condition. For all the four days at 09:00 hrs, the value of entropy generation number was comparatively less. For day 1, it was continuously raising with respect to time. For day 2, the value was minimum at 09:00 hrs, it started raising at 10:00 hrs, and then it's stable up to 11:00 hrs, later it increases after 11:00 hrs until 15:00 hrs. For day 3, the value was minimum at 09:00 hrs, then it raised at 10:00 hrs and its stable up to 12:00 hrs, again it's continuously started raising from 12:00 hrs until 15:00 hrs. For day 4, there was a constant stable value from 09:00 hrs to 14:00 hrs, later at 15:00 hrs, there was a little increase in the value.

So, therefore entropy generation number was dependent on various factors such as heat source input, system design parameters, operating conditions and environment (surroundings).

4.4.5.1 Irreversibility distribution ratio

In *Fig. 4.28***,** variation of irreversibility distribution ratio with respect to time for 0.01758 kg/s and 0.00985 kg/s plotted for the consecutive four days. From the experimental results, it is observed that the value of irreversibility distribution ratio varies for day 1 (1.3576 e^{-5} to 3.3305 e^{-5}), for day 2 (1.3264 e^{-5} to 3.5050 e^{-5}) of 0.01758 kg/s, similarly for day 3 (0.392 e^{-5} to 1.013 e^{-5}) and for day 4 (0.393 e^{-5} to 0.987 e^{-5}) of 0.00985 kg/s respectively. The minimum value of irreversibility distribution ratio represents either minimum of $(\Delta S)_{\Delta P}$ or maximum of $(\Delta S)_{HT.}$ The average value of irreversibility distribution ratio for the consecutive four days is 1.8756 e^{-5}, 1.8425 e^{-5}, 0.546 e^{-5}, 0.534 e^{-5} respectively. Calculation of irreversibility distribution ratio helps in determining the predominant type of entropy generation. By comparing the values in *Fig. 4.23* and *Fig. 4.24*, it is evident that the $(\Delta S)_{HT} >>> (\Delta S)_{\Delta P}$.

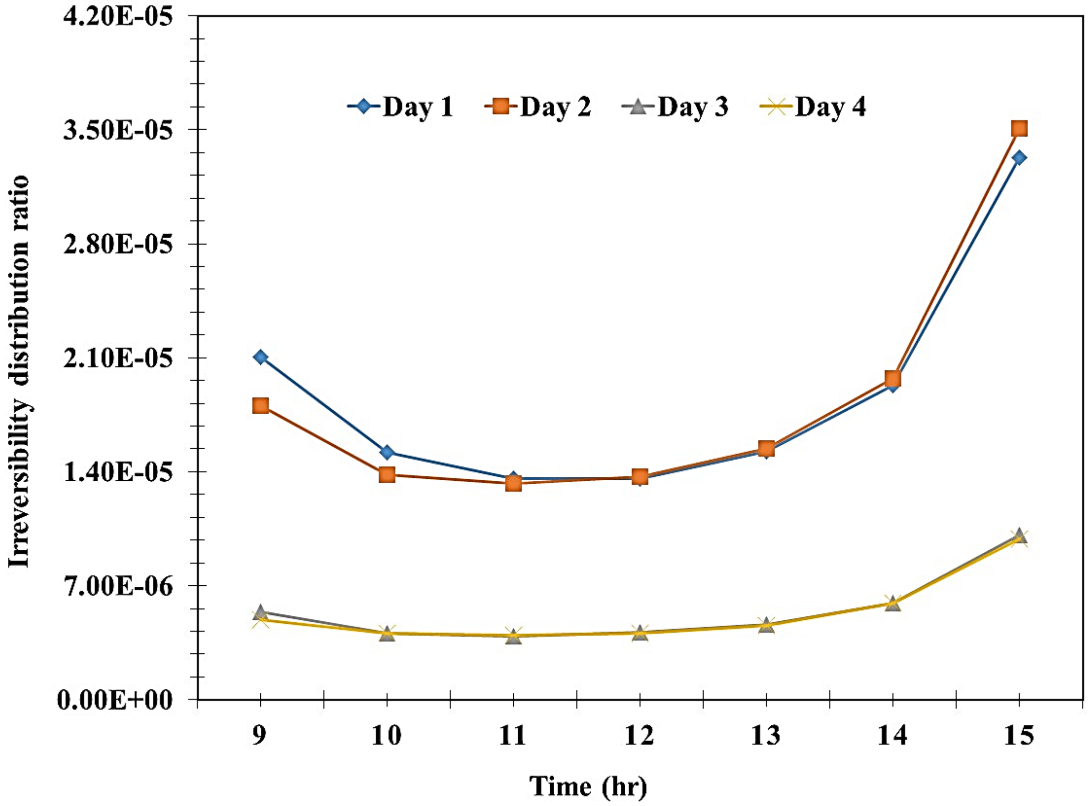

Fig. 4.28 Variations in irreversibility distribution ratio with time

4.4.6 Uncertainty Analysis of Derived Parameters

In this study, we calculate the following parameters based on experimentally measured values: (i) thermal efficiency, (ii) effective efficiency, and (iii) exergy efficiency. The uncertainties of the measured values are presented in Table 4.2. The uncertainties of the derived parameters are calculated for all three parameters as described below.

To calculate the uncertainty of the derived parameters, the following formula is used:

$$\Delta f = \sqrt{\left(\frac{\partial f}{\partial x}\Delta x\right)^2 + \left(\frac{\partial f}{\partial y}\Delta y\right)^2 + \left(\frac{\partial f}{\partial z}\Delta z\right)^2 + \ldots\ldots\ldots\ldots} \tag{4.1}$$

4.4.6.1 Uncertainty in thermal efficiency

The thermal efficiency of a solar air heater (SAH) is a measure of how effectively it converts incident solar radiation into usable heat energy. It is calculated by comparing the amount of heat energy absorbed by the SAH to the amount of solar radiation incident on the absorber plate.

There can be several sources of uncertainty in determining the thermal efficiency of a SAH. Some of these sources include:

1. Measurement errors: The accuracy of the instruments used to measure the temperature of the air and the absorber plate, as well as the flow rate of air, can introduce uncertainties in the calculation of thermal efficiency.
2. Heat losses: The SAH may experience heat losses through convection, conduction, and radiation. These losses can vary depending on factors such as insulation, wind speed, and ambient temperature. Uncertainties in estimating these heat losses can affect the accuracy of the thermal efficiency calculation.
3. Solar radiation measurement: The accuracy of the instruments used to measure solar radiation incident on the absorber plate can introduce uncertainties in the calculation of thermal efficiency. Factors such as cloud cover, shading, and the angle of incidence of the sun can affect the accuracy of these measurements.
4. Variability in operating conditions: The thermal efficiency of a SAH can depend on various operating conditions such as flow rate, temperature difference between the air and the absorber plate, and the angle of incidence of the sun. Variations in these operating conditions can introduce uncertainties in the thermal efficiency calculation.

In order to minimize uncertainties in calculating thermal efficiency, it is crucial to utilize precise measurement instruments, carefully regulate operating conditions, and account for potential heat loss sources. Furthermore, conducting multiple measurements and averaging the outcomes can decrease random errors and enhance the reliability of the thermal efficiency calculation. This study derives the uncertainty in thermal efficiency resulting from measured air temperature, velocity, and solar insolation, as shown in equation (4.2).

$$\Delta\eta_{Th} = \eta_{Th}\sqrt{\left(\frac{\Delta T}{T_O}\right)^2 + \left(\frac{\Delta T}{T_i}\right)^2 + \left(\frac{\Delta I}{I}\right)^2 + \left(\frac{\Delta m}{m}\right)^2} \tag{4.2}$$

Where

$$\eta_{Th} = \frac{Q_u}{IA_p(\tau\alpha)_e} = \frac{mC_P(T_o - T_i)}{IA_p(\tau\alpha)_e}$$

Table 4.5 Data for uncertainty analysis of thermal efficiency

S.No	Parameter	Unit	Value
1	Mass flow rate of air	Kg/s	0.0175
2	Specific heat capacity of air	J/kgK	1005
3	Hot air outlet temperature	K	340
4	Inlet air temperature	K	303
5	Solar insolation	W/m^2	720
6	Surface area of the absorber plate	m^2	2
7	Product of effective transmittance and absorptance $(\tau\alpha)_e$	-------	0.85

The calculated uncertainty for the thermal efficiency in the given experimental conditions is 0.5310 ± 0.027, which is equivalent to 5.08%. This level of uncertainty is considered acceptable for system analysis.

4.4.6.2 Uncertainty in effective efficiency

The pressure drop across the SAH duct can also contribute to the uncertainty in the effective efficiency of the system. This pressure drop is influenced by various factors such as the geometry of the duct, the flow rate of the air, and the presence of any obstructions or enhancements within the duct.

During the experimental studies, the pressure drop across the SAH duct can be measured using pressure sensors placed at different locations along the duct. However, there may be uncertainties associated with these measurements, such as the accuracy of the sensors and any potential disturbances in the flow caused by their presence.

Therefore, when evaluating the effective efficiency of the SAH system, it is important to consider the uncertainty associated with the pressure drop across the duct in addition to the uncertainty reported in the thermal efficiency. By accounting for both sources of uncertainty, a more accurate assessment of the overall performance of the SAH system can be obtained.

The derived equation of uncertainty in effective efficiency is given below

$$\Delta\eta_{eff} = \eta_{eff}\sqrt{\left(\frac{\Delta T}{T_o}\right)^2 + \left(\frac{\Delta T}{T_i}\right)^2 + \left(\frac{\Delta I}{I}\right)^2 + \left(\frac{\Delta m}{m}\right)^2 + \left(\frac{\Delta V}{V}\right)^2 + \left(\frac{\Delta P}{P_o}\right)^2 + \left(\frac{\Delta P}{P_i}\right)^2} \tag{4.3}$$

Where

$$\eta_{eff} = \frac{Q_u - \left(\frac{P_m}{C}\right)}{IA_P\left(\tau\alpha\right)_e}$$

Table 4.6 Data for uncertainty analysis of effective efficiency.

S.No	Parameter	Unit	Value
1	Mass flow rate of air	Kg/s	0.0175
2	Specific heat capacity of air	J/kgK	1005
3	Hot air outlet temperature	K	340
4	Inlet air temperature	K	303
5	Solar insolation	W/m^2	720
6	Surface area of the absorber plate	m^2	2
7	Product of effective transmittance and absorptance $(\tau\alpha)_e$	Dimensionless	0.85
8	Conversion factor (C)	Dimensionless	0.18
9	Blower power	W	2.58

The calculated uncertainty for the effective thermal efficiency in the given experimental conditions is 0.5199 ± 0.0276, which is equivalent to 5.31%. This level of uncertainty is considered acceptable for system analysis.

4.4.6.3 Uncertainty in Exergy efficiency

The uncertainty in exergy efficiency refers to the uncertainty or error associated with the calculation or measurement of the exergy efficiency of a system. Exergy efficiency is a measure of how effectively a system converts available energy into useful work, taking into account the quality of the energy. It is a more comprehensive measure than simple thermal efficiency, as it considers both the quantity and quality of energy.

Uncertainty in exergy efficiency can arise from various sources, such as measurement errors in determining the input and output energy flows, uncertainties in the thermodynamic properties of the working fluid, and assumptions or simplifications made in the analysis. These uncertainties can affect the accuracy and reliability of the exergy efficiency calculation.

To mitigate the uncertainty in exergy efficiency, it is important to carefully measure and analyse the energy flows in the system, using accurate and calibrated instruments. It is also important to account for any sources of energy loss or degradation, such as heat transfer losses, friction losses, or irreversibility, in the exergy analysis. Sensitivity analyses and error propagation techniques can also be used to assess the impact of uncertainties in the input parameters on the calculated exergy efficiency.

In summary, uncertainty in exergy efficiency is a measure of the potential error or uncertainty in the calculation or measurement of the efficiency of a system in terms of exergy. It is important to account for and minimize these uncertainties to ensure accurate and reliable assessments of the performance of energy systems.

In this system, the same source of uncertainty lies in the calculation of the effective efficiency and exergy efficiencies. The corresponding derivations to calculate these values are provided below.

$$\Delta\eta_{Ex}=\eta_{Ex}\sqrt{\left(\frac{\Delta T}{T_o}\right)^2+\left(\frac{\Delta T}{T_i}\right)^2+\left(\frac{\Delta I}{I}\right)^2+\left(\frac{\Delta m}{m}\right)^2+\left(\frac{\Delta T}{T_a}\right)^2+\left(\frac{\Delta V}{V}\right)^2+\left(\frac{\Delta P}{P_o}\right)^2+\left(\frac{\Delta P}{P_i}\right)^2}$$

(4.4)

Where

$$\eta_{Ex}=\frac{\left[mC_{Pa}\left(T_o-T_i\right)\right]-\left[\left(mC_{Pa}T_a\right)\left(\ln\left(\frac{T_o}{T_i}\right)\right)\right]-\left[\left(\frac{T_o}{T_i}\right)\left(P_m\right)\right]}{\left(I\right)\left(A_P\right)\left[1-\left(\frac{T_a}{T_{sun}}\right)\right]}$$

Table 4.7 Data for uncertainty analysis of exergy efficiency

S.No	Parameter	Unit	Value
1	Mass flow rate of air	Kg/s	0.0175
2	Specific heat capacity of air	J/kgK	1005
3	Hot air outlet temperature	K	340
4	Inlet air temperature	K	303
5	Solar insolation	W/m^2	720
6	Surface area of the absorber plate	m^2	2
7	Product of effective transmittance and absorptance $(\tau\alpha)_e$	Dimensionless	0.85
8	Conversion factor (C)	Dimensionless	0.18
9	Blower power	W	2.58

The calculated uncertainty for the exergy efficiency in the given experimental conditions is 0.02418 ± 0.000667, which is equivalent to 2.76%. This level of uncertainty is considered acceptable for system analysis.

4.5 Summary

A solar air heater having arc ribbed wire configuration was designed and tested at two different flow rates 0.0175 kg/s (day 1 and 2); 0.0098 kg/s (day 3 and 4). A solar air heater of length 2 m was embedded with arc ribbed wire of diameter 2 mm (up to 0.5 m) and 2.5 mm (0.5 m to 2 m). The temperature variation of air inside the duct and absorber plate along the length was reported. The variable arc rib assisted in utilizing maximum available energy from the absorber plate to air. The temperature difference between the absorber plate and air was reduced along the length due to variable arc ribbed wire configuration. The average outlet air temperature in a day was varied from 328.1 K to 333.5 K between day 1 and day 4. The average temperature difference between the outlet and inlet air temperature in the solar air heater was varied from 298.6 K to 304.6 K between day 1 and day 4. The thermal efficiency (50.4 %), effective (49.8 %), and exergy efficiency (2.1 %) was maximum at a high flow rate. As the flow rate increases, the collector efficiency factor and heat removal factor increase, whereas the total loss coefficient decreased. The proposed solar air heater's outlet temperature provided a favorable temperature range to dry various agricultural and food products, and hence it can be integrated with solar dryers.

Chapter 5 Economic and Environmental Evaluation

5.1 Preface

In order to assess the impact of SAH on annual energy savings, economic analysis has been performed by considering the capital cost, operational and maintenance cost, salvage value for the available sunshine hours in the life span of the operation. This economic analysis also helpful in finding the yearly useful heat gained by using solar energy, energy payback period, exergy payback period.

It's well known that solar energy is one of the cleanest energy for sustainable future. This environmental analysis will provide the solution of annual and life time CO_2 savings and carbon credits earned by utilising SAH. In this chapter, the economic and environmental analysis of fabricated VAR SAH performed based on the experimental values and the climatic condition data collected by Kalita et al., (2019) of Guwahati, Assam, India.

5.2 Solar energy potential in India

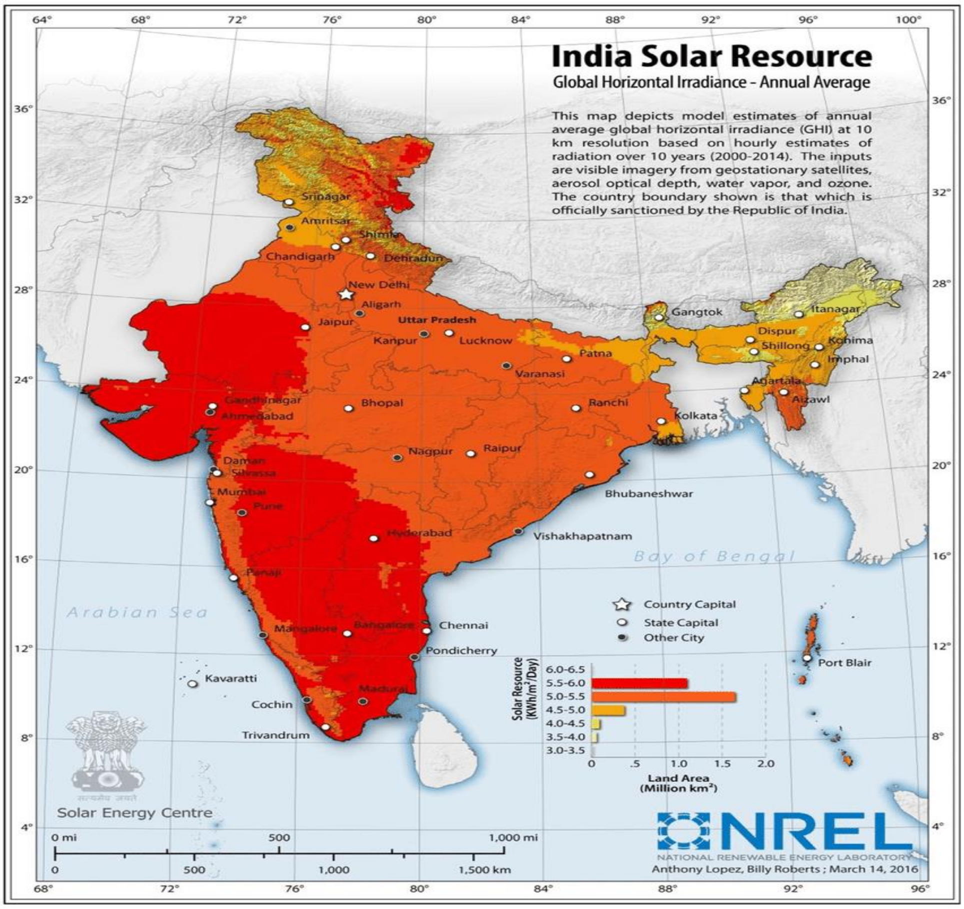

India Solar Resource

Global Horizontal Irradiance - Annual Average

This map depicts model estimates of annual average global horizontal irradiance (GHI) at 10 km resolution based on hourly estimates of radiation over 10 years (2000-2014). The inputs are visible imagery from geostationary satellites, aerosol optical depth, water vapor, and ozone. The country boundary shown is that which is officially sanctioned by the Republic of India.

Anthony Lopez, Billy Roberts ; March 14, 2016

Fig. *5.1* Solar energy potential in India

Due to the geographical locations, India has the good solar radiation potential. It was estimated that from solar energy, India can able to generate nearly 5000 trillion kW-hr / year. Sharma et al., (2012) and Jamil et al, (2016) reported that India has nearly 250 to 300 Sunny days with 2300 to 3200 sunshine hours per year with the daily average solar radiation ranging from 4 to 7 kW-hr / m^2 as given in *Fig. 5.1*.

5.3 Solar energy potential in North-Eastern states of India

Saharia and Kantatalukdar, (2014) performed energy potential resource assessment for Guwahati (26.13 °N, 91.66 °E), Assam, India. The resource assessment involves in recording the values of average solar insolation, number of sunshine hours, and ambient temperature. From the investigations, it was found that the location is most suitable for harnessing the solar radiation and utilise it for both the power generation and process heat. The assessed average solar insolation, climatic conditions are shown in *Table 5.1* as per the data collected by Saharia and Kantatalukdar, (2014).

Table 5.1 Monthly average values of Solar insolation, ambient temperature and number of sunshine hours (Saharia and Kantatalukdar, (2014))

S. No	Month	Average Solar insolation (W/m^2)	Ambient temperature (°C)	Sunshine hours (hrs)
1	January	400	11.7	10.7
2	February	440	14	11.3
3	March	470	17.6	12
4	April	450	19.5	12.7
5	May	390	21	13.4
6	June	324	22.4	13.7
7	July	308	22.7	13.6
8	August	333	22.7	13
9	September	329	21.6	12.3
10	October	400	19.2	11.5
11	November	417	15.8	10.9
12	December	398	12.8	10.5

National Institute for Solar Energy (NISE) during the period 2014-15 carried out a survey for harnessing the Solar energy in the North East region of India. The survey showed that North-east India has greater solar potential and it can be used to generate the electricity and also solar based thermal energy (hot air, hot water or steam). The direct normal solar radiation, estimated potential and current installed capacity of Solar energy in North-East India given as state-wise in *Table 5.2*. From this collected data, it was found that Assam receives the direct normal solar radiation of 806 kWh/m^2/year with the estimated solar energy capacity of 14 GW. Currently 11.18 MW capacity installed for energy harnessing using solar technology.

Table 5.2 Estimated Solar energy potential in North-Eastern states of India [Kalita et al., (2019)

S. No	Name of the State	Direct Normal Radiation (kWh/m^2/year)	Estimated capacity (MW)	Installed capacity (MW)
1	Assam	806	14000	11.18
2	Meghalaya	1181	6000	0.01
3	Arunachal Pradesh	784	9000	0.27
4	Nagaland	852	7000	0.5
5	Manipur	811	11000	0.01
6	Mizoram	1363	9000	0.1
7	Tripura	852	2000	17.1

5.4 Economic analysis

The economic analysis of the SAH is performed using the procedure followed by Hassan et al., (2021). The total sunshine hours for Guwahati location is calculated from the data given by Kalita et al., (2019) and the electricity cost of 6.5 Rs / kW-hr is used from Ganesh Kumar et al., (2022). Saharia and Kantatalukdar, (2014) mentioned that India has nearly 300 sunny days, performed solar energy assessment in Guwahati, India and found that the average solar radiation is 388 W/m^2.

The salvage value (SV) of the SAH can be calculated as,

$$SV = \frac{1}{5} P \tag{5.1}$$

The global recovery factor (Capital recovery factor or money recovery factor) (GRF) is given by,

$$GRF = \frac{(i)(1+i)^n}{(1+i)^n - 1} \tag{5.2}$$

The First yearly cost (FYC) calculated as,

$$FYC = (GRF)(P) \tag{5.3}$$

The Sinking fund factor (SFF) is described as,

$$SFF = \frac{i}{(1+i)^n - 1} \tag{5.4}$$

The Yearly salvage value (YSV) is given as

$$YSV = (SFF)(SV) \tag{5.5}$$

The Yearly maintenance cost (YMC) is given as

$$YMC = \left(\frac{1}{10}\right) FYC \tag{5.6}$$

Yearly cost (YC) is calculated as,

$$YC = (FYC) + (YMC) + (YEPC) - (YSV) \tag{5.7}$$

The yearly useful energy gain (YUEG) is given as,

$$YUEG = \left[I_{avg}\right](A_P)(\eta_{Th})(N_d)(t_{op}) \tag{5.8}$$

Table 5.3 Component costs of varied arc ribs embedded SAH

S. No	Economical parameters	Cost (in INR)
1	Wood, plywood	*12,000*
2	Absorber plate	*4,000*
3	Bottom plate	*2,500*
4	Aluminium cladding	*1,500*
5	Insulation	*1,000*
6	Glazing	*4,000*
7	Black paint	*1,000*
8	Pipes and fittings	*3,000*
9	Blower	*4,000*
10	Copper fins	*5,000*
11	Transportation	*1,000*
12	Labour charges	*6,000*
Initial investment (P)		***45,000***

Table 5.3 provides the detailed estimation of the capital cost of the SAH is 45,000 INR spent for manufacturing VAR SAH experimental setup. Also, from the calculation, it is found that the SAH can able to generate annual useful heat delivery of around 821 kW and 555 kW for the mass flow rates 0.0175 kg/s and 0.0098 kg/s respectively. Throughout the lifetime of 20 years, it produces heat energy of 16 MW and 11 MW for the mass flow rates 0.0175 kg/s and 0.0098 kg/s operates with the thermal conversion efficiency of 50.4% and 34.1% respectively.

5.5 Environmental analysis

The environmental analysis performed by following the procedure given by Reddy et al., (2021) as follows.

Sustainability index (SI) is used to determine the effective utilization of SAH and expressed by using exergy efficiency of the SAH,

$$SI = \frac{1}{1-\eta_{Ex}} \tag{5.9}$$

Waste exergy ratio (WER) is used to determine the amount of exergy wasted during energy conversion and is given as,

$$WER = \frac{\sum EX_{out}}{\sum EX_{in}} \tag{5.10}$$

Environmental impact factor (EIF) is used to determine the environmental harm generated due to the loss in exergy during energy conversion. It is given as,

$$EIF = \frac{WER}{\eta_{Ex}} \tag{5.11}$$

Tables 5.4 and 5.5 show the variation in sustainability index (SI), waste exergy ratio (WER) and environmental impact factor (EIF) for the consecutive four days of operation with two different mass flow rates (0.0175 kg/s - day1 and day2) and (0.0098 kg/s – day3 and 4) for VAR SAH. The Sustainability Index (SI) of the system is the function of exergy efficiency. Hence, the variations in SI depends upon ambient, solar insolation and other operating parameters such as hot air outlet temperature and mass flow rate of hot air. For all four days of operation, the value of SI increases during the peak solar intensity period. The waste exergy ratio (WER) and environmental impact factor also depend majorly on solar intensity input. Apart from the solar radiation input, the design of the SAH plays a vital role in improving all these factors.

Table 5.4 Hourly variations in Sustainability Index (SI), Waste exergy ratio (WER) and Environmental impact factor (EIF) for 0.0175 kg/s – Day1 and Day2

S. No	Time (Hrs)	Day 1			Day 2		
		SI	WER	EIF	SI	WER	EIF
1	09:00	1.013	0.276	0.223	1.018	0.321	0.177
2	10:00	1.022	0.326	0.151	1.028	0.353	0.131
3	11:00	1.027	0.346	0.131	1.029	0.356	0.126
4	12:00	1.028	0.357	0.129	1.029	0.362	0.129
5	13:00	1.026	0.362	0.144	1.026	0.369	0.143
6	14:00	1.021	0.370	0.179	1.021	0.376	0.180
7	15:00	1.012	0.366	0.307	1.012	0.378	0.315

Table 5.5 Hourly variations in Sustainability Index (SI), Waste exergy ratio (WER) and Environmental impact factor (EIF) for 0.0098 kg/s – Day3 and Day4

S. No	Time (Hrs)	Day 3			Day 4		
		SI	WER	EIF	SI	WER	EIF
1	09:00	1.014	0.236	0.171	1.017	0.256	0.154
2	10:00	1.022	0.268	0.126	1.021	0.264	0.127
3	11:00	1.023	0.270	0.121	1.022	0.263	0.122
4	12:00	1.022	0.270	0.127	1.021	0.262	0.128
5	13:00	1.020	0.278	0.142	1.019	0.264	0.142
6	14:00	1.016	0.289	0.178	1.015	0.262	0.184
7	15:00	1.010	0.301	0.295	1.009	0.268	0.301

5.6 Enviro-economic analysis

The impact on the economics of the operation and environment of utilising the solar energy using SAH can be accessed through the enviro-economic analysis. In this analysis, the various enviro-economical parameters such as annual useful energy and exergy gain, life of the equipment and its maintenance cost, annual fuel savings due to the utilisation of solar energy for hot air generation can be evaluated with the help of mathematical formulas used by several researchers. The CO_2 savings throughout the operation, carbon credits earned, and energy payback period are also evaluated with the help of the enviro-economic analysis.

The enviro-economic analysis comprises of amount of carbon credits earned and payback period is given by Abuska and Sevik, (2017) and Ganesh Kumar et al., (2022). The yearly CO_2 based on the useful thermal energy gain is given by,

$$\phi_{CO_2} = \frac{(YUEG)\left(\psi_{CO_2}\right)}{1000} \tag{5.12}$$

The annual income generated due to the usage of SAH to generate thermal energy is given by,

$$Z_{CO_2} = \left(z_{CO_2}\right)\left(\phi_{CO_2}\right) \tag{5.13}$$

The Energy payback time (EPBT) is described as,

$$\left(EPBT\right)_n = \frac{E_{emb}}{E_{gain}} \tag{5.14}$$

$$PBP = \frac{P}{(FCS) + \left(\phi_{CO_2}\right)} \tag{5.15}$$

$$FCS = \frac{E_n}{\eta_{Th}} \tag{5.16}$$

Table 5.6 Embodied energy in various components of VAR SAH

Material	**Embodied energy (kW-hr / kg)**	**Mass (kg)**	**Quantity (in numbers)**	**Total embodied energy (kW-hr)**
Solar air heater				
G.I Absorber plate	8.89	14.1	1	125.35
Glass cover (glazing)	8.72	8.5	1	74.12
Bottom plate	55.28	1.08	1	59.70
Wooden duct	2.89	15	1	43.35
Wooden stand	2.89	10	1	28.9
Bottom plywood	4.2	8	1	33.6
Total				***365.02***
Centrifugal blower				
Motor body, casing (Cast iron)	6.94	10	1	69.4
Copper wires	19.6	0.25	1	4.9
Nuts, screws, flanges	8.6	0.3	1	2.58
Total				***76.88***
Other accessories used for construction				
Black paint	25.11	1	1	25.11
PVC pipe fittings	20.9	5	1	104.5
Polyurethane insulation	19.4	1	1	19.4
Aluminium angles	55.28	0.3	1	16.58
Fittings	8.89	0.2	1	1.778
Total				***167.368***
Total embodied energy (kW-hr) = (365.02+76.88+167.368)				***609.268***

The embodied energy for VAR SAH comprises nearly 365.02 kW-hr, the components of centrifugal blower used to operate the VAR SAH comprises of 76.88 kW-hr and nearly 167.368 kW-hr required for other accessories used for constructing the whole VAR SAH lab-scale prototype. Totally 609.268 kW-hr energy spent for manufacturing and operating the VAR SAH. The embodied energy of each component is given in *Table. 5.6.*

The total CO_2 mitigated per kWh is nearly 2 kg and the world carbon price is 14.5 $/ton of CO_2 (Hassan et al., 2021). By using VAR SAH, 22 to 32 tonnes of CO_2 generation is reduced which provides the economical revenue of 315 $ to 466 $ for the whole life span. The energy payback period is estimated to be around 11 to 17 months. Also, the payback period of the VAR SAH is calculated as 3.25 to 3.57 years.

5.7 Summary

The enviro-economic assessment of the fabricated VAR SAH lab scale prototype is performed. It is estimated that 45,000 INR is the only initial investment required to construct a VAR SAH. The return of the investment is found to be nearly 3.25 to 3.57 years only. Hence the implementation of VAR SAH is both economically and environmentally beneficial.

Chapter 6 Conclusion and Future Scope

6.1 Preface

Varied arc ribs embedded in back pass type SAH (VARSAH) was designed and tested for the application of drying agricultural products. A summary of the key outcomes arrived from the comparison of varied arc ribs embedded SAH with available smooth duct and fixed arc rib embedded SAH performances are discussed. Experimental investigations of varied arc ribs embedded SAH have been performed under different mass flow rate conditions. Energy, exergy, environment and economic analyses are performed for the developed lab scale prototype. A summary of the major outcomes from the research work are discussed in this chapter.

6.2 Performance comparison of varied arc ribs embedded SAH with smooth duct and fixed arc rib embedded in SAH- analytical investigation

A theoretical model is developed to study the influences of absorber plate length and varied arc ribs fin arrangements on the performance of SAH. For different air flow rate conditions, the outlet air temperature of SAH and mean absorber plate temperature are predicted. The heat transfer characteristics of the SAH are determined by predicting the Nusselt number, friction factor, and THPP. The efficiencies (thermal, effective, and exergy), collector efficiency factor and collector heat removal factor are also predicted. Various exergy losses, entropy and parameters associated with entropy (entropy generation number, Bejan number, and irreversibility distribution ratio) are determined and the important outcomes are summarized below.

- The maximum air outlet temperature of 318 K is achieved in a variable arc rib fin arrangement of 2 m length SAH at a flow rate of 0.02 kg/s. The increase in the length of the absorber plate and variable arc rib fin arrangement results in gaining maximum heat energy from the absorber plate to the heat exchanging fluid, which increases the performance of the SAH.
- The mean absorber plate temperature is reported to be lower in 1 m (309.5 K) and 2 m (311.3 K) variable arc rib fin arrangement at a flow rate of 0.06 kg/s. It shows that the variable arc rib fin arrangement results in the effective utilization of heat energy from the absorber plate.
- It is observed that with increase in mass flow rate from 0.02 kg/s to 0.06 kg/s, the THPP and the Nusselt number increase, whereas the frictional factor reduces. The THPP,

Nusselt number, and frictional factor values of variable arc rib fin arrangement is reported to be higher than fixed arc rib fin arrangement and smooth duct.

- The thermal and effective efficiencies of SAH increase as the flow rate increases, whereas the exergy efficiency reduces. The thermal, effective, and exergy efficiencies of the variable arc rib fin arrangements obtained maximum over smooth duct and fixed arc rib SAH. The thermal and effective efficiencies of 1m length absorber plate is observed to be slightly higher than the 2m length absorber plate. This is attributed to the increase in surface area of the absorber plate in 2 m solar air heater, which leads to a minimal decrease in thermal and effective efficiency. The exergy efficiency in 1 m variable and fixed arc rib fin arrangements is negative at a higher flow rate. This occurs due to the reduction in net exergy flow at a higher flow rate, the pumping power requirement is high. Also, when the pumping power is higher than the thermal energy received by the system, exergy efficiency reduces and becomes negative.
- The collector efficiency factor and collector heat removal factor increase as the flow rate increases. The variable arc rib fin arrangement reported higher collector efficiency and collector heat removal factor, due to maximum energy gain.
- The length of the absorber plate plays a significant role, and it is observed that 2 m absorber plate with variable arc rib fin arrangement reported higher air outlet temperature, whereas 1 m absorber plate with variable arc rib fin arrangement reported higher heat transfer characteristics (Nusselt number and THPP) and lower mean absorber plate temperature. In the case of thermal and effective efficiencies, 1 m length variable arc rib fin arrangement in absorber plate reports a minimal increase in efficiency than a 2 m length plate, whereas the exergy efficiency is significantly higher in 2 m length. Also, a similar trend is observed in collector efficiency and collector heat removal factor.
- The arc rib fin arrangement influences the outlet air temperature of SAH and the mean absorber plate temperature. The heat transfer characteristics, efficiencies, collector efficiency, and collector heat removal factor are reported to be higher in the variable arc rib fin arrangement when compared with the fixed arc rib fin and smooth duct. Thus, incorporating a variable arc rib fin arrangement in the absorber plate will assist in achieving significant heat transfer enhancement and improve the overall THPP of the solar air heater.

- From the results, it is inferred that, exergy loss due to absorption of solar radiation contributes major to exergy loss (approximately 70 to 75 %), optical exergy loss (approximately 25 to 20%), whereas the exergy loss due to friction, heat transfer to the working fluid and heat transfer to environment contributes less than 5 %.
- It is observed that the variation of total entropy generated (degradation) increases with the increase in mass flow rate. Entropy generation due to heat transfer has significant effect than the entropy generated due to pressure drop. This is the reason the value of Bejan number is always near to 1, whereas the magnitude of irreversibility distribution ratio always varies inversely proportional to Bejan number.

6.3 Performance of varied arc ribs embedded in SAH under different mass flow rate conditions – Experimental investigation

After comparing the performance of varied arc ribs SAH with various kinds of rib models, it was found varied arc ribs embedded SAH performs better than other rib configuration. Hence VAR (2m) SAH was fabricated and tested. The fabricated set up was tested for two different mass flow rates (0.0175 kg/s and 0.0098 kg/s) during (09:00 hrs to 15:00 hrs) for consecutive four days (12-15 Nov, 2020) respectively.

- The average ambient temperature and solar intensity on each day were varied from 28.3 to 30.7 °C and from 525 W/m^2 to 556 W/m^2, respectively, between day 1 and day 4. The maximum average solar intensity was reported from 10:00 hour and 12:00 hour, and it was varied from 679 W/m^2 to 654 W/m^2 between day 1 and day 4.

- The maximum temperature of the absorber plate (356.3 K) and air inside the duct (336.7 K) was achieved at low mass flow (0.0098 kg/s). It was observed that the temperature drops between the absorber plate and air reduced along the length of the air flow inside the duct due to variable arc ribbed wire configuration. It was observed that at a flow rate of 0.0098 kg/s at 0.5 m length, the temperature drop between the absorber plate and air was 26.4 °C and reduced to 19.6°C at a length of 2 m.

- It was observed that the average temperature difference between the inlet and outlet on each day was 298.6 K (day 1), 299.5 K (day 2), 304 K (day 3) and 304.6 K (day 2). The average outlet air temperature on each day was observed to be 329.4 K (day 1), 328.1 K (day 2), 332.3 K (day 3) and 333.5 K (day 4). During the peak sunshine hours (10:00 hour to 12:00 hour) the SAH outlet temperature was from 334.4 K to 340.4 K between day 1 and day 4. The proposed SAH's outlet temperature provides a favourable temperature to dry various agricultural and food products and hence can be integrated with various type of solar dryers.

- The average heat gain in the SAH on each day was observed to be 454 W (day 1), 469 W (day 2), 307 W (day 3), and 313 W (day 4). The average heat gain in the SAH was maximum at a high mass flow rate. The average Nusselt number in the SAH on each day was observed to be 16.6 (day 1), 17.5 (day 2), 11.7 (day 3), 11.9 (day 4). As the flow rate was increased from 0.0098 kg/s to 0.0175 kg/s the average Nusselt number increased by 44.9 % (11.8 - 0.0098 kg/s; and 17.1 - 0.0175 kg/s).
- The average thermal efficiency on each day was observed to be 48.8 % (day 1), 52.0 % (day 2), 35.0 % (day 3), and 33.2 % (day 4). The average effective efficiency on each day was observed to be 48.2 % (day 1); 51.4 % (day 2); 34.6 % (day 3); 32.8 % (day 4). The effective and thermal efficiencies were reported to have minimal deviation when operated at a low Reynolds number. The average exergy efficiency on each day was observed to be 2.0 % (day 1); 2.2 % (day 2); 1.7 % (day 3); and 1.7 % (day 4). As the mass flow rate increased, the efficiency (thermal, effective, and exergy) also increased.
- It is reported that as the flow rate increases, the collector factors (FP and FR) increase whereas the total loss coefficient decreases. The total loss coefficient was inversely proportional to the collector factors (FP and FR).
- From the exergy analysis results, the exergy loss due to absorption of solar radiation distinguished because of contribution of higher magnitude of exergy loss. The variation of exergy loss due to absorption of solar radiation was ranged from 601 to 644 W.
- It was inferred from the results that, both mass flow rate and incident solar radiation have significant effect in total entropy generation. The variation of total entropy generation on each day was observed to be 224 to 549 W (day 1), 213 to 562 W (day 2), 143 to 368 W (day 3) and 146 to 368 W (day 4). The magnitude of entropy generated due to heat transfer was higher than entropy generated due to pressure drop. Due to this reason the value of Bejan number always close to 1.

6.4 Techno-enviro-economic analysis for the fabricated varied arc ribs embedded SAH

After the thermal performance investigation of the fabricated varied arc ribs embedded SAH, the techno-enviro-economic benefits were studied. From the techno-enviro-economic analysis, return of investment, sustainable index, waste exergy ratio, environmental impact factor, total embodied energy and amount of CO_2 generated were estimated.

- The initial investment for the varied arc ribs embedded SAH cost was around 45,000 INR, which produces annual solar thermal energy gain of 821 to 555 kW, with a return of investment of 3.25 to 3.57 years.

- The total embodied energy of 609.268 kW-hr was used for various materials and other accessories used for constructing the SAH.

- Implementing the VAR SAH for the applications of drying can reduce the maximum of 32 tonnes of CO2 generation, generating an economical revenue of up to 466 USD for the life span of operation.

6.5 Limitations of the present study

- The primary focus of this study is on analyzing the energy, exergy, and entropy aspects. The optimization of the system for precise design is not addressed in this thesis. However, it is important to note that optimizing the solar air heater or any thermal device during the design stage can significantly reduce manufacturing and operational costs. Therefore, it is recommended that designers incorporate optimization techniques during the development of the SAH, rather than relying solely on experimentation.
- Furthermore, when developing the next generation of any thermal system, it is crucial to examine the presence of disorder within the system thoroughly. Therefore, during a thermal system's design and development phase, it is essential to prioritize enhancing thermo-hydraulic performance while minimizing disorder.

6.6 Scope for future research

The work presented in this thesis demonstrated solar energy conversion into thermal energy using flat plate type SAH. Analytical investigation procedures, design methodology, and experimental procedures are presented. Based on the observations and outcomes of the study, the recommendations for the future scope of research works are briefly discussed as follows,

- The heat transfer rate along the length of SAH reduces, as the temperature difference between the absorber plate and air flowing inside the duct reduces. In order to extract and maximize the utilization of the energy available in the absorber plate of the SAH, the rib diameter, and pitch distance should be varied along the length. Also baffles need to be placed properly in-order to channelize the air flow inside the duct and to improve the heat transfer.
- The thermal conversion efficiency of the SAH decreases as the length increases, hence optimization of the design parameter and operating parameter plays a significant role in-order to develop an energy efficient SAH system. Therefore, proper dimensioning of the SAH duct, selection and design of physical parameters of the rib (fins) and baffles yields better performance.
- SAH systems always operated during sunshine period, hence there will be always an issue of variable air outlet temperature and thermal conversion efficiency due to the nature of the input solar radiation. Hence there should be a control system with thermal storage will be provided either at the outlet or over the solar incident radiation surface, in order to obtain a constant output.
- Since, SAH can only be operated during sunshine period, the system should be connected with any other alternative renewable energy source to generate thermal energy. Combined bio-solar system can be considered as an alternative system in order to operate the system all round the clock of 24 hours and also generates constant energy output from the system.
- Exergy Loss Minimization: The study indicates that thermal in-equilibrium contributes significantly to exergy loss and entropy generation. Future work should delve into the development of real-time control algorithms that dynamically adjust system parameters to maintain thermal equilibrium, thereby minimizing exergy loss.
- Adaptive Thermal Battery Integration: To achieve constant energy output, the integration of adaptive thermal batteries that can self-regulate based on real-time energy demand and supply should be explored. This could involve machine learning algorithms to predict energy needs.

- Sustainable Energy Transition: Given the focus on North-Eastern India and its unrealized solar potential, future research should also consider the socio-economic aspects of transitioning from fossil fuels to solar energy, including policy implications and community engagement.
- Advanced Material Science: The use of nano-coatings or phase-changing materials on the absorber plate could offer avenues for significant efficiency gains. This would be in line with the current work on roughness geometry over the absorber plate but could offer more substantial improvements.
- System Scalability: As the study focuses on a back pass type flat plate solar air heater, future work should investigate the scalability of the system, especially for industrial applications. This includes modular design approaches and the integration with existing industrial processes.
- Exergy Analysis Across Multiple Scales: Given that the study has been conducted for Reynolds numbers up to 40,000, it would be beneficial to extend this analysis to different scales, especially for micro and macro-systems, to understand how exergy loss scales with system size.
- Climate-Adaptive Designs: Considering the specific climatic conditions of North-Eastern India, future work should focus on developing SAH models that are adaptive to seasonal variations and extreme weather conditions.
- IoT and Data Analytics: Incorporating IoT sensors for real-time monitoring and data analytics could provide deeper insights into system performance and areas for optimization. This is particularly relevant for remote or rural installations.

REFERENCES

’Kumar, A., ’Bhagoria, J., & ’Sarviya, R. (2008). Heat transfer enhancement in channel of solar air collector by using discrete W-shaped artificial roughened absorber. In *19th national & 8th ISHMT-ASME heat and mass transfer conference*.

Abdullah, A. S., Abou Al-sood, M. M., Omara, Z. M., Bek, M. A., & Kabeel, A. E. (2018). Performance evaluation of a new counter flow double pass solar air heater with turbulators. *Solar Energy*, *173*(February), 398–406. http://doi.org/10.1016/j.solener.2018.07.073

Abo-Elfadl, S., El-Dosoky, M. F., & Hassan, H. (2021). Energy and exergy assessment of new designed solar air heater of V-shaped transverse finned absorber at single- and double-pass flow conditions. *Environmental Science and Pollution Research*. http://doi.org/10.1007/s11356-021-15163-z

Abo-Elfadl, S., Yousef, M. S., & Hassan, H. (2021). Energy, exergy, and enviroeconomic assessment of double and single pass solar air heaters having a new design absorber. *Process Safety and Environmental Protection*, *149*, 451–464. http://doi.org/10.1016/j.psep.2020.11.020

Abuska, M., & Sevik, S. (2017). Energy, exergy, economic and environmental (4E) analyses of flat-plate and V-groove solar air collectors based on aluminium and copper. *Solar Energy*, *158*(August), 259–277. http://doi.org/10.1016/j.solener.2017.09.045

Afshari, F., Sozen, A., Khanlari, A., Tuncer, A. D. D., Sirin, C., Sözen, A., … Şirin, C. (2020). Effect of turbulator modifications on the thermal performance of cost-effective alternative solar air heater. *Renewable Energy*, *158*, 297–310. http://doi.org/10.1016/j.renene.2020.05.148

Aharwal, K. R., Gandhi, B. K., & Saini, J. S. (2008a). Experimental investigation on heat-transfer enhancement due to a gap in an inclined continuous rib arrangement in a rectangular duct of solar air heater. *Renewable Energy*, *33*(4), 585–596. http://doi.org/10.1016/j.renene.2007.03.023

Aharwal, K. R., Gandhi, B. K., & Saini, J. S. (2008b). Experimental investigation on heat-transfer enhancement due to a gap in an inclined continuous rib arrangement in a rectangular duct of solar air heater. *Renewable Energy*, *33*(4), 585–596. http://doi.org/10.1016/j.renene.2007.03.023

Akpinar, E. K., Koçyiĝit, F., & Ebru Kavak Akpinar and Fatih Kocyigit. (2010). Energy and exergy analysis of a new flat-plate solar air heater having different obstacles on absorber plates. *Applied Energy*, *87*(11), 3438–3450. http://doi.org/10.1016/j.apenergy.2010.05.017

Alam, T., Saini, R. P., & Saini, J. S. (2014a). Effect of circularity of perforation holes in V-shaped blockages on heat transfer and friction characteristics of rectangular solar air heater duct. *Energy Conversion and Management*, *86*, 952–963. http://doi.org/10.1016/j.enconman.2014.06.050

Alam, T., Saini, R. P., & Saini, J. S. (2014b). Heat and flow characteristics of air heater ducts provided with turbulators - A review. *Renewable and Sustainable Energy Reviews*, *31*, 289–304. http://doi.org/10.1016/j.rser.2013.11.050

Aldabbagh, L. B. Y., Egelioglu, F., & Ilkan, M. (2010). Single and double pass solar air heaters with wire mesh as packing bed. *Energy*, *35*(9), 3783–3787. http://doi.org/10.1016/j.energy.2010.05.028

Ammari, H. D. (2003). A mathematical model of thermal performance of a solar air heater with slats, *28*, 1597–1615. http://doi.org/10.1016/S0960-1481(02)00253-7

Arunkumar, H. S., Vasudeva Karanth, K., & Kumar, S. (2020). Review on the design modifications of a solar air heater for improvement in the thermal performance. *Sustainable Energy Technologies and Assessments*, *39*(January), 100685. http://doi.org/10.1016/j.seta.2020.100685

Baissi, M. T., Brima, A., Aoues, K., Khanniche, R., & Moummi, N. (2020). Thermal behavior in a solar air heater channel roughened with delta-shaped vortex generators. *Applied Thermal Engineering*, *165*, 113563. http://doi.org/10.1016/j.applthermaleng.2019.03.134

Bayrak, F., Oztop, H. F., & Hepbasli, A. (2013). Energy and exergy analyses of porous baffles inserted solar air heaters for building applications. *Energy and Buildings*, *57*, 338–345. http://doi.org/10.1016/j.enbuild.2012.10.055

Behura, A. K., Prasad, B. N., & Prasad, L. (2016). Heat transfer, friction factor and thermal performance of three sides artificially roughened solar air heaters. *Solar Energy*, *130*, 46–59. http://doi.org/10.1016/j.solener.2016.02.006

Benhamza, A., Boubekri, A., Atia, A., El Ferouali, H., Hadibi, T., Arıcı, M., & Abdenouri, N. (2021). Multi-objective design optimization of solar air heater for food drying based on energy, exergy and improvement potential. *Renewable Energy*, *169*, 1190–1209. http://doi.org/10.1016/j.renene.2021.01.086

Benli, H. (2013). Experimentally derived efficiency and exergy analysis of a new solar air heater having different surface shapes. *Renewable Energy*, *50*, 58–67. http://doi.org/10.1016/j.renene.2012.06.022

Bhagoria, J. L., Saini, J. S., & Solanki, S. C. (2002). Heat transfer coefficient and friction factor correlations for rectangular solar air heater duct having transverse wedge shaped rib roughness on the absorber plate. *Renewable Energy*, *25*(3), 341–369. http://doi.org/10.1016/S0960-1481(01)00057-X

Bharadwaj, G., Kaushal, M., & Goel, V. (2013). Heat transfer and friction characteristics of an equilateral triangular solar air heater duct using inclined continuous ribs as roughness element on the absorber plate. *International Journal of Sustainable Energy*, *32*(6), 515–530. http://doi.org/10.1080/14786451.2012.724687

Bhushan, B., & Singh, R. (2011). Nusselt number and friction factor correlations for solar air heater duct having artificially roughened absorber plate. *Solar Energy*, *85*(5), 1109–1118. http://doi.org/10.1016/j.solener.2011.03.007

Bhushan, B., & Singh, R. (2012). Thermal and thermohydraulic performance of roughened solar air heater having protruded absorber plate. *Solar Energy*, *86*(11), 3388–3396. http://doi.org/10.1016/j.solener.2012.09.004

Chabane, F., Moummi, N., & Benramache, S. (2014). Experimental study of heat transfer and thermal performance with longitudinal fins of solar air heater. *Journal of Advanced Research*, *5*(2), 183–192. http://doi.org/10.1016/j.jare.2013.03.001

Chamoli, S., & Thakur, N. S. (2013). Heat transfer enhancement in solar air heater with V-shaped perforated baffles. *Journal of Renewable and Sustainable Energy*, *5*(023122). Retrieved from https://doi.org/10.1063/1.4798411

Chamoli, S., & Thakur, N. S. (2016). Correlations for solar air heater duct with V-shaped perforated baffles as roughness elements on absorber plate. *International Journal of Sustainable Energy*, *35*(1), 1–20. http://doi.org/10.1080/14786451.2013.857318

Chamoli, S., Thakur, N. S., & Saini, J. S. (2012). A review of turbulence promoters used in solar thermal systems. *Renewable and Sustainable Energy Reviews*, *16*(5), 3154–3175. http://doi.org/10.1016/j.rser.2012.01.021

Chand, S., & Chand, P. (2018). Parametric study on the performance of solar air heater equipped with louvered fins. *Journal of Mechanical Science and Technology*, *32*(8), 3965–3973. http://doi.org/10.1007/s12206-018-0747-y

Chandra, R., Singh, N. P., & Sodha, M. S. (1990). Thermal performance of a triple-pass solar air collector. *Energy Conversion and Management*, *30*(1). http://doi.org/10.1016/0196-8904(90)90054-3

Choudhury, C., Chauhan, P. M., & Garg, H. P. (1995). Design curves for conventional solar air heaters. *Renewable Energy*, *6*(7), 739–749. http://doi.org/10.1016/0960-1481(95)00007-7

Choudhury, C., & Garg, H. P. (1993). Performance of air-heating collectors with packed airflow passage. *Solar Energy*, *50*(3). http://doi.org/10.1016/0038-092X(93)90014-F

Deo, N. S., Chander, S., Saini, J. S., Deo, N. S., Chander, S., & Saini, J. S. (2016). Performance analysis of solar air heater duct roughened with multigap V-down ribs combined with staggered ribs. *Renewable Energy*, *91*, 484–500. http://doi.org/10.1016/j.renene.2016.01.067

Dincer, I., & Cengel, Y. A. (2001). *Energy, entropy and exergy concepts and their roles in thermal engineering*. *Entropy* (Vol. 3). http://doi.org/10.3390/e3030116

Dong, Z., Liu, P., Xiao, H., Liu, Z., & Liu, W. (2021). A study on heat transfer enhancement for solar air heaters with ripple surface. *Renewable Energy*, *172*, 477–487. http://doi.org/10.1016/j.renene.2021.03.042

Eddine, B. . (2021). *Doctorate in : Mechanical Engineering Effect of the artificial roughness dispositions on the thermal exchanges in a flat solar collector Presented by : BENSACI Charaf Eddine The jury members : Doctorat en : Génie Mécanique Spécialité (Option) : Energéti*.

Farahani, S. D., & Shadi, M. (2021). Optimization-decision making of roughened solar air heaters with impingement jets based on 3E analysis. *International Communications in Heat and Mass Transfer*, *129*, 105742. http://doi.org/10.1016/j.icheatmasstransfer.2021.105742

Forson, F. K., Nazha, M. A. A., & Rajakaruna, H. (2003). Experimental and simulation studies on a single pass, double duct solar air heater. *Energy Conversion and Management*, *44*(8), 1209–1227. http://doi.org/10.1016/S0196-8904(02)00139-5

Fudholi, A., & Sopian, K. (2018). Review on exergy and energy analysis of solar air heater. *International Journal of Power Electronics and Drive Systems*, *9*(1), 420–426. http://doi.org/10.11591/ijpeds.v9n1.pp420-426

Fudholi, A., Sopian, K., Alghoul, M. A., Ruslan, M. H., & Othman, M. Y. (2015). Performances and improvement potential of solar drying system for palm oil fronds. *Renewable Energy*, *78*, 561–565. http://doi.org/10.1016/j.renene.2015.01.050

Ganesh Kumar, P., Vigneswaran, V. S., Balaji, K., Vinothkumar, S., Prabakaran, R., Sakthivadivel, D., … Kim, S. C. (2022). Augmented v-corrugated absorber plate using shot-blasting for solar air heater – Energy, Exergy, Economic, and Environmental (4E) analysis. *Process Safety and Environmental Protection*, *165*(July), 514–531. http://doi.org/10.1016/j.psep.2022.07.036

Garg, H. P., Datta, G., & Bhargava, A. K. (1984). Some studies on the flow passage dimension for solar air heating collectors. *Energy Conversion and Management*, *24*(3), 181–184. http://doi.org/10.1016/0196-8904(84)90034-7

Gawande, V. B., Dhoble, A. S., & Zodpe, D. B. (2014). CFD Analysis to Study Effect of Circular Vortex Generator Placed in Inlet Section to Investigate Heat Transfer Aspects of Solar Air Heater. *Scientific World Journal*, *2014*. http://doi.org/10.1155/2014/567257

Gawande, V. B., Dhoble, A. S., Zodpe, D. B., & Chamoli, S. (2016a). A review of CFD methodology used in literature for predicting thermo-hydraulic performance of a roughened solar air heater. *Renewable and Sustainable Energy Reviews*, *54*, 550–605. http://doi.org/10.1016/j.rser.2015.10.025

Gawande, V. B., Dhoble, A. S., Zodpe, D. B., & Chamoli, S. (2016b). Experimental and CFD investigation of convection heat transfer in solar air heater with reverse L-shaped ribs. *Solar Energy*, *131*, 275–295. http://doi.org/10.1016/j.solener.2016.02.040

Gholami, A., Ajabshirchi, Y., & Ranjbar, S. F. (2019). Thermo-economic optimization of solar air heaters with arcuate-shaped obstacles. *Journal of Thermal Analysis and Calorimetry*, *138*(2), 1395–1403. http://doi.org/10.1007/s10973-019-08273-x

Ghritlahre, H. K. (2021). An experimental study of solar air heater using arc shaped wire rib roughness based on energy and exergy analysis, *42*(3), 115–139. http://doi.org/10.24425/ather.2021.138112

Gill, R. S., Hans, V. S., Saini, J. S., & Singh, S. (2017). Investigation on performance enhancement due to staggered piece in a broken arc rib roughened solar air heater duct. *Renewable Energy*, *104*, 148–162. http://doi.org/10.1016/j.renene.2016.12.002

Gill, R. S., Hans, V. S., & Singh, R. P. (2021). Optimization of artificial roughness parameters in a solar air heater duct roughened with hybrid ribs. *Applied Thermal Engineering*, *191*(March), 116871. http://doi.org/10.1016/j.applthermaleng.2021.116871

Gill, R. S., Hans, V. S., & Singh, S. (2017). Investigations on thermo-hydraulic performance of broken arc rib in a rectangular duct of solar air heater. *International Communications in Heat and Mass Transfer*, *88*(September), 20–27. http://doi.org/10.1016/j.icheatmasstransfer.2017.07.024

Goel, A. K., & Singh, S. N. (2021). Experimental performance evaluation of an impinging jet with fins type solar air heater. *Environmental Science and Pollution Research*, *28*(16), 19944–19957. http://doi.org/10.1007/s11356-020-12193-x

Guler, H. O., Sozen, A., Tuncer, A. D., Afshari, F., Khanlari, A., Sirin, C., & Gungor, A. (2020). Experimental and CFD survey of indirect solar dryer modified with low-cost iron mesh. *Solar Energy*, *197*(January), 371–384. http://doi.org/10.1016/j.solener.2020.01.021

Gupta, A. D., & Varshney, L. (2017). Performance prediction for solar air heater having rectangular sectioned tapered rib roughness using CFD. *Thermal Science and Engineering Progress*, *4*, 122–132. http://doi.org/10.1016/j.tsep.2017.09.005

Gupta, D., Solanki, S. C., & Saini, J. S. (1993). Heat and fluid flow in rectangular solar air heater ducts having transverse rib roughness on absorber plates. *Solar Energy*, *51*(1). http://doi.org/10.1016/0038-092X(93)90039-Q

Gupta, M. K., & Kaushik, S. C. (2009a). Performance evaluation of solar air heater for various artificial roughness geometries based on energy, effective and exergy efficiencies. *Renewable Energy*, *34*(3), 465–476. http://doi.org/10.1016/j.renene.2008.06.001

Gupta, M. K., & Kaushik, S. C. (2009b). Performance evaluation of solar air heater for various artificial roughness geometries based on energy, effective and exergy efficiencies. *Renewable Energy*, *34*(3), 465–476. http://doi.org/10.1016/j.renene.2008.06.001

Hans, V. S., Saini, R. P., & Saini, J. S. (2010). Heat transfer and friction factor correlations for a solar air heater duct roughened artificially with multiple v-ribs. *Solar Energy*, *84*(6). http://doi.org/10.1016/j.solener.2010.02.004

Hassan, H., S. Yousef, M., & Abo-Elfadl, S. (2021). Energy, exergy, economic and environmental assessment of double pass V-corrugated-perforated finned solar air heater at different air mass ratios. *Sustainable Energy Technologies and Assessments*, *43*(December 2020), 100936. http://doi.org/10.1016/j.seta.2020.100936

Heaton, H. S., Reynolds, W. C., & Kays, W. M. (1964). Heat transfer in annular passages. Simultaneous development of velocity and temperature fields in laminar flow.

International Journal of Heat and Mass Transfer, *7*(7). http://doi.org/10.1016/0017-9310(64)90006-7

Heydari, A., & Mesgarpour, M. (2018). Experimental analysis and numerical modeling of solar air heater with helical flow path. *Solar Energy*, *162*(November 2017), 278–288. http://doi.org/10.1016/j.solener.2018.01.030

Ho, C. D., Yeh, C. W., & Hsieh, S. M. (2005). Improvement in device performance of multi-pass flat-plate solar air heaters with external recycle. *Renewable Energy*, *30*(10). http://doi.org/10.1016/j.renene.2004.11.009

Ho, C. D., Yeh, H. M., & Wang, R. C. (2005). Heat-transfer enhancement in double-pass flat-plate solar air heaters with recycle. *Energy*, *30*(15). http://doi.org/10.1016/j.energy.2005.01.006

Jain, P. K., Lanjewar, A., Rana, K. B., & Meena, M. L. (2021). Effect of fabricated V-rib roughness experimentally investigated in a rectangular channel of solar air heater: a comprehensive review. *Environmental Science and Pollution Research*, *28*(4), 4019–4055. http://doi.org/10.1007/s11356-020-11415-6

Jamil, B., Siddiqui, A. T., & Akhtar, N. (2016). Estimation of solar radiation and optimum tilt angles for south-facing surfaces in Humid Subtropical Climatic Region of India. *Engineering Science and Technology, an International Journal*, *19*(4), 1826–1835. http://doi.org/10.1016/j.jestch.2016.10.004

Jaurker, A. R., Saini, J. S., & Gandhi, B. K. (2006a). Heat transfer and friction characteristics of rectangular solar air heater duct using rib-grooved artificial roughness. *Solar Energy*, *80*(8), 895–907. http://doi.org/10.1016/j.solener.2005.08.006

Jaurker, A. R., Saini, J. S., & Gandhi, B. K. (2006b). Heat transfer and friction characteristics of rectangular solar air heater duct using rib-grooved artificial roughness. *Solar Energy*, *80*(8), 895–907. http://doi.org/10.1016/j.solener.2005.08.006

Kabeel, A. E., Hamed, M. H., Omara, Z. M., & Kandeal, A. W. (2018). Influence of fin height on the performance of a glazed and bladed entrance single-pass solar air heater. *Solar Energy*, *162*(September 2017), 410–419. http://doi.org/10.1016/j.solener.2018.01.037

Kabeel, A. E., Khalil, A., Shalaby, S. M., & Zayed, M. E. (2016a). Experimental investigation of thermal performance of flat and v-corrugated plate solar air heaters with and without PCM as thermal energy storage. *Energy Conversion and Management*, *113*, 264–272. http://doi.org/10.1016/j.enconman.2016.01.068

Kabeel, A. E., Khalil, A., Shalaby, S. M., & Zayed, M. E. (2016b). Investigation of the Thermal Performances of Flat, Finned, and v-Corrugated Plate Solar Air Heaters. *Journal of Solar Energy Engineering, Transactions of the ASME*, *138*(5), 1–7. http://doi.org/10.1115/1.4034027

Kalita, P., Das, S., Das, D., Borgohain, P., Dewan, A., & Banik, R. K. (2019). Feasibility study of installation of MW level grid connected solar photovoltaic power plant for northeastern region of India. *Sadhana - Academy Proceedings in Engineering Sciences*, *44*(9). http://doi.org/10.1007/s12046-019-1192-z

Kant, K., Shukla, A., Sharma, A., Kumar, A., & Jain, A. (2016). Thermal energy storage based solar drying systems : A review. *Innovative Food Science and Emerging Technologies*, *34*, 86–99. http://doi.org/10.1016/j.ifset.2016.01.007

Karim, M. A., & Hawlader, M. N. A. (2006). Performance evaluation of a v-groove solar air collector for drying applications. *Applied Thermal Engineering*, *26*(1). http://doi.org/10.1016/j.applthermaleng.2005.03.017

Karmare, S. V., & Tikekar, A. N. (2007). Heat transfer and friction factor correlation for artificially roughened duct with metal grit ribs. *International Journal of Heat and Mass Transfer*, *50*(21–22), 4342–4351. http://doi.org/10.1016/j.ijheatmasstransfer.2007.01.065

Karwa, R., Solanki, S. C., & Saini, J. S. (1999). Heat transfer coefficient and friction factor correlations for the transitional flow regime in rib-roughened rectangular ducts. *International Journal of Heat and Mass Transfer*, *42*(9), 1597–1615. http://doi.org/10.1016/S0017-9310(98)00252-X

Khanlari, A., Guler, H. O., Tuncer, A. D., Sirin, C., Bilge, Y. C., Yılmaz, Y., & Gungor, A. (2020). Experimental and numerical study of the effect of integrating plus-shaped perforated baffles to solar air collector in drying application. *Renewable Energy*, *145*, 1677–1692. http://doi.org/10.1016/j.renene.2019.07.076

Khanlari, A., Sozen, A., Afshari, F., Sirin, C., Tuncer, A. D., & Gungor, A. (2020). Drying municipal sewage sludge with v-groove triple-pass and quadruple-pass solar air heaters along with testing of a solar absorber drying chamber. *Science of the Total Environment*, *709*. http://doi.org/10.1016/j.scitotenv.2019.136198

Kumar, A., & Layek, A. (2021). Energetic and exergetic based performance evaluation of solar air heater having winglet type roughness on absorber surface. *Solar Energy Materials and Solar Cells*, *230*(May), 111147. http://doi.org/10.1016/j.solmat.2021.111147

Kumar, A., Saini, R. P., & Saini, J. S. (2012). Experimental investigation on heat transfer and fluid flow characteristics of air flow in a rectangular duct with Multi v-shaped rib with gap roughness on the heated plate. *Solar Energy*, *86*(6), 1733–1749. http://doi.org/10.1016/j.solener.2012.03.014

Kumar, K., Prajapati, D. R., & Samir, S. (2015). Determination of Effective Efficiency of Artificially Roughened Solar Air Heater Duct Using Ribs. *Distributed Generation & Alternative Energy Journal*, *30*(2), 57–77. http://doi.org/10.1080/21563306.2015.11432421

Kumar, & Layek, A. (2019a). Energetic and exergetic performance evaluation of solar air heater with twisted rib roughness on absorber plate. *Journal of Cleaner Production*, *232*, 617–628. http://doi.org/10.1016/j.jclepro.2019.05.363

Kumar, & Layek, A. (2019b). Nusselt number and friction factor correlation of solar air heater having twisted-rib roughness on absorber plate. *Renewable Energy*, *130*, 687–699. http://doi.org/10.1016/j.renene.2018.06.076

Kumar, R., Kumar, A., & Goel, V. (2019). Performance improvement and development of correlation for friction factor and heat transfer using computational fluid dynamics for ribbed triangular duct solar air heater. *Renewable Energy*, *131*, 788–799. http://doi.org/10.1016/j.renene.2018.07.078

Kumar, R., Kumar, R., Kumar, S., Thapa, S., Sethi, M., Fekete, G., & Singh, T. (2022). Impact of artificial roughness variation on heat transfer and friction characteristics of solar air heating system. *Alexandria Engineering Journal*, *61*(1), 481–491. http://doi.org/10.1016/j.aej.2021.06.031

Kumar, R., & Verma, S. K. (2021). Exergetic And Energetic Evaluation Of An Innovative Solar Air Heating System Coated With Graphene And Copper Oxide Nano-Particles. *Journal of Thermal Engineering*, *7*(3), 447–467. http://doi.org/10.18186/THERMAL.887023

Kumar, S., Kumar, R., Goel, V., Bhattacharyya, S., & Issakhov, A. (2021). Exergetic performance estimation for roughened triangular duct used in solar air heaters. *Journal of Thermal Analysis and Calorimetry*, *145*(3), 1661–1672. http://doi.org/10.1007/s10973-021-10852-w

Kumar, S., & Saini, R. P. (2009). CFD based performance analysis of a solar air heater duct provided with artificial roughness. *Renewable Energy*, *34*(5), 1285–1291. http://doi.org/10.1016/j.renene.2008.09.015

Kumar, S., & Verma, S. K. (2022). Heat transfer and fluid flow analysis of sinusoidal protrusion rib in solar air heater. *International Journal of Thermal Sciences*, *172*(PB), 107323. http://doi.org/10.1016/j.ijthermalsci.2021.107323

Kumar, T. S., Mittal, V., Thakur, N. S., & Kumar, A. (2010). Second law analysis of a solar air heater having 60° inclined discrete rib roughness on absorber plate. *African Journal of Environmental Science and Technology*, *4*(13), 913-929–929.

Lanjewar, A., Bhagoria, J. L. L., & Sarviya, R. M. M. (2011a). Heat transfer and friction in solar air heater duct with W-shaped rib roughness on absorber plate. *Energy*, *36*(7), 4531–4541. http://doi.org/10.1016/j.energy.2011.03.054

Lanjewar, A., Bhagoria, J. L., & Sarviya, R. M. (2011b). Heat transfer and friction in solar air heater duct with W-shaped rib roughness on absorber plate. *Energy*, *36*(7), 4531–4541. http://doi.org/10.1016/j.energy.2011.03.054

Lanjewar, A. M., Bhagoria, J. L., & Agrawal, M. K. (2015). Review of development of artificial roughness in solar air heater and performance evaluation of different orientations for double arc rib roughness. *Renewable and Sustainable Energy Reviews*, *43*, 1214–1223. http://doi.org/10.1016/j.rser.2014.11.081

Layek, A., Saini, J. S., & Solanki, S. C. (2007). Second law optimization of a solar air heater having chamfered rib-groove roughness on absorber plate. *Renewable Energy*, *32*(12), 1967–1980. http://doi.org/10.1016/j.renene.2006.11.005

Luan, N. T., & Phu, N. M. (2020). Thermohydraulic correlations and exergy analysis of a solar air heater duct with inclined baffles. *Case Studies in Thermal Engineering*, *21*(May), 100672. http://doi.org/10.1016/j.csite.2020.100672

Luan, N. T., & Phu, N. M. (2021). First and second law evaluation of multipass flat-plate solar air collector and optimization using preference selection index method. *Mathematical Problems in Engineering*, *2021*. http://doi.org/10.1155/2021/5563882

Mahanand, Y., & Senapati, J. R. (2021). Thermo-hydraulic performance analysis of a solar air heater (SAH) with quarter-circular ribs on the absorber plate: A comparative study. *International Journal of Thermal Sciences*, *161*(November 2020), 106747. http://doi.org/10.1016/j.ijthermalsci.2020.106747

Matrawy, K. K. (1998). Theoretical analysis for an air heater with a box-type absorber.

Solar Energy, *63*(3). http://doi.org/10.1016/S0038-092X(98)00044-9

Mittal, M., Varun Saini, R., & Singal, S. (2007). Effective efficiency of solar air heaters having different types of roughness elements on the absorber plate. *Energy*, *32*(5), 739–745. http://doi.org/10.1016/j.energy.2006.05.009

Momin, A. E., Saini, J. S., & Solanki, S. C. (2002). Heat transfer and friction in solar air heater duct with V-shaped rib roughness on absorber plate. *International Journal of Heat and Mass Transfer*, *45*, 3383–3396.

Mugi, V. R., & Chandramohan, V. P. (2021). Energy and exergy analysis of forced and natural convection indirect solar dryers: Estimation of exergy inflow, outflow, losses, exergy efficiencies and sustainability indicators from drying experiments. *Journal of Cleaner Production*, *282*. http://doi.org/10.1016/j.jclepro.2020.124421

Nadda, R., Kumar, A., & Maithani, R. (2017). Developing heat transfer and friction loss in an impingement jets solar air heater with multiple arc protrusion obstacles. *Solar Energy*, *158*(June), 117–131. http://doi.org/10.1016/j.solener.2017.09.042

Naphon, P. (2005). On the performance and entropy generation of the double-pass solar air heater with longitudinal fins. *Renewable Energy*, *30*(9), 1345–1357. http://doi.org/10.1016/j.renene.2004.10.014

Ngo, T. T., & Phu, N. M. (2020). Computational fluid dynamics analysis of the heat transfer and pressure drop of solar air heater with conic-curve profile ribs. *Journal of Thermal Analysis and Calorimetry*, *139*(5), 3235–3246. http://doi.org/10.1007/s10973-019-08709-4

Nidhul, K., Kumar, S., Yadav, A. K., & Anish, S. (2020). Enhanced thermo-hydraulic performance in a V-ribbed triangular duct solar air heater: CFD and exergy analysis. *Energy*, *200*, 117448. http://doi.org/10.1016/j.energy.2020.117448

Nidhul, K., Yadav, A. K., Anish, S., & Kumar, S. (2021). Critical review of ribbed solar air heater and performance evaluation of various V-rib configuration. *Renewable and Sustainable Energy Reviews*, *142*(March), 110871. http://doi.org/10.1016/j.rser.2021.110871

Ong, K. S. (1995). Thermal performance of solar air heaters: Mathematical model and solution procedure. *Solar Energy*, *55*(2), 93–109. http://doi.org/10.1016/0038-092X(95)00021-I

Pandey, R., & Kumar, M. (2021). Efficiencies assessment of an indoor designed solar air heater characterized by V baffle blocks having staggered racetrack-shaped perforation geometry. *Sustainable Energy Technologies and Assessments*, *47*(December 2020), 101362. http://doi.org/10.1016/j.seta.2021.101362

Pashchenko, D. I. (2018). ANSYS Fluent CFD Modeling of Solar Air-Heater Thermoaerodynamics. *Applied Solar Energy (English Translation of Geliotekhnika)*, *54*(1), 32–39. http://doi.org/10.3103/S0003701X18010103

Pashchenko, D. I. (2019). CFD Modeling of Operating Processes of a Solar Air Heater in ANSYS Fluent. *Journal of Engineering Physics and Thermophysics*, *92*(1), 73–79. http://doi.org/10.1007/s10891-019-01908-8

Phila, A., Eiamsa-ard, S., & Thianpong, C. (2020). Thermal Performance Evaluation of a Channel Installed with Inclined-Baffle Turbulators. *Arabian Journal for Science and Engineering*, *45*(2), 609–621. http://doi.org/10.1007/s13369-019-04097-x

Phu, N. M., Bao, T. T., Hung, H. N., Tu, N. T., & Van Hap, N. (2020). Analytical predictions of exergoeconomic performance of a solar air heater with surface roughness of metal waste. *Journal of Thermal Analysis and Calorimetry*, *144*(5), 1727–1740. http://doi.org/10.1007/s10973-020-09787-5

Phu, N. M., & Hap, N. Van. (2020). Performance Evaluation of a Solar Air Heater Roughened with Conic-Curve Profile Ribs Based on Efficiencies and Entropy Generation. *Arabian Journal for Science and Engineering*, *45*(11), 9023–9035. http://doi.org/10.1007/s13369-020-04676-3

Phu, N. M., Luan, N. T., Phu, N. M., Luan, N. T., & Luan, N. T. (2020). A Review of Energy and Exergy Analyses of a Roughened Solar Air Heater. *Journal of Advanced Research in Fluid Mechanics and Thermal Sciences*, *77*(2), 160–175. http://doi.org/10.37934/arfmts.77.2.160175

Phu, N. M., Tuyen, V., & Ngo, T. T. (2019). Augmented heat transfer and friction investigations in solar air heater artificially roughened with metal shavings. *Journal of Mechanical Science and Technology*, *33*(7), 3521–3529. http://doi.org/10.1007/s12206-019-0646-x

Prasad, B. N. (2013). Thermal performance of artificially roughened solar air heaters. *Solar Energy*, *91*, 59–67. http://doi.org/10.1016/j.solener.2013.01.014

Prasad, R. K., & Sahu, M. K. (2017). Entropy generation and thermodynamic analysis of solar air heaters with artificial roughness on absorber plate. *Archives of Thermodynamics*, *38*(3), 23–48. http://doi.org/10.1515/aoter-2017-0014

Priyam, A., & Chand, P. (2016). Thermal and thermohydraulic performance of wavy finned absorber solar air heater. *Solar Energy*, *130*, 250–259. http://doi.org/10.1016/j.solener.2016.02.030

Priyam, A., & Chand, P. (2018). Effect of wavelength and amplitude on the performance of wavy finned absorber solar air heater. *Renewable Energy*, *119*, 690–702. http://doi.org/10.1016/j.renene.2017.12.010

Promvonge, P., Khanoknaiyakarn, C., Kwankaomeng, S., & Thianpong, C. (2011). Thermal behavior in solar air heater channel fitted with combined rib and delta-winglet. *International Communications in Heat and Mass Transfer*, *38*(6), 749–756. http://doi.org/10.1016/j.icheatmasstransfer.2011.03.014

Qasem, N. A. A., Arnous, M. N., & Zubair, S. M. (2020). A comprehensive thermal-hydraulic assessment of solar flat-plate air heaters. *Energy Conversion and Management*, *215*. http://doi.org/10.1016/j.enconman.2020.112922

Rabha, D. K. K., Muthukumar, P., & Somayaji, C. (2017). Energy and exergy analyses of the solar drying processes of ghost chilli pepper and ginger. *Renewable Energy*, *105*, 764–773. http://doi.org/10.1016/j.renene.2017.01.007

Rahmani and Nikbakht. (2017). Heat flux : thermohydraulic investigation of solar air heaters used in agro - industrial applications. *Heat and Mass Transfer*, *53*(3), 917–928. http://doi.org/10.1007/s00231-016-1864-8

Ramadan, M. R. I., El-Sebaii, A. A., Aboul-Enein, S., & El-Bialy, E. (2007). Thermal performance of a packed bed double-pass solar air heater. *Energy*, *32*(8). http://doi.org/10.1016/j.energy.2006.09.019

Reddy, J., Das, B., Jagadish, & Negi, S. (2021). Energy, exergy, and environmental (3E) analyses of reverse and cross-corrugated trapezoidal solar air collectors: An experimental study. *Journal of Building Engineering*, *41*(March). http://doi.org/10.1016/j.jobe.2021.102434

Saharia, B. J., & Kantatalukdar, B. (2014). Theoretical Assessment of PV Energy Potential At Assam Engineering College using PV Indices, *3*(8), 1230–1233.

Sahu, M. K., Matheswaran, M. M., & Bishnoi, P. (2021). Experimental study of thermal performance and pressure drop on a solar air heater with different orientations of arc-shape rib roughness. *Journal of Thermal Analysis and Calorimetry*, *144*(4), 1417–1434. http://doi.org/10.1007/s10973-020-09569-z

Sahu, M. K., & Prasad, R. K. (2016). Exergy based performance evaluation of solar air heater with arc-shaped wire roughened absorber plate. *Renewable Energy*.

http://doi.org/10.1016/j.renene.2016.04.083

Sahu, M. K., & Prasad, R. K. (2017). Thermohydraulic performance analysis of an arc shape wire roughened solar air heater. *Renewable Energy*, *108*, 598–614. http://doi.org/10.1016/j.renene.2017.02.075

Sahu, M. K., & Prasad, R. K. (2019). Second law optimization and parametric study of a solar air heater having artificially roughened absorber plate. *Archives of Thermodynamics*, *40*(2), 107–135. http://doi.org/10.24425/ather.2019.129544

Sahu, M. M., & Bhagoria, J. L. (2005). Augmentation of heat transfer coefficient by using 90° broken transverse ribs on absorber plate of solar air heater. *Renewable Energy*, *30*(13), 2057–2073. http://doi.org/10.1016/j.renene.2004.10.016

Saini, R. P. Ã., & Verma, J. (2008). Heat transfer and friction factor correlations for a duct having dimple-shape artificial roughness for solar air heaters. *Energy*, *33*(8), 1277–1287. http://doi.org/10.1016/j.energy.2008.02.017

Saini, R. P., & Saini, J. S. (1997). Heat transfer and friction factor correlations for artificially roughened ducts with expanded metal mesh as roughness element. *International Journal of Heat and Mass Transfer*, *40*(4), 973–986. http://doi.org/10.1016/0017-9310(96)00019-1

Saini, S. K., & Saini, R. P. (2008). Development of correlations for Nusselt number and friction factor for solar air heater with roughened duct having arc-shaped wire as artificial roughness. *Solar Energy*, *82*(12), 1118–1130. http://doi.org/10.1016/j.solener.2008.05.010

Sansaniwal, S. K., Sharma, V., & Mathur, J. (2018). Energy and exergy analyses of various typical solar energy applications: A comprehensive review. *Renewable and Sustainable Energy Reviews*, *82*(January 2017), 1576–1601. http://doi.org/10.1016/j.rser.2017.07.003

Sari, A., Sadi, M., Shafiei Sabet, G., Mohammadiun, M., & Mohammadiun, H. (2021). Experimental analysis and exergetic assessment of the solar air collector with delta winglet vortex generators and baffles. *Journal of Thermal Analysis and Calorimetry*, *145*(3), 867–885. http://doi.org/10.1007/s10973-020-10298-6

Saxena, A., Varun, & El-Sebaii, A. A. (2015). A thermodynamic review of solar air heaters. *Renewable and Sustainable Energy Reviews*, *43*, 863–890. http://doi.org/10.1016/j.rser.2014.11.059

Sciacovelli, A., Verda, V., & Sciubba, E. (2015). Entropy generation analysis as a design tool - A review. *Renewable and Sustainable Energy Reviews*, *43*, 1167–1181. http://doi.org/10.1016/j.rser.2014.11.104

Sethi, M., Thakur, N. S., Varun, Thakur, N. S., Varun, & Thakur, N. S. (2012). Correlations for solar air heater duct with dimpled shape roughness elements on absorber plate. *Solar Energy*, *86*(9), 2852–2861. http://doi.org/10.1016/j.solener.2012.06.024

Sharma, N. K., Tiwari, P. K., & Sood, Y. R. (2012). Solar energy in India: Strategies, policies, perspectives and future potential. *Renewable and Sustainable Energy Reviews*, *16*(1), 933–941. http://doi.org/10.1016/j.rser.2011.09.014

Sharma, S., Das, R. K., & Kulkarni, K. (2021). Computational and experimental assessment of solar air heater roughened with six different baffles. *Case Studies in Thermal Engineering*, *27*(August), 101350. http://doi.org/10.1016/j.csite.2021.101350

Sharma, V. R., S, S. S., Fernandes, D. V., & Manjunath, M. (2022). Numerical Analysis of Heat Transfer Enhancement of Solar Air Heater using Discrete Triangle Wave Corrugations. *Cogent Engineering*, *00*(00). http://doi.org/10.1080/23311916.2022.2051312

Singh, A., Kumar, M., Sharma, A., & Kumar, V. (2022). CFD based heat transfer correlation for ribbed solar air heater. *Materials Today: Proceedings*, (xxxx). http://doi.org/10.1016/j.matpr.2021.12.382

Singh, A. P., Varun, & Siddhartha. (2014). Heat transfer and friction factor correlations for multiple arc shape roughness elements on the absorber plate used in solar air heaters. *Experimental Thermal and Fluid Science*, *54*, 117–126. http://doi.org/10.1016/j.expthermflusci.2014.02.004

Singh, A., Prakash, O., Sharma, A., & Ahmad, I. (2022). CFD analysis of heat transfer performance of ribbed solar air heater. *Materials Today: Proceedings*, (xxxx). http://doi.org/10.1016/j.matpr.2021.12.560

Singh Bisht, V., Kumar Patil, A., Gupta, A., Bisht, V. S., Patil, A. K., Gupta, A., … Gupta, A. (2018). Review and performance evaluation of roughened solar air heaters. *Renewable and Sustainable Energy Reviews*, *81*(July 2017), 954–977. http://doi.org/10.1016/j.rser.2017.08.036

Singh, H., Chavadaki, S., Kishore, C., Kumar, K. C. N., & Avikal, S. (2021). Numerical analysis of roughened solar air heater with arc and fan shape roughness to understand heat transfer and fluid flow characteristics. *Materials Today: Proceedings*, *46*, 10662–10667. http://doi.org/10.1016/j.matpr.2021.01.399

Singh, I., & Singh, S. (2018a). A review of artificial roughness geometries employed in solar air heaters. *Renewable and Sustainable Energy Reviews*, *92*(May), 405–425. http://doi.org/10.1016/j.rser.2018.04.108

Singh, I., & Singh, S. (2018b). A review of artificial roughness geometries employed in solar air heaters. *Renewable and Sustainable Energy Reviews*, *92*(May), 405–425. http://doi.org/10.1016/j.rser.2018.04.108

Singh, I., & Singh, S. (2018c). CFD analysis of solar air heater duct having square wave profiled transverse ribs as roughness elements. *Solar Energy*, *162*(January), 442–453. http://doi.org/10.1016/j.solener.2018.01.019

Singh, I., Vardhan, S., Singh, S., & Singh, A. (2019). Experimental and CFD analysis of solar air heater duct roughened with multiple broken transverse ribs : A comparative study. *Solar Energy*, *188*(February), 519–532. http://doi.org/10.1016/j.solener.2019.06.022

Singh, S., Chander, S., & Saini, J. S. (2011a). Heat transfer and friction factor correlations of solar air heater ducts artificially roughened with discrete V-down ribs. *Energy*, *36*(8), 5053–5064. http://doi.org/10.1016/j.energy.2011.05.052

Singh, S., Chander, S., & Saini, J. S. (2011b). Thermal and effective efficiency based analysis of discrete V-down rib-roughened solar air heaters. *Journal of Renewable and Sustainable Energy*, *3*(2). http://doi.org/10.1063/1.3574430

Sokhansefat, T., Kasaeian, A., Rahmani, K., & Mohasseb, S. (2014). Comparing the performance of flat plate collectors and evacuated tube collectors for buildings and industrial usage. *Civil-Comp Proceedings*, *105*(November). http://doi.org/10.4203/ccp.105.93

Srivastava, R. K., & Rai, A. K. (2017). A review on solar air heater technology. *International Journal of Mechanical Engineering and Technology*, *8*(7), 1122–1131.

Sureandhar, G., Srinivasan, G., Muthukumar, P., & Senthilmurugan, S. (2021). Performance analysis of arc rib fin embedded in a solar air heater. *Thermal Science and Engineering Progress*, *23*(October 2020), 100891. http://doi.org/10.1016/j.tsep.2021.100891

Sureandhar, G., Srinivasan, G., Muthukumar, P., & Senthilmurugan, S. (2022). Investigation of thermal performance in a solar air heater having variable arc ribbed fin configuration. *Sustainable Energy Technologies and Assessments*, *52*(PA), 102069. http://doi.org/10.1016/j.seta.2022.102069

Tan, H. M., & Charters, W. W. S. (1969). Effect of thermal entrance region on turbulent forced-convective heat transfer for an asymmetrically heated rectangular duct with uniform heat flux. *Solar Energy*, *12*(4). http://doi.org/10.1016/0038-092X(69)90072-3

Tan, H. M., & Charters, W. W. S. (1970). An experimental investigation of forced-convective heat transfer for fully-developed turbulent flow in a rectangular duct with asymmetric heating. *Solar Energy*, *13*(1). http://doi.org/10.1016/0038-092X(70)90012-5

Tanda, G. (2011). Performance of solar air heater ducts with different types of ribs on the absorber plate. *Energy*, *36*(11), 6651–6660. http://doi.org/10.1016/j.energy.2011.08.043

Tchinda, R. (2008). Thermal behaviour of solar air heater with compound parabolic concentrator. *Energy Conversion and Management*, *49*(4). http://doi.org/10.1016/j.enconman.2007.08.004

Tchinda, R. (2009). A review of the mathematical models for predicting solar air heaters systems. *Renewable and Sustainable Energy Reviews*, *13*(8), 1734–1759. http://doi.org/10.1016/j.rser.2009.01.008

Thanh Luan, N., & Minh Phu, N. (2021). Thermohydraulic Performance and Entropy Generation of Baffled Channel: Numerical Analysis and Optimization. *Journal of Thermophysics and Heat Transfer*, 1–11. http://doi.org/10.2514/1.t6332

Torres-Reyes, E., Cervantes-de Gortari, J. ., Ibarra-Salazar, B. ., & Picon-Nuñez, M. (2001). A design method of flat-plate solar collectors based on minimum entropy generation. *Exergy, An International Journal*, *1*(1), 46–52. http://doi.org/10.1016/s1164-0235(01)00009-7

Torres-Reyes, E., Navarrete-González, J. J., & Cervantes-De Gortari, J. G. (2004). Thermodynamic optimization as an effective tool to design solar heating systems. *Energy*, *29*(12–15 SPEC. ISS.), 2305–2315. http://doi.org/10.1016/j.energy.2004.03.052

Tuncer, A. D. D., Khanlari, A., Sozen, A., Gurbuz, E. Y., Sirin, C., Gungor, A., … Gungor, A. (2020). Energy-exergy and enviro-economic survey of solar air heaters with various air channel modifications. *Renewable Energy*, *160*, 67–85. http://doi.org/10.1016/j.renene.2020.06.087

Varun, Saini, R. P., & Singal, S. K. (2008). Investigation of thermal performance of solar air heater having roughness elements as a combination of inclined and transverse ribs on the absorber plate. *Renewable Energy*, *33*(6), 1398–1405. http://doi.org/10.1016/j.renene.2007.07.013

Verma, R., Chandra, R., & Garg, H. P. (1992). Optimization of solar air heaters of different designs. *Renewable Energy*, *2*(4–5). http://doi.org/10.1016/0960-1481(92)90091-G

Wang, D., Liu, J., Liu, Y., Wang, Y., Li, B., & Liu, J. (2020). Evaluation of the performance of an improved solar air heater with "S" shaped ribs with gap. *Solar Energy*, *195*, 89–101. http://doi.org/10.1016/j.solener.2019.11.034

Wijeysundera, N. E., Ah, L. L., & Tjioe, L. E. (1982). Thermal performance study of two-pass solar air heaters. *Solar Energy*, *28*(5). http://doi.org/10.1016/0038-092X(82)90253-5

Xiao, H., Dong, Z., Liu, Z., & Liu, W. (2020). Heat transfer performance and flow characteristics of solar air heaters with inclined trapezoidal vortex generators. *Applied Thermal Engineering*, *179*. http://doi.org/10.1016/j.applthermaleng.2020.115484

Yadav, A. S., & Bhagoria, J. L. (2013a). A CFD (computational fluid dynamics) based heat transfer and fluid flow analysis of a solar air heater provided with circular transverse wire rib roughness on the absorber plate. *Energy*, *55*, 1127–1142. http://doi.org/10.1016/j.energy.2013.03.066

Yadav, A. S., & Bhagoria, J. L. (2014a). A CFD based thermo-hydraulic performance analysis of an artificially roughened solar air heater having equilateral triangular sectioned rib roughness on the absorber plate. *International Journal of Heat and Mass Transfer*, *70*, 1016–1039. http://doi.org/10.1016/j.ijheatmasstransfer.2013.11.074

Yadav, A. S., & Bhagoria, J. L. (2014b). A numerical investigation of square sectioned transverse rib roughened solar air heater. *International Journal of Thermal Sciences*, *79*, 111–131. http://doi.org/10.1016/j.ijthermalsci.2014.01.008

Yadav, A. S., & Bhagoria, J. L. L. (2013b). A CFD (computational fluid dynamics) based heat transfer and fluid flow analysis of a solar air heater provided with circular transverse wire rib roughness on the absorber plate. *Energy*, *55*, 1127–1142. http://doi.org/10.1016/j.energy.2013.03.066

Yadav, A. S., & Thapak, M. K. (2016a). Artificially roughened solar air heater: A comparative study. *International Journal of Green Energy*, *13*(2), 143–172. http://doi.org/10.1080/15435075.2014.917419

Yadav, A. S., & Thapak, M. K. (2016b). Artificially roughened solar air heater: A comparative study. *International Journal of Green Energy*, *13*(2), 143–172. http://doi.org/10.1080/15435075.2014.917419

Yadav, S., Kaushal, M., Varun, & Siddhartha. (2013). Nusselt number and friction factor correlations for solar air heater duct having protrusions as roughness elements on absorber plate. *Experimental Thermal and Fluid Science*, *44*, 34–41. http://doi.org/10.1016/j.expthermflusci.2012.05.011

Yadav, S., Kaushal, M., Varun, & Siddhartha. (2014). Exergetic performance evaluation of solar air heater having arc shape oriented protrusions as roughness element. *Solar Energy*, *105*, 181–189. http://doi.org/10.1016/j.solener.2014.04.001

Youcef-Ali, S., & Desmons, J. Y. (2006). Numerical and experimental study of a solar equipped with offset rectangular plate fin absorber plate. *Renewable Energy*, *31*(13), 2063–2075. http://doi.org/10.1016/j.renene.2005.10.008

Zhu, J., Jia, H., Cheng, X., Huang, X., Liu, X., & Guo, J. (2019). The design and performance evaluation of a high-efficient flexible solar air heater based on transparent spacer fabric composite. *Solar Energy Materials and Solar Cells*, *201*(July), 110089. http://doi.org/10.1016/j.solmat.2019.110089

LIST OF PUBLICATIONS

Journals

1. G. Sureandhar, G. Srinivasan, P. Muthukumar, S. Senthilmurugan. “Performance analysis of arc rib fin embedded in a solar air heater”, Thermal Science and Engineering Progress (2021): 23: 100891.

2. G. Sureandhar, G. Srinivasan, P. Muthukumar, S. Senthilmurugan. “Investigation of thermal performance in a solar air heater having variable arc ribbed fin configuration”, Sustainable Energy Technologies and Assessments (2022): 52: 102069.

Conferences

1. G. Sureandhar, G. Srinivasan, P. Muthukumar, S. Senthilmurugan. “Performance evaluation of solar air heater having arc-shaped wire rib with varying roughness height on absorber plate” International conference on innovations in Thermo-Fluid Engineering Sciences, ICITFES – 2020, NIT Rourkela, India, 10-12 February, 2019.

2. G. Sureandhar, K. Nayanita, G. Srinivasan, P. Muthukumar. “Selection of Solar Dryers for Winter Drying of Agricultural Products” Sixth International Conference on Poly-generation, 2021.

3. K. Nayanita, G. Srinivasan, G. Sureandhar, and P. Muthukumar. “Numerical Analysis of Drying Kinetics of Spherical Products in a Solar Dryer” 26th National and 4th International ISHMTASTFE Heat and Mass Transfer Conference, 2021.